Fall 2013

# Spectroscopic and Kinetic Study of Copper-Exchanged Zeolites for the Selective Catalytic Reduction of NOx with Ammonia

Shane Adam Bates
*Purdue University*

Graduate School ETD Form 9
(Revised 12/07)

# PURDUE UNIVERSITY
## GRADUATE SCHOOL
## Thesis/Dissertation Acceptance

This is to certify that the thesis/dissertation prepared

By Shane A. Bates

Entitled
Spectroscopic and Kinetic Study of Copper-Exchanged Zeolites for the Selective Catalytic Reduction of NOx with Ammonia

For the degree of Doctor of Philosophy

Is approved by the final examining committee:

Fabio H. Ribeiro
Chair

W. Nicholas Delgass

Bryan W. Boudouris

Aleksey Yezerets

To the best of my knowledge and as understood by the student in the *Research Integrity and Copyright Disclaimer (Graduate School Form 20)*, this thesis/dissertation adheres to the provisions of Purdue University's "Policy on Integrity in Research" and the use of copyrighted material.

Approved by Major Professor(s): Fabio H. Ribeiro

W. Nicholas Delgass

Approved by: Michael Harris 10/14/2013
Head of the Graduate Program Date

# SPECTROSCOPIC AND KINETIC STUDY OF COPPER-EXCHANGED ZEOLITES FOR THE SELECTIVE CATALYTIC REDUCTION OF $NO_X$ WITH AMMONIA

A Dissertation

Submitted to the Faculty

of

Purdue University

by

Shane Adam Bates

In Partial Fulfillment of the

Requirements for the Degree

of

Doctor of Philosophy

December 2013

Purdue University

West Lafayette, Indiana

# ACKNOWLEDGEMENTS

This Ph.D. has been quite a journey. I found myself moving in and out of research groups like it was no one's business. Some may think I am crazy, but it all worked out just fine and I ended up where I needed to be. Of course, all of this would not have been possible without many people I have met along the way. This is where I would like to thank them for continually pushing and encouraging me along the way.

First, I would like to thank my amazing advisors. Professor Fabio Ribeiro has been an inspiration for me as his expansive knowledge of catalysis, his mastery of experimental techniques and troubleshooting, and his attention to detail has allowed me to achieve things I wouldn't have thought possible. Of course, his kindness and sense of humor have also kept me sane at times when I was facing major issues. I hope to be able to carry the things I have learned from him in my future career. Professor Delgass was also an inspiration for me. His vision of catalysis - his "mosaic" as he likes to call it, was a concept I tried to keep in mind throughout my research. His great knowledge of catalysis and spectroscopic techniques was also a great help in understanding my work. I really enjoyed his excitability from hearing about the research in our group and in general, his sociability. I consider Professor Delgass to be a true gentleman. I really appreciate that both of my advisors are the biggest advocates for their students. This is very evident

to me. They may grill us internally, but have nothing but good things to say to someone outside the group. I really believe they have prepared me for a job, not just in catalysis, but in any field because the way they approach problems is applicable in any field. To my advisors – Thank you.

I would also like to acknowledge my former advisor, Professor Chelsey Baertsch, who left at the end of 2010 to be a mom for a while. While working under her, I began to grasp the concepts in catalysis, and I believe the work I did with her prepared me for the work I did with Professor Ribeiro and Professor Delgass. I would like to thank her for instilling her knowledge of catalysis on me and I wish her well on the west coast.

I would also like to thank the other main collaborators I have worked with along the way. I would like to acknowledge Dr. Jeffrey T. Miller, who I have worked with on countless occasions at the Advanced Photon Source at Argonne National Labs. He has spent many days and nights teaching me about X-ray absorption spectroscopy and has been a part of my work since the beginning. His extensive knowledge in many fields of catalysis makes conversations with him very enjoyable as he is a "Jack of all trades." Professor William F. Schneider has also had a great impact on my work. His group at Notre Dame has collaborated with ours from the beginning of my work. His conceptual understanding of the way reactions work at a molecular level has always amazed me. Needless to say, his point of view from a theoretical perspective has been a great contribution to the work I have done and I thank him for that. Dr. Aleksey Yezerets is the external member of my committee and his group has aided our group in our work the whole way through. I

would like to thank him for his great insight into our work and his ability to give amazing suggestions to improve my work. He has a way to explain complicated concepts in a very simple way that makes everything make sense. His perspective coming from industry has always been a welcomed change and has allowed me to think about things in a different way. Of course, his research group at Cummins has also given very valuable input to my work and I would also like to thank them for their support.

I would like to thank Professor Bryan Boudouris for his willingness to be the final member of my committee and spend his time to help me become a better researcher.

I would also like to thank Deb Bowman for essentially keeping me on track with the whole process of getting through graduate school. All the paperwork she has filed for me over the years is ridiculous. It is unfortunate she is not here in the department anymore. We all miss her, but we are glad things worked out for her. I would also like to thank other people in the department including Yury Zvinevich, Jeff Valley and Jason Davenport.

Now, I would like to thank many of the people I have met here at Purdue who have become very close friends and helped me along the way in no particular order. These people include Vincent Kerspersker, Bryce Sturtevant, Sara Yohe, Steve Gaik, Paul Dietrich, Julie Renner, and Mike Detwiler, Grayson Ford, Andrew Smeltz, Rob McCarthy, Dave Balachandran, and Clancy Kadrmas. I would like to thank all of them

for their support over this time in graduate school. These people have kept me sane. They have provided encouragement and positive attitudes when I needed it the most.

Finally, I would like to thank my entire family back home in Pennsylvania. I know I did not get to see them a lot over the past five years and I have missed a lot, but they have been there with me every step of the way. I love them and thank them for keeping with me through this. I love you guys!

TABLE OF CONTENTS

Page

Page

Page

# LIST OF TABLES

Appendix Table Page

# LIST OF FIGURES

Figure Page

Figure Page



Appendix Figure

Appendix Figure Page

Appendix Figure Page

Appendix Figure Page

Appendix Figure Page

Appendix Figure Page

Appendix Figure Page

Appendix Figure Page

# NOMENCLATURE

Various nomenclatures will be used throughout this document for names of samples. In this study, two zeolites will be used. Those are SSZ-13 and ZSM-5. When a zeolite is in the H-form, the name will have an H- in front of it. When Cu or ammonium exchanged, it has a Cu- or $NH_4$- in front. Additionally, there are multiple ways which these different papers have identified the Cu weight loading. The first is by weight percent. This nomenclature was used primarily in Chapter 3. When that manuscript was written, we had not decided on the best way to report Cu loading. Chapter 2 uses a copper to aluminum atomic ratio (Cu:Al), which allows us to incorporate the Al content. In chapter 4, many samples are tested, therefore a new naming scheme was devised. The SSZ or ZSM were used as identifiers for the zeolite type. The first number after the identifier was the Si:Al ratio. The second number was the Cu:Al ratio. For example, Cu-SSZ-4.5-0.09 is a Cu exchanged SSZ-13 sample with Si:Al =4.5 and Cu:Al = 0.09. To summarize:

Chapter 2: Cu:Al ratios used to identify samples

Chapter 3: Cu wt% used to identify samples. Cu:Al ratios are also given initially.

Chapter 4: Each specific sample identified by zeolite identifier, Si:Al, and Cu:Al. When speaking in general terms, SSZ-13 and ZSM-5 are used.

# ABSTRACT

Bates, Shane A. Ph.D., Purdue University, December 2013. Spectroscopic and Kinetic Study of Copper-Exchanged Zeolites for the Selective Catalytic Reduction of $NO_x$ with Ammonia Major Professors: Fabio H. Ribeiro and W. Nicholas Delgass.

The recent application of metal-exchanged, small-pore zeolites for use in the selective catalytic reduction (SCR) of $NO_x$ with ammonia ($NH_3$) for automotive deNOx applications has been a great stride in achieving emission standard goals. Copper-exchanged SSZ-13 (Cu-SSZ-13), the small-pore zeolite in this study, has been shown to be very hydrothermally stable and active under conditions presented in the exhaust of the lean-burn diesel engine [1-3]. In this work, detailed studies were performed to identify many aspects of the active site(s) in Cu-SSZ-13 in order to learn about the standard SCR mechanism.

A series of seven Cu-SSZ-13 samples were created with silicon to aluminum atomic ratios (Si:Al) of 4.5 and varying Cu loadings ranging from a copper to aluminum atomic ratio (Cu:Al) of 0 to 0.35. Standard SCR kinetics were collected over each with the standard conditions being 320 ppm NO, 320 ppm $NH_3$, 10% $O_2$, 8% $CO_2$, and 6% $H_2O$ at 473 K. A linear increase in rate per gram was observed as the Cu:Al ratio increased up to

Cu:Al = 0.2, indicating the active Cu species was being populated in that region of Cu loading. Further characterization of the Cu in this region with *operando* x-ray absorption spectroscopy (XAS) revealed this Cu species to be a mix of isolated Cu(I) and Cu(II) under reaction conditions. Density functional theory (DFT) and statistical simulations were able to identify the location for the active Cu species as exchanged into the six-membered ring of the SSZ-13 structure. Ambient ultraviolet–visible–near infrared spectroscopy (UV-Vis-NIR) and XAS showed the precursor to the active Cu species was a hydrated Cu(II) which tracked with the standard SCR rate. Above Cu:Al = 0.2, ambient UV-Vis-NIR and XAS showed a $Cu_xO_y$ species began to form which was not active for standard SCR. Thus, the active Cu was identified to be an isolated Cu exchanged into the six-membered ring of the SSZ-13 and after Cu:Al = 0.2, a new $Cu_xO_y$ species began to form. Additionally, the number of Brønsted acid sites was determined to not track with the standard SCR rate per gram, indicating the kinetically relevant steps in these samples took place on the Cu.

The active state of the isolated Cu was also explored. Under reaction conditions, our group has previously observed a mix of Cu(I) and Cu(II) to be present [4, 5]. Additionally, from DFT, the most stable Cu species under various oxidizing conditions in SCR were a two-coordinate Cu(I) and four-coordinate Cu(II). From these observations, we proposed a redox cycle between isolated Cu(I) and isolated Cu(II) [4, 5]. To probe this redox cycle and refute other hypotheses [6], the proposed half-reactions were removed in order to drive the Cu into primarily a Cu(I) state or Cu(II) state. When $O_2$ was removed, the Cu was driven into primarily an isolated Cu(I) state. When NO or $NH_3$

were removed, the Cu became completely Cu(II). Thus, we illustrated the redox cycle existed in the active Cu and should be incorporated into proposed standard SCR mechanisms.

Finally, techniques for determining the accurate number of Brønsted acid sites were developed. Three techniques using $NH_3$ as a titrant were proven to selectively titrate Brønsted acid sites when compared to site counts from n-propylamine decomposition over H-ZSM-5. In Cu-ZSM-5, the results also matched, suggesting the $NH_3$ procedures could also avoid titrating Cu sites. In H- and Cu-SSZ-13, the $NH_3$ titrations gave close to four times higher counts of Brønsted acid sites, suggesting the small pore openings cause n-propylamine to be mass transfer limited and the close proximity of Brønsted sites to cause n-propylamine to block itself. We suggest that $NH_3$ is an ideal titrant to use for small-pore zeolites. Thus, these procedures may be attractive for deNOx applications where $NH_3$ is a reactant in the selective catalytic reduction reactions.

# CHAPTER 1. INTRODUCTION

## 1.1 Introduction to the Selective Catalytic Reduction of $NO_x$ with $NH_3$

### 1.1.1 $NO_x$ Abatement through Vehicular Exhaust After-treatment

When hydrocarbon-based fuels are combusted for energy, they release a variety of environmentally unfavorable products, including nitrogen oxides ($NO_x$), carbon monoxide (CO), carbon dioxide ($CO_2$), and unused hydrocarbons[7]. $NO_x$ gases have been associated with helping to produce smog, acid rain, and global warming, which makes them an unwanted side products[8]. Figure 1.1 shows how different sectors perform in the area of $NO_x$ emissions. In the US, the automobile industry is responsible for nearly one third of all $NO_x$ emissions.


Figure 1.1 NOx emissions in the US separated by sector adapted from EPA data collected in 2008 [7]

Other major producers of $NO_x$ in the US are stationary applications which produce power through combustion processes, chemical or industrial processes, and non-road equipment. In the past 35 years, the allowable amount of $NO_x$ released into the air from on-highway vehicles has become more stringent. Figure 1.2 visualizes this trend of increased regulations. The current regulations for allowable $NO_x$ and particulate matter are much lower now, with the current maximum values being close to 1% of what they were in the 1970s.

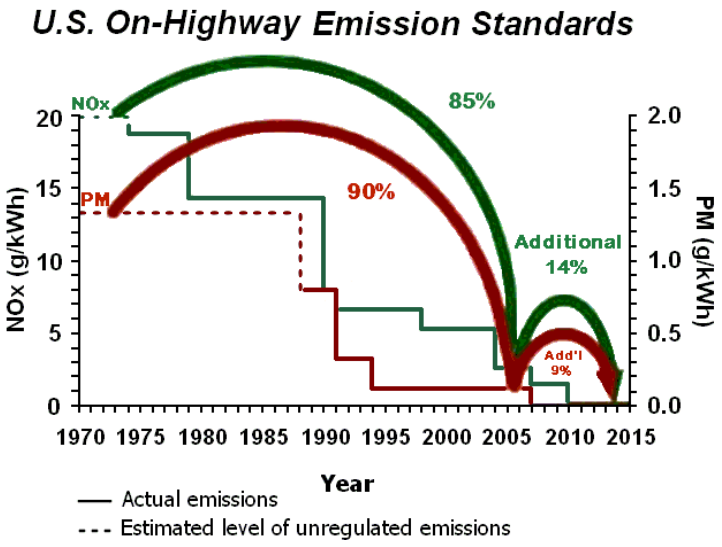


Figure 1.2. Schematic of regulations to step down NOx automotive emissions proposed by the US EPA [8].

This illustrates the need for improved technology that can meet the increasing regulations. Catalytic technologies are preferred for $NO_x$ abatement because they are very efficient and relatively inexpensive[9]. NO decomposition to nitrogen ($N_2$) and oxygen ($O_2$) has

been considered as a possible solution, however, no catalyst has been successful in achieving conversions high enough to make it a viable option in an automotive application[10]. $NO_x$ from gasoline combustion is efficiently removed by a three-way catalyst (TWC), which reduces $NO_x$ to $N_2$, oxidizes CO to $CO_2$, and oxidizes unreacted hydrocarbons to $CO_2$ [10, 11]. Unfortunately, TWC cannot be utilized in the case of a lean-burn diesel engine because of its oxygen-rich exhaust. The TWC needs to have a stoichiometric air to fuel (ATF) ratio of 14.6:1, whereas lean fuel combustion occurs closer to ATF ratios of 25 [12]. Figure 1.3 illustrates the regions of ATF ratio where the TWC can be utilized.

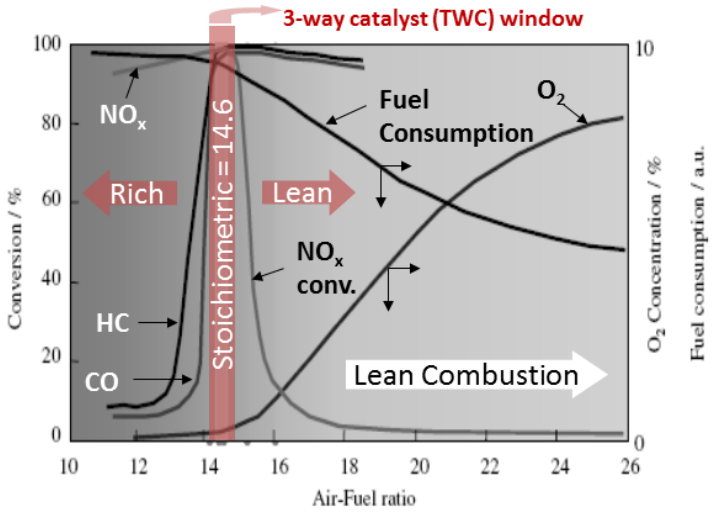


Figure 1.3 NOx conversion, fuel consumption and $O_2$ concentration as a function of ATF. LNT catalysts operate at ATF ratios higher than stoichiometric [12].

Given the inability of the TWC to perform at the conditions produced by a diesel engine, other technologies have been researched and developed. Two of the technologies that

have been implemented are selective catalytic reduction (SCR) and $NO_x$ storage-reduction (NSR). NSR works based on cyclic operation between lean and rich phases over a catalyst with two components which typically are a noble metal redox component and an alkaline-earth storage component on a high surface area support[13]. $NO_x$ is stored as nitrates during lean operation and periodically, hydrogen gas is flown over to reduce the nitrates to $N_2$. The SCR reaction operates with the introduction of a reductant such as ammonia ($NH_3$), urea, or small hydrocarbons, which allow for continuous conversion of $NO_x$ to $N_2$ with very high selectivity[14]. The focus of this work has been on the standard SCR reaction over metal-exchanged zeolites. With the new small-pore, metal-exchanged zeolites which have been found to be very active for these reactions, it is a very exciting time to be a part of this field of research.

### 1.1.2 The SCR Reactions

There are several reactions involving SCR with $NH_3$. Today's diesel exhaust contains $NO_x$ mostly in the form of nitric oxide (NO). Only a small portion of $NO_2$ is usually present, which makes standard SCR the most basic SCR reaction that is encountered (Eq. 1) [15].

$$4NO + 4NH_3 + O_2 \rightarrow 4N_2 + 6H_2O \qquad (1)$$

When a mixture of NO and $NO_2$ are present in a ratio of 1:1, the reaction proceeds much faster, which has been called the fast SCR reaction (Eq. 2) [16-18].

$$2NO + 2NO_2 + 4NH_3 \rightarrow 4N_2 + 6H_2O \qquad (2)$$

When an NO:$NO_2$ ratio exists higher than 1:1, $NO_2$ can react with $NH_3$ by itself, which has been called slow SCR (Eq. 3)), however, it is been seen to exhibit similar rates as standard SCR despite its name[5].

$$4NO_2 + 3NH_3 \rightarrow 3.5N_2 + 6H_2O \quad (3)$$

Together, these three reactions form the most common SCR reactions encountered under various gas conditions.

### 1.1.3 SCR Catalyst Formulations

Vanadia-type catalysts were the first to be studied widely for the SCR reaction. They have been used most efficiently in commercial de$NO_x$ processes for stack gases from power plants and other stationary applications[19]. The typical formulations that have been studied are $V_2O_5/TiO_2$ and $V_2O_2$-$WO_3/TiO_2$[20, 21]. Though very useful in stationary applications, dynamic operations necessary for mobile applications limit the ability of these catalysts to effectively remove $NO_x$. High activity for the oxidation of $SO_2$ to $SO_3$, a decrease in activity and selectivity above 823 K, and the volatility and toxicity of the vanadia species above 823 K are all concerns with these types of catalysts[22-24]. This has led researchers to look for different catalyst formulations for mobile applications.

Metal-exchanged zeolites have been found to be especially suited for lean-burn conditions. Zeolites containing narrow pores have been extensively researched, especially ZSM-5[23, 25-30]. The downfall of these catalysts is that they begin to break down at high temperatures in the presence of water, making the hydrothermal stability of

these zeolites the main issue for commercial use. Most recently, zeolites containing the chabazite structure (CHA), including SSZ-13 and SAPO-34, have been shown to be very hydrothermally stable where other zeolites fall short [2, 3, 31, 32]. This was suggested to be attributed to the small pores of the CHA structure and where Cu tends to be located in the structure just above the six ring[33]. The largest pore opening is 3.8 Å, whereas in ZSM-5, pores are 5.1Å [34].

### 1.1.4 The SCR Mechanism

With the addition of $NO_2$ significantly increasing SCR rates (as in fast SCR), it has been presumed that NO oxidation to $NO_2$ is the rate limiting step of the reaction[23, 26, 27]. The increase in SCR rate over NO oxidation rates has been explained by adsorbed $NO_2$ reacting away before $NO_2$ desorption, which is the proposed rate limiting step of NO oxidation alone[35]. The exchanged metal in these zeolites plays an important role in standard SCR. H-ZSM-5 was found to be active for fast SCR, but not for standard SCR, suggesting that a metal needs to be present for NO oxidation to proceed. This was found to be true for Fe-ZSM-5, which could perform standard SCR. This suggests NO oxidation takes place on exchanged metal and the reduction to $N_2$ occurring elsewhere in the zeolite structure[23, 25-27]. The stoichiometry of Equations 1 and 2 implies that one N from $NO_x$ species and one N from $NH_3$ form the final product, $N_2$. Sun et al. [25] showed this to be true with isotope switching experiments.

There are several proposed SCR mechanisms. With its complexity, only a few proposed mechanisms will be discussed here in detail. A recent publication by Metkar et al. [36]

goes into detail for the mechanisms of NO oxidation and standard SCR over Fe-ZSM-5 monolith catalysts. They derive the standard SCR mechanism based on the similarities they see between NO oxidation and standard SCR rates, activation energies, and reaction orders with respect to NO and $O_2$. In each case, they find similar values, leading them to conclude that the NO oxidation step is rate limiting. In their NO oxidation study, they propose NO and $O_2$ can adsorb on two nearby metal sites (S1). NO adsorbs intact, while $O_2$ dissociates. NO and dissociated O react to form $NO_2$. When water is present, adsorbed $NO_2$ follows steps directly and indirectly to a nitrite formation (acid form) on a metal site (HONO-$S_1$). When $NH_3$ is present (as in standard SCR conditions), it reacts from an acid site (S2) with the adsorbed nitrite to form an intermediate ammonium nitrite ($NH_4NO_2$) species which decomposes to the final products of $N_2$ and $H_2O$.

$$HONO - S_1 + NH_3 - S_2 \leftrightarrow [NH_4NO_2] \rightarrow N_2 + 2H_2O + S_1 + S_2 \quad (4)$$

It was implied that this work could be generalized for all metal-exchanged zeolite systems; however, work in our group on Cu-SSZ-13 and Cu-ZSM-5 catalysts does not show any similarities between dry NO oxidation and standard SCR kinetics, suggesting that a different mechanism and site could be in play for standard SCR. Our NO oxidation experiments on Cu-SSZ-13 show a reaction order for NO of approximately 1.6 under dry NO oxidation conditions (300 ppm NO, 150 ppm $NO_2$ 10% $O_2$) and ~1.1 under wet NO oxidation ($H_2O$ added), while our SCR data shows an NO order of approximately 0.8 (300 ppm NO, 300 ppm $NH_3$ 10% $O_2$, 7% $H_2O$, 8% $CO_2$). The order of $O_2$ under NO oxidation is nearly 1, whereas under standard SCR it is 0.5. Additionally, we have several catalysts which are active for standard SCR and not for dry NO oxidation. These signs point to the possibility that NO oxidation may not be rate limiting under certain

conditions or even a step in the mechanism. However, it is possible that the presence of $NH_3$ allows NO oxidation to occur and for it to be rate limiting. There is still a gap in the knowledge between NO oxidation and NO oxidation under standard SCR conditions, and this gap represents some of ongoing work within our research group.

Grossalle et al. [37] proposed a mechanism for fast SCR which can encompass all types of SCR reactions ($NO_2/NO_x$ varied from 0 to 1) on Fe-ZSM-5 that indicates the roles of each reactant and rate limiting step. The role of $NO_2$ is to form surface nitrates and nitrites via $NO_2$ dimerization and disproportionation as seen in reactions 5-7

$$2NO_2 \leftrightarrow N_2O_4 \qquad (5)$$

$$N_2O_4 + O^{2-} \leftrightarrow NO_2^- + NO_3^- \qquad (6)$$

$$NO_2 + NO_2^- \leftrightarrow NO + NO_3^- \qquad (7)$$

The role of NO is to reduce the nitrates to nitrites (a second type of NO oxidation).

$$NO + NO_3^- \leftrightarrow NO_2 + NO_2^- \qquad (8)$$

The role of $NH_3$ is then to react with nitrites to form the unstable compound, ammonium nitrite, which selectively decomposes to $N_2$.

$$2NH_3 + H_2O \leftrightarrow 2NH_4^+ + O^{2-} \qquad (9)$$

$$NH_4^+ + NO_2^- \leftrightarrow [NH_4NO_2] \rightarrow N_2 + 2H_2O \qquad (10)$$

The full kinetic model can be seen in Figure 1.4. In this model, an alternate mechanism can occur through nitrate species, which, if not reduced by NO, form ammonium nitrate ($NH_4NO_3$). Indeed, a significant amount of $NH_4NO_3$ was expected based on their nitrogen balance, leading them to believe that the rate determining step in fast SCR was the reduction of nitrates to nitrites by NO, or NO oxidation. Many parallels are seen

between this mechanism and that proposed by Metkar et al.[36], with the main difference being the initial NO oxidation to an adsorbed $NO_2$ species over a metal site is not necessary when $NO_2$ is already present in the gas phase.

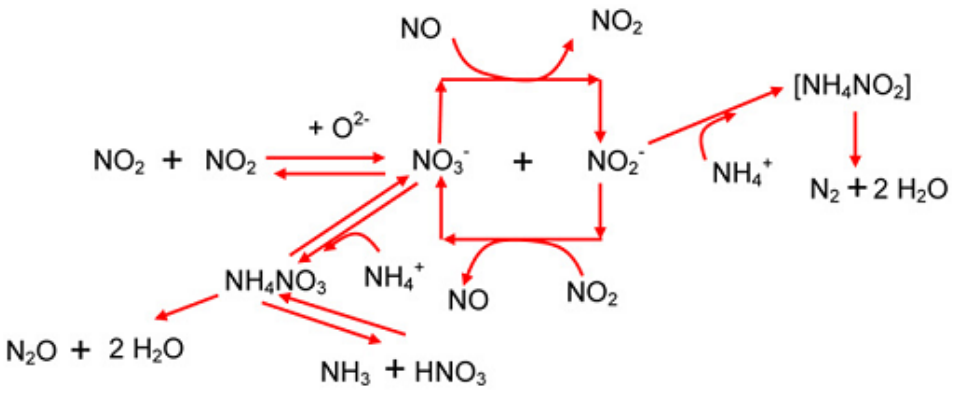


Figure 1.4 Full SCR mechanism proposed by Grossale et al. [37]

Still, other mechanisms over Fe-ZSM-5 catalysts are proposed in which two nearby Brønsted sites with $NH_3$ adsorbed form a bridge with $NO_2$ across a zeolite cage and then NO reacts with the resulting complex to form the products[27, 38]. These mechanisms are all performed on Fe exchanged zeolites, which may or may not be true for all metal exchanged zeolites.

A recent mechanism proposed by Gao et al. [39] on Cu-SSZ-13 suggests the chemistry with $NH_3$ and NO happen on the active Cu, with the Brønsted acid sites playing a limited role. Figure 1.5 shows the proposed mechanism. With many different interpretations of the mechanistic steps of reaction as well as role of different sites (active metal and

Brønsted acid sites) in metal-exchanged zeolites, the primary goal of the work presented here is to have a better understanding of the active site(s) so that accurate mechanistic models can be determined.

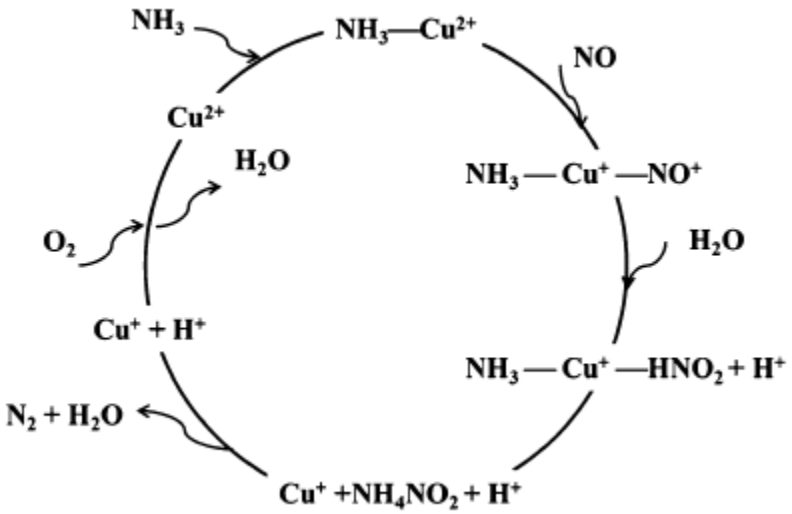


Figure 1.5 Proposed low temperature standard SCR reaction mechanism by Gao et al. [39] on Cu-SSZ-13 which proceeds through active isolated Cu species.

### 1.1.5 Thesis Overview

Understanding the active sites for standard SCR on Cu-SSZ-13 is the primary focus of this work. Specific details and literature review of the sites are reserved for the introductions of Chapter 2-4. The primary contribution in Chapter 2 is the identification of the active Cu site in SSZ-13 for standard SCR as an isolated Cu exchanged into two Brønsted acid sites in the six-membered ring of the zeolite. This was determined through a kinetic study in conjunction with spectroscopic techniques and statistical analysis. Secondary Cu species were also observed after the active sites were saturated and

explored. Chapter 3 uses *operando* x-ray absorption spectroscopy to look at the state of the active Cu under standard SCR conditions and verify the Cu(I)-Cu(II) redox cycle proposed in previous work in our group [40] by transient reactant cutoff experiments. From these two studies, we gained a clear view of the Cu species active for standard SCR. We learned the specific Cu species and location as well as the active state of the Cu. The final study focused on discovering techniques to quantify Brønsted acid sites in order to determine their role in the standard SCR kinetics. Three techniques were developed in which $NH_3$ could selectively and quantitatively titrate Brønsted acid sites. The study also showed that $NH_3$ is an ideal probe molecule for SSZ-13 as larger probe molecules (n-propylamine) may have difficulty accessing all the sites. In our study, the number of Brønsted acid sites did not affect the standard SCR rate per gram. The isolated Cu site was the location for the kinetically relevant steps.

# CHAPTER 2. KINETIC AND SPECTROSCOPIC EVIDENCE FOR THE ACTIVE COPPER SITE IN STANDARD SCR ON CU-SSZ-13

## 2.1 Abstract

Copper exchanged SSZ-13 catalysts were used for the standard selective catalytic reduction (SCR) reaction at 473 K with 320 ppm NO, 320 ppm $NH_3$, 10% $O_2$, 8% $CO_2$, and 6% $H_2O$. The copper to aluminum atomic ratio (Cu:Al) was varied from 0 to 0.35 over seven H- and Cu-SSZ-13 samples with silicon to aluminum atomic ratio (Si:Al) of 4.5, or an effective Si:Al = 6.9 based on the number of Brønsted acid sites per total Al ($H^+$:Al) of 0.65 in the H-SSZ-13 determined in a previous study [41]. The standard SCR rate per gram was observed to increase linearly up to Cu:Al = 0.2 with a maximum rate of 3.8 x $10^{-6}$ mol NO g $cat^{-1}$ $s^{-1}$. The rate per gram was observed to track with a hydrated Cu(II) species in ultraviolet-visible spectroscopy, which was shown to become the active Cu under *operando* x-ray absorption spectroscopy (XAS). Density functional theory calculations showed that an exchanged isolated Cu(II) in the six-membered ring of SSZ-13 is the most stable position for isolated Cu(II). Statistical simulations show a maximum number of isolated Cu in six-membered rings exchanged with 2 Al reach a maximum at Cu:Al = 0.23 for Si:Al = 5, which matched with the maximum observed rate per gram, indicating Cu(II) was the active Cu species. Above Cu:Al = 0.2, a new $Cu_xO_y$ species was observed from ambient XAS measurements which was not active for standard SCR because the Cu:Al = 0.35 rate tracked with the amount of hydrated Cu(II).

The number of available Brønsted acid sites in the samples was shown to not be involved in the kinetically relevant steps for standard SCR due to the inverse relationship of the rate per gram and number of Brønsted acid sites.

## 2.2 Introduction

Metal-exchanged small pore zeolites have recently been adopted for use in the selective catalytic reduction (SCR) with ammonia reaction for mobile deNOx applications. The metal exchanged chabazite (CHA) structure has been of particular interest, which has two analogues, SSZ-13 and SAPO-34. When exchanged with Cu or Fe, they have been shown to be able to withstand the harsh hydrothermal conditions present in a diesel exhaust system yet still efficiently remove $NO_x$[1-3].

One current area of interest is the role of the exchanged metal in the standard SCR reaction. Fickel et al.[33] using Rietveld refinement of variable temperature XRD identified the location of isolated Cu species in the SSZ-13 structure centered slightly above the six-membered ring. A follow-up study by Korhonen et al. [42] ruled out the possibility of Cu dimers in a Cu-SSZ-13 sample with copper to aluminum atomic ratio (Cu:Al) equal to 0.18 and silicon to aluminum atomic ratio (Si:Al) equal to 9, and concluded that isolated Cu(II) near the six-membered ring was the active site for standard SCR in Cu-SSZ-13. Kwak et al.[43] suggested multiple positions for isolated Cu(II) rather than only one near the six-membered ring based on two different Cu(II) signatures in low Cu loading samples during $H_2$-TPR and FTIR. Gao et al.[44] used EPR to probe isolated Cu(II) up to near 100% ion exchange and identified two possible positions for

isolated Cu. Wang et al.[45] observed the standard SCR rate per total Cu to be significantly improved in SAPO-34 which contained isolated Cu(II) over a sample which contained extra-framework CuO clusters. While most studies have regarded isolated Cu to be in the 2+ oxidation state under reaction conditions, work in our group using *operando* X-ray absorption spectroscopy experiments [4, 5] has demonstrated the appearance of a Cu(I) signature at 8983 eV under standard SCR conditions, indicative of a redox cycle between the two during SCR. In this study, we demonstrate through reaction kinetics, UV-Vis NIR, and *operando* XAS that this isolated Cu is the active site for standard SCR. The Cu species that is the precursor to the active isolated Cu was also identified under ambient conditions using UV-Vis-NIR.

Because exchanged, isolated Cu(II) must be charge-compensated by two framework Al tetrahedral (T-) sites, the density of these species is a function both of the Si:Al ratio and the Cu loading. The distribution of Al T-sites and thus of candidate Cu(II) sites is difficult to assess experimentally. Here we estimate the density of candidate sites by statistical analysis [46] of the SSZ-13 framework under the assumption that the Al obey the Loewenstein's rule [47] prohibition against first-nearest-neighbor Al T-sites. We show that this model gives an estimate of Cu(II) site density consistent with the experimentally observed saturation of these sites.

Kinetic measurements on Cu-SSZ-13 under standard SCR conditions have been reported in the literature[44, 48] and there is a large body of work on other zeolites, including significant contributions on ZSM-5[28, 29, 36, 38, 49-51]. The work by Gao et al.[44]

described the possibility of internal mass transfer effects in the SSZ-13 crystal structure, which they believed to occur based on a loss in rate per mole Cu with increasing Cu loading up to 100% ion exchange and calculation of effectiveness factors much less than unity. In the current study, we were able to report differential kinetic information on Cu-SSZ-13 samples for standard SCR in the low temperature region (< 473 K) in the absence of mass transfer effects. Metkar et al.[36, 52] also explored diffusion limitations while varying washcoat thicknesses in Cu and Fe zeolite monoliths in which they concluded were negligible in the lower temperature region.

The role of Brønsted acidity is another important aspect of standard SCR. One reaction mechanism suggests $NH_3$ is activated on a Brønsted acid site, forming $NH_4^+$, which then reacts with $NO_x$ species [23, 24, 28, 36, 53, 54]; however, a study by Brandenberger et al. [55] has suggested that it is only important for binding and dispersing metal ions as they saw similar conversions of NO and $NH_3$ between 473-573 K in Fe-ZSM-5 with 96% of its Brønsted acid sites poisoned. In this study, ammonia stored under standard SCR conditions will be quantified via transient $NH_3$ cutoff experiments, which probe the role of Brønsted acidity on the reaction mechanism. The total amount of Brønsted acid sites will also be determined for each sample and compared with the $NH_3$ quantification experiments and standard SCR rates.

## 2.3 Experimental Methods

### 2.3.1 Cu-SSZ-13 Synthesis and Characterization

The H-SSZ-13 was synthesized following a recipe published by Fickel et al. [2, 33], which was derived from the original synthesis by Zones et al. [56-58]. The resulting H-SSZ-13 structure was confirmed via X-ray diffraction (XRD) with a Bruker D8 Focus X-ray Diffractometer with a Cu K (alpha) source. The diffraction pattern was observed to have all the appropriate crystal planes for the CHA structure present [34, 59-61]. BET surface areas for many different batches of H-SSZ-13 ranged in from 580 – 601 $m^2$ $g^{-1}$ and t-plot pore volumes ranged from 0.24-0.26 $cm^3$ $g^{-1}$[61, 62]. Copper was deposited into the H-SSZ-13 by liquid phase ion exchange with a $Cu(NO_3)_2$ solution at a pH of 5 ±0.2. Atomic absorption spectroscopy experiments gave Si:Al ratios ranging from 4.3-4.5 and Cu:Al ratios ranging from 0.02 to 0.35, depending on the concentration of Cu in the solution. The number of Brønsted acid sites was measured by dosing each sample with 500 ppm $NH_3$ (from 3.0% $NH_3$/ Ar, Praxair) in UHP He (99.995%, Indiana Oxygen) at 433 K for two hours until complete saturation. The sample was flushed for eight hours at 433 K [41, 63]. The sample was then placed in U-shaped quartz tube surrounded by quartz wool and inserted into a Micromeritics Autochem II 2920 Chemisorption Analyzer equipped with a thermal conductivity detector (TCD) and Agilent 5975C mass selective detector (MSD). A temperature programmed desorption (TPD) was performed with a 10 K $min^{-1}$ temperature ramp from 298 K to 873 K in 50 sccm UHP He. Contributions from fragments of $H_2O$ in m/z = 17 were removed to give a signal only resulting from $NH_3$. The $NH_3$ feature in m/z = 17 was quantified to determine the number of available Brønsted acid sites.

### 2.3.2 Kinetic Data Collection

SCR kinetic experiments were performed via a bench top tubular glass reactor with a quartz frit located in the middle of the tube to hold a catalyst bed. The diameter of the center section of the reactor was narrowed to 3/8" and catalysts were diluted with silica gel (Fisher Chemical, Catalog No. S817-1) so that the catalyst bed height could be increased to help prevent bypass of any reaction mixture. The standard SCR reaction (conditions are described below) was performed on the silica gel and no conversion of NO or $NH_3$ was observed; therefore, it was considered inert. Particle sizes used were 125 – 250 μm. A plug of small quartz beads of *ca.* 3 mm diameter were placed on a wire mesh approximately 6 inches above the catalyst bed in order to ensure proper gas mixing before reaching the bed. Thermocouples were placed just above and just below the bed to ensure that no significant temperature gradients existed through the bed. Before entering the reactor, all gases except $NH_3$ passed through a pre-heater assembly consisting of a helical coil of 3 in. diameter made out of 0.25 in. diameter stainless steel tubing inside a temperature controlled hollow cylindrical Watlow® ceramic fiber heater. Water was introduced into the system by a heated shell-type humidifier (Perma Pure MH-Series) where the diffusion of water across a Nafion membrane into the gas mixture was controlled by the temperature setting. Ammonia was added just above the plug of quartz beads in the reactor in order to remove the possibility of thermal gas phase reactions occurring before reaching the reactor. All kinetic measurements were taken at <20% conversion, so that all portions of the catalyst bed were exposed to nearly the same gas concentrations and the kinetics remained consistent through the entire bed. Typical gas conditions used were ~320 ppm NO (from 3.6% NO/Ar, Praxair), ~320 ppm $NH_3$ (from

3.0% $NH_3$/ Ar, Praxair), 8% $CO_2$ (liquid, Indiana Oxygen), 10% $O_2$,(from 99.5%, Indiana Oxygen), 6% $H_2O$ (de-ionized water), and balance He (99.995%, Indiana Oxygen). Total flow rates used were approximately 1.5 L $min^{-1}$. The effluent gases from the reactor were analyzed online by an MKS Multigas™ 2030 gas phase FT-IR spectrometer. With on-board calibrations provided by MKS, the spectrometer was used to monitor NO, $NO_2$, $N_2O$, $NH_3$, $CO_2$, and $H_2O$ concentrations with a 0.95 second resolution. Dinitrogen in the effluent gas was measured in initial samples using an Agilent 6890 gas chromatography unit with a series of packed columns including Porapak Q, Carboxen 1000, and Molsieve 5Å. The $N_2$ value obtained during steady state reaction in initial samples was compared to the reactants consumed through the reactor to ensure no side reactions were occurring on this set of catalysts, which matched within the 90% confidence interval.

Transient $NH_3$ cutoff experiments were performed starting under steady state standard SCR conditions at 433 K in the same PFR unit in the absence of $CO_2$ with a total flowrate of 1.5 L $min^{-1}$. Ammonia was removed from the standard SCR gas mixture and replaced with an equal flowrate of $CO_2$ with a 2 position, 6 port, actuated valve (Valco Instrument Company, Inc.; Model E26UWE) to keep the same total feed flowrate. The reverse switch was also performed on a clean catalyst surface by adding $NH_3$ and removing $CO_2$. The temperature programmed desorption (TPD) following the cutoff of $NH_3$ was performed after ~60 minutes of flushing the catalyst in UHP He at 1.5 L $min^{-1}$. A 5 K $min^{-1}$ ramp was used up to 823 K. The temperature ramp was non-linear due to the system not being built for TPD experiments.

### 2.3.3 X-ray Absorption Measurements

The Cu K (8.979 keV) edge XAS data were collected on the insertion-device beam line of the Materials Research Collaborative Access Team (MRCAT, Sector 10 ID) at the Advanced Photon Source, Argonne National Laboratory. A cryogenically cooled double-crystal Si (111) monochromator was used in conjunction with an uncoated glass mirror to minimize the presence of harmonics. Measurements were made in transmission mode with the ionization chambers optimized for the maximum current with linear response ($\sim 10^{10}$ photons detected $s^{-1}$) using gas mixtures to give 10% absorption in the incident X-ray detector and 70% absorption in the transmission X-ray detector. A Cu foil spectrum was acquired simultaneously with each measurement for energy calibration. The *operando* reactor gave a total absorption ($\mu x$) between 1 and 3 and an edge step ($\Delta \mu x$) between 0.5 and 1.5. X-ray absorption near edge structure (XANES) and extended X-ray absorption fine structure (EXAFS) measurements were collected in quick scan mode while the catalyst was exposed to different conditions, which allowed for a spectrum to be collected every 135 seconds. In each case, the data were averaged over three spectra. The Cu K edge has a number of features which were utilized to determine the extent of Cu reduction under various gas conditions. The peak at 8977 eV is representative of a symmetry forbidden transition from 1s to 3d for Cu(II), which is able to be seen because of mixing of the 3d and 4p orbitals [64]. The peak at 8983 eV represents the 1s to 4p transition for Cu(I) in a two coordinate state [65-72]. The peak at 8987 corresponds to the 1s to 4p transition for Cu(II) [66], and the white line intensity seen at 8995 eV corresponds to Cu(II) [71].

### 2.3.4 Operando XAS Experimental Setup

A low X-ray absorbing carbon tube reactor was utilized to perform *operando* XAS experiments [5, 73]. A 4 mm ID carbon reactor was secured inside an aluminum heating block which had a 25.4 x 2 mm wide slit in the center to allow x-rays to pass through the reactor. Four 100 W heating cartridges (Omega Engineering) were inserted into the aluminum block to provide heating. Wire mesh was used to hold the catalyst bed in the correct position to be analyzed by XAS, and was supported by a 1/16" tube stretching from the wire mesh to the bottom of the reactor. Starting at the bottom of the catalyst bed, a plug of quartz wool was pushed into place for support. Following this, a layer of glassy carbon beads consisting of the same material of the reactor was added to the quartz wool to create a flat surface for the catalyst bed to sit. Next, 8-20 mg of catalyst powder sieved to 125-250 μm was added. Another layer of quartz wool was inserted and finally, a layer of crushed quartz (> 250 μm) was added to help mix the gases entering the bed. A thermocouple was inserted into the top of the catalyst bed to monitor temperature. Gases were introduced sequentially into the lines going to the reactor. Helium carrier gas flowed through a heated shell-type humidifier (Perma Pure MH-Series) to bring DI $H_2O$ into the system. Following this, NO (3000 ppm in $N_2$, Matheson Tri-Gas) was introduced. Next, $O_2$ (20% in He, Airgas, Inc.) was added once the $NO_x$ gas was diluted in the mixture to avoid any gas phase reactions. The reaction mixture was preheated to 473 K via heat tracing and a preheater coil designed in-house before entering the reactor. Inside the reactor, just above the bed, $NH_3$ (3000 ppm in He, Matheson Tri-gas) was allowed to enter to minimize the chance of gas phase reactions, which could produce $NH_4NO_3$. To measure the gas concentrations without reaction, the gas flow was switched to a bypass

which went directly into the MKS Multi-Gas 2030 gas analyzer FTIR. The cell temperature of the FTIR was kept at 464 K based on company provided calibration files. A total flow rate of 0.5 L $min^{-1}$ and a reactor temperature of 463K were kept during the experiments. Under *operando* standard SCR conditions, 300 ppm NO, 300 ppm $NH_3$, 5% $H_2O$, 10% $O_2$, 8% $CO_2$, and balance He gas was used.

### 2.3.5 UV-Visible Near IR Measurements

UV-Vis-NIR spectra were taken under ambient conditions with a Varian UV-Vis-NIR spectrophotometer (Cary 5000) and a Harrick-Scientific Praying-Mantis diffuse reflectance cell. Barium sulphate ($BaSO_4$, Sigma-Aldrich, 99%) was used in background scans. Each sample and $BaSO_4$ background reference was sieved to 125-250 μm before use. Spectra were collected from 7000 to 50000 $cm^{-1}$ with a scan speed of 2000 $cm^{-1}$ $min^{-1}$. Each H- and Cu-SSZ-13 sample were pre-treated in dry air (Comm. grade, Indiana Oxygen) up to 823 K elsewhere and then exposed to ambient conditions. Time of exposure to ambient conditions was not controlled as these samples were used in our lab for months beforehand. Close to 0.1 g of each sample was put in a sample cup where UV-Vis-NIR measurements were then performed.

### 2.3.6 Density Functional Theory Calculations

Periodic density function theory (DFT) calculations were performed using the Vienna *ab-initio* simulation package (VASP) [74-76]. Core states were treated using the projector augmented wave (PAW) [77] method and exchange and correlation treated within the PW91 generalized gradient approximation (GGA) [78]. Plane waves were included to a

cutoff of 400 eV and the Brillouin zone sampled at the Γ-point. Electronic energies were converged to $10^{-8}$ eV and optimized geometries relaxed using the conjugant gradient method until forces on atoms were less than 0.01 eV/Å.

## 2.4 Results

### 2.4.1 Kinetics of Standard SCR on Cu-SSZ-13

Kinetic measurements were taken on seven samples with Cu:Al ratios ranging from 0 to 0.35. This range of Cu loading was chosen based on existing studies which suggested isolated Cu was the active site for standard SCR and present initially as Cu loading was increased [2, 33, 42, 43]. The H-SSZ-13 sample exhibited no rate per gram catalyst at the low temperature SCR range of 433-473 K, indicating that Cu was required for the reaction. Apparent activation energies and associated rates were calculated from the conversion of NO and $NH_3$, as shown below.

$$NO_x\ conversion = \frac{NO_{in} - NO_{out}}{NO_{in}}\ x\ 100 \qquad (1)$$

$$NH_3\ conversion = \frac{NH_{3,in} - NH_{3,out}}{NH_{3,in}}\ x\ 100 \qquad (2)$$

The $N_2O$ and $NO_2$ quantities, which are usually present in reported conversion expressions, have been ruled out as the amounts observed were within the error of the FTIR instrument. Dinitrogen was quantified using the GC and compared to the amount of NO and $NH_3$ converted in initial samples within a 90% confidence interval (See Figure A.1). Figure 2.1a shows the Arrhenius plots for all of the standard SCR active catalysts. The activation energies extracted from Figure.2.1a are located in Table A.1. They range from 42 – 71 kJ $mol^{-1}$ with all but the Cu:Al = 0.02 sample (lowest loading of Cu) falling

in between 64-71 kJ $mol^{-1}$. This higher range (64-71 kJ $mol^{-1}$) was near what has been reported by Gao et al.[44] for Cu-SSZ-13 and others on metal-ZSM-5 [28]. The Cu:Al = 0.02 sample had an activation energy which fell in line with previously reported metal-exchanged zeolites for standard SCR [36, 49, 51]. The reaction orders obtained for each of these samples are depicted in Figure 2.1b.

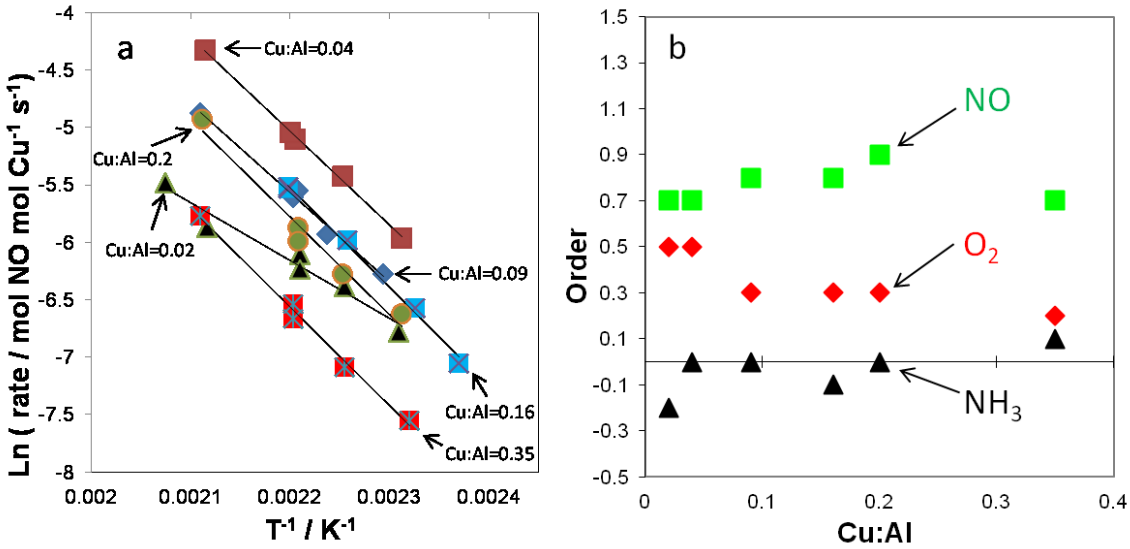


Figure 2.1a-b Arrhenius Plots and reaction orders of the 6 Cu-SSZ-13 catalysts active for standard SCR. The temperature range used for the Arrhenius plots was 433-473K. The standard SCR conditions used are 320 ppm NO, 320 ppm $NH_3$, 10% O2, 6% $H_2O$, and 8% 2. Reaction orders for NO, $NH_3$, and $O_2$ shown as a function of Cu:Al ratio. Individual gas concentrations were changed while all other gases were held constant. NO orders were taken with NO concentrations ranging from 75 – 600 ppm, $NH_3$ orders were taken from 250 ppm – 600 ppm, and $O_2$ orders were taken from 2.5 – 20% of the feed. 90% confidence interval activation energies and reaction orders were ±5 kJ $mol^{-1}$ and ±0.1, respectively.

The NO reaction order was observed to remain constant across all samples between 0.7-0.9, which is consistent with reports in literature for SCR on zeolites [28, 29, 36, 49]. The $NH_3$ order above 250 ppm was observed to be between -0.2 – 0.1, which was also

consistent with reports in literature that $NH_3$ order is zero or slightly negative [28, 29, 36, 49]. The $O_2$ order ranged from 0.2 to 0.5. With the kinetic data presented, the standard SCR reaction can be represented with the following power law model.

$$-R_{SCR} = A_o exp\left(\frac{-E_{a,app}}{RT}\right)(NO)^{\alpha}(NH_3)^{\beta}(O_2)^{\gamma} \qquad (3)$$

Figure 2.2 shows the standard SCR rate per gram of catalyst which has a linear increase from Cu:Al = 0 to Cu:Al = 0.2 and a maximum rate per gram of 3.8 x $10^{-6}$ mole NO g cat$^{-1}$ $s^{-1}$.

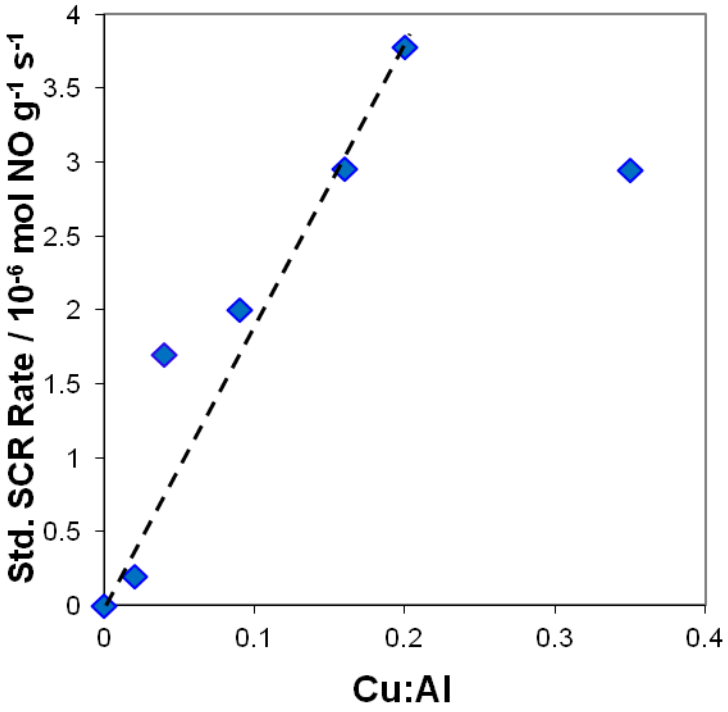


Figure 2.2 Standard SCR rates per gram of catalyst ranging from samples with Cu:Al = 0 to 0.35. Rates are reported at 473 K. Standard SCR conditions used were 320 ppm NO, 320 ppm $NH_3$, 10% $O_2$, 8% $CO_2$, 6% $H_2O$, and balance Helium at 473 K. 90% confidence interval for rate per gram was ±0.2 mol NO $g^{-1}$ $s^{-1}$.

The linear trend up to Cu:Al = 0.2 (< 40% theoretical ion exchanged) observed in these samples allowed the Koros-Nowak criterion for mass transfer to be applied. If a linear trend is observed in a series of samples with variable amounts of the same active site on the same support, it indicates that all the active sites can be accessed, thus ruling out any mass transfer limitations and ensuring the catalyst is running in the kinetic regime. These samples met the criterion up to Cu:Al = 0.2. After Cu:Al = 0.2, a drop in rate per gram was observed from 3.8 to 3.0 x $10^{-6}$ mole NO g $cat^{-1}$ $s^{-1}$ for the sample with Cu:Al = 0.35, which will be explained later as a change in the type of sites available.

### 2.4.2 Brønsted Acid Site Counting

The number of Brønsted acid sites in each sample was determined using an $NH_3$ saturation at an intermediate temperature of 433 K, an eight hour flushing step, and a TPD, which was based on our own study [41] (Chapter 4) of Brønsted acid sites in SSZ-13 and a study by Woolery et al. [63]. By keeping the catalyst at 433 K, all the weakly bound $NH_3$ which could be in the sample, including on the Cu, was not allowed to adsorb on the surface. Table A.1 shows the $H^+$:Al determined on each sample and Figure A.2 shows the TPD spectra. The H-form contained 0.65 $H^+$:Al. Increasing the Cu loading decreased the amount of available Brønsted acid sites until Cu:Al = 0.35 which had $H^+$:Al=0.24. More explanation on the Brønsted acid site counting technique will be given in the discussion section.

To further investigate the role of Brønsted acid sites in standard SCR, transient $NH_3$ cutoff experiments were performed on Cu-SSZ-13 samples to probe the different $NH_3$

species under standard SCR reaction conditions. A "reactive $NH_3$" species was identified and quantified by tracking the NO concentration in the gas phase IR after removing $NH_3$ from the standard SCR gas mixture at 433 K. A $CO_2$ tracer was added into the mixture via a 6-port switching valve to keep the same total flowrate. It was determined that $CO_2$ did not play a role in the kinetics of the reaction (Figure A.3 and Table A.2); therefore, it could act as an inert tracer to probe the hydrodynamic delay in the system and enable $NH_3$ quantification associated with the reaction. Figure A.6 shows a representative experiment for the Cu:Al = 0.09 sample. The NO did not stabilize for close to 60 minutes after $NH_3$ was out of the gas mixture, suggesting an $NH_3$ species on the surface was still reacting with NO. In the quantification of reactive $NH_3$ species, one NO molecule reacting was attributed to one reactive $NH_3$ still present on the catalyst surface based on the stoichiometry of standard SCR. Figure 2.3 shows the quantity of reactive $NH_3$ determined on several samples. A trend was observed, which showed an increase in reactive $NH_3$ species up to Cu:Al = 0.2, and had a maximum of 0.16 $NH_3$:Al. This was also where the maximum standard SCR rate per gram was observed. After Cu:Al = 0.2, the amount of reactive $NH_3$ levels off with a value of 0.15 $NH_3$:Al for the Cu:Al = 0.35 sample.

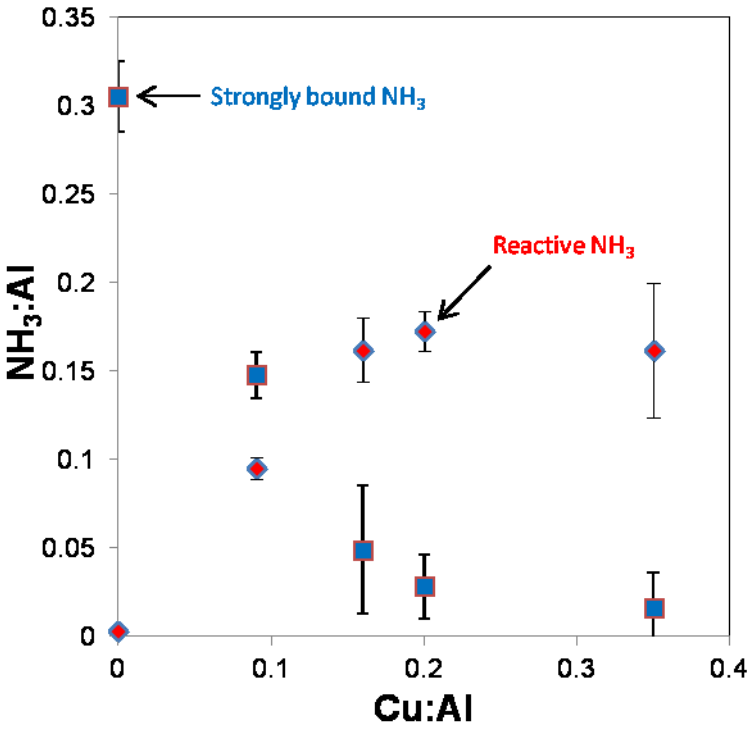


Figure 2.3 Quantities of reactive $NH_3$ (blue square) and strongly bound $NH_3$ (red diamond). The amount of reactive $NH_3$ determined in $NH_3$ cutoff experiments from standard SCR over different Cu:Al samples. Before $NH_3$ was removed, standard SCR conditions were present with 320 ppm NO, 320 ppm $NH_3$, 10% $O_2$, 6% $H_2O$, 8% $CO_2$, and balance Helium at 433 K. Strongly bound $NH_3$ determined from an $NH_3$ TPD after $NH_3$ cutoff experiments and system flush. The TPD had 1.5 L $min^{-1}$ with 5 K $min^{-1}$ temperature ramp to 823 K. 90% confidence interval reported.

After the $NH_3$ cutoff experiment, the system was flushed for ~60 minutes until the reactants were removed from the gas and only UHP He was present, followed by a temperature programmed desorption. Figure A.7 shows an example of a TPD for the Cu:Al = 0.09 sample This procedure was performed on several samples and the result after $NH_3$ quantification can be seen in Figure 2.3. The H-form showed 0.28 $NH_3$:Al. From there, a decrease in the strongly bound species was observed up to Cu:Al = 0.2, at which point, less than 0.03 $NH_3$:Al was observed. This species was observed to not vary

after several standard SCR conditions on the same sample with different $NH_3$ gas concentrations. Figure A.8 shows that different SCR gas mixtures played no role in the amount of $NH_3$ stored in these sites in the Cu:Al = 0.09 sample.

### 2.4.3 Active Cu Characterization

Figure 2.4 shows UV-Vis-NIR spectra collected in air at ambient conditions for all of the Cu-SSZ-13 samples. Two prominent features were observed. At 12,500 $cm^{-1}$, a feature corresponding to a d-d transition for isolated, hydrated Cu(II), or $[Cu(H_2O)_6]^{2+}$, was identified [79]. This feature reached a maximum at Cu:Al = 0.2. After Cu:Al = 0.2, the intensity of the feature at 12,500 $cm^{-1}$ saturated (Figure A.11). The second feature observed was close to 42,000 $cm^{-1}$ and first became visible over the transitions associated with the zeolite in the Cu:Al = 0.16 and 0.20. The presence of the second feature was at a maximum for the Cu:Al = 0.35.

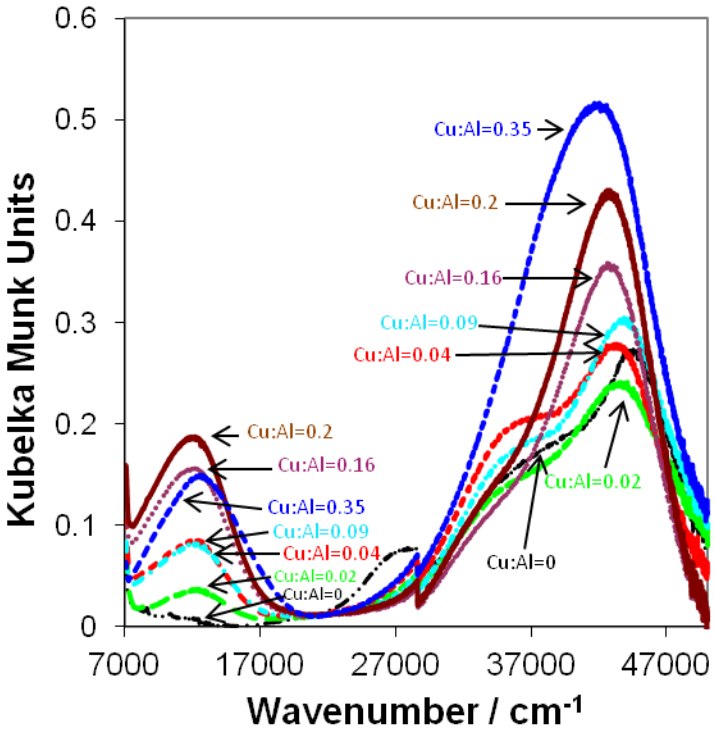


Figure 2.4 UV-Vis-NIR Spectra for each Cu-SSZ-13 sample in this study in air at room temperature.

Hydrated Cu(II) was also observed in XANES spectra in Figure 2.5 for each sample under ambient conditions. A bulk Cu(II)O and hydrated Cu(II) ($[Cu(H_2O)_6]^{2+}$) reference are shown alongside the six Cu-SSZ-13 samples. From the shapes of the XANES spectra, it appears each sample is predominantly in the hydrated Cu(II) form at room temperature, and does not have any bulk Cu(II)O, which has a pre-edge for Cu(II) at 8987 eV and a drop in white line intensity when compared to the hydrated Cu(II) reference. The Cu:Al = 0.35 sample is the only one which has a drop in white line intensity below the hydrated Cu(II) reference. Additionally, the formation of a small pre-edge feature at 8987 eV similar to the bulk Cu(II)O is beginning to form. Linear combination XANES fits were performed using the hydrated Cu(II) and bulk Cu(II)O references as well as isolated

Cu(II) and isolated Cu(I) determined from our lowest Cu loading on SSZ-13. Every sample was about 100% hydrated Cu(II) except the Cu:Al = 0.35 sample, which had a 25% contribution from the bulk Cu(II)O reference (Table A.4). No contribution was seen from the isolated Cu(I) or isolated Cu(II) references. The isolated Cu references will be identified in the next paragraph. The corresponding EXAFS spectra and data fits are shown in the Figure A.13 and Table A.5, which exhibit only a first shell Cu-O feature at 1.94Å and a coordination number of 4 for all samples. No second shell was observed, as no features were distinguishable from the noise of the spectra.

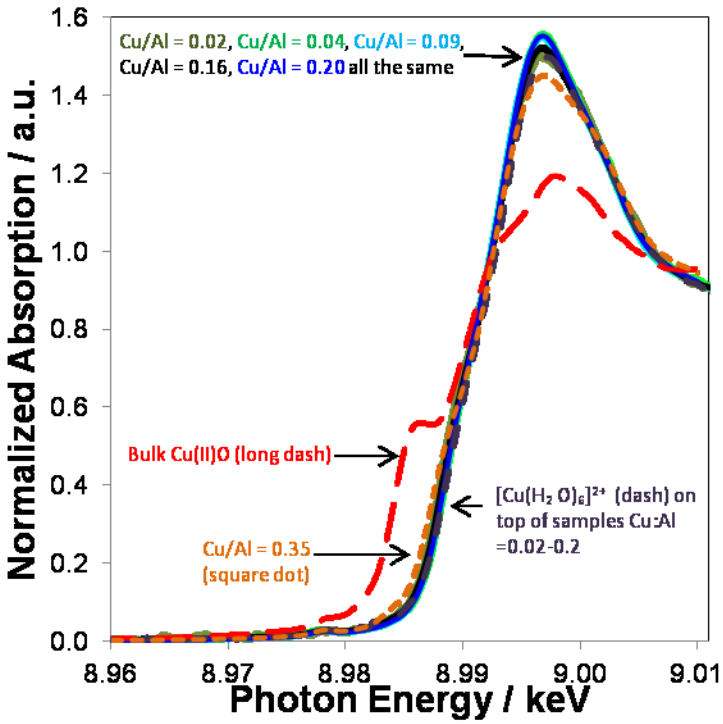


Figure 2.5 XANES spectra for all Cu-SSZ-13 samples in this study in air at room temperature. A $[Cu(H_2O)_6]^{2+}$ was used as the hydrated Cu(II) reference. Bulk Cu(II)O was also shown along side the spectra.

*Operando* XAS was used to study the state of the catalyst under reaction conditions and observe changes to the Cu while maintaining the concentration of reactants and products approxiamtely constant. Figure 2.6 shows the XANES spectra for two Cu-SSZ-13 samples with Cu:Al = 0.09 and 0.16 under standard SCR reaction conditions.

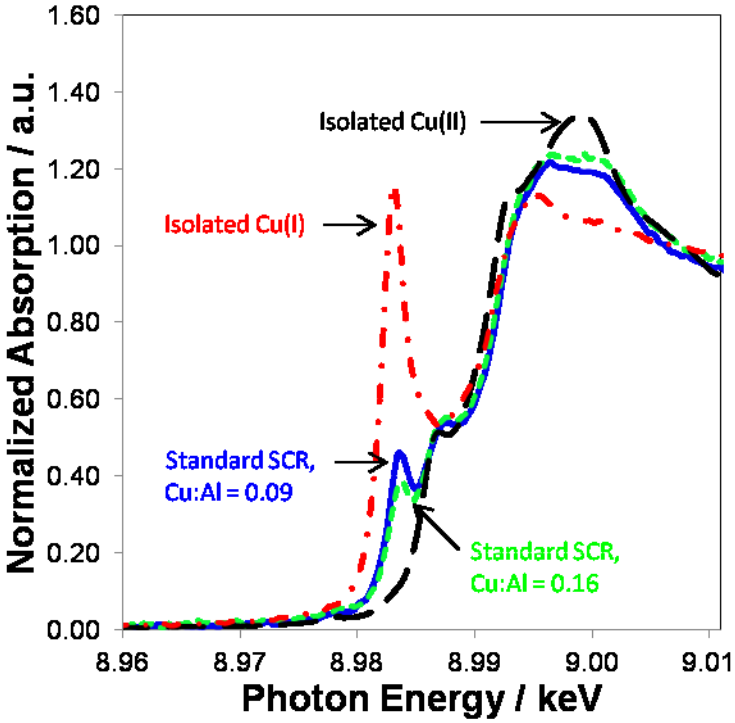


Figure 2.6 XANES spectra for Cu-SSZ-13 samples with Cu:Al = 0.09 and 0.16 under standard SCR reaction conditions compared with the isolated Cu(I) and isolated Cu(II) references. Standard SCR conditions used were 320 ppm NO, 320 ppm $NH_3$, 10% $O_2$, 8% $CO_2$, 6% $H_2O$, and balance He at 453 K.

The feature observed at 8983 eV for a 2-coordinate Cu(I) is present in both samples. The small pre-edge features corresponding to transitions for Cu(II) are also present at 8977 and 8987 eV. To quantify the extent of isolated Cu, the SSZ-13 sample with Cu:Al = 0.02, which was the lowest loading of Cu obtained, was assumed to contain only isolated

Cu based on previous studies in the very low Cu loading regime on Cu-SSZ-13 [43]. This sample was used to create isolated Cu(I) and isolated Cu(II) references with different gas conditions. The isolated Cu(II) reference was made with 10% $O_2$ in UHP Helium at 473 K while the isolated Cu(I) reference was created with 1000 ppm NO and 1000 ppm $NH_3$ at 473 K. Each reference exhibited the expected pre-edge features corresponding for Cu(II) and Cu(I) and can be seen in Figure 2.6 along with the samples under standard SCR reaction conditions. When compared side by side with the two isolated Cu references, the samples under reaction conditions were a combination of the two references. The pre-edge at 8983 eV corresponding to the 2-coordinate isolated Cu(I) was present in both samples. Table A.6 reports linear combination XANES fits for the two Cu-SSZ-13 samples under *operando* standard SCR conditions. The contributions from isolated Cu(I) in the samples were 37% and 26% for the Cu:Al = 0.09 and 0.16, respectively. Both contained negligible amounts of hydrated Cu(II) (<5%) and no bulk Cu(II)O character. The remainder of the fit was the isolated Cu(II) contribution.

The steady state reaction parameters are reported in Table A.6 with a comparison to the rates collected on our laboratory scale plug-flow reactor. An agreement was seen between the rates collected in-house and those collected during the *operando* XAS experiments. The Cu:Al = 0.09 sample exhibited a rate of 4.3 x $10^{-3}$ mole NO mole $Cu^{-1}$ $s^{-1}$ at 453 K for both the *operando* experiments and in-house experiments. The Cu:Al = 0.16 sample had a rate of 4.7 x $10^{-3}$ and 3.7 x $10^{-3}$ mole NO mole $Cu^{-1}$ $s^{-1}$ for *operando* experiments and in house experiments, respectively.

To count the number and type of potential Cu(II) sites, we used a combination of DFT and statistical analysis. The SSZ-13 lattice presents 4-, 6-, and 8-membered rings. In a first set of DFT calculations, we constructed an SSZ-13 supercell containing four Al T-sites (equivalent to an Si:Al ratio of 5) distributed such that two Al are in each of a 4-, 6-, and 8-membered rings. We computed the energy to exchange Cu(II) into each ring according to:

$$Z_4H_4 + Cu^{2+}(aq) \rightarrow Z_4H_2Cu + 2H^+(aq) \qquad (4)$$

We find that the optimized Cu(II) ions uniformally prefer to maintain 4-fold coordination to lattice O in each ring; further, Cu(II) is 1.13 eV more stable in the 6- than the 4-membered ring and 1.5 eV more stable in the 6- than the 8- membered ring. These results support the hypothesis that the 6-ring is the preferred site of Cu(II) exchange, consistent with previous suggestions for this site as the center of standard SCR activity [6, 33, 42].

We next constructed a 768 T site periodic supercell of SSZ-13 using the crystal structure from the International Zeolite Association database [34]. We randomly seeded the lattice with Al up to target Si:Al ratios from approximately 3 to 47, avoiding nearest neighbor Al-O-Al structures in accordance with Loewenstein's rule [46, 80]. Next, random Si to Al swaps were performed that satisfied Loewenstein's rule, and at each iteration the number of six-membered rings containing exactly two Al counted. A total of $10^7$ iterations were performed, and multiple replicates performed to ensure convergence. Figure 2.7 shows the computed number of six-membered rings with two Al per total Al as a function of Si:Al ratio. The density rises rapidly with increasing Si:Al ratio until it

maximizes near a ratio of 3, at which point six-membered rings with 3 Al T-sites dominate the lattice. At a Si:Al ratio of 5, the density of two-Al six-membered rings is 0.23. Assuming Cu(II) exchange to obey the stoichiometry of Eq. 4, the theoretical maximum six-membered ring Cu:Al ratio is also 0.23 for for a sample in which every Al is a Brønsted acid site.

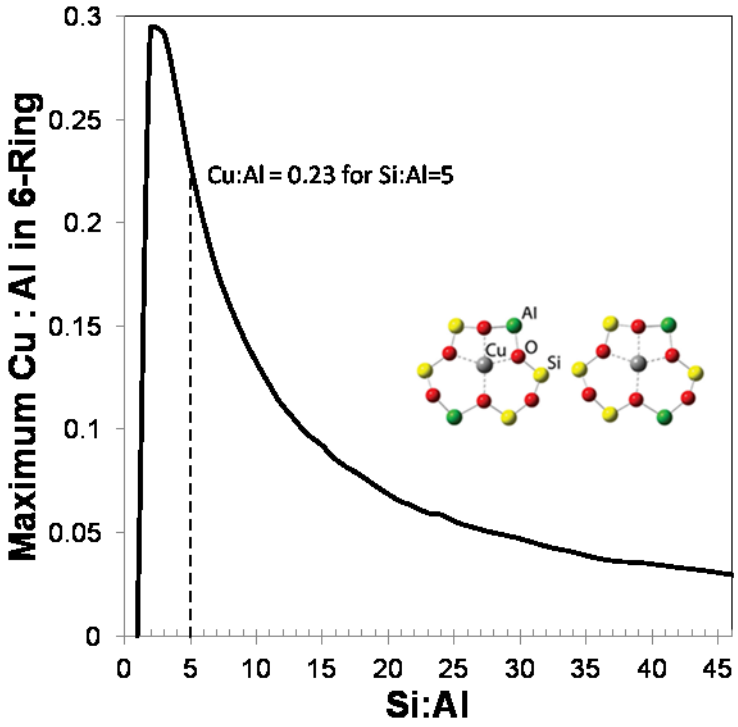


Figure 2.7 The maximum Cu(II) associated with 2 Al in the six-membered ring in SSZ-13 which can theoretically be present for a given Si:Al.

## 2.5 Discussion

### 2.5.1 Identification and Location of the Active Cu Species

The combination of standard SCR kinetics and spectroscopic techniques used under ambient and reaction conditions allows the active Cu for standard SCR in SSZ-13 to be identified as an isolated Cu species. The linear increase in standard SCR rate per gram up to Cu:Al=0.2 in Figure 2.2 indicates that the active Cu species is populated in the low loading region. Other studies [43, 44] have identified isolated Cu to be present in this regime, suggesting it is the active Cu based on the standard SCR rate that is observed. The linearity of the trend of increasing standard SCR rate per gram also allows the series of Cu-SSZ-13 samples to pass the Koros-Nowak test for mass transfer [81, 82], a debated effect within SSZ-13. Gao et al.[44] have concluded that internal mass transfer can inhibit the reaction by calculating the effectiveness factors from the Thiele relationship and making comparisons of rate per mole Cu in samples with different Cu loadings. However, it is not present in the samples in this study because of the linearity of the rate per gram with the addition of active Cu species up to Cu:Al = 0.2. The Cu:Al = 0.35 sample was also determined to not have any mass transfer issues either, which will be discussed later on.

Figure 2.4 shows an increasing intensity of hydrated (isolated) Cu(II) species based on d-d transitions at 12,500 $cm^{-1}$. Further confirmation of a hydrated Cu(II) species was seen in Figure 2.5, in which all samples below Cu:Al = 0.2 showed nearly 100% hydrated Cu(II) character when a linear combination fit was used (Table A.4). The intensity in the UV-Vis-NIR measurements was observed to reach a maximum intensity of 0.18 Kubelka

Munk units at Cu:Al = 0.2, which suggests there may be a connection between the hydrated Cu(II) species and the active Cu(II). When shown together in Figure 2.8, the rate per gram is seen to track linearly with the intensity of d-d transitions for hydrated Cu(II). The Cu:Al=0.35 sample, which was observed to have a decrease in rate per gram after the Cu:Al=0.2 sample, falls on the line as well. This correlation suggests that hydrated Cu(II) within SSZ-13 is a precursor to the active Cu under standard SCR conditions.

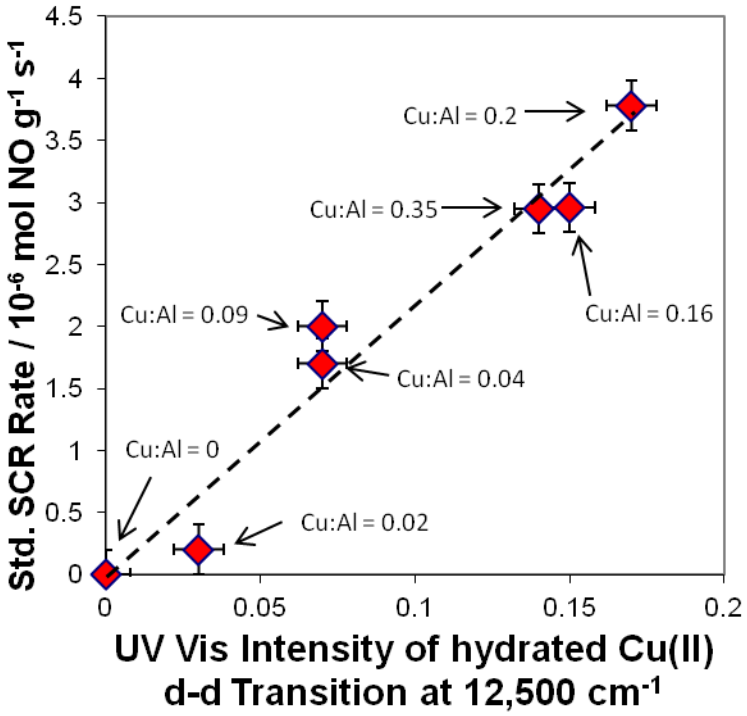


Figure 2.8 Correlation of standard SCR rate per gram with the UV-Vis-NIR intensity of hydrated Cu(II) d-d transition at 12,500 $cm^{-1}$ in Kubelka-Munk units in air at room temperature in the Cu-SSZ-13 samples. Standard SCR conditions used were 320 ppm NO, 320 ppm $NH_3$, 10% $O_2$, 8% $CO_2$, 6% $H_2O$, and balance Helium at 473 K. 90% confidence intervals used.

When two of the samples (Cu:Al=0.09 and 0.16) were observed under reaction conditions with *operando* x-ray absorption spectroscopy, several changes took place in the shape of the XANES spectra as shown in Figure 2.6. A feature at 8983 eV for a two-coordinate Cu(I) is present because of the expected Cu redox cycle between Cu(I) and Cu(II) under standard SCR [4, 40]. Other features at 8977 and 8987 eV are indiciative of Cu(II) coordinated to the zeolite. None of these transitions were present under ambient conditions when Cu was surrounded by water, indicating that Cu became coordinated to the zeolite and shed its sphere of hydrated under reaction conditions. Linear combination XANES fits in Table A.6 show that there is now 5% or less contribution from hydrated Cu(II) with only isolated Cu(I) and Cu(II) contributions. This change from 100% hydrated Cu(II) to greater than 95% isolated Cu(I)-Cu(II) under reaction conditions signals two things. The first is that the active Cu is an isolated species since we observe the active Cu to build in this region based on our kinetic results and this is the only Cu species we see from *operando* XAS. The second is that the hydrated Cu(II) under ambient conditions is the precursor to the active Cu. Using UV-Vis-NIR to look at the precursor under ambient conditions is a very simple experiment and it can give an estimate of the quantity of active Cu present. Based on these new conclusions, the Cu:Al=0.35 sample does not suffer from mass transfer effects because its rate depends on the amount of hydrated Cu, which falls in line with all the other samples.

The location of the active isolated Cu species was determined to be located at the six-membered ring and exchanged into two Brønsted acid sites. The DFT calculations support a strong Cu(II) preference for six-membered rings, and statistical analysis

provides a density of these Cu(II) sites consistent with the maximum rate per gram vs. Cu loading observed in the experiments (Figure 2.7). Thus, the active Cu species for standard SCR in Cu-SSZ-13 is isolated and located within the six-membered ring of the CHA structure.

### 2.5.2 Transitions to Other Cu species after Cu:Al = 0.2

After Cu:Al = 0.2, several pieces of evidence are present in the data which suggest a new Cu species formed which has multiple Cu in its structure. The linear combinatation XANES fits of Cu-SSZ-13 under ambient conditions (Table A.4) show that the Cu:Al=0.35 sample exhibits a 25% contribution from a bulk Cu(II)O reference. Therefore, it is likely a new Cu species has emerged above the threshold of Cu:Al=0.2 which has multiple Cu, which will be denoted $Cu_xO_y$. The UV-Vis-NIR spectra (Figure 2.4) reach a maximum amount of d-d transitions for hydrated Cu(II) at Cu:Al = 0.2. Following this, a small drop in intensity from 0.18 to 0.14 Kubelka Munk units was seen, suggesting a new Cu species other than hydrated Cu(II) was forming and likely scavenging isolated Cu. It is not clear what has changed in the UV-Vis-NIR in the broad range of wavenumbers from ~27,000 – 50,000 $cm^{-1}$, but the entire region has reached a maximum in the Cu:Al=0.35 sample. This region was not analyzed for further information.

Another study in our group [83] used dry NO oxidation reaction conditions over the same set of samples here and found samples with Cu:Al greater than 0.2 to be catalytically active with 300 ppm NO, 150 ppm $NO_2$, and 10% $O_2$ at 573 K. Several samples in that study, all with Cu:Al > 0.2, showed increase in rate from zero mol NO mol $Cu^{-1}$ $s^{-1}$ at

Cu:Al =0.2 up to 1.7 x $10^{-4}$ mol NO mol $Cu^{-1}$ $s^{-1}$ in a Cu:Al = 1.6 sample. This indicated a new $Cu_xO_y$ species began to populate after the isolated Cu sites in the six-membered rings were full. Thus, dry NO oxidation was used as a probe reaction to determine the threshold of the formation of new $Cu_xO_y$ species. The new species was not active for standard SCR because the standard SCR rate per gram in the Cu:Al = 0.35 sample tracked with the amount of hydrated Cu(II) in Figure 2.8.

### 2.5.3 Choice of Brønsted Acid Site Measurement Technique

In a previous study [41] (Chapter 4), three different $NH_3$ treatments followed by TPDs were shown to be able to selectively titrate Brønsted acid sites. The $NH_3$ treatments were compared with an n-propylamine decomposition reaction previously described [84-86] and produced an equivalent result in both H- and Cu-ZSM-5 samples. When the third $NH_3$ treatment (data used in this study) and n-propylamine decomposition were used in H- and Cu-SSZ-13, we found the n-propylamine unable to access close to 75% of the Brønsted acid sites as calculated from the $NH_3$ titration. From this, we suggested n-propylamine was unable to accurately count sites in the treatment conditions used because of the combination of the small pore-openings in SSZ-13 and the high aluminum content in ths samples (Si:Al=4.5). Thus, for SSZ-13 in this study, we used $NH_3$ to titrate the Brønsted acid sites.

The parent H-SSZ-13 sample exhibited ~0.65 $H^+$:Al from the $NH_3$ titration, which indicated that one-third of the Al were not contributing to the Brønsted acid sites. This effect has also been observed in other zeolites [87] and the quantity of Al not counted as

Brønsted acid sites has typically been identified as extraframework, which is likely the case in our samples.

### 2.5.4 The Role of Brønsted Acid Sites

The standard SCR rate per gram catalyst did not appear to be affected by the number of Brønsted acid sites measured by $NH_3$ treatment #3 and TPD which are detailed in the previous paragraph. Figure A.16 shows the normalized rate per gram catalyst and normalized $H^+$:Al together with an inverse correlation to each other. The drop in rate per gram after Cu:Al = 0.2 was not indicative of a shift in kinetically relevant step(s) to the Brønsted acid site. It was only a drop in the number of active Cu species, as indicated by the amount of hydrated Cu(II) tracking with the rate per gram in Figure 2.8. The activation energies and reaction orders in Figure 2.1a-b and Table A.1 also show that the kinetics were not changing over the course of Cu addition into the samples aside from the Cu:Al =0.02 sample.

The amount of strongly bound $NH_3$ also had an inverse correlation with the standard SCR rate per gram, suggesting it was also part of the total Brønsted acid site quantity. Figure A.17 shows the calculated total number of Brønsted acid sites based on the sum of strongly bound $NH_3$ and the two Brønsted acid sites for every Cu(II) exchanged. This sum did not include the reactive $NH_3$ species, which will be discussed next. Each total Brønsted acid site quantity based on the strongly bound species was observed to have a similar offset between 0.23-0.36 $H^+$:Al lower than the total Brønsted acid sites from the $NH_3$ titration study [41]. Previous studies [88] have shown that the $NH_3$ storage capacity

can be significantly reduced under reaction conditions due to reaction of the $NH_3$ species. Since the steady state reactions performed before the $NH_3$ cutoff and TPD were at 433 K, the rates collected were less than 0.8 x $10^{-6}$ mol NO g $cat^{-1}$ $s^{-1}$ (Cu:Al = 0.2 sample), which corresponded to less than 4% conversion. The reaction of $NH_3$ off the Brønsted sites may contribute to the offset, but it is not likely to have much of an effect, or no effect in the case of the H-SSZ-13 sample, which exhibits no rate. A likely scenario is that the partial pressures of the different gases in the mixture shift the equilibrium coverage of $NH_3$ on Brønsted acid sites. A recent study [89] used $NH_3$ and $H_2O$ adsorption and desorption experiments and microkinetic modeling to determine coverages over $NH_3$ on Brønsted acid sites with and without $H_2O$ present on Fe-ZSM-5 at 423 K. The study found the coverage of $NH_3$ on Brønsted acid sites dropped from ~0.9 to 0.3 when water was present. Based on that study, the combination of 6% $H_2O$ in the reaction mixture along with the other gases could have a profound effect on the $NH_3$ coverage on Brønsted acid sites under reaction conditions. To prove this was the effect we observed, three different gas conditions were used before an $NH_3$ cutoff and TPD on the H-SSZ-13 sample. The first was standard SCR as described previously, the second was dry standard SCR (no $H_2O$), and the third was $NH_3$ only. Total flowrates during each experiment were kept at 1.5 L $min^{-1}$ just as in the original $NH_3$ cutoff and TPD experiments. Following the $NH_3$ cutoff, the TPDs were performed to observe any changes in strongly bound $NH_3$. Figure A.18 shows water had a large impact on the strongly bound $NH_3$ coverage. When quantified, the dry standard SCR showed 0.54 $NH_3$:Al, while the regular standard SCR showed 0.26 $NH_3$:Al. The final experiment used $NH_3$ only before the $NH_3$ cutoff, which gave 0.62 $NH_3$:Al in the TPD, which was in

agreement with our previous study with ~0.65 $H^+$:Al for the H-SSZ-13 sample [41]. From these results, it appears that the reaction mixture does not allow for all Brønsted acid sites to be occupied under standard SCR conditions, with the presence of 6% $H_2O$ contributing the most to the difference in values obtained. Since the amount of Brønsted acid sites as determined from the strongly bound $NH_3$ after standard SCR reaction are even smaller in quantity than the $NH_3$ titration procedures, this is an even stronger indication that the number of sites are not kinetically relevant for the standard SCR rate in these samples.

The reactive $NH_3$ species may be associated with the active Cu species, a Brønsted acid site, or a combination of both. Recall, the standard SCR rate on each sample correlated with the amount of hydrated Cu(II), a precursor to the active Cu site. The reactive $NH_3$ also track well with the standard SCR rate seen in Figure A.19, suggesting it is related to the active Cu. A recent mechanism [39] proposed for standard SCR in SSZ-13 suggests the reaction occurs through an intermediate with $NH_3$ on the active Cu. This also falls in line with our previous study [40] (Chapter 3) where we suggested $NH_3$ may react or desorb from Cu, but also keeps water from adsorbing on the active Cu under reaction conditions using transient cutoff experiments with *operando* XAS. The long time for the NO signal to stabilize in the $NH_3$ cutoff experiment (~60 min) may suggest there is migration of $NH_3$ species to an active site, in which case, the Brønsted acid site storage may become important in this transient process. Thus, we cannot rule out the possibility that some or all of the reactive $NH_3$ comes from Brønsted acid sites surrounding the Cu.

Further studies need to be performed to determine the correct position(s) for the reactive $NH_3$.

### 2.5.5 The Importance of Cu:Al = 0.2

The agreement of multiple techniques giving a maximum (standard SCR rate per gram, hydrated Cu(II) in UV-Vis-NIR, isolated Cu in six membered ring from statistical calculation) at Cu:Al = 0.2 suggests this is an important transitional region in Cu-SSZ-13 for a Si:Al = 4.5. From the results discussed, the transition is caused by isolated Cu sites in the six-membered rings filling to a maximum value. At this point, the standard SCR rate per gram catalyst is at a maximum, which confirms kinetically that this is the active site for standard SCR. At this transition, another Cu species begins to form which is not located in the six-membered ring, and our results show that multiple Cu are involved. The UV-Vis NIR data show this species may begin to remove isolated Cu after Cu:Al=0.2, which causes a loss in standard SCR rate per gram. The statistical approach used here to confirm experimental results should be used as a road map to make high-performance Cu-SSZ-13 with varying Si:Al for standard SCR.

## 2.6 Conclusions

Seven H- and Cu-SSZ-13 samples with Si:Al = 4.5 and Cu:Al ranging from 0 to 0.35 were used to determine standard SCR reaction kinetics and probe the active Cu site under standard SCR reaction conditions. The standard SCR rate per gram increased linearly with Cu:Al ratio up to Cu:Al = 0.2, indicating the active site was formed in this regime. This matched with statistical calculations of the maximum amount of isolated Cu

occupying 2 Al on the six-membered ring of the SSZ-13 at Cu:Al = 0.23. This linear trend also rules out any mass transfer limitations.

The state of the Cu in SSZ-13 under ambient conditions was tested with UV-Vis-NIR and XAS. The UV-Vis-NIR showed the build up of a hydrated Cu(II) species until Cu:Al = 0.2, which agreed with the trend in standard SCR rate per gram with increasing Cu loading up to Cu:Al = 0.2. Ambient XAS confirmed the state of Cu in all samples with Cu:Al = 0.2 or below to have only this hydrated species. *Operando* XAS showed that all the hydrated Cu became an isolated Cu(I)-Cu(II) mix under standard SCR conditions, confirming the active species of Cu for standard SCR. Hydrated Cu(II) was also determined to be the precursor to the active Cu species because it tracked with the standard SCR rate in all samples and transformed completely to isolated Cu under reaction conditions.

The number of Brønsted acid sites found in each sample were determined to not be involved in the kinetically relevant steps because of an inverse correlation between rate per gram and number of sites. Individual $NH_3$ species were also quantified under reaction conditions. A strongly bound $NH_3$ found by TPD after reaction conditions and corresponding to a fraction of the total Brønsted acid sites also showed an inverse correlation with the rate. A reactive $NH_3$ species found by quantifying the NO reacted after $NH_3$ was removed from standard SCR mixture tracked with the standard SCR rate suggesting it was on the active Cu or on a nearby Brønsted acid site .

This study suggests a transition region in Cu-SSZ-13 near Cu:Al = 0.2 for our samples which have Si:Al = 4.5, where a $Cu_xO_y$ species not associated with the six-membered ring begins to form. Ambient XAS show the appearance of transitions similar to what have been observed in Cu(II)O in the Cu:Al = 0.35 sample. Thus, the transition region for a given Si:Al in Cu-SSZ-13 must be considered when trying to maximize the isolated Cu for standard SCR and not create other unwanted Cu species.

## 2.7 Acknowledgements

A lengthy author list is associated with this manuscript. Because this is a dissertation, these people will be listed here. Those people are Anuj Verma, Christopher Paolucci, Trunojoyo Anggara, Atish Parekh, William F. Schneider, Jeffrey T. Miller, W. Nicholas Delgass and Fabio H. Ribeiro. We would also like to thank Paul Dietrich for his help in executing the XAS experiments at the APS. Use of the Advanced Photon Source is supported by the U. S. Department of Energy, Office of Science, and Office of Basic Energy Sciences, under Contract DE-AC02-06CH11357. MRCAT operations are supported by the Department of Energy and the MRCAT member institutions. Support for JTM was provided under the auspices of the U.S. DOE, Office of Basic Energy Sciences, Division of Chemical Sciences, Geosciences, and Biosciences under contract number DE-AC0-06CH11357. We would also like to thank Sachem, Inc. for their gracious donation of the structure directing agent for SSZ-13 synthesis.

# CHAPTER 3. INVESTIGACTION OF THE REDOX SITES OF THE HALF-REACTIONS OF SELECTIVE CATALYTIC REDUCTION OF NOX BY NH3 VIA OPERANDO X-RAY ABSORPTION ON CU-SSZ-13

## 3.1 Abstract

Using *operando* X-ray absorption spectroscopy (XAS), we performed a series of experiments designed to isolate the oxidizing or reducing half reactions of the $NH_3$ selective catalytic reduction (SCR) of $NO_x$ on Cu-SSZ-13. The molecules $O_2$, NO or $NH_3$ were removed from the steady state standard SCR reaction and the time-dependent changes in Cu oxidation state were followed by XAS along with the simultaneous evolution in gas compositions. The redox nature of the Cu active site on Cu-SSZ-13 in each half reaction of the catalytic cycle is shown. With only NO, $NH_3$ and $H_2O$ ($O_2$ removal), Cu(II) is reduced to Cu(I). Re-addition of $O_2$ into the reaction mixture readily oxidized the Cu and it returned to its steady state mixed Cu oxidation states under standard SCR. Over the same timeframe, the reactor effluent gases reached their steady state conversion composition. Cutting off NO from standard SCR ($NH_3$ + $O_2$ feed) led to fully oxidized Cu(II) suggesting that $NH_3$ is a less effective reductant than $NH_3$ + NO. Re-addition of NO returned the catalyst to its mixed Cu(I)-Cu(II) oxidation state. Removing $NH_3$ from standard SCR (NO + $O_2$) led to a fully oxidized Cu(II), with a portion of the Cu(II) becoming hydrated, suggesting $NH_3$ kept isolated Cu from becoming hydrated under reaction conditions. Addition of $NH_3$ led to the same mixed

Cu(I)-Cu(II) state under standard SCR. The cutoff of $NO_2$ from fast SCR lead to the partial reduction of Cu(I), which is oxidized upon $NO_2$ re-addition, suggesting $NO_2$ oxidized Cu(I).

The effect of the $NO_2$ gas concentration demonstrated that $NO_2$ is strongly oxidizing. We show that this can be used to control the distribution of Cu oxidation states at the top and bottom of the reactor by adjusting the concentration of $NO_2$ in the feed. At a $NO_2$:$NO_x$ ratio of 1:10 nearly all $NO_2$ was consumed by the time the reactants reached the bottom of the catalyst bed at which point the distribution of Cu oxidation states appeared no different than under standard SCR conditions. Where $NO_2$ was in higher concentration, like at the top of the bed before being consumed by reaction, the catalyst was more oxidized with a distribution of Cu oxidation states more similar to the catalyst with a 1:1 $NO_2$:$NO_x$ ratio in the feed. This draws attention to the importance of differential conditions on performing *operando* experiments on a system sensitive to the gas conditions.

We use the transient state experiments to show the explicit effect of the two half reactions on the Cu oxidation state, which we believe make up the reaction cycle of the $NH_3$-SCR reaction on Cu-zeolites. We discuss the kinetic and mechanistic implications that arise from the results.

## 3.2 Introduction

Recent developments in heavy duty diesel exhaust after-treatment have led to the adoption of chabazite (CHA) zeolite based Cu catalysts for use in mobile source $NO_x$ reduction by selective catalytic reduction (SCR) of $NO_x$ with $NH_3$ [1-3]. The Cu and Fe zeolite catalysts for NO reduction by NO decomposition [90], $NH_3$-SCR [15, 91] and hydrocarbon (HC) -SCR [92] had been discovered some time ago. Of particular interest was Cu-ZSM-5, which showed the highest catalytic rates, but tended to de-aluminate under the harsh hydrothermal atmospheres experienced by automotive exhaust catalysts and was consequently never commercially implemented [14, 93-96]. The new CHA based catalysts, both Cu-SAPO-34 [2, 31] and Cu-SSZ-13 [3, 32], stand as major improvements in hydrothermal stability under true reaction conditions. A flurry of activity now surrounds these materials as researchers begin to try to understand their remarkable stability. The reaction mechanism and specifically the active site for SCR on these CHA catalysts is, of course, of particular interest, especially considering the much debated and unique active sites present on Cu-ZSM-5 [49, 97, 98]. Wang et al. [45] found that isolated ion-exchanged Cu proved to be significantly more active than extra framework CuO clusters on two different Cu-SAPO-34 catalysts prepared by ion exchange and precipitation-deposition, respectively. Fickel and Lobo [33] used Rietveld refinement of variable temperature XRD to show that Cu atoms were isolated, typically resided within, or slightly above the 6-membered rings of Cu-SSZ-13, and coordinated to three oxygen atoms of the ring in dry He or dry $O_2$/He mixtures. Further investigation by Korhonen et al. [42] used XAS and UV-Vis to rule out the presence of Cu dimers and found that the active site on their Cu-SSZ-13 catalyst was isolated Cu(II) atoms, again in

3-fold coordinated sites. A combined modeling and XAS study of Cu-SSZ-13 by our lab and collaborators [99] showed similar triply-coordinated, isolated Cu(II) atoms as the most energetically favorable site so long as adsorbates were not taken into account. With the adsorption of various $O_xH_y$ species the Cu could take on a number of conformations, typically 2- and 4-fold coordinate (but not 3-fold), of which a first-principles thermodynamic simulation found the most stable to be the redox couple described by a two-fold coordinate $ZCuH_2O$ and a four-fold coordinate $ZCu(OH)_2$ (where Z represents an Al T-site in the zeolite). These model species matched bond distances and coordination numbers determined by *operando* XAS data which showed the catalyst in a mixed Cu(I)-Cu(II) oxidation state under steady state standard SCR conditions. Thus, we proposed that the active site was also isolated Cu, but that the reaction progressed via a Cu(I)-Cu(II) redox cycle that, under standard SCR reaction conditions, led to the presence of a steady state amount of Cu(I) on the catalyst. Redox of the Cu active site being involved in the SCR mechanism has been proposed by Kieger *et al.* for $NH_3$-SCR on Cu-FAU [29] and Gomez *et al*. on ZSM-5 [30]. A second investigation by our group [5] including the same Cu-SSZ-13 as well as a Cu-ZSM-5 and commercial Cu-SAPO-34 found varying and large fractions of Cu(I) on the catalysts in *operando* XAS under standard SCR conditions, depending on the zeolite support. The lack of correlation between the amounts of Cu(I) or Cu(II) and the different rates on each catalyst led us to conclude that Cu redox was involved in the reaction mechanism.

This manuscript is a follow-up investigation into the redox nature of the Cu active site on Cu-SSZ-13. By designing experiments to specifically isolate the oxidizing or reducing

portion of the SCR reaction and by simultaneously monitoring the catalyst in *operando* XAS, we can capture the redox cycle as it transiently oxidizes or reduces Cu on the catalyst. We also probe the effect of $NO_2$ on the oxidation state of the Cu active site by varying the $NO_2$:$NO_x$ ratio fed to the catalyst and again monitoring the Cu oxidation state in *operando* XAS.

## 3.3 Experimental Methods

### 3.3.1 Catalyst Preparation

The catalyst was prepared by ion exchange of $Cu(NO_3)_2$ into H-SSZ-13 zeolite powder. The zeolite was synthesized in house following the recipe published by Fickel *et al.* [33] based on the original development of this zeolite by S. I. Zones [56]. The details of the zeolite synthesis, as well as comparisons with XRD in literature and AA characterization were discussed in a previous publication [5]. A solution of 970 mg of H-SSZ-13 in 40 mL of deionized (DI) $H_2O$ was stirred and heated to 40 ˚C for 30 min. After dropwise addition of a solution of 47 mg of $Cu(NO_3)_2$ (Alfa-Aesar) dissolved in 10 mL of DI $H_2O$ more DI $H_2O$ was added to bring the total solution volume to 200 mL. The mixture was allowed to stir for 5 h while the pH was maintained between 5 and 5.2 by dropwise addition of 0.1 M $NH_4OH$. The resulting slurry went through three centrifuge and rinse cycles before vacuum drying for 12 h. After drying, the catalyst was calcined at 798 for 6 h with a 0.5 K $min^{-1}$ ramp rate. The zeolite had a 4.5:1 Si:Al ratio and the two samples tested had 2.1 and 3.04 wt.% Cu weight loading for Cu:Al ratios of 0.11 and 0.16, respectively, as determined by atomic absorption spectroscopy.

### 3.3.2 X-ray Absorption Spectroscopy

All X-ray absorption spectroscopy (XAS) experiments were performed at Sector 10 of the Advanced Photon Source, the Materials Research Collaborative Access Team (MR-CAT), of Argonne National Laboratory. The insertion device beamline at Sector 10 (10-ID) was necessary for the experiments due to the high photon flux generated by the beamline. The 10-ID, therefore, allowed us to make time-dependent and positional measurements along the length of the catalyst bed with a 200 x 200 μm beam size without compromising data quality. Incident X-rays were measured in an ion chamber filled with 20% He in $N_2$ while the transmitted beam was measured in an ion chamber with 20% Ar in $N_2$ to obtain roughly 70% absorption of the beam after the sample. A third detector was used to simultaneously measure a Cu metal foil reference with each spectrum. The Cu metal foil, 8979 eV edge energy, was used to calibrate the X-ray beam for the Cu absorption K edge. All data was normalized with a $1^{st}$-order polynomial subtraction of the pre-edge and $3^{rd}$-order polynomial subtraction of the post edge backgrounds.

Total absorption ($\mu x$) due only to the sample and carbon tube reactor was around 1.2-1.3, with a step height ($\Delta\mu x$) of around 0.9. Data were collected in quick scan mode, ranged from 8730 to 9890 eV, and each spectrum took 2 min and 15 s or 2 min and 22 s to complete. Steady state data and data collected during $NO_2$:$NO_x$ ratio experiments were averaged over three spectra. Transient data collected during the cutoff experiments were not averaged.

The Cu K-edge XANES has four distinct features indicative of the various electronic transitions occurring on the sample in XAS. The different features represent different Cu oxidation states and since XAS is a bulk technique the spectrum represents a combination of the spectra for each oxidation state. The first peak is centered at 8977 eV and is representative of the symmetry forbidden 1s → 3d transition of Cu(II) atoms which becomes an allowed transition when mixing of the 3d and 4p orbitals occurs [64]. The next peak is centered around 8983 eV but has been known to be present from 8982-8985 eV. This feature represents the 1s → 4p transition of two coordinate Cu(I) atoms and there is substantial literature identifying it in XAS over a vast array of environments including ZSM-5 in HC-SCR [65, 66] and NO decomposition [67, 68], Y-Zeolite [100], SAPO-5 and SAPO-11 in HC-SCR [70], as well as Cu(I) ammine complexes [71, 72] and a large number of ligated organic compounds [64]. The edge feature occurring at 8987 eV represents the 1s → 4p electronic transition of Cu(II) atoms [66]. Finally, the white line is also indicative of Cu(II). As such, losing intensity in the 8995 eV peak represents a loss of Cu(II) on the catalyst. A weak dip between 8995 and 8999 eV of the white line can be detected and may be associated with $NH_3$ bound to Cu(II) based on reference XAS spectra of Cu(II)-tetraamine complexes (See Figure B.1) [71].

### 3.3.3 *Operando* XAS Reactor

*Operando* XAS experiments were performed in a custom built, down-flow, plug-flow reactor using a low X-ray absorbing vitreous carbon tube reactor. The design and implementation of the reactor have been discussed in detail in previous publications [5, 73]. The 4 mm ID carbon tube reactor was held inside an aluminum heater block which

had 1" long x 2 mm wide slits cut into the side to let the X-ray beam pass through the block and sample within the tube. Four 5" long, 100W heat cartridges (Chromalux CIR-1051) were used to heat the block. A wire mesh welded to a length of 1/16" tubing was used to hold the catalyst bed in place. From bottom to top, the catalyst bed was composed of a layer of quartz wool on top of the wire mesh, a layer of glassy carbon beads, the same material as the reactor tube, to create a flat surface upon which the catalyst could sit, followed by 20.5 mg of catalyst powder sieved to 125-250 μm, then another layer of quartz wool followed by a layer of crushed quartz (< 60 mesh) to help mix the gas flow. The catalyst bed height was roughly 3 mm and while this bed size was small compared to the bed diameter, the quality of the kinetics was not affected. An extensive discussion and comparison of the *operando* reactor with a conventional, bench top laboratory reactor can be found in our previous publication [5].

Temperature was measured with a thermocouple fed into the reactor and placed into the top layer of quartz wool just above the catalyst bed. Gases were mixed and introduced into the reactor in precise order to minimize potential formation of $NH_4NO_3$ as well as prevent other side reactions from taking place. The He carrier gas flowed through a heated shell-type humidifier (Perma Pure MH-Series) to introduce DI $H_2O$ into the gas stream. All gas lines downstream of the humidifier were kept heated above 373 K to prevent $H_2O$ condensation. After $H_2O$ introduction, NO and $NO_2$ (3000 ppm in $N_2$ each; Matheson Tri-Gas) were introduced into the gas stream to further dilute them before introduction of $O_2$ (20% in He; Airgas, Inc.). The reaction mixture was then preheated to 473 K before entering the reactor. The reactor was found to be well below the Mears

criterion for radial heat transfer gradients within the catalyst bed [5, 101, 102]. Ammonia (3000 ppm in He; Matheson Tri-Gas) was introduced through a feed through which ended a few inches above the catalyst bed to minimize the chances of gas phase side reactions from taking place. When the gas concentrations were measured in bypass of the reactor, the $NH_3$ was switched such that it was introduced into the gas mixture moments before passing through a 7 μm stainless steel particulate filter and entering the gas analysis system. Gas concentrations were measured using an MKS Multi-Gas 2030 gas analyzer FTIR with a cell temperature of 464 K based on the calibration files provided by the company. A total flow rate of 500 sccm and a temperature of 467 K were maintained throughout all of the experiments. Two types of the SCR reaction were considered, standard SCR and fast SCR. Standard SCR contained 300 ppm NO, 300 ppm $NH_3$, 5% $H_2O$ and 10% $O_2$ while fast SCR contained 150 ppm NO, 150 ppm $NO_2$, 300 ppm $NH_3$, 5% $H_2O$ and 10% $O_2$. In all experiments, the total $NO_x$:$NH_3$ ratio was maintained at unity where $NO_x$ contained either NO only or a mixture of NO and $NO_2$. Contrary to our previous experiments, $CO_2$ was not included as a reactant, because it was used as a tracer in the cut-off experiments discussed below. The presence or absence of $CO_2$ as a reactant was found to have no effect on the catalyst kinetics (see Table B.1 and Figure B.2).

### 3.3.4 Transient Cutoff Experiments

The cutoff experiments were designed to dynamically isolate the reducing or oxidizing portion of the SCR reaction. Each portion of the SCR redox cycle was isolated by systematically cutting off individual reactants, thereby unsettling the steady state balance

of redox sites, while tracking Cu active site changes in XAS under the modified gas conditions. Thus, if redox of Cu were central to the SCR reaction, the catalyst, which starts in a mixed Cu(I) – Cu(II) oxidation state under steady state standard SCR, should become more reduced when the oxidant is removed. Correspondingly, the catalyst should become more oxidized when a reducing agent is removed. Four different cutoff experiments were designed to test this hypothesis. For each experiment, the catalyst was first allowed to come to steady state under the standard or fast SCR reaction at which point steady state XAS and kinetic data were collected. After steady state data were collected, one of the reactants was cut off from the gas flow and the transient changes in catalyst and gas compositions were monitored by time-dependent XAS and the FTIR gas analyzer, respectively. Once changes in the XAS and the gas concentrations could no longer be identified, the gas was reintroduced, and again the changes were monitored in XAS and FTIR until the SCR reaction returned to steady state. For these experiments, $CO_2$ was used as a tracer to track the exchange of gases throughout the dead volume of the system upon cutoff of one of the reactants.

In the first experiment, $O_2$ was cut off from the standard SCR reaction mixture, isolating the reducing portion of the reaction, NO + $NH_3$. Second, NO was cut off from standard SCR, interrupting the reducing portion of the reaction and only allowing oxidation by $O_2$ in the presence of $NH_3$. Third, the $NH_3$ was removed to disrupt the reducing portion again and complete the series of reactant cutoffs from standard SCR. Finally, $NO_2$ was cut off from fast SCR conditions, converting the reaction mixture from fast SCR into standard SCR. The nature of the $NO_2$ cutoff experiment left an imbalance in the NO and

$NH_3$ concentrations where, for experimental reasons, the 150 ppm of lost $NO_2$ could not be replaced by an additional flow of NO to bring the $NO_x$:$NH_3$ ratio to unity. So the reaction conditions for this experiment only had 150 ppm NO and 300 ppm $NH_3$. The effects of this difference will be discussed in further detail later and were found to be negligible. For all steady state standard SCR conditions, the catalyst was maintained under differential conditions of less than 20% conversion of $NO_x$ in the 2.1 wt% Cu-SSZ-13 sample. For fast SCR with $NO_2$:$NO_x$ = 0.5 the steady state conversion was 23%. The 3.04 wt% sample exhibited higher than differential conversions typically close to 30%, however, the same trends were observed in the XAS data, indicating the samples were acting similarly. Only 8 mg were used in the catalyst bed in the *operando* reactor, which was approaching the limit of the system, therefore, a 30% conversion was unavoidable in order to maintain consistency in flow rates.

Only minor modifications to the gas manifold feeding the *operando* reactor needed to be made to allow for consistent switching. The most important aspect of the switch was to maintain the same total overall flow rate, so that gas concentrations remained unchanged. The gas switch was performed using an electronically actuated 2 position, 6-port switching valve (Valco Instrument Company, Inc.; Model E26UWE). In one position, the valve would feed the cutoff gas into the reactor. In the other position the valve would feed a mixture of $CO_2$ and He with the same total flow rate as the cutoff gas into the reactor. The cutoff valve could not be switched from outside of the X-ray hutch, so there was a slight delay between when the valve was switched and the XAS data collection started. The process between switching the valve and beginning the XAS scan took

around 5-10 seconds, but we do not have an exact measure of this time for each experiment. The computer logged XAS scan start times were used to arbitrarily set a t = 0 s value for the gas analyzer data. The true t = 0 s value is therefore somewhere between 5 and 10 s *after* the switch was made.

The resulting spectra from the transient cut off and addition experiments were fitted with three references in linear combination XANES fits. The first reference was a hydrated Cu(II), $[Cu(H_2O)_6]^{2+}$, which we have observed to be the primary Cu species in Cu-SSZ-13 under ambient conditions (see Figure B.4), thus making it a reasonable reference to use under reaction conditions. Isolated Cu(II) and isolated Cu(I) references were obtained by treating the lowest obtained Cu loading in SSZ-13 (0.31 wt% Cu corresponding to Cu:Al = 0.02) assuming that only the isolated Cu species was present as is suggested in literature[33, 42, 43]. The isolated Cu(II) was created with 10% $O_2$ in UHP He at 473 K and the isolated Cu(I) was obtained with 1000 ppm NO and 1000 ppm $NH_3$ in UHP He at 473 K. The XANES and EXAFS spectra for these can be found in the supplemental information (Figures B.4-B.5, Table B.2).

### 3.3.5 $NO_2$:$NO_x$ Ratio Experiments

In addition to the cutoff experiments, we also investigated the role of $NO_2$ in the fast SCR reaction with relation to the Cu oxidation state. Our previous work suggested that the presence of $NO_2$ eliminated nearly all Cu(I) on the catalyst irrespective of the catalyst composition (Cu-ZSM-5, Cu-SSZ-13 and Cu-SAPO-34) when $NO_2/NO_x$ = 0.5 [5, 103]. It was hypothesized that since $NO_2$ was a strong oxidant, it acted to oxidize Cu(I) so

quickly that when a Cu(I) was formed by the reducing reaction it would be reoxidized by $NO_2$, making it appear in XAS as if Cu(I) was absent from the catalyst. However, since only one $NO_2$:$NO_x$ ratio was evaluated, it was unclear at what concentrations, if at all, the oxidative strength of $NO_2$ would break down. To investigate the effects of $NO_2$ the gas concentrations were varied to produce four different $NO_2$:$NO_x$ ratios of 2:5, 1:4, and 1:10. In all cases the total $NO_x$ concentration summed to 300 ppm, where the makeup $NO_x$ gas was NO. Hence, the gas concentrations were varied from 120 ppm $NO_2$ + 180 ppm NO, to 75 ppm $NO_2$ + 225 ppm NO, to 50 ppm $NO_2$ + 250 ppm NO, to 30 ppm $NO_2$ + 270 ppm NO, and always included 300 ppm $NH_3$, 5% $O_2$, 5% $H_2O$, 5% $CO_2$ and balance He at a constant total flow rate of 500 sccm at 467 K. Only for these particular experiments was the catalyst operated at non-differential conditions with conversion of $NO_x$, and more specifically $NO_2$, greater than 20%. There was no way to prevent the high $NO_2$ conversion, especially when $NO_2$ was at low concentrations, since the higher fast SCR rates consumed greater amounts of reactants at the same gas conditions and temperatures used for standard SCR. However, allowing non-differential conversions produced large changes in the $NO_2$ concentration over the length of the catalyst bed and provided a secondary opportunity to test the effect of $NO_2$ concentration. By changing the $NO_2$ concentration sufficiently throughout the catalyst bed (i.e. >20% conversions of $NO_2$) the upper portion of the catalyst experienced a reaction environment that caused measurable changes in the Cu oxidation state. To probe the catalyst by XAS over the length of the bed the X-ray beam size was reduced to 200 x 200 μm and XAS data were collected at the top third and bottom third of the catalyst bed once the catalyst reached steady state.

In all cases, $NO_2$ conversion was between 25 and 85% and a minimum of 5 ppm of $NO_2$ or more always exited the reactor.

## 3.4 Results

### 3.4.1 Transient Cutoff Experiments

Four transient cutoff experiments were performed on two Cu loadings of SSZ-13, each removing a different reactant. The results and discussion sections will focus on the 2.1 wt% Cu-SSZ-13 (Cu:Al =0.11) sample unless otherwise noted. The reader is referred to the supplemental material (Appendix B) for a complete data set on the 3.04 wt% sample (Cu:Al = 0.16). Dioxygen was cut off from standard SCR gas conditions to isolate the reducing portion of the reaction, NO and $NH_3$ were removed in individual experiments from the standard SCR reaction to isolate the oxidizing portion of the reaction, and $NO_2$ was removed from fast SCR to transition to standard SCR. The corresponding reverse experiments, where the cut off reactant was reintroduced, were also captured. The transient changes in gas concentrations are presented in supplemental material (Figures B.6, B.7, B.9, B.10, B.12, B.13, B.15, and B.16). The simultaneously collected, time-resolved XAS for each cutoff experiment are presented in Figures 3.1, 3.3, 3.5, 3.7, B.8, B.11, B.14, and B.17. Before examining the individual figures in detail a few general points need to be discussed.

First, the gas concentrations presented in Figures B.6, B.7, B.9, B.10, B.12, B.13, B.15, and B.16 for the 2.1 wt% Cu-SSZ-13 sample were normalized to the gas concentrations measured as they bypassed the reactor, typically before the cutoff experiment was

performed. During the cutoff experiments, the $NH_3$ mass flow controller (MFC) became unstable and the flow fluctuated. The fluctuations increased the $NH_3$ concentration by 10-15% compared to the bypass and, as can be seen particularly well in Figures B.6 and B.9, this resulted in normalized $NH_3$ concentrations greater than unity. Since the reaction was maintained under differential conditions with < 20% conversion, a 10-15% change in $NH_3$ concentration would not greatly change the overall gas concentrations, for example, at 10% conversion the reactor outlet concentration was 270 ppm NO and 270 ppm $NH_3$ compared to the inlet concentration of 300 ppm $NH_3$ and is unlikely to affect catalyst kinetics or the steady state oxidation state of Cu within the error analysis of between ± 5-10%. $NH_3$ orders published on Cu-ZSM-5 [14, 49], as well as our own kinetic data on Cu-SSZ-13 and Cu-SAPO-34 indicate only a weak dependence of the rate on $NH_3$ with an order of ~0 in this range of concentrations. In terms of the other gas concentrations, the changes in the $NH_3$ MFC flowrates manifested themselves as an increase of up to 5-6 sccm into a total flow rate of 500 sccm. For concentrations of the other reaction gases, especially NO, this equated to a change in the NO concentration of up to 3-4 ppm which was just slightly larger than the error in the NO measurement of ±2-3 ppm. Lastly, flowing $NH_3$ alone over the catalyst could not generate significant amounts of Cu(I) (see Figure B.3). Thus, the fluctuation in the $NH_3$ concentration would not have any substantial effects on the Cu oxidation state or any of the other results presented herein.

Second, the ‘slow’ actuation of the switching valve and the high flow rates used in the experiments caused pressure swings downstream which were apparent in noticeable swings in the gas concentrations measured by the gas analyzer. The variations were

limited to the period just after the gas was cutoff but before it had flushed out of the system. Since these variations only changed apparent gas concentrations by up to 10% (with one exception being the $NO_2$ cutoff in Figure B.15) and subsided before the cutoff gas was flushed out of the system they had no major effect on the experiment.

Finally, a brief discussion of the cutoff curves is warranted. Figure B.9 provides a comparison of how the signals of the cutoff gas and tracer should look in a typical experiment. In Figure B.9, NO was cutoff and replaced by the tracer, $CO_2$. The tracer is used to obtain a measurement for how quickly a gas that ideally has no interaction with the catalyst, reactant gases or experimental equipment would reach its steady state concentration. It represents an *in situ* measure of the time it takes for the system to be purged of one gas and replaced by another, also referred to in terms of the dead volume of a system. The $CO_2$ gas curve shows no concentration change for the first 35 s and then rises to its maximum. Similarly, the NO curve, after the pressure fluctuation from the gas switch, began dropping after 35 s and decreased to 0. At the same time, the $NH_3$ concentration began to increase from its steady state reaction concentration to its bypass concentration, indicating no further $NH_3$ consumption once NO was removed. For the NO cutoff experiments, the tracer required 59 seconds to reach 95% of its maximum concentration. Note the similar, but opposite decay of the curve for NO over the same 59 s time frame. The curves also cross each other very near 0.5, a testament to the symmetric nature of the behavior of the two gases and an indication that NO and $CO_2$ experienced the same gas phase hold-up and that, therefore, NO was not significantly consumed or delayed by reaction or adsorption/desorption processes. A more strongly

adsorbing gas, like $NH_3$, will tend to take longer than the tracer to decay as it interacts with the environment along the way. For this reason, $NH_3$ always tended to adjust to the cutoff at a slower rate than the $CO_2$ tracer or even other reactant gases. For a detailed discussion of these types of switching experiments and how the curves are affected by dead volumes, catalyst surface interaction and reaction processes the reader is referred to the literature on steady state isotopic transient kinetic analysis (SSITKA) [104, 105]. The roughly one minute exchange time for the $CO_2$ tracer is self-consistent with the overall dead volume of the system, which is dominated by the 500 $cm^3$ volume of the FTIR gas analyzer chamber, however, each experiment required the lines to be reconfigured and the dead volume of the system could change slightly depending on the experiment. At a total flow rate of 500 sccm the exchange time for $CO_2$ should be close to 60 s. A table of exchange times for each of the individual gases and the corresponding XAS Cu oxidation state conversion times is presented in Table 3.1

Table 3.1 Table of times for 95% signal decay or 95% signal growth in gas concentrations after gas cutoff or addition measured by the gas analyzer compared to the corresponding timeframes for which the Cu reaches 95% of the final steady state oxidation state measured by XAS.

| Cu wt% of Sample | Gas | $O_2$ Cutoff / s | $O_2$ Addition / s | NO Cutoff / s | NO Addition / s | $NH_3$ Cutoff / s | $NH_3$ Addition / s | $NO_2$ Cutoff / s | $NO_2$ Addition / s |
|---|---|---|---|---|---|---|---|---|---|
| 2.1 | NO | 576 | 76 | 59 | 67 | 1395 | 391 | 120 | 80 |
| | $NH_3$ | 611 | 147 | 84 | N/A* | 143 | 392 | 245 | 93 |
| | $CO_2$ | 64 | 66 | 59 | 59 | 59 | 47 | 80 | 67 |
| | $NO_2$ | N/A | N/A | N/A | N/A | N/A | N/A | 87 | 491 |
| | Time for Cu to stabilize in XANES | 1247-1382 | 32-167 | 437-572 | 707-842 | 2327 | 1026 | 167-302 | 302 |
| 3.04 | NO | 117 | 70 | 45 | 56 | 412 | 224 | 92 | 1704 |
| | $NH_3$ | 174 | 85 | 60 | 47 | 445 | 340 | 100 | 1895 |
| | $CO_2$ | 76 | 73 | 44 | 51 | 85 | 86 | 102 | 73 |
| | $NO_2$ | N/A | N/A | N/A | N/A | N/A | N/A | 100 | 1975 |
| | Time for Cu to stabilize in XANES | 742-884 | 32-174 | 316-458 | 32-174 | 1736-1878 | 316 | 1736-1878 | 174-316 |

*For this experiment only, $NH_3$ concentration did not approach a steady value, and so no 'steady state' concentration could be measured to use for comparison.

The XAS measured simultaneously to the gas cutoff curves are presented in Figures 3.1, 3.3, 3.5, 3.7, B.8, B.11, B.14, and B.17. The figures emphasize the XANES range, the fingerprint region for different oxidation states. Due to noise in the EXAFS region we were unable to extract structural information about the Cu coordination environment. Based on previous data analysis by our group [5, 103] as well as the literature [49, 66, 106, 107], however, the XANES can still be used to qualitatively and quantitatively determine the amounts of Cu(I) and Cu(II) on the catalyst. In each figure, the last time point for which data was collected is shown to identify when the catalyst had reached a steady state. Table 3.2 shows the linear combination XANES fits for contributions of Cu species in the steady states achieved before and after each transient cutoff experiment.

Table 3.2 Table of XANES linear combination fits for each reactant cutoff and addition experiment. The conditions analyzed correspond to the steady state value (SS value) and after the reactant is removed or before it is added to the gas mixture. ±5% error involved in fitting procedures.

| Cu wt% of Sample | Experiment | Condition | Hydrated Cu(II) / % | Isolated Cu(II) / % | Isolated Cu(I) / % | Sum of Cu(II) / % |
|---|---|---|---|---|---|---|
| 2.1 | O2 Cutoff | SS Value | 7 | 64 | 29 | 71 |
| | | After $O_2$ Cutoff | 1 | 23 | 76 | 24 |
| | O2 Addition | Before $O_2$ Addition | 1 | 23 | 76 | 24 |
| | | SS Value | 7 | 61 | 32 | 68 |
| | NO Cutoff | SS Value | 8 | 65 | 27 | 73 |
| | | After NO Cutoff | 10 | 78 | 12 | 88 |
| | NO Addition | Before NO Addition | 10 | 78 | 12 | 88 |
| | | SS Value | 8 | 65 | 27 | 73 |
| | NH3 Cutoff | SS Value | 3 | 73 | 24 | 76 |
| | | After $NH_3$ Cutoff | 41 | 55 | 4 | 96 |
| | NH3 Addition | Before $NH_3$ Addition | 41 | 55 | 4 | 96 |
| | | SS Value | 4 | 71 | 25 | 75 |
| | NO2 Cutoff | SS Value | 18 | 82 | 0 | 100 |
| | | After $NO_2$ Cutoff | 12 | 68 | 20 | 80 |
| | NO2 Addition | Before $NO_2$ Cutoff | 12 | 68 | 20 | 80 |
| | | SS Value | 15 | 83 | 2 | 98 |
| 3.04 | O2 Cutoff | SS Value | 4 | 60 | 36 | 64 |
| | | After $O_2$ Cutoff | 0 | 5 | 95 | 5 |
| | O2 Addition | Before $O_2$ Addition | 0 | 5 | 95 | 5 |
| | | SS Value | 4 | 60 | 36 | 64 |
| | NO Cutoff | SS Value | 4 | 62 | 34 | 66 |
| | | After NO Cutoff | 6 | 79 | 15 | 85 |
| | NO Addition | Before NO Addition | 8 | 80 | 12 | 88 |
| | | SS Value | 4 | 62 | 34 | 66 |
| | NH3 Cutoff | SS Value | 4 | 59 | 34 | 63 |
| | | After $NH_3$ Cutoff | 48 | 47 | 5 | 95 |
| | NH3 Addition | Before $NH_3$ Addition | 48 | 47 | 5 | 95 |
| | | SS Value | 4 | 61 | 35 | 65 |
| | NO2 Cutoff | SS Value | 21 | 76 | 3 | 0 |
| | | After $NO_2$ Cutoff | 9 | 69 | 22 | 0 |
| | NO2 Addition | Beofre $NO_2$ Cutoff | 9 | 69 | 22 | 0 |
| | | SS Value | 20 | 76 | 4 | 0 |

Figure B.6 reveals the transient changes in gas concentrations as $O_2$ was cut off and replaced by $CO_2$. After the concentration swings, the $CO_2$ curve rises and reaches its normalized maximum. The NO and $NH_3$ curves start at levels that represent their steady state conversion of around 12% and upon the switch begin climbing to their bypass concentrations as the reaction slows and less consumption of the reductants takes place. It took 64 seconds for the $CO_2$ signal to reach 95% of its maximum with a roughly 30 second rise time to go from zero to 95% signal maximum. It is expected that the $O_2$ cutoff would have reached 95% signal decay over a similar time period as the $CO_2$. (Visually, the $O_2$ curve would be similar to the NO cutoff curve in Figure B.9, but $O_2$ cannot be measured by IR so we are not able to provide this data.). The transient NO and $NH_3$ concentration curves, on the other hand, took 576 s and 611 s to reach 95% of their signal maxima, respectively (Table 3.1). The difference in slope and especially the time it took to reach their inlet concentration for the NO and $NH_3$ compared with the $CO_2$ indicate that NO and $NH_3$ were being consumed via the reducing portion of the SCR reaction for some period after the vast majority of $O_2$ had been removed from the system. It should be noted that during all cutoff experiments no new products were measured in the gas analyzer that would indicate a change in the reaction mechanism or activity of some side reaction. A similar result was obtained for the 3.04 wt% Cu-SSZ-13 sample, as indicated by Figure B.18 and Table 3.1. The difference observed in time for the gases to stabilize in the NO and $NH_3$ traces when compared to the $CO_2$ tracer was roughly doubled at 117 s and 174, respectively, with a similar curve shape as the 2.1 wt% sample.

The XANES data collected simultaneously during $O_2$ cutoff were analyzed and are shown in Figure 3.1. Upon cutting off the oxidant to the reaction mixture, the Cu(I) peak at 8983 eV increased rapidly beyond the steady state height characteristic of standard SCR. The concentration of isolated Cu(I) on the catalyst increased from the steady state value of 29% isolated Cu(I) until a large fraction of the Cu on the catalyst had been reduced with a final value of 76%. The extent of reduction is also evident in the decrease of the 8995 eV peak.

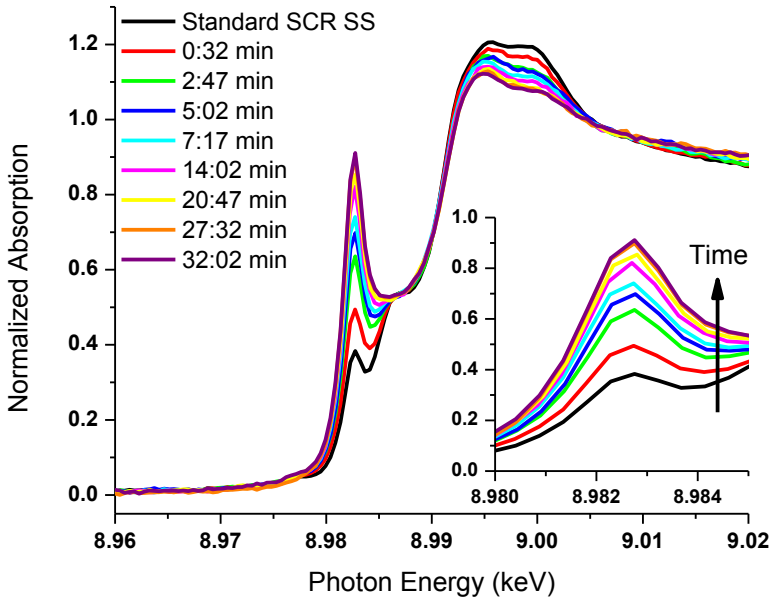


Figure 3.1 Time resolved XAS of the 2.1 wt.% Cu-SSZ-13 catalyst after O2 was cut off from the standard SCR reactant stream. Inset zooms in on the edge feature at ~9.9828 keV, the identifying feature of Cu(I) species. To clearly present the data, spectra are not linear in time scale.

The XANES data show that the growth of the Cu(I) edge feature reached steady state after the 27:32 min mark. Using this peak area as the normalization point, the catalyst reached 95% of this Cu(I) concentration somewhere between the 20:47 min (1247 s) and the 23:02min (1382 s) mark. The broad time range for this determination is due to the errors associated with linear combination XANES fitting that are on the order of ± 5%. The catalyst was reduced to roughly 75% of its maximum Cu(I) concentration at the 9:32 min (572 s) mark where the NO curve reached its 95% maximum. Ideally, the gas exchange times and the XAS times should be identical, and in this case, there is moderately good agreement between the two although the data still are almost four minutes off from one another. The hydrated Cu(II) present during the transient process was negligible with only 7% present under steady state standard SCR conditions and the final value of 1% after the cutoff. The normalized transient NO and $NH_3$ rates per mole Cu during the $O_2$ cutoff were observed to track with the normalized change in the ratio of isolated Cu(II) to isolated Cu(I), which is shown in Figure 3.2.

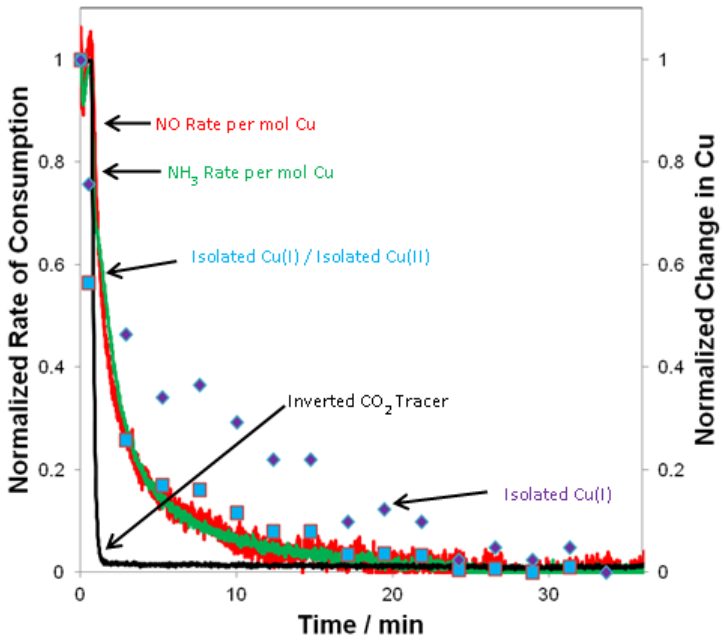


Figure 3.2 Transient NO and $NH_3$ rates per mole of Cu and changes in Cu species after $O_2$ was removed from the reactant mixture in the 2.1 wt% Cu-SSZ-13 sample. An inverted $CO_2$ signal is shown to illustrate the gas holdup of the system.

The individual isolated Cu(I) species did not do a good job at describing the transient rate and were particularly inadequate in the elbow region of the figure (between 0-15 min). The dependence on a ratio of Cu species could only come about if a step or multiple steps in the reaction mechanism involving both Cu species were quasi-equilibrated. This would give a relationship through an equilibrium constant(s) with a ratio of isolated Cu species and products and reactants. This relationship was directly probed in the cutoff experiments described in this study. This relationship is a secondary evidence that a Cu redox cycle exists and that both Cu species are related through a complicated relationship. The hydrated Cu(II) was not included in the ratio, as it appeared to not change significantly, only contributing up to a 6% change.

The gas concentration and XAS figures from the reverse experiment, where $O_2$ was added to the NO, $NH_3$, and $H_2O$ mixture to return to standard SCR gas conditions, are presented in Figures B.7 and B.8. The NO concentration reached 95% of its steady state conversion after 76 s, only ten seconds slower than the $CO_2$ tracer. $NH_3$ took about twice as long as NO to reach 95% of its steady state conversion at 147 s (Table 3.1). Contrary to the cutoff experiment, reintroducing $O_2$ brought the Cu oxidation state to its steady state close to 8 times faster. Within 32 s of $O_2$ addition more than half of Cu(I) had been converted to Cu(II) and by the time the second XAS measurement had reached the Cu(I) region (147 s), the catalyst had effectively reached the steady state Cu(I) concentration expected during standard SCR. (In Figure B.8, the teal spectrum (2:47 min) is covered by the other two spectra at 9:32 min and 16:17 min.).

The NO cutoff experiments are shown in Figure 3.3 and Figure B.9 for the Cu XANES edge and gas concentration profiles, respectively. The NO signal decayed to 5%

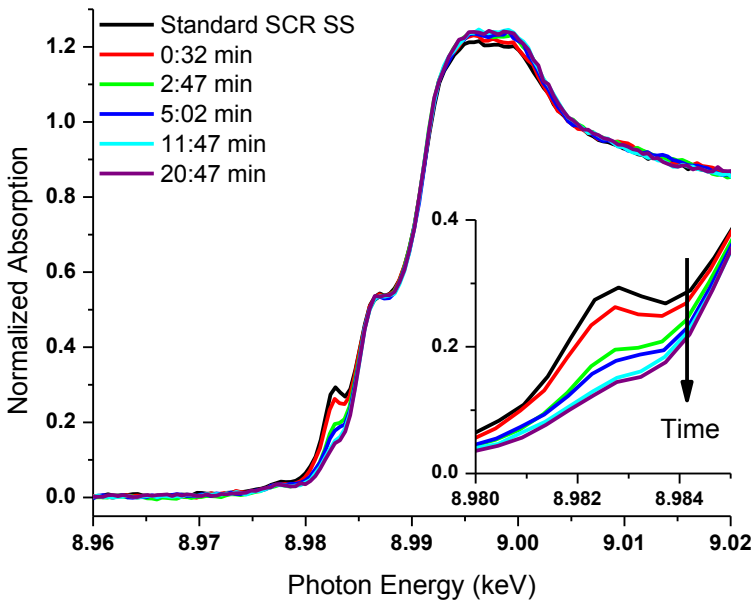


Figure 3.3 Time resolved XAS of the 2.1 wt.% Cu-SSZ-13 catalyst after NO was cut off from the standard SCR reactant stream. Inset zooms in on the edge feature at ~9.9828 keV, the identifying feature of Cu(I) species. To clearly present the data, spectra are not linear in time resolution.

of its inlet concentration in 59 s and matched with the $CO_2$ tracer which took 59 s to reach 95% of its maximum concentration. $NH_3$ required another 25 s longer before adjusting to the concentration change and reached 95% of its signal maximum at 84 s (Table 3.1). The corresponding XAS data show that Cu took between 7:17 min and 9:32 min to oxidize most of the Cu(I) produced under the steady state SCR gas conditions. These results indicate that $NH_3$ is not oxidized by $O_2$ and that oxidation of Cu(I) by $O_2$ is slow compared to standard SCR. The rate of Cu(I) oxidation for this experiment ($O_2$ +

$NH_3$) is significantly slower than under other conditions. (see Table 3.1). $O_2$ addition to NO + $NH_3$ and $NO_2$ addition to standard SCR, for example, oxidized Cu(I) to Cu(II) faster than $O_2$ plus $NH_3$. This fast re-oxidation was also illustrated by the transient NO and $NH_3$ rate per mole Cu compared to the ratio of isolated Cu(I) to isolated Cu(II) shown in Figure 3.4. Again, the ratio of isolated Cu species was tracking with the observed transient rates. In this case, the inverse of the $O_2$ cutoff (isolated Cu(I)/isolated Cu(II)) was being probed since we were pushing the redox cycle in the opposite direction to a Cu(II) state.

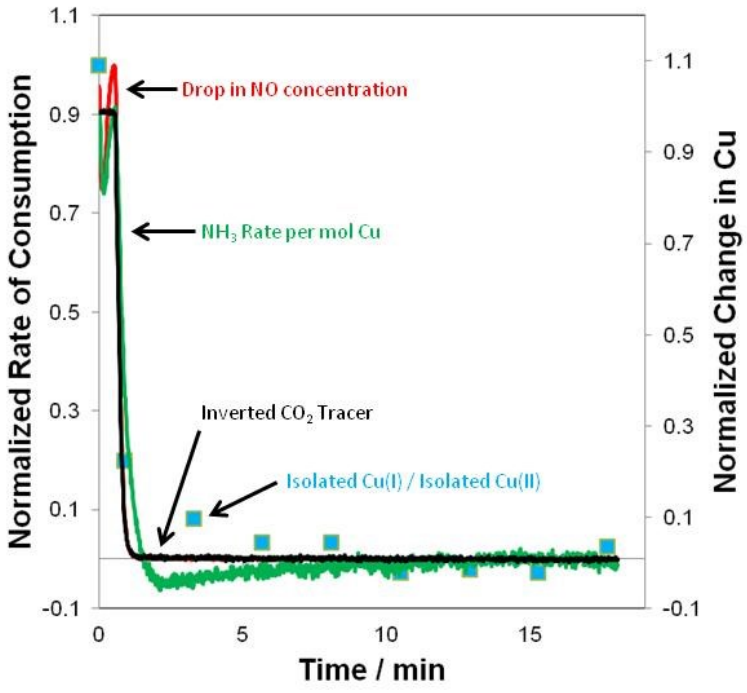


Figure 3.4 Transient $NH_3$ rate per mole of Cu and changes in Cu species after NO was removed from the reactant mixture in the 2.1 wt% Cu-SSZ-13 sample. An inverted $CO_2$ signal is shown to illustrate the gas holdup of the system along with the drop in NO concentration during the cutoff.

The complementary NO addition experiment in Figures B.10 and B.11, where the NO was added back into the $NH_3$, $O_2$, and $H_2O$ gas mixture to return to standard SCR conditions, showed a similar trend to the NO cutoff, but in the reverse direction. The catalyst began in the fully oxidized state and once NO was introduced the redox capability of the catalyst was restored and it began approaching its steady state Cu(I) concentration. As per Table 3.1 and Figure B.10, it took 59 s for $CO_2$ to decay to 95% of its inlet concentration and 68 s for the NO to reach 95% of its steady state concentration. The 95% growth point of the $NH_3$ could not be measured for this experiment (Figure B.10). In the XAS in Figure B.11, the effect of adding the NO back into the reaction mixture was immediately evident on the catalyst as within 30 s of NO addition, the Cu(I) edge feature became apparent. The process of reaching the steady state Cu(I) concentration was very slow, however, and not until the 11:47 min mark did the Cu(I) approach the previously measured steady state Cu(I) concentration. This compares unfavorably with the gas concentrations which reach their steady state SCR concentrations much quicker, however, the first 75% of the change in Cu occurred in the first 302 s.

The $NH_3$ cutoff experiments are shown in Figure 3.5 and B.12 for the Cu-K edge XANES and gas concentration profiles, respectively. The $NH_3$ signal reached 95% of its initial value within 143 s, while the $CO_2$ reached 95% of its maximum value acting as a system tracer within 59 seconds.

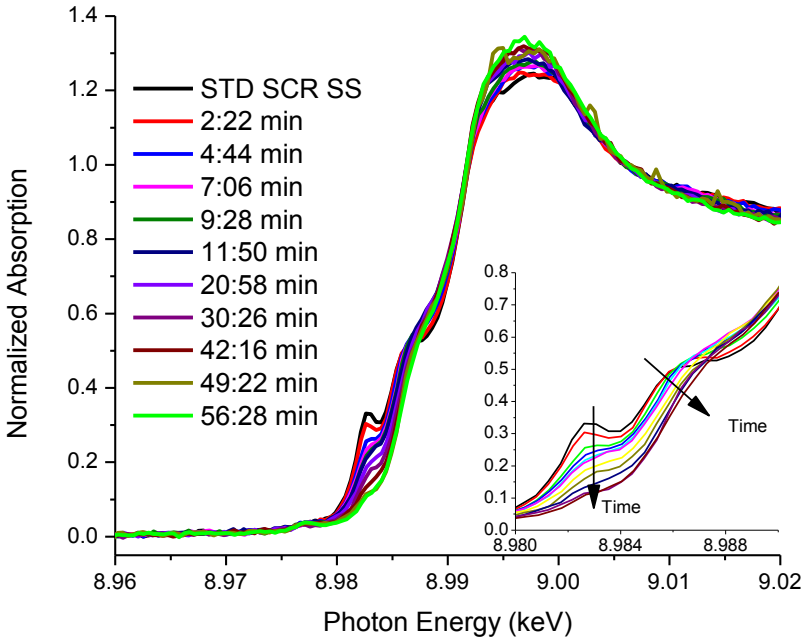


Figure 3.5 Time resolved XAS of the 2.1 wt.% Cu-SSZ-13 catalyst after $NH_3$ was cut off from the standard SCR reactant stream. Inset zooms in on the edge feature at ~9.9828 keV, the identifying feature of Cu(I) species. To clearly present the data, spectra are not linear in time resolution.

The NO was observed to have 95% of its exchange occur around 23:15 min (1395 s), with a very slow ascent to its final concentration. The slow NO response strongly suggests it continued to react with an adsorbed $NH_3$ species somewhere within the catalyst. Figure 3.6 shows the transient rate per mole Cu of NO along with the drop in $NH_3$ concentration as it left the system. The ratio of isolated Cu species (isolated Cu(I) / isolated Cu(II)) did not track with the transient NO rate as it did in the NO and $O_2$ cutoff experiments.

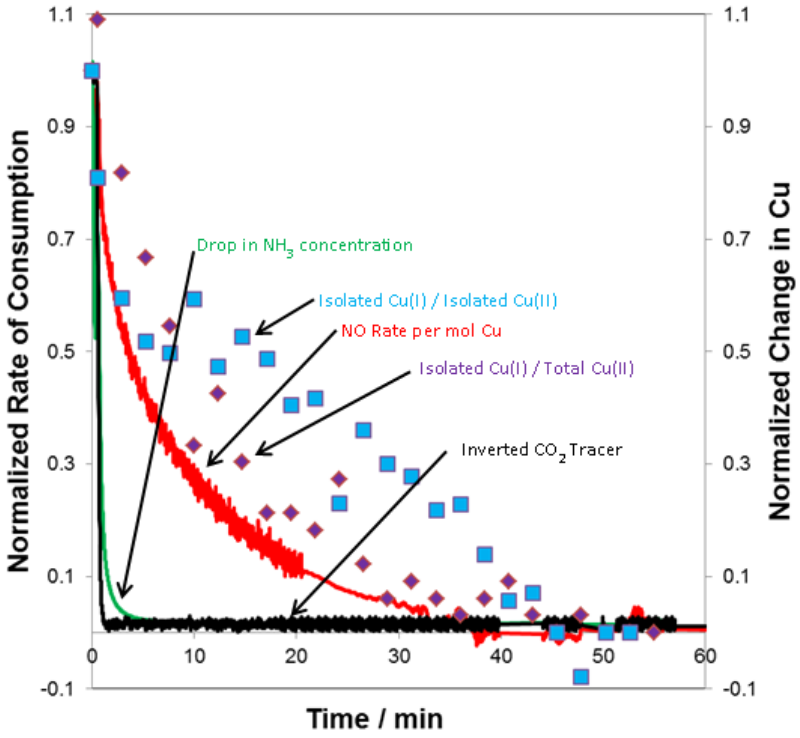


Figure 3.6 Transient NO rate per mole of Cu and changes in Cu species after $NH_3$ was removed from the reactant mixture in the 2.1 wt% Cu-SSZ-13 sample. An inverted $CO_2$ signal is shown to illustrate the gas holdup of the system along with the drop in $NH_3$ concentration during the cutoff. The data became noisy after 20 minutes passed because the IR detector began to warm up, thus the data was averaged after 20 minutes to remove the noise.

During the process, the Cu appeared to become significantly hydrated, with a 36% contribution from the hydrated Cu(II) reference by the end of the experiment (Table 3.2). With a third species appearing in significant quantities, the changes became too complex to be described by the ratio of isolated Cu species. When the $NH_3$ reacted or desorbed off the Cu, an isolated Cu(I) may have been oxidized to Cu(II) and then converted to a hydrated Cu(II) with water being prevalent in the gas mixture. If this was the case, the ratio of isolated Cu(I) to total Cu(II) would track closely with the transient NO rate rather

than the isolated Cu ratio. Figure 3.6 shows this Cu ratio does a better job of capturing the shape of the transient NO rate rather than the ratio of isolated species; however, the Cu curve appears to lag behind transient NO rate per mole Cu. This was reflected in the time for the isolated Cu(I) to reach 5% of its initial value of 2327 s, which was 15 minutes slower than the time for the NO gas concentrations to settle. The lag may suggest that some Cu had $NH_3$ adsorbed which did not react, but slowly desorbed over time as the sample was flushed and $NH_3$ was removed from the gas phase. The slow shift to a 36% contribution from hydrated Cu(II) during the cutoff clearly indicated that $NH_3$ was present on the Cu under reaction conditions, but from this experiment, it is too difficult to de-convolute the competing effects.

The $NH_3$ addition experiment is shown in Figures B.13 and B.14 for the gas concentrations and Cu-K edge XANES, respectively. Both NO and $NH_3$ took nearly 6:30 min (391 and 392 s, respectively) for 95% of their changes to occur while the $CO_2$ stabilized to 95% of its value within 47 s. The slower response of the NO and $NH_3$ when compared to the $CO_2$ can be attributed to $NH_3$ storage within the zeolite as well as reaction occurring during the transient process. The time for Cu(I) to reach 95% of its final value was considerably slower than the gas concentrations at 1026 s.

Depicted in Figures 3.7 and B.15 are XAS of the catalyst and the gas concentrations during the $NO_2$ cutoff experiments from fast SCR. In these experiments we were not isolating either the oxidative or reducing portion of the reaction as we were with the NO and $O_2$ cutoff experiments. For these experiments the idea was to gain insight into how

the Cu oxidation state is affected by the presence of the strong oxidant, $NO_2$. Cutting off $NO_2$ from fast SCR produced the standard SCR reaction mixture. As expected, the cutoff drove the catalyst from the fully oxidized state to the standard SCR steady state mixed oxidation state.

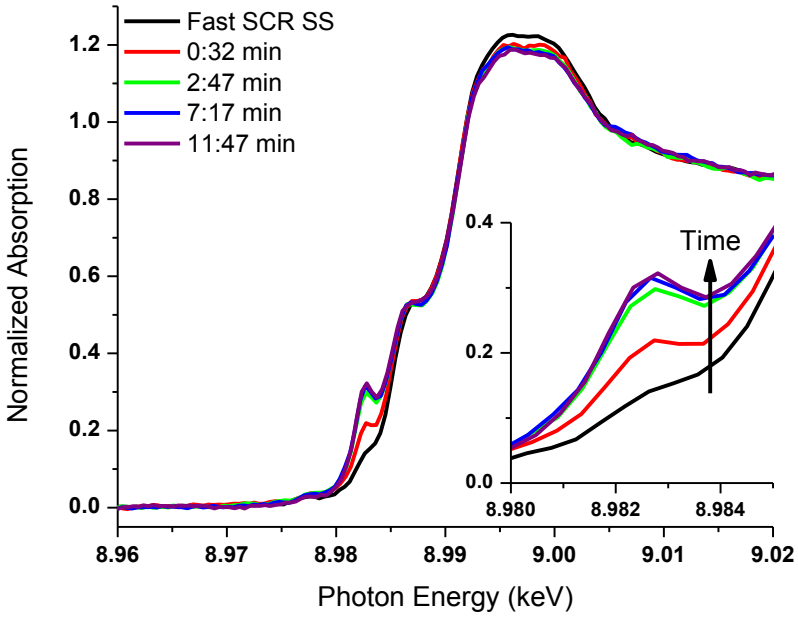


Figure 3.7 Time resolved XAS of the 2.1 wt.% Cu-SSZ-13 catalyst after $NO_2$ was cut off from the fast SCR reactant stream. Inset zooms in on the edge feature at ~9.9828 keV, the identifying feature of Cu(I) species. To clearly present the data, spectra are not linear in time resolution.

$NO_2$ decayed to 95% of its steady state concentration within 87 s (Table 3.1) and $CO_2$ grew to 95% of its maximum signal in 80 s (Figure B.15). The NO and $NH_3$ reached 95% of their standard SCR steady state concentrations in 120 and 245 s, respectively. The XAS showed a swift response and 30 s after the cutoff, Cu(I) was already present in the

XANES (Figure 3.7). By the second XAS measurement at 167 s the Cu(I) concentration had reached 95% of the steady state standard SCR Cu(I) concentration. In contrast to the quick response of the Cu in the 2.1wt.% sample, the 3.04 wt.% sample exhibited a much slower response in Cu with 28:56 min to change 95%. It is possible that the 3.04 wt.% sample suffered from the formation of ammonium nitrate through a nitrate intermediate because the conversions observed in standard SCR after the $NO_2$ cutoff in Figure B.30 were 15% lower than the standard SCR conditions before $NO_2$ was introduced to the mixture (Figure B.18). One proof of this was that after the $NO_2$ transient experiments were finished, the catalyst was heated to 573 K in UHP He to decompose the ammonium nitrates formed. Once the temperature cooled to 473 K again, the catalyst regained its ability to perform standard SCR as it did before $NO_2$ was introduced into the gas feed (not shown). So, the slow changes seen in the Cu ($NO_2$ cutoff experiment) or gas concentrations ($NO_2$ addition experiment) could be attributed to ammonium nitrate building up or decomposing in the 3.04 wt% sample. Since the 2.1 wt% sample did not have the slow responses or problems with regaining its original rate, we concluded that the 2.1 wt% sample did not suffer from formation of ammonium nitrate.

Reintroduction of $NO_2$ to the standard SCR mixture in the 2.1 wt% sample led to swift removal of Cu(I) on the catalyst (Figure B.17). More than half of the Cu(I) was removed within 30 s of $NO_2$ addition and after 167 s the catalyst had reached 95% of the fast SCR steady state Cu oxidation state, which essentially is the fully oxidized catalyst. Correspondingly, the gas concentrations for $CO_2$, NO and $NH_3$ (Figure B.16) steadied quickly, reaching 95% signal decay/growth in 67, 80 and 93 seconds, respectively. $NO_2$

on the other hand, required 491 seconds to reach 95% of its maximum steady state concentration. As mentioned, the 3.04 wt% Cu-SSZ-13 sample exhibited a much slower change in the gas concentrations with 28:24 min (1704 s) and 31:35 min (1895 s) for NO and $NH_3$, respectively. The time for Cu to stabilize in the XANES region was between 174-316 s, which was significantly faster than the gas concentrations, but with the powerful oxidizing ability of $NO_2$, it was not a surprise it occurred quickly. The long response of the NO and $NH_3$ to reach a steady state suggested that ammonium nitrates were building up. It is not clear why there were differences in the two samples as they were both expected to contain only isolated Cu species based on our own characterization of the samples and from comparison to the recent report by Kwak et al.[43] using $H_2$ TPR to probe different Cu species.

### 3.4.2 $NO_2$:$NO_x$ Ratio Experiments

In Cu-zeolite catalysts for SCR, $NO_2$ appears to have a particularly strong effect on the oxidation state of Cu. Our previous work with a 50:50 mixture of NO and $NO_2$ as the $NO_x$ source, as in fast SCR, has shown that nearly all detectable Cu(I) that would have otherwise been present with NO as the sole $NO_x$ source (i.e. standard SCR) was eliminated from the catalyst [5, 103]. To further investigate the effects of $NO_2$, we performed a set of experiments where we adjusted the fraction of $NO_2$ that $NO_x$ was composed of, effectively lowering the oxidative strength of the mixture as we lowered the $NO_2$:$NO_x$ ratio. The general results of the experiments are presented in Figure 3.8 for the SCR reaction with steady state $NO_2$:$NO_x$ ratios of 4:10, 2.5:10, and 1:10 as well as the reference standard SCR condition at steady state. The ‘Top’ designation in the plot refers

to the location along the length of the catalyst bed where the XAS data was collected. In other words, we can reasonably expect that the top of the catalyst bed experienced gas conditions similar to the feed conditions, whereas, due to the non-differential $NO_2$ conversion, the bottom of the catalyst bed experienced $NO_2$ concentrations 25 – 80% less than at the inlet.

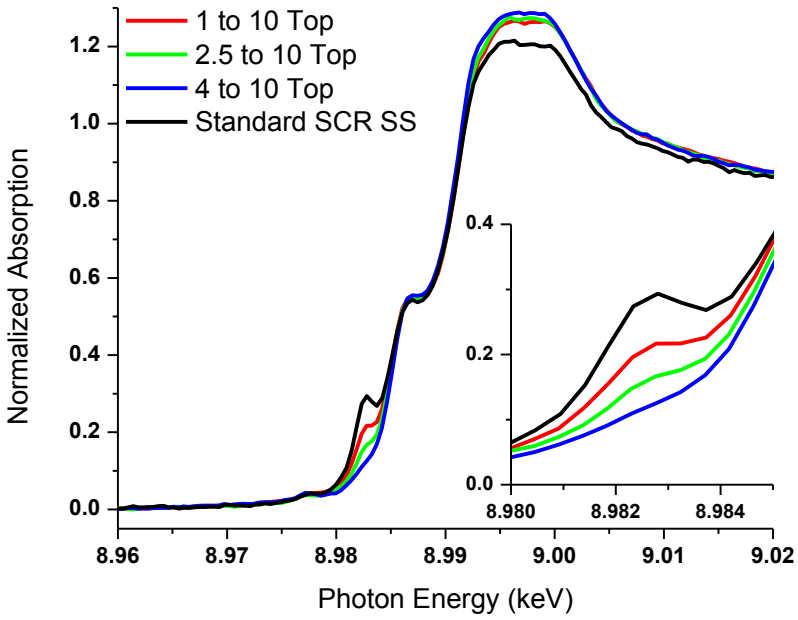


Figure 3.8 XAS of the 2.1 wt.% Cu-SSZ-13 catalyst under SCR conditions with varying $NO_2$:NOx ratios measured at the top of the catalyst bed. For reference, the XAS of the catalyst under the $NO_2$ free, standard SCR, gas conditions was also included.

Compared to the catalyst under standard SCR conditions, the presence of $NO_2$ acts to decrease the amount of Cu(I) on the catalyst even if only 10% of the $NO_x$ feed is composed of $NO_2$. At the top of the bed in the 1:10 $NO_2$:$NO_x$ ratio experiment, only half

of the Cu(I) was present compared to the steady state amount of Cu(I) on the catalyst under standard SCR. Furthermore, as the amount of $NO_2$ in the $NO_x$ feed was increased, the amount of Cu(I) measured at the top of the catalyst bed decreased until the measurement with $NO_2$:$NO_x$ of 4:10 showed that effectively no Cu(I) was identifiable at the top of the catalyst bed under these conditions.

In addition to comparing the catalysts across different gas concentrations, we also compared the top and bottom of the catalyst bed in XAS at each gas condition. Since the fast SCR reaction is the kinetically dominant mechanism for SCR when $NO_2$ is involved, the higher rate of reaction led to high consumption of $NO_2$. Thus, over the length of the catalyst bed as much as 80% of the $NO_2$ was consumed by the time the reactants exited the catalyst. As can be seen in Figures 3.9, 3.10, and 311, the non-differential conversion of $NO_2$ greatly affected the Cu oxidation state at the top and bottom of the catalyst bed.

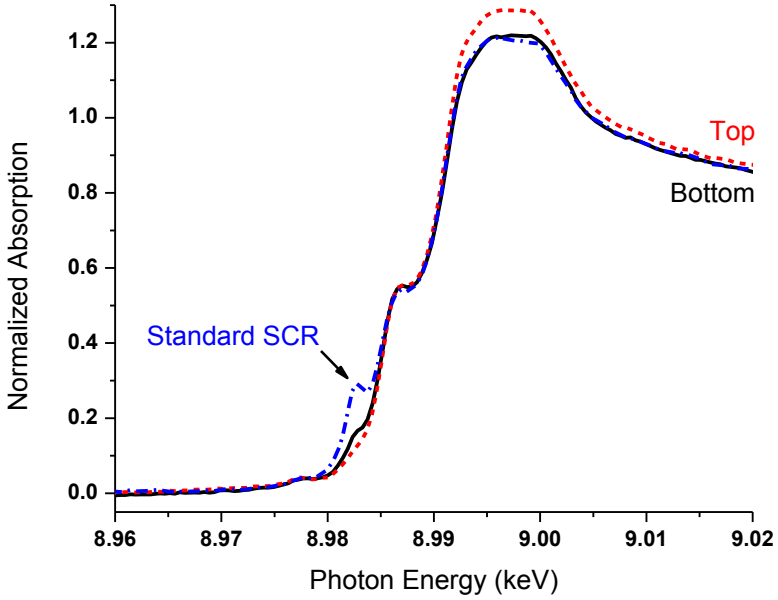


Figure 3.9 XAS of the 2.1 wt.% Cu-SSZ-13 catalyst under SCR conditions with an $NO_2$:NOx ratio of 4:10 at the top (red dashed line) and bottom (black solid line) of the catalyst bed. For reference, the same catalyst under the standard SCR condition is also included (blue dash-dotted line).

Even with a 4:10 ratio, the most oxidizing conditions tested and with 23% conversion of $NO_2$, there was a visible change in Cu oxidation state over the length of the bed (Figure 3.9). Comparing Figure 3.9 with Figure 3.10 it becomes clear that the 2.5:10 ratio led to a small increase in Cu(I) population at the top of the bed and a significantly increased Cu(I) population at the bottom of the bed.

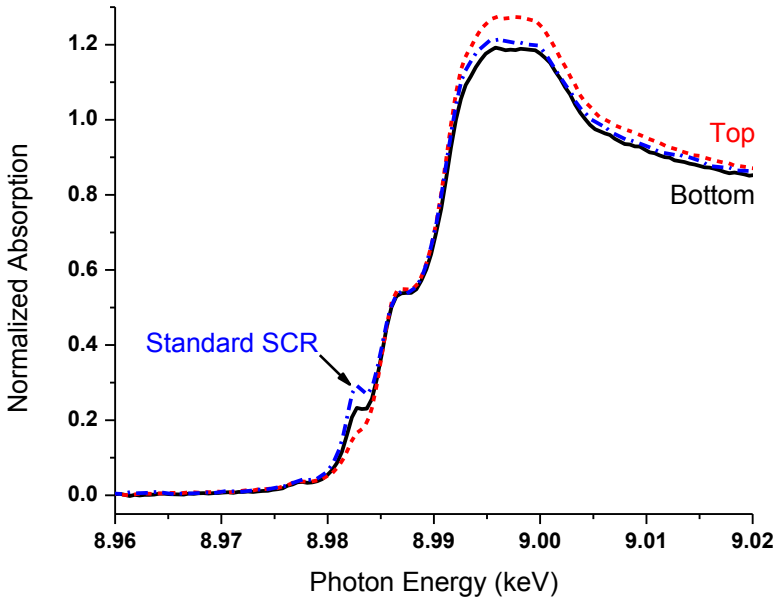


Figure 3.10 XAS of the 2.1 wt.% Cu-SSZ-13 catalyst under SCR conditions with an $NO_2$:NOx ratio of 2:10 at the top (red dashed line) and bottom (black solid line) of the catalyst bed. For reference, the same catalyst under the standard SCR condition is also included (blue dash-dotted line).

In Figure 3.11, for the 1:10 $NO_2$: $NO_x$ ratio, the Cu(I) population at the top and bottom of the bed had increased even further, a testament to how sensitive the catalyst can be to the steady state concentrations in the gas mixture. With about 80% $NO_2$ conversion, only 5 ppm $NO_2$ exited the reactor, a concentration no longer significant enough to distinguish the Cu(I) population under these gas conditions from standard SCR conditions.

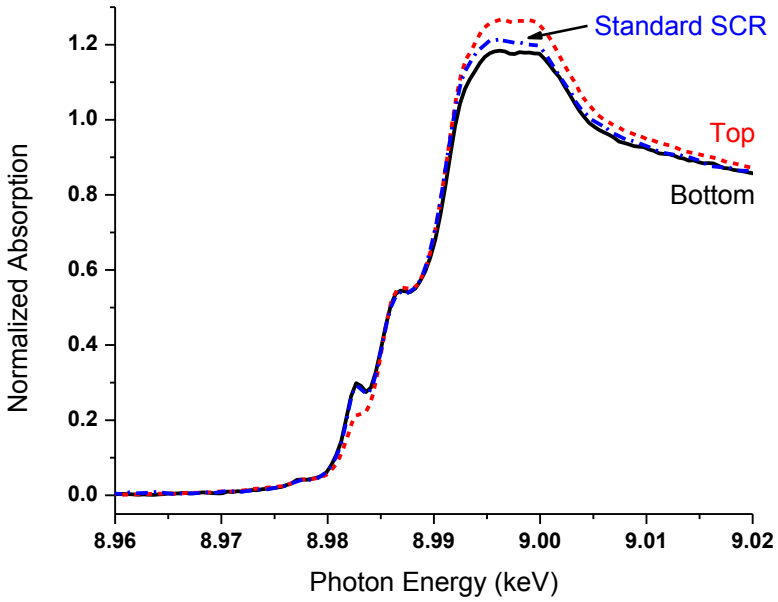


Figure 3.11 XAS of the 2.1 wt.% Cu-SSZ-13 catalyst under SCR conditions with an $NO_2$:NOx ratio of 1:10 at the top (red dashed line) and bottom (black solid line) of the catalyst bed. For reference, the same catalyst under the standard SCR condition is also included (blue dash-dotted line).

## 3.5 Discussion

### 3.5.1 Cutoff/Addition Experiments

The cutoff experiments highlight the redox nature of the Cu catalyst. Removing oxygen does not end the consumption of the reductants. In fact, as can be seen from Figures 3.1 and B.6 that NO and $NH_3$ consumption continue for many minutes after $O_2$ has presumably been flushed from the system, which corresponded to 2.0 x $10^{-6}$ moles of NO reacted. $NH_3$ was not quantified as the mass flow controller was faulty and caused inconsistent flow. As NO and $NH_3$ were consumed, the Cu(I) edge feature in XANES also grew substantially, eventually reaching steady state at approximately the same time

as the reductant concentrations. In a flow of $NH_3$ alone (Figure B.3) the catalyst reduced no more than 5% of total Cu from Cu(II) to Cu(I) over 15 minutes of exposure time before reaching a steady state. Addition of $O_2$ back into the gas feed removed about half of the Cu(I) not present under steady state standard SCR conditions within the first 32 s and slowly approached the steady state SCR Cu(I) concentration thereafter (Figure B.8). The reversibility of the change in oxidation states of Cu and the fast rate of re-oxidation, compared to reduction, of the catalyst and return to steady state rates are all indicators that this catalyst is not only well suited to perform redox operations but that redox is a fundamental part of the reaction mechanism for the SCR reaction.

The oxidizing half reaction of the standard SCR reaction is highlighted by the NO and $NH_3$ cutoff experiments. Upon removal of NO from standard SCR, the steady state amount of Cu(I) was oxidized to Cu(II). The $NH_3$ returned to its bypass concentration around 1 to 1.5 minutes after the switch indicating that $NH_3$ is unreactive with $O_2$ at these temperatures. As mentioned in the results, the rate of Cu(I) oxidation with $O_2$ + $NH_3$ is slow compared to standard SCR or addition of $NO_2$ to standard SCR, i.e., fast SCR. In other words, higher Cu(I) oxidation rates are observed whenever the reaction gases contain $NO_x$, $NH_3$ and $O_2$, but not when $NH_3$ and $O_2$ (or NO + $O_2$, e.g., $NH_3$ cutoff conditions) are the reactants. The increased Cu(I) oxidation rate of standard SCR suggests that NO oxidation may occur yielding $NO_2$, which is responsible for the higher Cu(I) oxidation rate. However, wet NO oxidation on Cu-CHA and Cu-ZSM-5 has negligible turnover rates at temperatures below 523 K [108, 109]. It is possible, that under SCR conditions NO oxidation is kinetically possible, but $NO_2$ strongly adsorbs at

the Cu site inhibiting the rate and requiring higher reaction temperatures to desorb $NO_2$. In the presence of $NH_3$, it is possible that the adsorbed $NO_2$ reacts, decreasing the $NO_2$ surface coverage and increasing the apparent NO oxidation rate as $NO_2$ desorption is no longer the rate limiting step for NO oxidation. A similar mechanism has been suggested for Fe-ZSM-5 catalysts[26]. If $NO_2$ is formed under standard SCR conditions, it would lead to higher Cu(I) oxidation rates. Little $NO_2$ might be observed in the product gas, since the rates of $NO_2$ reduction (to $N_2$) are high. Reintroduction of NO (to $O_2$, $NH_3$ and a Cu(II) catalyst) to return to standard SCR conditions also required a long time, approximately 8 minutes, to reach the steady state mixed Cu oxidation state. By comparison, $O_2$ addition (to NO, $NH_3$ and a Cu(II) catalyst) to return to standard SCR steady state conditions is rapid (~2 min). The difference in the rate to come to steady state under the same gas composition could represent the rates of Cu(I) oxidation versus Cu(II) reduction with the latter slower than the former.

A slower Cu(I) oxidation is observed during the $NH_3$ cutoff when only NO and $O_2$ (e.g., NO oxidation reactants) are present from the standard SCR mixture as 95% of the change in Cu(I) occurred by 2327 s. The NO was observed to have a very slow response at 23:15 min (1395 s) for 95% of its change to a bypass concentration while the $NH_3$ was removed from the gas phase during the first 143 s. The difference in these two curves indicated that a well of $NH_3$ was reacting from somewhere on the catalyst surface. Some possibilities exist which could explain this behavior. The $NH_3$ could react from a well of Brønsted sites with the $NO_x$ species either associated with the Cu or in the gas phase. A slightly more complicated scenario is where $NH_3$ reacts from Cu and a well of $NH_3$ on

Brønsted acid sites can supply the $NH_3$ on the Cu when none exist in the gas phase (as in $NH_3$ cutoff experiments). This "spillover" effect was incorporated into a mechanistic study by Metkar et al.[36]. It also falls in line with the proposed mechanism by Gao et al. [39] which has $NH_3$ reacting from the active Cu site. More complicated still, both mechanisms may exist under standard SCR conditions. Whether one or multiple pools of $NH_3$ were present which contributed to the standard SCR reaction, the transient NO rate was expected to track with the change in isolated Cu ratio. Instead, Figure 3.6 shows the ratio of isolated Cu(I) to total Cu(II) appeared to track better. Since the total Cu(II) was incorporated into the Cu ratio, it suggests that hydrated Cu(II) was created directly from an isolated Cu(II). The isolated Cu(II) was formed in the re-oxidation of isolated Cu(I) after $NH_3$ was removed or reacted away. The lag in Cu(I) re-oxidation with the transient rate in Figure 3.6 may suggest that some of the $NH_3$ did not react off the Cu, but very slowly desorbed.

The final set of cutoff experiments investigated the nature of the oxidation state of Cu under the different SCR gas conditions. Under the steady state fast SCR condition (with $NO_2$), Cu was fully oxidized, with no Cu(I) detectable (Figure 3.7) a result we have reported before [5, 103]. By removing $NO_2$, the presumed oxidizing agent on account of its strength as an oxidant, we were able to partially reduce Cu from fully oxidized Cu(II) (fast SCR) to a mixed Cu(II) and Cu(I) oxidation state (standard SCR). The catalyst reached the standard SCR oxidation state within 2.5 minutes, between 3 to 6 times faster when compared with Cu reduction times in the $O_2$ cutoff and NO addition experiments. The fast response of the Cu can be attributed to the oxidative strength of $NO_2$. At steady

state with the stronger oxidant, the fraction of Cu(I) is zero. The $NO_2$ is more efficient at performing the oxidation than $O_2$, and so not only did it increase the catalytic rate, but it also ensured that the average Cu oxidation state measured by XAS was always Cu(II). Removing this $NO_2$, reestablished the distribution of Cu(I) and Cu(II) present under standard SCR conditions. In this case, the initial state of the catalyst was generated under fast SCR conditions, which is comparable to the state of the catalyst under standard SCR. Thus, the catalyst was able to reach steady state more quickly, despite the presence of $NH_3$ during the standard SCR condition, than during the NO cutoff/addition experiments where the initial state was substantially different.

The $NO_2$ addition data for the 2.1 wt% sample exhibit a rapid return to the fast SCR condition and a fully Cu(II) oxidized catalyst after 5 minutes on stream. Here the oxidation process measured by XAS (Figure B.17) matches very well with the approach to steady state in the gas concentrations except for $NO_2$ where both are on the order of 1-5 minutes. The $NO_2$ gas concentration took far longer to reach steady state, however. Since only a small amount of $NO_2$ is required to fully oxidize the catalyst, the slow return to the equilibrium conditions suggests $NO_2$ is reacting at sites different from Cu, perhaps $NH_3$ adsorbed on the Brønsted acid sites of the SSZ-13 zeolite.

### 3.5.2 $NO_2$:$NO_x$ Ratio Experiments

The $NO_2$:$NO_x$ ratio experiments provide an interesting picture of the redox character of the Cu active site on this Cu-SSZ-13 catalyst. Even with as little as 30 ppm $NO_2$ (10% of total $NO_x$,Figure 3.11), the oxidation state of the catalyst, at least near the top of the bed,

was greatly affected compared to the standard SCR condition. Additional $NO_2$ only acted to further remove Cu(I) from the catalyst (Figures 3.9 and 3.10). In all cases, however, more Cu(I) was measured at the bottom of the catalyst bed as the fast SCR reaction consumed $NO_2$ altering the gas conditions enough to change the Cu oxidation state before the reaction gases exited the bed. Nevertheless, some $NO_2$ always exited the reactor, indicating less than 100% conversion. These experiments highlight how sensitive the catalyst is to the gas environment. Moreover, the experiments also show just how weak $O_2$ is as an oxidant, since only 30 ppm of $NO_2$ can reduce the amount of Cu(I) on the catalyst by half, something that 5% $O_2$ was incapable of doing during standard SCR. This is also a testament to how strong an effect $NO_2$ has on the state of the catalyst, underscoring the fast changes in oxidation state measured in the $NO_2$ cutoff/addition experiments.

The difference in Cu oxidation state emphasizes the necessity of operating the catalyst under differential conditions when performing these kinds of *operando* experiments. Much like our discussion about the differences between *in situ* and *operando* experiments in our previous publication [5], we show here how the location chosen to place the X-ray beam within the catalyst bed could produce very different results under non-differential conditions. It is therefore imperative that the gas conditions remain relatively unchanged over the length of the catalyst bed, i.e. differential, lest the researcher collect improper results. In much the same way, if one were to operate these catalysts under standard SCR with 100% conversion, as would be typical in their intended application, a large fraction of the bed could be inactive since the reactants are consumed at some unknown point

within the bed before exiting the catalyst. The inactive portions are hence exposed to a modified mixture of gases dominated by $O_2$ and no reductants and thus the catalyst will appear either fully oxidized, i.e. all Cu(II), or in a mixed oxidation state depending on whether the spectroscopic technique is sampling the inactive or active portion of the catalyst bed. Differential operation is necessary to capture the catalyst in its working state, particularly when *operando* experiments are involved.

### 3.5.3 Implications for the $NH_3$ SCR Mechanism for Cu-SSZ-13

The facile reduction and oxidation of Cu during the SCR half-reactions indicates that the redox step should be present. Clearly, $NH_3$ alone is a poor reductant of Cu(II), while the combination of NO + $NH_3$ is highly capable of reducing Cu(II) to Cu(I). In standard SCR, $O_2$ is the added oxidant; however, the rate of oxidation of Cu(I) with $NH_3$ and $O_2$ is lower than that of standard SCR and much lower than that of fast SCR (with $NO_2$). This may suggest that during SCR, NO oxidation may give small amounts of $NO_2$, increasing the rate of the oxidation half reaction.

When any of the reactants are removed from standard SCR conditions, a ratio of Cu species shows a correlation with the transient rate. The ratio of isolated Cu(II) to Cu(I) tracked with the transient standard SCR rate when $O_2$ was removed. The ratio of isolated Cu(I) to Cu(II) tracked with the rate when NO was removed. Additionally, the ratio of isolated Cu(I) to total Cu(II) tracked with rate when $NH_3$ was removed, with a time lag, but the same curve shape. These are secondary evidences that a redox cycle must exist in the isolated Cu species in SSZ-13. The Cu quasi-equilibrates very fast at each step

during the transient experiments and gives a dependence on the ratio of Cu species. The shift from isolated Cu(I) to isolated Cu(II) to hydrated Cu(II) in the $NH_3$ cutoff suggests $NH_3$ is present on the Cu under reaction conditions. When $NH_3$ is not present in the gas phase, it could react away or very slowly desorb, at which point the Cu becomes oxidized and hydrated.

While Cu(I)/Cu(II) undergo redox reactions, $NO_2$ also appears to react at sites different from Cu, perhaps with $NH_3$ chemisorbed on the acid sites of the zeolite. Devadas *et al*[26]. showed that despite the capability of the zeolite to perform SCR, addition of a metal species, such as Fe, increased the fast SCR rates from which they suggested that the metal was not only responsible for NO oxidation activity but was also catalyzing the SCR reaction [16]. Previous experiments in the literature [110] on supported Pt catalysts and Na-Ba-Y zeolites showed that one N atom from the product $N_2$ came from $NH_3$ and the other came from $NO_x$.

When NOx, $O_2$ and $NH_3$ are present in the gas mixture, the rate of the oxidation half reaction is significantly faster than that of the reduction half reaction. Under steady state conditions, of course, the rate of both reactions is the same. However, since the overall rate is determined by the slowest step, in order to increase the steady state rate, one needs to increase the rate of the reduction half reaction. For example, the use of stronger reducing agents or metals that undergo reduction at lower temperature are expected to give SCR conversions at lower temperature.

## 3.6 Conclusions

In our previous publication we proposed that the SCR reaction progressed via a redox cycle of Cu(I) and Cu(II) on Cu-Zeolite catalysts. By exposing the catalyst to the oxidation or reduction half reactions, we have suggested that both Cu(I) and Cu(II) are involved with the SCR catalytic cycle. Cutting off $O_2$ from standard SCR gas conditions (NO + $NH_3$) led to the growth of a large increase in pre-edge feature in *operando* XAS identified as Cu(I). The corresponding gas conditions showed consumption of NO and $NH_3$ occurred over a similar time frame as the conversion of Cu(II) to Cu(I), giving a final amount of 76% Cu(I). Reintroduction of $O_2$ (with NO plus $NH_3$) rapidly re-oxidized Cu(I) to Cu(II) giving a mixture of Cu oxidation states typical of steady state SCR. $NH_3$ alone was a much less effective reducing agent than NO + $NH_3$. Cutoff of NO, resulted in fully oxidized Cu(II) although this occurred at a slow rate suggesting that $O_2$ is a poor oxidant. This also suggests that the higher oxidation rate under SCR may be due to the formation of $NO_2$ by NO oxidation, which is speculated to occur at lower temperature due to the presence of $NH_3$. Addition of NO (to $NH_3$ and $O_2$) and Cu(II), returned the catalyst to the mixed Cu oxidation state of steady state standard SCR but required long reaction times consistent with the rate of the reduction half reaction being much slower than the rate of the oxidation half reaction. The removal of $NH_3$ allowed the catalyst to become primarily Cu(II), however, over time Cu became hydrated with $H_2O$ indicating the $NH_3$ was reacting off of the Cu and/or slowly desorbing from the Cu. Addition of $NO_2$ to standard SCR, i.e., fast SCR, lead to rapid oxidation of Cu(I) to Cu(II) indicating $NO_2$ is a much more effective oxidant than $O_2$. Although Cu oxidation was rapid upon $NO_2$ addition, the $NO_2$ concentration was slow to return to the steady state

values suggesting the $NO_2$ was also reacting at a site different from Cu, perhaps with adsorbed $NH_3$ on Brønsted sites.

## 3.7 Acknowledgements

Other authors on this manuscript include Vincent F. Kispersky, Aleksey Yezerets, William F. Schneider, Jeffrey T. Miller, W. Nicholas Delgass, and Fabio H. Ribeiro. We would also like to thank Atish Parekh, Anuj Verma, and Paul Dietrich for their help in executing the XAS experiments at the APS. Use of the Advanced Photon Source is supported by the U. S. Department of Energy, Office of Science, and Office of Basic Energy Sciences, under Contract DE-AC02-06CH11357. MRCAT operations are supported by the Department of Energy and the MRCAT member institutions. Support for JTM was provided under the auspices of the U.S. DOE, Office of Basic Energy Sciences, Division of Chemical Sciences, Geosciences, and Biosciences under contract number DE-AC0-06CH11357. We would also like to thank Sachem, Inc. for their gracious donation of the structure directing agent for SSZ-13 synthesis.

## 3.8 Copyright and Legal Matters



Chapter two expanded upon the initial manuscript written by Vincent F. Kispersky. I was a second author on the initial draft. After the additions to the manuscript, I became first author.

# CHAPTER 4. PRACTICAL BRONSTED SITE QUANTIFICATION TECHNIQUES UTILIZING NH3 AS A CHEMICAL TITRANT IN CU-ZEOLITES ACTIVE FOR THE SELECTIVE CATALYTIC REDUCTION OF NOX WITH NH3

## 4.1 Abstract

The total number of Brønsted acid sites in four H- and Cu-ZSM-5 and seven H- and Cu-SSZ-13 samples was determined. Three techniques using $NH_3$ as a titrant were proven to selectively titrate Brønsted acid sites when compared to site counts from n-propylamine decomposition over H-ZSM-5. In Cu-ZSM-5, the results also matched, suggesting the $NH_3$ procedures could also avoid titrating Cu sites. In H- and Cu-SSZ-13, the $NH_3$ titrations gave four times higher counts of Brønsted acid sites, suggesting the pore openings cause n-propylamine to be mass transfer limited or the close proximity of Brønsted sites to cause n-propylamine to block itself. We suggest that $NH_3$ is an ideal titrant to use for small-pore zeolites. Thus, these procedures may be attractive for deNOx applications where $NH_3$ is a reactant in the selective catalytic reduction reactions.

## 4.2 Introduction

Copper-exchanged small-pore zeolites with the chabazite (CHA) structure (SSZ-13 and SAPO-34) have recently been adopted for commercial use in de$NO_x$ applications utilizing the selective catalytic reduction (SCR) reactions with $NH_3$ because of their excellent hydrothermal stability[1-3, 31]. The addition of Cu into CHA has been

characterized extensively with kinetic studies [44, 83, 111], temperature programmed measurements [43, 44], *in situ* [6] and *operando* [4, 5, 40, 111] x-ray absorption spectroscopy, electron paramagnetic resonance [44], and ultraviolet-visible spectroscopy[42, 83, 111] Most studies agree the active site for standard SCR is an isolated Cu species exchanged into a Brønsted acid site(s) [6, 33, 40, 42-45, 48, 83, 111]. This active metal in SCR-active zeolites has typically been proposed to perform NO oxidation, which is rate limiting in some standard SCR mechanisms [23, 26-28, 35, 36].

While much of the focus has been on the active metal site, there is less understanding of the role of the Brønsted acid sites ($H^+$) in the reaction mechanism. Schwidder et al. [112] observed a 0.7 wt% Fe-silicalite with no Brønsted acid sites to obtain an $NH_3$ and NO conversion of ~20% through 850 K, suggesting the reaction can occur without them; however, a similar weight loading of Fe-ZSM-5 with Brønsted acid sites showed enhanced conversion to ~80% through 850 K. A study by Brandenberger et al. [55] observed a Fe-ZSM-5 sample with Brønsted acid sites poisoned by silanization to have NOx conversions with less than 10% difference in the 473-573 K temperature range, from which they suggested Brønsted acid sites only influence the binding and dispersion of the active metal sites. Several authors have proposed that $NH_3$ adsorbs on Brønsted acid sites to form $NH_4^+$, which is an active intermediate in a two-site mechanism that reacts with $NO_x$ species on the active metal site [22, 23, 28, 36, 53, 54, 113]. If the role of Brønsted acid sites is to stabilize reactive $NH_4^+$ intermediates and mediate their reaction with metal-bound $NO_X$ species in SCR cycles, this implies that SCR rates and selectivities on a given metal-exchanged zeolite depend on number of Brønsted acid sites

and on the metal:$H^+$ ratio. In turn, accurate methods to count or titrate Brønsted acid sites on metal-exchanged zeolites are required.

It would be advantageous to have a technique which can be selective to only Brønsted acid sites while being able to access the small pores of the CHA framework. Infrared (IR) spectroscopy can identify hydroxyl (-OH) sites by stretching frequencies. However, in ZSM-5, three –OH bands can be observed over the range of ~3500-3740 $cm^{-1}$, while only one is known to be Brønsted acidic [114]. $^{27}$Al NMR is able to accurately determine the fraction of framework Al, which are structural surrogates for Brønsted acid sites; however, a study by Gounder et al. [115] showed that not all framework Al are Brønsted acidic. This was evidenced by lower Brønsted acid site counts using chemical titrants in USY-zeolites. A similar study by Biaglow et al. [116] estimated framework Al in chemically-dealuminated FAU using XRD-derived lattice parameters and compared with an isopropylamine titrant to find smaller site counts with the amine. Pyridine is a chemical titrant which can be protonated to the pyridinium ion over Brønsted acid sites with characteristic features at 1485 and 1540 $cm^{-1}$ in the IR. [117]; however, its size may hinder it from successfully titrating all Brønsted acid sites if six-membered rings are present in the zeolite [115]. A series of reactive alkylamines with different chain lengths have also been used to titrate Brønsted acid sites in zeolites in a one-to one ratio [84]. The alkylamine is protonated by the Brønsted acid site to form an alkylammonium ion which then decomposes to ammonia and an alkene in a temperature programmed desoprtion (TPD) [84, 86, 118]. The products exit the zeolite in a very narrow temperature range in the gas, making the quantification straightforward, but the size of

the pore openings may become a limiting factor in determining accurate Brønsted acid site counts if the alkyamine chosen is too large[85]. In this study, we use n-propylamine, which produces $NH_3$ and propylene ($C_3H_6$) upon decomposition as one technique to quantify Brønsted acid sites

For small pore zeolites, a smaller chemical titrant would be ideal to ensure that all Brønsted acid sites are accessed. Ammonia is the smallest amine which could titrate a Brønsted acid site; however, it is not selective to just Brønsted acid sites, making the de-convolution and interpretation of a TPD spectra a difficult task [119]. Additionally, determination of an accurate acid site strength can be difficult as Farneth and Gorte [118] showed the desorption temperature of Brønsted acid sites varied by ~150 K between a TPD in vacuum and under flow conditions. They warned that factors such as flowrates, catalyst bed heights, and particle sizes used could contribute significantly because $NH_3$ is "sticky" and can re-adsorb on its way out [118]. Techniques in this study have been developed or expanded upon [63], which are able to use $NH_3$ to selectively titrate only Brønsted acid sites in both H- and Cu-ZSM-5 and SSZ-13 to determine the available number of Brønsted acid sites. No claims were made about the strength of the acid sites due to the complexities of using $NH_3$.

This study will establish that three different treatments with $NH_3$ in H-ZSM-5 allow for the quantification of available Brønsted acid sites without interference of $NH_3$ associated with physisorbed or Lewis-type $NH_3$ (associated with zeolite or exchanged metals). The results will be compared with n-propylamine titration [84, 86, 120, 121] to validate the

techniques. The techniques will then be applied to catalysts active for standard SCR, including Cu-ZSM-5 and small-pore Cu-SSZ-13. We will show that $NH_3$ is a more suitable titrant than n-propylamine in SSZ-13 because of the small pore openings and high Al content in these zeolites. The most appealing aspect of using the $NH_3$ in SCR catalysts is that it is a reactant in all the SCR reactions. Thus, titrating with $NH_3$ allows for quantification of all Brønsted acid sites accessible under reaction conditions.

## 4.3 Experimental Methods

### 4.3.1 Catalyst Synthesis and Characterization

Four $NH_4$-ZSM-5 zeolites were obtained with expected silicon to aluminum atomic ratios (Si:Al) of 15, 25, 40, and 75 (Zeolyst International, CBV 3024E, CBV 5524G, CBV 8014, and CBV 1504, respectively). The H-form of each sample was obtained by heating in dry air (commercial grade, Indiana Oxygen) up to 823 K at 0.5 K $min^{-1}$ and held for 8 hours. H-SSZ-13 samples were synthesized using a method described by Fickel et al. [33], which was derived from the original procedure by Zones et al. [56-58]. Cu was deposited into both the H-ZSM-5 and H-SSZ-13 by liquid phase ion exchange with a $Cu(NO_3)_2$ solution at a pH of 5 ± 0.2. In this study, ZSM will denote ZSM-5 and SSZ will denote SSZ-13 when specific samples are referenced. The first number following the ZSM or SSZ is the silicon to aluminum atomic ratio (Si:Al) and the second is copper to aluminum atomic ratio (Cu:Al). For example, a Cu-SSZ-13 sample with Si:Al = 4.5 and Cu:Al = 0.02 would be shown as Cu-SSZ-4.5-0.02. The Si, Al, and Cu atomic composition of each sample was determined with atomic absorption (AA) on a Perkin Elmer AAnalyst 3000 Atomic Absorption Spectrometer. Dinitrogen isotherms were

obtained from a Micromeritics ASAP 202 unit. Samples were degassed at 673 K for eight hours before obtaining $N_2$ adsorption/desorption isotherms. The t-plot micropore volumes were determined by extrapolating the linear increase in the mesoporous range until the line intersected the y-axis. BET surface areas were also extracted from the isotherms. The MFI structure of H-ZSM-5 and chabazite (CHA) structure of H-SSZ-13 was determined from x-ray diffraction (XRD) patterns obtained from a Bruker D8 Focus X-ray Diffractometer with a Cu K (alpha) source with a scan speed of 0.5° $min^{-1}$.

Aluminum magic angle spinning nuclear magnetic resonance ($^{27}$Al MAS NMR) spectra of H-form and $NH_4$-form ZSM-5 were collected using a Bruker Avance 500 MHz spectrometer in a wide-bore 11.7 Tesla magnet (Caltech Solid State NMR Facility). Zeolite samples were hydrated by holding for >48 h in a desiccator containing 1.0 M KCl prior to packing within a 4 mm $ZrO_2$ rotor. $^{27}$Al NMR spectra were acquired at ambient temperature from 512 scans with 0.5 μs pulses and a 6 s delay, and were measured at 130.35 MHz using a 4 mm cross polarization (CP) MAS probe, strong proton decoupling, and a magic angle spinning rate of 12 kHz. All $^{27}$Al NMR spectra are referenced to aqueous 1.0 M $Al(NO_3)_3$ solutions.

### 4.3.2 Temperature Programmed Desorption Unit

Initial $NH_3$ and n-propylamine (NPA) TPD experiments on H-ZSM-5 were performed on a bench top tubular glass reactor with a quartz frit located in the middle of the tube to hold a catalyst bed and surrounded by a tube furnace (Applied Test Systems, Inc. 3210 Series). The diameter of the center section of the reactor was narrowed to 3/8” so that the

catalyst bed height could be increased to help prevent bypass of any reaction mixture. The catalyst was sieved to particle sizes between 125 and 250 μm. Between 30-50 mg of sample were used for each experiment. Thermocouples were positioned at the very top of the catalyst bed and just below the frit to ensure that no large temperature gradient existed. A plug of small quartz beads of ca. 3 mm diameter was poured onto a screen situated six inches above the catalyst bed to help with proper gas mixing. Before entering the reactor, any gases except $NH_3$ or n-propylamine passed through a pre-heater assembly consisting of a helical coil of 3 in. diameter made out of 0.25 in. diameter stainless steel tubing inside a temperature controlled hollow cylindrical Watlow® ceramic fiber heater. The $NH_3$ or n-propylamine was added just above the plug of quartz beads into the reactor. The system is equipped with a residual gas analyzer (RGA200, Stanford Research Systems) and a gas phase FT-IR spectrometer (MKS Multigas™ 2030). The on-board calibrations provided by MKS were used to monitor $NH_3$, $C_3H_6$, and $H_2O$ concentrations with a 0.95 second resolution. The design of the furnace surrounding the reactor did not allow for a perfect linear temperature ramp, as this unit was meant for steady state reactions. The TPD experiments performed on this unit were with a 5 K $min^{-1}$ temperature ramp and a total flowrate of 350 ml $min^{-1}$. Other details on individual TPD experiments are described in the different procedures for treatments of samples.

TPD experiments on Cu-ZSM-5 and Cu-SSZ-13 were performed on a Micromeritics AutoChem II 2920 Chemisorption analyzer equipped with a thermal conductivity detector (TCD) and Agilent 5975C mass selective detector (MSD) to monitor the eluting species. Samples were treated in the plug flow reactor unit described in the previous

paragraph then removed to air and placed in a specially designed U-shaped quartz cell surrounded by quartz wool plugs for TPD in the Autochem II unit. All TPD experiments in the Autochem II unit had a total flowrate of 50 sccm UHP He with a linear temperature ramp from 298 K to 873 K at 10 K $min^{-1}$. The $NH_3$ and $C_3H_6$ quantities were determined from m/z 17 and m/z 41, respectively. The contributions from fragments of $H_2O$ in m/z = 17 and n-propylamine in m/z 41 were subtracted, which then gave signals corresponding only to $NH_3$ and $C_3H_6$. Argon was used as an internal standard to account for the drift in the MSD signal over time. After each experiment, a fixed amount of Ar was injected through the sample tube using a fixed injection loop volume (0.5 $cm^3$).

### 4.3.3 Brønsted Acid Site Counting Procedure #1

Approximately 70 mg of H-ZSM-5 with a given Si:Al ratio was treated in 500 ppm $NH_3$ (3% $NH_3$ in Ar, Praxair) at 323 K with a total flow rate of 350 ml $min^{-1}$ with balance UHP He (99.999%, Indiana Oxygen) for 2 hours at which point a stable baseline was obtained in the $NH_3$ signal indicating the sample was saturated. The sample was then flushed in UHP He (99.999%, Indiana Oxygen) for two hours, removed from the quartz reactor, and placed in 250 ml DI water. The solids were stirred for 1 hour at ambient temperature and isolated via centrifugation. A second wash and separation was then performed using the identical procedure to the first washing step. Following this, the sample was dried overnight at 423 K in stagnant air and loaded into the bench top reactor unit. A TPD was performed on the sample with 350 ml $min^{-1}$ total flow of UHP He starting at 323 K and ramped to 823 K at 5 K $min^{-1}$. The amount of $NH_3$ desorbed was quantified with the MKS Multigas™ 2030 gas phase FT-IR spectrometer.

### 4.3.4 Brønsted Acid Site Counting Procedure #2

A 500 ml solution of 0.1 M $NH_4NO_3$ was added to 0.5 g of an H-ZSM-5 sample with a Si:Al ratio ranging from 17-89. The solution was covered and stirred at 353 K for 10 hours. The sample was removed from the solution via centrifugation and washed two times with 250 ml DI water with the same washing procedure as in procedure #1. Following this, the sample was dried overnight at 423 K in stagnant air and loaded into the bench top reactor unit. A TPD was performed with the same settings as procedure #1.

### 4.3.5 Brønsted Acid Site Counting Procedure #3

A given H-ZSM-5, Cu-ZSM-5, H-SSZ-13, or Cu-SSZ-13 sample was loaded into the bench top reactor unit and treated with 500 ppm $NH_3$ at 533 K with a total flowrate of 350 mL $min^{-1}$ for 2 hours until saturation. The sample was then flushed for eight hours at the same temperature and flowrate in UHP He. Following this, TPDs on the H-ZSM-5 samples were performed in the bench top reactor unit with the same settings used in procedures #1-2. All other samples were removed and loaded into the Micromeritics Autochem II 2920 Chemisorption analyzer.

### 4.3.6 Brønsted Acid Site Counting Procedure #4: N-propylamine Titration

An n-propylamine gas mixture (1000 ppm n-propylamine / 1% Ar / He, Airgas) was flown at 150 ml $min^{-1}$ over each sample at 323 K for 2 hours to saturate the sample. The n-propylamine was tracked using the RGA200 mass spectrometer at m/z 30 and 59 to ensure the sample was saturated. The system was then flushed for 2 hours in UHP He at 350 ml $min^{-1}$. Following this, TPDs on the H-ZSM-5 samples were performed in the

bench top reactor unit. The $NH_3$ and propylene ($C_3H_6$) produced in the decomposition of n-propylamine were monitored using the MKS Multigas™ 2030 gas phase FT-IR spectrometer. All other samples were removed and loaded into the Micromeritics Autochem II 2920 Chemisorption analyzer for TPDs. To ensure the sample was saturated at 2 hours, a 4 hour saturation was also performed and equivalent results were found (See Figure C.1 and Table C.1).

## 4.4 Results

### 4.4.1 Catalyst Characterization

Elemental composition and BET surface area and t-plot micropore volume results for the catalysts are shown in Table C.2. The experimentally obtained Si:Al values were used in the calculations for the total amount of Al in the samples. X-ray diffraction measurements were also performed on the H-form of the zeolites. Figure C.2 shows that all H-ZSM-5 and H-SSZ-13 samples exhibit an x-ray diffraction pattern consistent with the MFI and CHA framework structures, respectively. A significant background was observed up to $2\theta = 20^{o}$, which was attributed to a contribution from the sample holder. No significant differences were observed between the H-ZSM-5 samples with different Si:Al, with each exhibiting the appropriate crystal planes. The measured t-plot micropore volumes for the H-ZSM-5 samples extracted from $N_2$ isotherms were observed to be consistent with a well formed MFI structure with pore volumes ranging between 0.13-0.17 $cm^3\ g^{-1}$ for H-ZSM-17, H-ZSM-30, and H-ZSM-43 samples. The H-ZSM-89 sample exhibited a significantly smaller micropore volume of 0.06 $cm^3\ g^{-1}$. The Cu-ZSM-17 samples had similar micropore volumes between 0.14-0.15 $cm^3\ g^{-1}$ compared to

0.15 $cm^3$ $g^{-1}$ for the H-ZSM-17 sample. The H-SSZ-4.5 sample had a micropore volume of 0.26 $cm^3$ $g^{-1}$ with all Cu-SSZ-13 samples ranging in between 0.2-0.24 $cm^3$ $g^{-1}$.

$^{27}Al$ NMR was also used on the $NH_4$- and H-forms of the ZSM-5 samples to give an estimate of the extent of Al in the framework of the ZSM-5 structure. Figure C.3 shows $^{27}Al$ NMR spectra of all the samples in the H-form and $NH_4$-form. NMR lines centered at 52 ppm were present for tetrahedral Al along with a small shoulder for penta-coordinated Al, which increased in relative intensity as the total Al content increased [115, 122, 123]. When referring to framework aluminum (Al_fr), the sum of the tetrahedral and penta-coordinated Al is the quantity being referenced. NMR lines centered at 0 ppm for octahedral Al, also referred to as extra-framework Al (Al_ex), were also present in the NMR spectra of the H-ZSM-43 and H-ZSM-89 samples, which showed that 6% and 7% contribution, respectively. All other $^{27}Al$ NMR spectra of samples in H- and $NH_4$-form showed less than 2% Al_ex. A small increase in octahedral Al was observed in the H-form over the $NH_4$-form, which has been previously observed and attributed to either framework aluminum (Al_fr) irreversibly removed from the lattice to become extra-framework aluminum (Al_ex) or the presence of Al species which could alternate between tetrahedral and octahedral coordination depending on the conditions applied to the sample [115, 124, 125] Tables C.3 and C.4 give the complete results for amount of Al_fr and Al_ex as well as de-convolution of the tetrahedral and penta-coordinated Al features.

### 4.4.2 Counting Brønsted Acid Sites on H-ZSM-5 and H-SSZ-13

Figure 4.1a gives the result for the first three Brønsted acid site counting techniques on H-ZSM-17 utilizing $NH_3$ as a titrant. The quantities of Brønsted acid sites normalized by total Al are shown in Table 4.1. Procedure #1, which utilized a gas phase saturation of $NH_3$ followed by physical washing with $H_2O$, gave 0.76 $H^+$:Al. Procedure #2 was a liquid phase exchange with $NH_4NO_3$ solution followed by washing steps with $H_2O$, in which a similar result of 0.77 $H^+$:Al was obtained. Procedure #3 involved a gas phase saturation of $NH_3$ at an intermediate temperature of 433 K, which gave 0.75 $H^+$:Al. Only one symmetric feature was present in all the TPD experiments, indicating that the weakly bound species had successfully been removed with the three different $NH_3$ procedures[63]. The only remaining feature corresponded to the $NH_3$ associated with Brønsted acid sites in the zeolite, and was consistent across all three procedures.

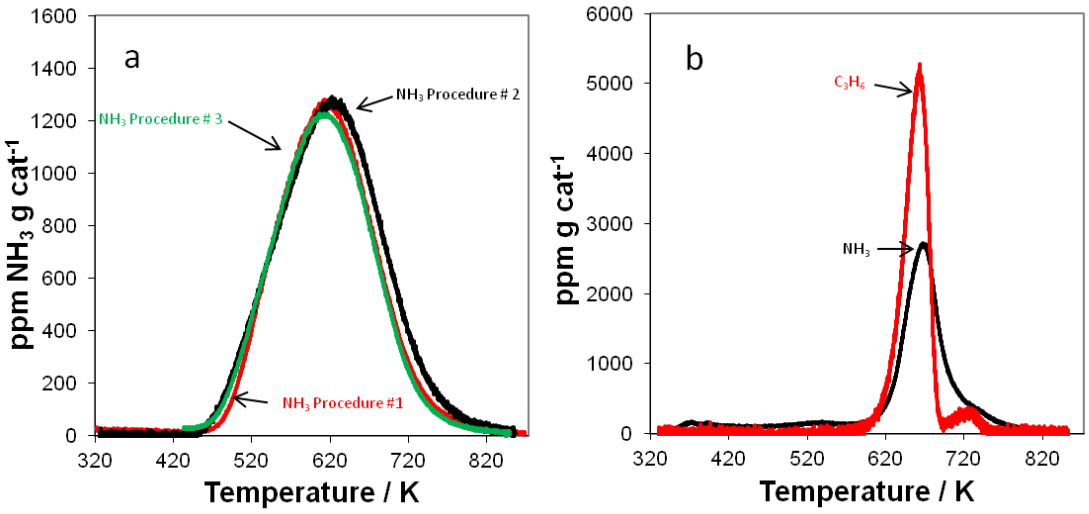


Figure 4.1a-b TPD spectra for the H-ZSM-17 sample for a) $NH_3$ titration procedures #1-3 and b) n-propylamine decomposition procedure #4.

To confirm the measurement of Brønsted acid sites by $NH_3$, an n-propylamine decomposition similar to the methods described by Gorte et al. [84-86] was performed. Figure 4.1b shows the result of the n-propylamine decomposition. The decomposition products, $NH_3$ and $C_3H_6$, were quantified and determined to not only match each other, but also the results of the other three $NH_3$ procedures. Quantifying the $NH_3$ and $C_3H_6$ signals gave 0.80 and 0.77 $H^+$:Al, respectively. The number of Brønsted acid sites in the other three H-ZSM-5 samples with different Si:Al ratios was also determined with all four procedures (Figures C.4-C.9). In each sample, an agreement was observed between all procedures. The H-ZSM-30 and H-ZSM-43 each exhibited Brønsted acid sites close to 1 $H^+$:Al, while the H-ZSM-89 gave values around 0.70 $H^+$:Al. Table 4.1 contains a complete summary of the quantification results on all H-ZSM-5 samples.

Table 4.1 Summary of Brønsted acid site counting for all samples in each chemical titration procedure. Each $NH_3$ or $C_3H_6$ quantified was assumed equivalent to one Brønsted site (H+). Each quantity was normalized by the total amount of Al contained within a sample.

| | $NH_3$ Proc. # 1 | $NH_3$ Proc. # 2 | $NH_3$ Proc. # 3 | N-propylamine Proc. #4 | |
|---|---|---|---|---|---|
| Sample | $H^+$:Al | $H^+$:Al | $H^+$:Al | $H^+$:Al from $NH_3$ | $H^+$:Al from $C_3H_6$ |
| H-ZSM-17 | 0.76* | 0.77* | 0.75* | 0.8* | 0.77* |
| H-ZSM-30 | 0.9* | 0.96* | 1.02* | 0.98* | 0.99* |
| H-ZSM-43 | 0.93* | 0.98* | 0.94* | 1.06* | 0.95* |
| H-ZSM-89 | 0.68* | 0.74* | 0.68* | 0.71* | 0.67* |
| H-SSZ-4.5 | - | - | 0.65 | 0.16 | 0.18 |
| Cu-ZSM-17-0.15 | - | - | 0.35 | 0.4 | 0.46 |
| Cu-ZSM-17-0.20 | - | - | 0.34 | 0.33 | 0.3 |
| Cu-ZSM-17-0.27 | - | - | 0.38 | 0.35 | 0.32 |
| Cu-SSZ-4.3-0.02 | - | - | 0.45 | 0.06 | 0.06 |
| Cu-SSZ-4.3-0.04 | - | - | 0.6 | 0.08 | 0.08 |
| Cu-SSZ-4.5-0.09 | - | - | 0.43 | 0.04 | 0.03 |
| Cu-SSZ-4.5-0.16 | - | - | 0.32 | 0.05 | 0.03 |
| Cu-SSZ-4.5-0.20 | - | - | 0.31 | 0.02 | 0.02 |
| Cu-SSZ-4.5-0.35 | - | - | 0.24 | 0 | 0 |

* Indicates this experiment was performed on the bench-top reactor unit instead of the Autochem II unit. 90% confidence intervals for $NH_3$ procedures in bench top reactor and Autochem II unit are ±0.08 $H^+$:Al, for n-propylamine in bench-top reactor, 0.07$H^+$:Al, and for n-propylamine in Autochem II, ±0.02 $H^+$:Al.

The H-ZSM-5 samples established that all three $NH_3$ titration techniques were equivalent to the n-propylamine decomposition; therefore, only $NH_3$ titration procedure #3 and the n-propylamine decomposition (procedure #4) were used on the remainder of the samples. The H-SSZ-4.5 sample was the first to be tested in this way. The $NH_3$ titration (procedure #3) resulted in one feature at ~725 K with 0.65 $H^+$:Al, while the n-propylamine decomposition gave 0.16 $H^+$:Al from $NH_3$ in a feature centered at ~725 K and 0.18 $H^+$:Al from $C_3H_6$ in a feature centered at ~675 K. Figure 4.2 and Figure 4.3a-b show the spectra for the $NH_3$ titration and n-propylamine decomposition, respectively.

This result was the first to not agree between procedures and will be explored in the discussion section.

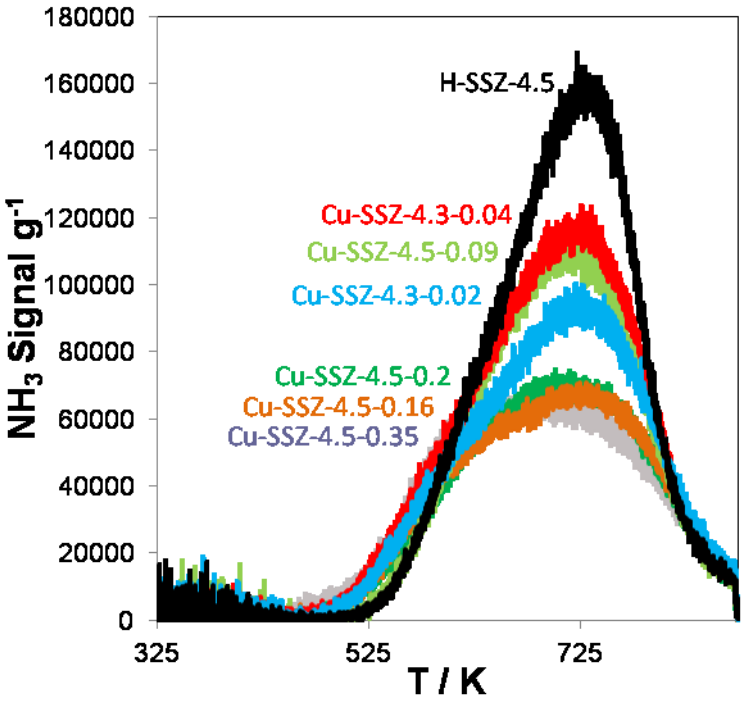


Figure 4.2 $NH_3$ –TPDs performed on H- and Cu–SSZ-13 samples with Si:Al = 4.5. This figure includes results from Procedure #3 where NH3 was used to saturate the samples in the gas phase at 433 K and flushed following the adsorption.

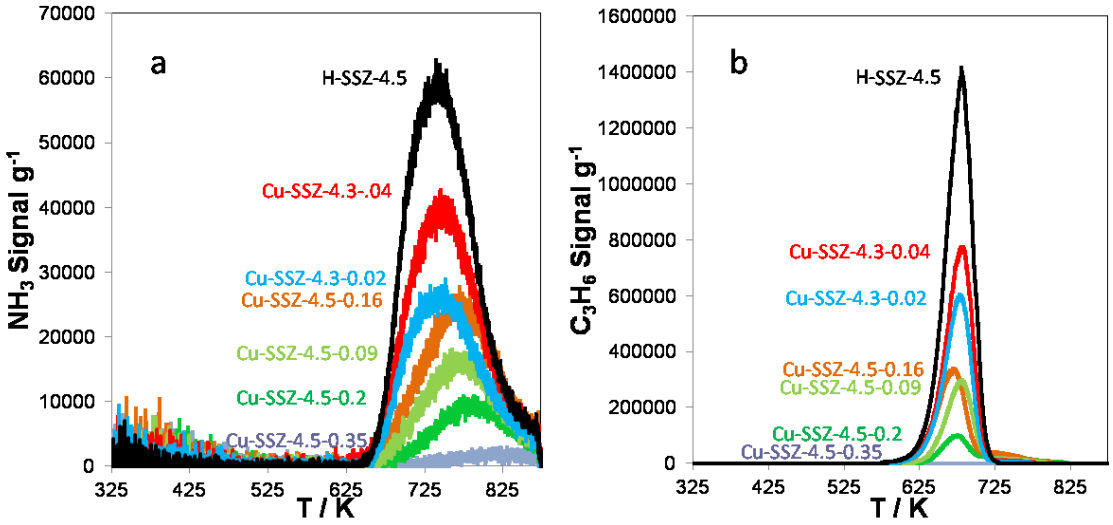


Figure 4.3 N-propylamine decomposition reactions on H- and Cu –SSZ-13 samples with Si:Al = 4.5. This figure shows the decomposition products, a) $NH_3$ and b) $C_3H_6$.

### 4.4.3 Counting Brønsted Acid Sites on Catalysts Active for Standard SCR

The number of Brønsted acid sites in several Cu-ZSM-5 samples which were active for standard SCR was determined with $NH_3$ titration (procedure #3) and n-propylamine decomposition (procedure #4). Figure C.10 reports the standard SCR rate per gram for the ZSM-17 samples. The Cu-ZSM-17-0.15 sample had a rate per gram of 0.6 x $10^{-7}$ mol NO g cat $^{-1}$ $s^{-1}$ which increased up to 4.0 x $10^{-7}$ mol NO g $cat^{-1}$ $s^{-1}$ for the Cu-ZSM-17-0.27 sample. The H-ZSM-17 did not show any rate per gram. Figure 4.4 shows the result of the $NH_3$ TPD (procedure #3) with the quantification in Table 4.1. The primary feature eluted between 500-800 K in each sample. A small shoulder was also present in the Cu-ZSM-17-0.2 and Cu-ZSM-17-0.27 near 800 K. The number of Brønsted acid sites were between 0.35-0.38 $H^+$:Al in all the Cu samples. The quantification included

the entire area under the curve including the shoulder. The reasons for this will be provided in the discussion section.

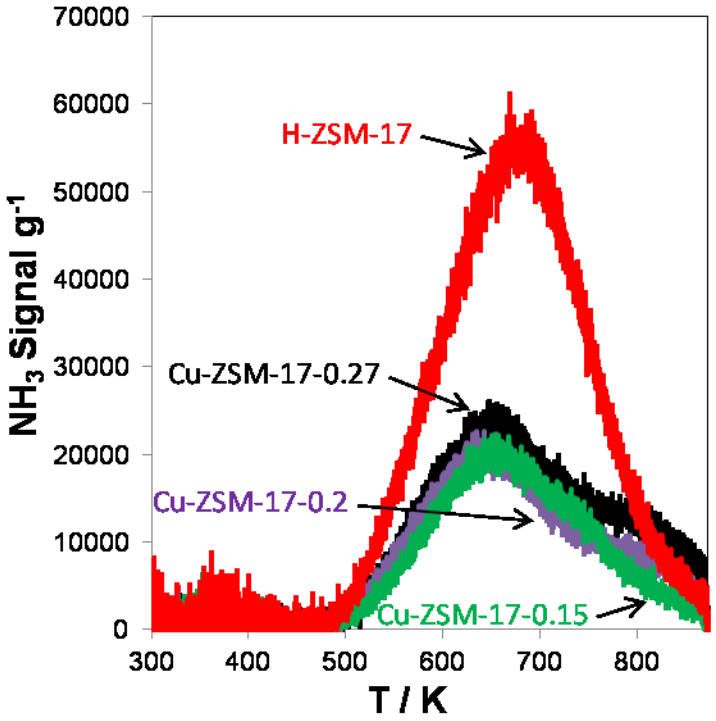


Figure 4.4 $NH_3$ –TPDs performed on Cu –ZSM-5 samples with Si:Al = 17. This figure includes results from Procedure #3 where $NH_3$ was used to saturate the samples in the gas phase at 433 K and flushed following the adsorption.

Figures 4.5a-b shows the $NH_3$ and $C_3H_6$ signals, respectively, for the n-propylamine decomposition experiments on the Cu-ZSM-5 samples. The $NH_3$ signal in Figure 4.5a shows the H-ZSM-17 (Cu:Al = 0) has one primary feature eluting at ~660 K identified as the Brønsted acid sites and a second small feature at 520 K. The Cu exchanged samples also have their primary Brønsted acid feature at ~660 K. The Cu-ZSM-17-0.27 sample has a small feature at 400 K which is not present in the corresponding $C_3H_6$ signal,

indicating it was not part of a n-propylamine decomposition over a Brønsted acid site. The Brønsted acid site feature was integrated to determine the total number of sites (Table 4.1). The Cu-ZSM-17-0.15, Cu-ZSM-17-0.2, and Cu-ZSM-17-0.27 gave $H^+$:Al values of 0.4, 0.33, and 0.35, respectively. Figure 4.5b shows the $C_3H_6$ signal for the H-ZSM-17 and Cu-ZSM-17 samples to have a maximum at ~650 K, which is in agreement with the maximum $NH_3$ signal at ~660 K in the n-propylamine decomposition reaction. The addition of Cu removed a high temperature shoulder at ~725 K, while a new shoulder at ~700 K also appeared in the process and increased slowly in intensity with increasing Cu loading. The entire area under the main feature, including the small shoulder, was integrated to get the total number of Brønsted acid sites (Table 4.1) in each sample. The inclusion of the shoulder peak will be discussed in the discussion section. The $C_3H_6$ signal for Cu-ZSM-17-0.15, Cu-ZSM-17-0.2, and Cu-ZSM-17-0.27 gave $H^+$:Al values of 0.46, 0.3, and 0.32, respectively. The number of Brønsted acid sites calculated from the $NH_3$ signal and $C_3H_6$ signal were in agreement with each other.

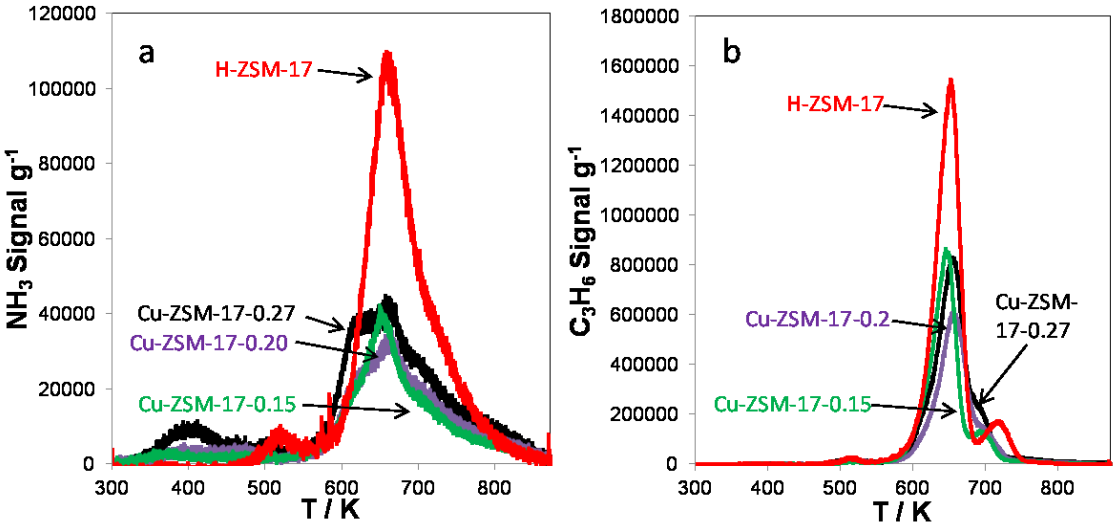


Figure 4.5 N-propylamine – TPDs performed on Cu –ZSM-5 samples with Si:Al = 17. This figure includes a) $NH_3$ signal and b) $C_3H_6$ from Procedure #4 where n-propylamine was used to saturate the samples in the gas phase at 323 K and flushed following the adsorption.

The $NH_3$ titration results also agreed with the n-propylamine decomposition results for the H and Cu-ZSM-17 samples. Figure 4.6a shows a comparison of the results for the two procedures. For each sample, including the H-ZSM-17 sample, the three results matched within a 90% confidence interval, suggesting these two Brønsted acid site counting techniques to be equivalent in Cu-ZSM-5 with Si:Al = 17.

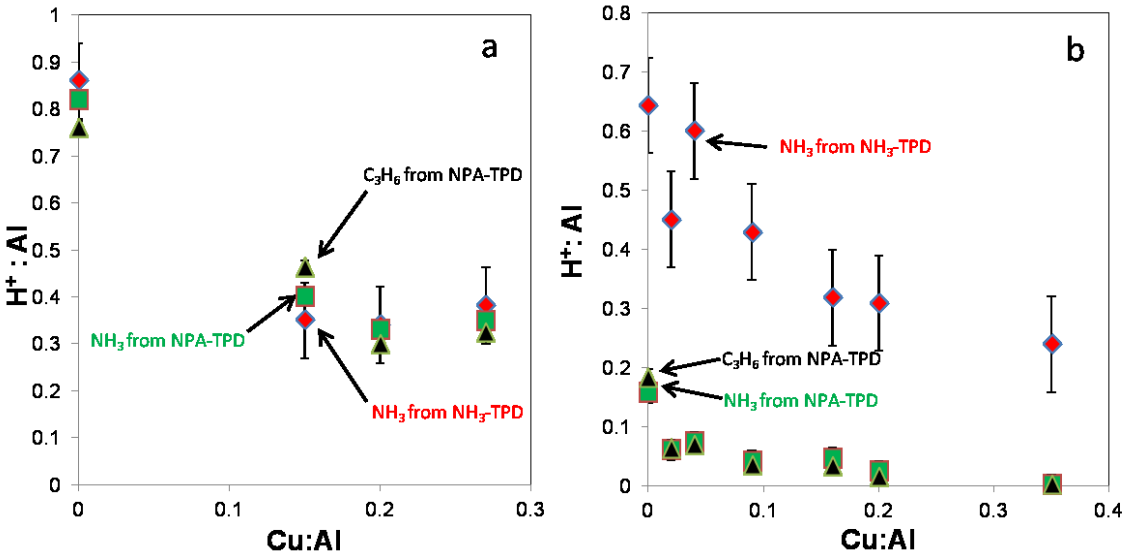


Figure 4.6 Summary of Brønsted acid site quantification techniques on a) Cu-ZSM-5 and b) Cu-SSZ-13. NH3 TPD results shown are from Procedure #3. N-propylamine results are from procedure #4. X-axis corresponds to the last number in the catalyst identifier (Cu-ZSM-17-XX) 90% confidence intervals shown.

Figure C.11 shows that unreacted n-propylamine was also observed in each H- and Cu-ZSM-17 sample. Two features appear to be present. The first is between 400-550 K, which is present in both H- and Cu forms. The second feature is a shoulder at ~575 K which is only present on the samples with Cu. The low temperature, unreacted species has been attributed to a weakly adsorbed species not associated with Brønsted acid sites or exchanged Cu, but in the zeolite. [120]. The second feature at ~575 K, which is present in all the Cu-ZSM-5 samples, has been attributed to n-propylamine associated with Cu that is not in an exchanged position. Parrillo et al. [120] inserted Cu into S-1 and observed the same feature which they concluded to be from Cu not exchanged in Brønsted acid sites.

Figure 4.2 shows the result of $NH_3$ titration (procedure #3) on all Cu-SSZ-4.5 samples. Table 4.1 summarizes the quantification of peak areas and Figure C.10 shows the standard SCR rates per gram of catalyst. The standard SCR rate per gram was observed to increase linearly from zero up to 3.8 x $10^{-6}$ mol NO g $cat^{-1}$ $s^{-1}$ from Cu:Al = 0 to 0.2. Above Cu:Al = 0.2, the rate per gram dropped to 3.0 x $10^{-6}$ mol NO g $cat^{-1}$ $s^{-1}$. The number of Brønsted acid sites determined from the $NH_3$ titration showed a decrease from 0.65 $H^+$:Al to 0.24 $H^+$:Al from Cu:Al = 0 to 0.35. The only outlier in the trend was the Cu-SSZ-4.3-0.02 sample which gave 0.45 $H^+$:Al.

The n-propylamine decomposition (procedure #4) over the Cu-SSZ-4.5 samples yielded different results, which is in contrast to the agreement of techniques with the H- and Cu-ZSM-17 samples. Figure 4.3a and 4.3b show the $NH_3$ and $C_3H_6$ signals from the decomposition reaction. The H-SSZ-4.5 sample had 0.16 and 0.18 $H^+$:Al from $NH_3$ and $C_3H_6$, respectively. The addition of Cu into the structure decreased the number of Brønsted acid sites with increasing Cu loading. The Cu-SSZ-4.5-0.35 sample showed no Brønsted acid sites by n-propylamine decomposition (Table 4.1). No physisorbed n-propylamine was observed in the H- or Cu-SSZ-4.5 samples, which was also different from the H- and Cu-ZSM-17 samples.

Figure 4.6b shows the comparison of the $NH_3$ titration and n-propylamine decomposition for the SSZ-13 samples. A large difference was observed between the two techniques in the H-SSZ-4.5 sample showing a factor of close to four times less Brønsted acid sites according to the n-propylamine decomposition. All the Cu exchanged SSZ-13 samples

also had a very large discrepancy between the results for the $NH_3$ titration and n-propylamine decomposition, suggesting that n-propylamine was unable to access many of the Brønsted sites.

## 4.5 Discussion

### 4.5.1 Interpretation of Features in $NH_3$ Titrations and N-propylamine Decompositions

One important aspect of the described $NH_3$ titration (procedure #3) is that $NH_3$ on Cu does not appear to interfere with the quantification of available Brønsted acid sites. Figure 4.4 shows the results for $NH_3$ titration procedure 3 on H- and Cu-ZSM-17 samples, and it appears that the two higher loadings of Cu (Cu-ZSM-17-0.2 and Cu-ZSM-17-0.27) may have a slight shoulder at ~800 K. To rule this out as $NH_3$ associated with Cu, we calculated the total Brønsted acid sites in each sample accounting for the Cu exchanged as well as the results of the $NH_3$ titration. If a significant contribution of $NH_3$ on Cu was present, the count of total $H^+$:Al would not be consistent. The Cu in the ZSM-17 was assumed to be in a Cu(II) state under ambient conditions based on several studies on the state of Cu in zeolites within our own group [4, 5, 111] and others [6, 33, 42-44]. Assuming each Cu(II) is charge compensated by two Brønsted acid sites and each $NH_3$ titrated corresponds to one Brønsted acid site, the results for the Cu-ZSM-17 samples are shown in Figure 4.7a. The data fluctuate closely around the $H^+$:Al = 0.81 line shown, suggesting that the slight shoulder at ~800 K is due to $NH_3$ diffusion or re-adsorption on a Brønsted acid site and not $NH_3$ on a Cu site. For this reason, the entire area under the primary Brønsted acid site feature and slight shoulder was integrated to get the available Brønsted acid sites.

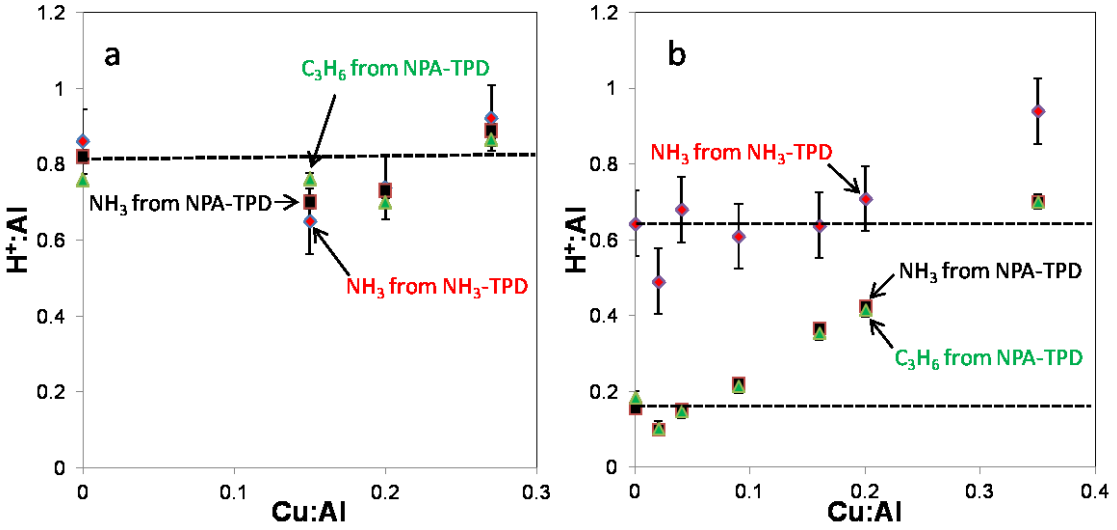


Figure 4.7a-b Calculation of the total number of Brønsted acid sites in each a) H- and Cu-ZSM-17 sample and b) H- and Cu-SSZ-4.5 sample which accounts for 1 Brønsted acid site per $NH_3$ or $C_3H_6$ in $NH_3$ titration procedure #3 or n-propylamine (NPA) decomposition and 2 Brønsted acid sites for each Cu(II) exchanged into the sample. The result is the total Brønsted acid sites before Cu exchange.

The Cu-SSZ-4.5 samples did not have a shoulder present in any of the $NH_3$ titration (procedure #3) experiments. Only one well-defined feature centered at ~725 K was present in each sample which was assigned to available Brønsted acid sites. To confirm this, the number of Brønsted acid sites was again back-calculated based on the amount of Cu exchanged and the results of the $NH_3$ titration just like the Cu-ZSM-17 samples. Figure 4.7b shows that the Cu-SSZ-4.5 samples have an excellent agreement of ~0.65 $H^+$:Al between all samples except the Cu-SSZ-4.5-0.35 sample, which has an $H^+$:Al = 0.94. Another study in our group [111] (Chapter 2) has shown that up to Cu:Al ~0.2, Cu(II) exchanges into two Brønsted acid sites present the in the six-membered rings of SSZ-13 with Si:Al = 4.5. This makes the assumption of two Brønsted acid sites per Cu(II) a reasonable one. After Cu:Al = 0.2, a transition occurs where a secondary multi-Cu

species begins to form which has bulk Cu(II)O character and thus, one Cu(II) may not correspond to two Brønsted acid sites anymore. This would make an $H^+$:Al = 0.94 for Cu-SSZ-4.5-0.35 an inflated value not corresponding to the actual amount of Brønsted acid sites in the sample. Based on the agreement of total number of Brønsted acid sites in H- and Cu-ZSM-17 and H-and CuSSZ-4.5(Figure 4.7a-b), $NH_3$ appears to be a suitable titrant for quantification of Brønsted acid sites because $NH_3$ on Cu does not interfere with the measurements.

The analysis and identification of features corresponding to n-propylamine decomposition are based on studies by Parrillo et al. [120, 121] which used isopropylamine to titrate the Brønsted acid sites in Cu-ZSM-5 and Cu-Y zeolites. The differences between n-propylamine and isopropylamine decomposition have previously been explored in ZSM-5 [84] with the primary difference being $NH_3$ and $C_3H_6$ formed ~50 K higher in n-propylamine. The features in $NH_3$ and $C_3H_6$ signals assigned to Brønsted acid sites in that study appeared between 575-650 K for isopropylamine, which was in agreement with what we observed using n-propylamine for the H-and Cu-ZSM-17 samples. Our Brønsted acid feature eluted primarily between 600-700 K (Figure 4.5a-b). The H-and Cu-SSZ-4.5 samples had a single $NH_3$ feature elute between 650-850 K and the $C_3H_6$ signal between 600-700 K, both of which corresponded to the Brønsted acid sites.

In the study by Parrillo et al. [120], a high temperature feature appeared between 650-800 K when Cu was introduced into ZSM-5. They attributed the increase in intensity to –propylamine associated with an exchanged Cu at a Brønsted acid site and determined that

the loss of one Brønsted acid site corresponded to one Cu site. Figure 4.5a-b shows that our Cu-ZSM-17 samples exhibit a small shoulder at ~700K in $NH_3$ and $C_3H_6$ signal which could be caused by decomposition of n-propylamine on exchanged Cu. However, if we de-convolute and quantify the Brønsted acid feature and shoulder present in each Cu-ZSM-17 sample in the $C_3H_6$ signal, the drop in available Brønsted acid sites is significantly larger than the increase in shoulder intensity, which can be seen in Figure C.12. The available number of Brønsted acid sites dropped from 0.76 to 0.27 $H^+$:Al in the H-ZSM-17 and Cu-ZSM-17-0.27 samples, respectively. The maximum contribution from the shoulder was 0.05 $H^+$:Al in the Cu-ZSM-17-0.15 sample. If this feature was due to exchanged Cu, the efficiency at which n-propylamine titrated those sites was much lower than the efficiency for titrating available Brønsted acid sites. Given that the amines procedures described by Parrillo et al. [84, 120] are supposed to titrate only Brønsted acid sites, the decomposition of n-propylamine on a Cu, or Lewis acid, does not fully support the n-propylamine being selective to Brønsted acid sites. One possibility is the n-propylamine does associate with an exchanged Cu until an open Brønsted acid site is available. Then, it could move to the Brønsted acid site and be decomposed there. This would then suggest some Brønsted acid sites are double counted. Palkhiwala et al. [85] observed a high temperature feature in H-FER, where no metals were present and suggested the n-propylamine was caught in the side cages until a Brønsted acid site became available for it decompose on. Thus, we cannot rule it out as a possibility that this feature allows for the double counting of Brønsted acid sites. We have already suggested, however, that there are issues with slow diffusion and re-adsorption in the $NH_3$ titration (procedure #3) on these samples, and this could also be the case in the n-

propylamine decomposition. An evidence that it may not associated with Cu is the consistency of the total number of Brønsted acid sites, as seen in Figure 4.7a. The values fluctuate closely around 0.81 $H^+$:Al and also match with the results of the $NH_3$ titration (procedure #3). Realizing the uncertainty of this feature, we tentatively assigned it to Brønsted acid sites which were not double counted. Thus, the quantification of Brønsted acid sites from $NH_3$ and $C_3H_6$ in the n-propylamine decompositions over the Cu-ZSM-17 samples included both the primary Brønsted acid site feature as well as the small shoulder at ~700 K.

The Cu-SSZ-4.5 samples did not appear to suffer from extra features in the n-propylamine decomposition experiments aside from a negligible high temperature shoulder in the $C_3H_6$ signal of the Cu-SSZ-4.5-0.16 sample. The calculations for the total Brønsted acid sites from n-propylamine decomposition are over the Cu-SSZ-4.5 (Figure 7b) are not consistent like the result from the $NH_3$ titration. They show an increasing $H^+$:Al with increasing Cu:Al. The linear increase of the $H^+$:Al is primarily due to the increase in exchanged Cu and not the available Brønsted acid sites. Because the total $H^+$:Al in each sample did not give a constant value, the implication is that n-propylamine is not suited for use in SSZ-13, which will be discussed in the next section.

### 4.5.2 Can N-propylamine Titrate Brønsted Acid Sites in SSZ-13?

The n-propylamine decomposition over H- and Cu-ZSM-5 samples appeared to be successful at titrating Brønsted acid sites in this study as well as other studies [84, 86]. We had an agreement of n-propylamine with the other $NH_3$ titration procedures in H- and

Cu-ZSM-17 samples, which validated the $NH_3$ procedures. However, when n-propylamine was introduced to the H- and Cu-SSZ-4.5 samples, a significant difference was observed between the n-propyalmine results and the $NH_3$ titration results. A possibility for the difference is that the pores of SSZ-13 are too small for n-propylamine to fit into completely. The largest pore opening diameter in the MFI (for ZSM-5) is a 10-membered ring with a 5.1 Å diameter in one direction and a 5.6 Å diameter in the perpendicular direction. The largest ring opening diameter in the CHA structure (SSZ-13) is 3.8Å. Using basic molecular mechanics simulations, the longest dimension of n-propylamine would be between 5.1-5.4 Å and the diameter 3.1 Å. Based on these dimensions, n-propylamine may move into a ZSM-5 pore in almost any direction while it would have to move into the SSZ-13 pore head-on to be able to enter, making mass transfer into the SSZ-13 a probable cause of the low Brønsted site counts. Another evidence that n-propylamine may have trouble entering the pores of SSZ-13 is that no physisorbed n-propylamine species were observed like they were in the H- and Cu-ZSM-17 samples.

A second possible issue with reacting n-propylamine over Brønsted acid sites in our SSZ-13 is the sites are too close together in our low Si:Al ratio of 4.5. N-propylamine may only be able to titrate a portion of the sites because of other molecules blocking their access. At this Si:Al ratio, we have performed statistical calculation to determine there are, at the least, enough pairs of Al in the six-membered rings for a single Cu(II) to charge compensate up to a Cu:Al = 0.18 [83, 111]. This does not include other

possibilities of two Al in close proximity of each other. Thus, plenty of opportunity exists for n-propylamine to block nearby sites.

A third scenario could be a combination of both the small pores and high Al content which contribute to the low counts of Brønsted acid sites. Since we are able to titrate 0.18 $H^+$:Al in the H-SSZ-4.5 sample, this indicates that n-propylamine can enter the pores to some extent. There may be some Brønsted acid sites just inside the pore opening or on the pore entrance which get titrated, but block the pore from allowing any other molecules to enter. In other cases, an n-propylamine may get inside the pore completely and titrate a site inside, but a second molecule would not be able to titrate any Brønsted acid site in the vicinity of the first molecule already inside.

Based on the low Brønsted acid site counts obtained in the H- and Cu-SSZ-4.5 samples in this study and the arguments presented on pore size and high Al content, we believe n-propylamine is not suited for counted Brønsted acid sites in SSZ-13. This does not exclude other amines studied by Parrillo et al. [84], which we have not tested. Methylamine or ethylamine may be suitable replacements for the n-propylamine. Larger molecules may suffer from the same issues as n-propylamine. This was documented by Palkhiwala et al. [85] where isopropylamine was shown to have difficulty with a similar sized eight-membered ring in H-FER, but n-propylamine was observed to give higher Brønsted acid site densities. The Si:Al ratio in the H-FER sample was also larger than in our H- and Cu-SSZ-4.5 samples with a Si:Al = 10.5, suggesting the distance may have been larger and therefore easier for n-propylamine to access. Some possible ways to

allow a mass transfer problem become a non-issue would be to have a significantly longer exposure time or a different temperature of saturation, although this would not solve the problem of close proximity of Brønsted acid sites. Different conditions were not explored in this study.

### 4.5.3 Utility of $NH_3$-titrations for Counting Brønsted Acid Sites

The $NH_3$ titration procedures described in this study were shown to have equivalent results to n-propylamine decomposition in H- and Cu- ZSM-5 with varying Si:Al ratios from 17-89, which is evidence that these techniques are useful for quantifying the number of Brønsted acid sites. When the correct treatment was applied, we showed that all the weakly bound $NH_3$ features were removed from the TPD spectra, which allowed for meaningful interpretation of the results.

In SSZ-13, a comparison of the $NH_3$ titration (procedure #3) and n-propylamine decomposition (procedure #4) revealed that $NH_3$ was able to titrate sites that were inaccessible to n-propylamine either because of the small pores, close vicinity of Brønsted acid sites (from high Al content), or a combination of the two. This makes the described $NH_3$ titration techniques ideal for small-pore zeolites used for current SCR technologies, such as SAPO-34 or SSZ-13. The most useful aspect of the $NH_3$ titration procedures for SCR is the ability of $NH_3$ to access the Brønsted acid sites available under reaction conditions. Since $NH_3$ is a reactant in SCR, it is an ideal probe molecule to learn about the domain in which $NH_3$ exists for those reactions.

Since the three $NH_3$ treatments are equivalent, the tools accessible to an individual or the state of a sample may determine the appropriate method to use. The $NH_3$ saturation via gas phase followed by water wash in procedure #1 would be appropriate to use after a reaction was performed on the sample as a check for acid site poisoning. The first procedure, however, would be more laborious for testing a sample as it requires the maximum number of steps. Procedure #2, in which $NH_3$ is exchanged via $NH_4NO_3$ solution, would be ideal for Brønsted site counting before a reaction is performed on the sample. It also allows the ability to create large amounts of the $NH_4$-form with no weakly bound $NH_3$ at one time which can be saved for later use in multiple experiments. The combination of the first two procedures would be useful for before and after a reaction to see the change in number of sites. Procedure #3 appears to be the best suited for measurements after a reaction because it can be performed immediately following without unloading the sample. By saturating with $NH_3$ at a higher temperature, there is no need for the washing step. One caveat of the third procedure was that the temperature used to saturate with $NH_3$ could change depending on the specific conditions employed in the experiment. The particle size, the flow-rate, and bed height were all parameters that could change the outcome; therefore, when using procedure #3, an initial $NH_3$-TPD without the intermediate $NH_3$ saturation is required to determine the appropriate temperature setting to keep weakly bound $NH_3$ off the surface (Figures C.13-C.14).

It should be noted, however, that these procedures with $NH_3$ should only be used for quantifying the number of Brønsted acid sites. Ammonia should not be used to

determine strength of acidity as many factors can contribute to a change in peak position, including particle size, flow-rate, and bed height [118].

## 4.6 Conclusions

The current study utilizes three different $NH_3$ titration procedures and an n-propylamine decomposition reaction to determine the number of Brønsted acid sites present in H-ZSM-5, H-SSZ-13, Cu-ZSM-5, and Cu-SSZ-13, with the Cu-ZSM-5 and Cu-SSZ-13 being active catalysts for standard SCR. Each $NH_3$ titration procedure was observed to be able to selectively remove weakly bound or Lewis-type $NH_3$ species while allowing for quantification of only available Brønsted acid sites.

On H- and Cu-ZSM-5, the $NH_3$ titration results agreed with n-propylamine decomposition results which validated the $NH_3$ titration procedures. In H- and Cu-SSZ-13, the $NH_3$ procedures were able to titrate significantly more Brønsted acid sites than the n-propylamine decomposition reaction. This was attributed to n-propylamine being unable to access all the Brønsted acid sites because of the high Brønsted acid site density and small pores of SSZ-13.

In SCR technologies, small-pore zeolites such as SSZ-13 or SAPO-34 are utilized, making $NH_3$ an ideal choice to titrate Brønsted acid sites. Most importantly, $NH_3$ is a reactant in the SCR reactions, which makes it an ideal probe molecule to titrate Brønsted acid sites as it can quantify the number of sites available under reaction conditions.

# CHAPTER 5. CONCLUSIONS AND RECOMMENDATIONS

The studies described in this document were meant to probe the sites for reaction under standard SCR in Cu-SSZ-13. To understand the active Cu site, the reaction kinetics of standard SCR in combination with ambient and *operando* techniques and DFT calculations were used to give a very good argument for the species and location to be an isolated Cu exchanged in two Brønsted acid sites in the six-membered ring. The maximum reaction rates per gram catalysts were observed to match with the amount of Cu(II) able to be exchanged into the six-membered ring of SSZ-13. At the same time, we observed only hydrated (isolated) Cu(II) under ambient conditions or isolated Cu under *operando* conditions in the samples with Cu:Al < 0.2. After Cu:Al = 0.2, a transition occurs and a new Cu species is formed. We observed this under ambient XAS conditions as well as the saturation of hydrated Cu(II) in UV-Vis-NIR. Another study in our group has also seen dry NO oxidation to take place on this new form of Cu, where it cannot take place on the isolated Cu [83].

We further delved into the active Cu species by learning about its active state, meaning its oxidation state under reaction conditions. Based on previous work in our group [5, 99], we hypothesized a redox mechanism between isolated Cu(I) and Cu(II) in standard SCR was present. A series of experiments were designed to isolate the oxidizing or

reducing portion of the redox cycle. Dioxygen, NO, or $NH_3$ was removed from steady state, preventing the redox cycle from closing and forcing the catalysts to be driven by one half of the redox cycle. Collection of XAS data at the same time allowed us to observe the change in the active Cu species over time. Removing $O_2$ pushed the catalyst to a severely reduced state, with ~75% Cu(I). Removing NO pushed the catalyst to a Cu(II) state. Removing $NH_3$ drove the Cu to a Cu(II) state while also becoming hydrated by water. The reverse experiments were performed where the reactants were added back into the reaction mixture which allowed the Cu and reaction rates to return to their steady state values. Thus, we proved a redox cycle was present because we could drive it into one direction or another by removing its half-reactions.

The role of Brønsted acid sites was also studied. First, a quantitative technique was needed to determine the number of Brønsted acid sites in our samples. For this we looked to the amine decomposition work by Gorte et al. [84, 86, 118] and decided to use n-propylamine. We also used three methods with $NH_3$ involving washing steps or intermediate temperatures to drive off the weakly bound species present in our samples. The $NH_3$ techniques were shown to be able to equivalently titrate Brønsted acid sites in H-ZSM-5. In Cu-ZSM-5, similar results were also obtained and the total number of Brønsted sites remained near the parent $H^+$:Al, therefore, the $NH_3$ was likely not associated with any Cu species in the counting procedures. In H- and Cu-SSZ-13, the n-propylamine performed poorly while the $NH_3$ procedure used gave consistent total Brønsted acid site counts indicating it was performing properly. We suggested that n-propylamine and other larger titrant molecules may be mass transfer limited in the

temperatures and conditions used for the saturation steps of this study. We also speculated Brønsted acid sites may have been too close together for n-propylamine to titrate all the sites. When we determined the number of Brønsted acid sites in our Cu-SSZ-13 samples, the rate was seen to increase with decreasing number of Brønsted acid sites suggesting that the Brønsted acid sites are not involved with the kinetically relevant steps of standard SCR in our samples with a given Si:Al=4.5. A further study of Brønsted acid sites reveals that under reaction conditions, the coverage of $NH_3$ on Brønsted acid sites (strongly bound $NH_3$) is severely depleted, again suggesting that kinetically relevant steps do not take place on Brønsted acid sites. The use of $NH_3$ as a titrant of Brønsted acid sites is ideal for small pore zeolites such as SSZ-13 or SAPO-34 which are used for standard SCR. The $NH_3$ can access all sites available under reaction conditions making it a good probe molecule.

From this work, we have a good understanding of the contributions of different sites under reaction conditions, which can be a building block for future work. We still do not have a plausible mechanism to explain the things we see in the kinetic data. I strongly suggest that the group utilize the isotopic transient experimental tools it has available while there are still questions to be answered about the mechanism. The location of the active $NH_3$ is also still one question which could be easily solved by using some of the $NH_3$ cutoff techniques developed here and *operando* transmission IR. Based on the results of the initial Brønsted acid site study in these samples, I would suggest a separate study in which a series of Cu samples with the same initial amount of Cu and parent number of Brønsted acid sites be poisoned to various extents in order to see if there really

is a turning point where the number of Brønsted acid sites becomes important for kinetics. If this can be shown in CHA, it could be a nice contribution. Finally, based on the statistical distribution of active Cu with different Si:Al, I would suggest a future student try to put some more points on the curve to go along with the study on the Si:Al = 4.5 samples to verify the statistical roadmap used in Chapter 2.

# REFERENCES

# REFERENCES

[1] J.H. Kwak, R.G. Tonkyn, D.H. Kim, J. Szanyi, C.H.F. Peden, Excellent activity and selectivity of Cu-SSZ-13 in the selective catalytic reduction of NO(x) with NH(3), Journal of Catalysis, 275 (2010) 187-190.

[2] D.W. Fickel, E. D'Addio, J.A. Lauterbach, R.F. Lobo, The ammonia selective catalytic reduction activity of copper-exchanged small-pore zeolites, Applied Catalysis B-Environmental, 102 (2011) 441-448.

[3] I. Bull, R.S. Boorse, W.M. Jaglowski, G.S. Koermer, A. Moini, J.A. Patchett, W.M. Xue, P. Burk, J.C. Dettling, M.T. Caudle, 7601662, in, US, 2009.

[4] J.-S. McEwen, T. Anggara, W.F. Schneider, V.F. Kispersky, J.T. Miller, W.N. Delgass, F.H. Ribeiro, Integrated operando X-ray absorption and DFT characterization of Cu–SSZ-13 exchange sites during the selective catalytic reduction of NOx with NH3, Catal. Today, 184 (2012) 129-144.

[5] V.F. Kispersky, A.J. Kropf, F.H. Ribeiro, J.T. Miller, Low absorption vitreous carbon reactors for operando XAS: a case study on Cu/Zeolites for selective catalytic reduction of NOx by NH3, Physical Chemistry Chemical Physics, 14 (2012) 2229-2238.

[6] U. Deka, A. Juhin, E.A. Eilertsen, H. Emerich, M.A. Green, S.T. Korhonen, B.M. Weckhuysen, A.M. Beale, Confirmation of Isolated Cu2+ Ions in SSZ-13 Zeolite as Active Sites in NH3-Selective Catalytic Reduction, Journal of Physical Chemistry C, 116 (2012) 4809-4818.

[7] USEPA, in.

[8] USEPA, Health Assessment Document for Diesel Engine Exhaust, in: U.E.P. Agency (Ed.), National Center for Environmental Assessment, 2002.

[9] R.M. Heck, R.J. Farrauto, S.T. Gulati, Catalytic air pollution control : commercial technology, 2nd ed., Wiley-Interscience, New York, 2002.

[10] A. Martinez-Arias, J.C. Conesa, M. Fernandez-Garcia, J.A. Anderson, In Supported Metals in Catalysis, Imperial College Press, London, 2005

[11] P.L.T. Gabrielsson, Urea-SCR in Automotive Applications, Topics in Catalysis, 28 (2004) 177-184.

[12] M. Takeuchi, S. Matsumoto, NOx storage-reduction catalysts for gasoline engines, Topics in Catalysis, 28 (2004) 151-156.
[13] W.S. Epling, L.E. Campbell, A. Yezerets, N.W. Currier, J.E. Parks, Overview of the fundamental reactions and degradation mechanisms of NOx storage/reduction catalysts, Catalysis Reviews - Science and Engineering, 46 (2004) 163-245.

[14] S. Brandenberger, O. Kroecher, A. Tissler, R. Althoff, The State of the Art in Selective Catalytic Reduction of NOx by Ammonia Using Metal-Exchanged Zeolite Catalysts, Catalysis Reviews-Science and Engineering, 50 (2008) 492-531 [15] M. Koebel, M. Elsener, M. Kleemann, Urea-SCR: a promising technique to reduce NOx emissions from automotive diesel engines, Catalysis Today, 59 (2000) 335-345.

[16] M. Devadas, O. Kroecher, M. Elsener, A. Wokaun, N. Soeger, M. Pfeifer, Y. Demel, L. Mussmann, Influence of NO2 on the selective catalytic reduction of NO with ammonia over Fe-ZSM5, Applied Catalysis B-Environmental, 67 (2006) 187-196.

[17] G. Tuenter, W.F. Vanleeuwen, L.J.M. Snepvangers, KINETICS AND MECHANISM OF THE NOX REDUCTION WITH NH3 ON V2O5-WO3-TIO2 CATALYST, Industrial & Engineering Chemistry Product Research and Development, 25 (1986) 633-636.

[18] M. Koebel, M. Elsener, G. Madia, Recent Advances in the Development of Urea-SCR for Automotive Applications, SAE, 01-3625 (2001).

[19] P. Forzatti, L. Lietti, E. Tronconi, Nitrogen Oxides Removal—Industrial, in: Encyclopedia of Catalysis, John Wiley & Sons, Inc., 2002.

[20] P. Forzatti, L. Lietti, Recent Advances in the De-NO(x)ing Catalysis for Stationary Applications, Heterogen. Chem. Rev., 3 (1996) 33-51.

[21] S.C. Wood, Select the Right NOx Control Technology - Consider the Degree of Emission Reduction Needed, the Type of Fuel, Combustion Device Design, and Operational Factors, Chem. Eng. Prog., 90 (1994) 32-38.

[22] R.Q. Long, R.T. Yang, Catalytic performance of Fe-ZSM-5 catalysts for selective catalytic reduction of nitric oxide by ammonia, Journal of Catalysis, 188 (1999) 332-339.

[23] K. Rahkamaa-Tolonen, T. Maunula, M. Lomma, M. Huuhtanen, R.L. Keiski, The effect of NO2 on the activity of fresh and aged zeolite catalysts in the NH3-SCR reaction, Catalysis Today, 100 (2005) 217-222.

[24] R.Q. Long, R.T. Yang, Superior Fe-ZSM-5 catalyst for selective catalytic reduction of nitric oxide by ammonia, Journal of the American Chemical Society, 121 (1999) 5595-5596.

[25] Q. Sun, Z.-X. Gao, H.-Y. Chen, W.M.H. Sachtler, Reduction of NOx with Ammonia over Fe/MFI: Reaction Mechanism Based on Isotopic Labeling, Journal of Catalysis, 201 (2001) 88-99.

[26] M. Devadas, O. Kröcher, M. Elsener, A. Wokaun, N. Söger, M. Pfeifer, Y. Demel, L. Mussmann, Influence of NO2 on the selective catalytic reduction of NO with ammonia over Fe-ZSM5, Applied Catalysis B: Environmental, 67 (2006) 187-196.

[27] R.Q. Long, R.T. Yang, Reaction mechanism of selective catalytic reduction of NO with NH3 over Fe-ZSM-5 catalyst, Journal of Catalysis, 207 (2002) 224-231.

[28] H.Y. Huang, R.Q. Long, R.T. Yang, Kinetics of selective catalytic reduction of NO with NH3 on Fe-ZSM-5 catalyst, Applied Catalysis A: General, 235 (2002) 241-251.

[29] R. Delahay, S. Kieger, N. Tanchoux, P. Trens, B. Coq, Kinetics of the selective catalytic reduction of NO by NH3 on a Cu-faujasite catalyst, Applied Catalysis B-Environmental, 52 (2004) 251-257.

[30] S.A. Gomez, A. Campero, A. Martinez-Hernandez, G.A. Fuentes, Changes in Cu2+ environment upon wet deactivation of Cu-ZSM-5 deNO(x) catalysts, Applied Catalysis a-General, 197 (2000) 157-164.

[31] T. Ishihara, M. Kagawa, F. Hadama, Y. Takita, Copper ion-exchanged SAPO-34 as a thermostable catalyst for selective reduction of NO with C3H6, Journal of Catalysis, 169 (1997) 93-102.

[32] J.H. Kwak, D. Tran, S.D. Burton, J. Szanyi, J.H. Lee, C.H.F. Peden, Effects of hydrothermal aging on NH3-SCR reaction over Cu/zeolites, Journal of Catalysis, 287 (2012) 203-209.

[33] D.W. Fickel, J.M. Fedeyko, R.F. Lobo, Copper Coordination in Cu-SSZ-13 and Cu-SSZ-16 Investigated by Variable-Temperature XRD, Journal of Physical Chemistry C, 114 (2010) 1633-1640.

[34] International Zeolite Association, in.

[35] G. Delahay, D. Valade, A. Guzmán-Vargas, B. Coq, Selective catalytic reduction of nitric oxide with ammonia on Fe-ZSM-5 catalysts prepared by different methods, Applied Catalysis B: Environmental, 55 (2005) 149-155.

[36] P.S. Metkar, N. Salazar, R. Muncrief, V. Balakotaiah, M.P. Harold, Selective catalytic reduction of NO with NH3 on iron zeolite monolithic catalysts: Steady-state and transient kinetics, Applied Catalysis B: Environmental, 104 (2011) 110-126.

[37] A. Grossale, I. Nova, E. Tronconi, D. Chatterjee, M. Weibel, The chemistry of the NO/NO2-NH3 "fast" SCR reaction over Fe-ZSM5 investigated by transient reaction analysis, Journal of Catalysis, 256 (2008) 312-322.

[38] J. Eng, C.H. Bartholomew, Kinetic and Mechanistic Study of NOxReduction by NH3over H-Form Zeolites, Journal of Catalysis, 171 (1997) 27-44.

[39] F. Gao, J.H. Kwak, J. Szanyi, C.H.F. Peden, Current Understanding of Cu Exchanged Chabazite Molecular Sieves for Use as Commercial Diesel Engine DeNOx Catalysts, Topics in Catalysis, (2013).

[40] S.A. Bates, V.F. Kispersky, A. Yezerets, W.F. Schnieder, J.T. Miller, W.N. Delgass, F.H. Ribeiro, Investigation of the Redox Sites of the Half-reactions of Selective Catalytic Reduction of NOx by NH3 via Operando X-ray Absorption of Cu/SSZ-13, in preparation.

[41] S.A. Bates, K.D. Sabnis, R. Gounder, J.T. Miller, W.N. Delgass, F.H. Ribeiro, Practical Bronsted Site Quantification Techniques Utilizing NH3 as a Chemical Titrant in Cu-Zeolites Active for the Selective Catalytic Reduction of NOx with NH3, in preparation.

[42] S.T. Korhonen, D.W. Fickel, R.F. Lobo, B.M. Weckhuysen, A.M. Beale, Isolated Cu(2+) ions: active sites for selective catalytic reduction of NO, Chemical Communications, 47 (2011) 800-802.

[43] J.H. Kwak, H.Y. Zhu, J.H. Lee, C.H.F. Peden, J. Szanyi, Two different cationic positions in Cu-SSZ-13?, Chem. Commun., 48 (2012) 4758.

[44] F. Gao, E.D. Walter, E.M. Karp, J. Luo, R.G. Tonkyn, J.H. Kwak, J. Szanyi, C.H.F. Peden, Structure–activity relationships in NH3-SCR over Cu-SSZ-13 as probed by reaction kinetics and EPR studies, Journal of Catalysis, 300 (2013) 20-29.

[45] L. Wang, W. Li, D. Weng, Location and nature of Cu species in Cu/SAPO-34 for selective catalytic reduction
of NO with NH3, Journal of Catalysis, doi: 10.1016/j.jcat.2012.01.012 (2012).

[46] B.R. Goodman, K.C. Hass, W.F. Schneider, J.B. Adams, Statistical Analysis of Al Distributions and Metal Ion Pairing Probabilies in Zeolites, Catalysis Letters, 68 (2000) 85-93.

[47] W. Loewenstein, The Distribution of aluminum in the tetrahedra of silicates and aluminates, American Mineralogist, 39 (1954) 92-96.

[48] J.H. Kwak, D. Tran, J. Szanyi, C.H.F. Peden, J.H. Lee, The Effect of Copper Loading on the Selective Catalytic Reduction of Nitric Oxide by Ammonia Over Cu-SSZ-13, Catalysis Letters, 142 (2012) 295-301.

[49] T. Komatsu, M. Nunokawa, I.S. Moon, T. Takahara, S. Namba, T. Yashima, KINETIC-STUDIES OF REDUCTION OF NITRIC-OXIDE WITH AMMONIA ON CU2+-EXCHANGED ZEOLITES, Journal of Catalysis, 148 (1994) 427-437.

[50] S.A. Stevenson, J.C. Vartuli, C.F. Brooks, Kinetics of the Selective Catalytic Reduction of NO over HZSM-5, Journal of Catalysis, 190 (2000) 228-239.

[51] J. Eng, C.H. Bartholomew, Kinetic and Mechanistic Study of NOxReduction by NH3over H-Form Zeolites, Journal of Catalysis, 171 (1997) 14-26.

[52] P.S. Metkar, M.P. Harold, V. Balakotaiah, Selective catalytic reduction of NOx on combined Fe- and Cu-zeolite monolithic catalysts: Sequential and dual layer configurations, Applied Catalysis B: Environmental, 111–112 (2012) 67-80.

[53] H. Sjövall, L. Olsson, E. Fridell, R.J. Blint, Selective catalytic reduction of NOx with NH3 over Cu-ZSM-5—The effect of changing the gas composition, Applied Catalysis B: Environmental, 64 (2006) 180-188.

[54] A.L. Kustov, T.W. Hansen, M. Kustova, C.H. Christensen, Selective catalytic reduction of NO by ammonia using mesoporous Fe-containing HZSM-5 and HZSM-12 zeolite catalysts: An option for automotive applications, Applied Catalysis B: Environmental, 76 (2007) 311-319.

[55] S. Brandenberger, O. Kröcher, A. Wokaun, A. Tissler, R. Althoff, The role of Brønsted acidity in the selective catalytic reduction of NO with ammonia over Fe-ZSM-5, Journal of Catalysis, 268 (2009) 297-306.

[56] S.I. Zones, 4544538, in, US, 1985.

[57] S.I. Zones, R.A. Vannordstrand, NOVEL ZEOLITE TRANSFORMATIONS - THE TEMPLATE-MEDIATED CONVERSION OF CUBIC-P ZEOLITE TO SSZ-13, Zeolites, 8 (1988) 166-174.

[58] S.I. Zones, CONVERSION OF FAUJASITES TO HIGH-SILICA CHABAZITE SSZ-13 IN THE PRESENCE OF N,N,N-TRIMETHYL-1-ADAMANTAMMONIUM IODIDE, Journal of the Chemical Society-Faraday Transactions, 87 (1991) 3709-3716.

[59] H. Robson, How to read a patent, Microporous and Mesoporous Materials, 22 (1998) 551-551.

[60] Q. Zhu, J.N. Kondo, T. Tatsumi, S. Inagaki, R. Ohnuma, Y. Kubota, Y. Shimodaira, H. Kobayashi, K. Domen, A comparative study of methanol to olefin over CHA and MTF zeolites, Journal of Physical Chemistry C, 111 (2007) 5409-5415.

[61] A. Zecchina, S. Bordiga, J.G. Vitillo, G. Ricchiardi, C. Lamberti, G. Spoto, M. Bjørgen, K.P. Lillerud, Liquid Hydrogen in Protonic Chabazite, Journal of the American Chemical Society, 127 (2005) 6361-6366.

[62] L. Sommer, D. Mores, S. Svelle, M. Stocker, B.M. Weckhuysen, U. Olsbye, Mesopore formation in zeolite H-SSZ-13 by desilication with NaOH, Microporous and Mesoporous Materials, 132 (2010) 384-394.

[63] G.L. Woolery, G.H. Kuehl, H.C. Timken, A.W. Chester, J.C. Vartuli, On the nature of framework Brønsted and Lewis acid sites in ZSM-5, Zeolites, 19 (1997) 288-296.

[64] L.S. Kau, D.J. Spirasolomon, J.E. Pennerhahn, K.O. Hodgson, E.I. Solomon, X-RAY ABSORPTION-EDGE DETERMINATION OF THE OXIDATION-STATE AND COORDINATION-NUMBER OF COPPER - APPLICATION TO THE TYPE-3 SITE IN RHUS-VERNICIFERA LACCASE AND ITS REACTION WITH OXYGEN, Journal of the American Chemical Society, 109 (1987) 6433-6442.

[65] D.J. Liu, H.J. Robota, IN-SITU CHARACTERIZATION OF CU-ZSM-5 BY X-RAY-ABSORPTION SPECTROSCOPY - XANES STUDY OF THE COPPER OXIDATION-STATE DURING SELECTIVE CATALYTIC REDUCTION OF NITRIC-OXIDE BY HYDROCARBONS, Applied Catalysis B-Environmental, 4 (1994) 155-165.

[66] K.C.C. Kharas, D.J. Liu, H.J. Robota, STRUCTURE-FUNCTION PROPERTIES IN CU-ZSM-5 NO DECOMPOSITION AND NO SCR CATALYSTS, Catalysis Today, 26 (1995) 129-145.

[67] D.J. Liu, H.J. Robota, IN-SITU XANES CHARACTERIZATION OF THE CU OXIDATION-STATE IN CU-ZSM-5 DURING NO DECOMPOSITION CATALYSIS, Catalysis Letters, 21 (1993) 291-301.

[68] C. Lamberti, S. Bordiga, M. Salvalaggio, G. Spoto, A. Zecchina, F. Geobaldo, G. Vlaic, M. Bellatreccia, XAFS, IR, and UV-vis study of the Cu-I environment in Cu-I-ZSM-5, Journal of Physical Chemistry B, 101 (1997) 344-360.

[69] I.J. Drake, Y.H. Zhang, M.K. Gilles, C.N.T. Liu, P. Nachimuthu, R.C.C. Perera, H. Wakita, A.T. Bell, An in situ AlK-edge XAS investigation of the local environment of H+- and Cu+-exchanged USY and ZSM-5 zeolites, Journal of Physical Chemistry B, 110 (2006) 11665-11676.

[70] K. Mathisen, M. Stockenhuber, D.G. Nicholson, In situ XAS and IR studies on Cu:SAPO-5 and Cu:SAPO-11: the contributory role of monomeric linear copper(I) species in the selective catalytic reduction of NO(x) by propene, Physical Chemistry Chemical Physics, 11 (2009) 5476-5488.

[71] G. Lamble, A. Moen, D.G. Nicholson, STRUCTURE OF THE DIAMMINECOPPER(I) ION IN SOLUTION - AN X-RAY-ABSORPTION SPECTROSCOPIC STUDY, Journal of the Chemical Society-Faraday Transactions, 90 (1994) 2211-2213.

[72] A. Moen, D.G. Nicholson, M. Ronning, STUDIES ON THE PRE-EDGE REGION OF THE X-RAY-ABSORPTION SPECTRA OF COPPER(I) OXIDE AND THE DIAMMINECOPPER(I) ION, Journal of the Chemical Society-Faraday Transactions, 91 (1995) 3189-3194.

[73] B. Fingland, F. Ribeiro, J. Miller, Simultaneous Measurement of X-ray Absorption Spectra and Kinetics: A Fixed-bed, Plug-flow Operando Reactor, Catalysis Letters, 131 (2009) 1-6.

[74] G. Kresse, J. Furthmuller, Efficiency of ab-initio total energy calculations for metals and semiconductors using a plane-wave basis set, Computational Materials Science, 6 (1996) 15-50.

[75] G. Kresse, J. Furthmuller, Efficient iterative schemes for ab initio total-energy calculations using a plane-wave basis set, Physical Review B, 54 (1996) 11169-11186.

[76] VASP, in, http://cms.mpi.univie.ac.at/vasp/.

[77] G. Kresse, D. Joubert, From ultrasoft pseudopotentials to the projector augmented-wave method, Physical Review B, 59 (1999) 1758-1775.

[78] J.P. Perdew, Y. Wang, Accurate and simple analytic representation of the electron-gas correlation energy, Physical Review B, 45 (1992) 13244-13249.

[79] J. Dědeček, B. Wichterlová, Role of Hydrated Cu Ion Complexes and Aluminum Distribution in the Framework on the Cu Ion Siting in ZSM-5, The Journal of Physical Chemistry B, 101 (1997) 10233-10240.

[80] M.J. Rice, A.K. Chakraborty, A.T. Bell, Al Next Nearest Neighbor, Ring Occupation, and Proximity Statistics in ZSM-5, Journal of Catalysis, 186 (1999) 222-227.

[81] R.J. Madon, M. Boudart, Experimental criterion for the absence of artifacts in the measurement of rates of heterogeneous catalytic reactions, Industrial & Engineering Chemistry Fundamentals, 21 (1982) 438-447.

[82] R.M. Koros, E.J. Nowak, A diagnostic test of the kinetic regime in a packed bed reactor, Chemical Engineering Science, 22 (1967) 470.

[83] A. Verma, S.A. Bates, T. Anggara, C. Paolucci, A. Parekh, X. Du, K. Kamasamudram, A. Yezerets, J. Miller, T., W.N. Delgass, W.F. Schneider, F.H. Ribeiro, NO Oxidation: A Probe Reaction on Cu-SSZ-13, in preparation.

[84] D.J. Parrillo, A.T. Adamo, G.T. Kokotailo, R.J. Gorte, Amine adsorption in H-ZSM-5, Applied Catalysis, 67 (1990) 107-118.

[85] A.G. Palkhiwala, R.J. Gorte, Characterization of H-FER and H-TON using temperature-programmed desorption of alkylamines, Catalysis Letters, 57 (1999) 19-23.

[86] O. Kresnawahjuesa, R.J. Gorte, D.d. Oliveira, L.Y. Lau, A Simple, Inexpensive, and Reliable Method for Measuring Bronsted-acid Site Densities in Solid Acids, Catalysis Letters, 82 (2002) 155-160.

[87] S.M. Campbell, X.-Z. Jiang, R.F. Howe, Methanol to hydrocarbons: spectroscopic studies and the significance of extra-framework aluminium, Microporous and Mesoporous Materials, 29 (1999) 91-108.

[88] K. Kamasamudram, N.W. Currier, X. Chen, A. Yezerets, Overview of the practically important behaviors of zeolite-based urea-SCR catalysts, using compact experimental protocol, Catalysis Today, 151 (2010) 212-222.

[89] H. Sjövall, R.J. Blint, L. Olsson, Detailed Kinetic Modeling of NH3 and H2O Adsorption, and NH3 Oxidation over Cu-ZSM-5, The Journal of Physical Chemistry C, 113 (2009) 1393-1405.

[90] M. Iwamoto, H. Furukawa, Y. Mine, F. Uemura, S.I. Mikuriya, S. Kagawa, COPPER(II) ION-EXCHANGED ZSM-5 ZEOLITES AS HIGHLY-ACTIVE CATALYSTS FOR DIRECT AND CONTINUOUS DECOMPOSITION OF NITROGEN MONOXIDE, Journal of the Chemical Society-Chemical Communications, (1986) 1272-1273.

[91] W. Held, A. Konig, T. Richter, L. Puppe, SAE, (1990) 900496.

[92] M. Iwamoto, H. Hamada, REMOVAL OF NITROGEN MONOXIDE FROM EXHAUST GASES THROUGH NOVEL CATALYTIC PROCESSES, Catalysis Today, 10 (1991) 57-71.

[93] T. Tanabe, T. Iijima, A. Koiwai, J. Mizuno, K. Yokota, A. Isogai, ESR STUDY OF THE DEACTIVATION OF CU-ZSM-5 IN A NET OXIDIZING ATMOSPHERE, Applied Catalysis B-Environmental, 6 (1995) 145-153.

[94] J.Y. Yan, W.M.H. Sachtler, H.H. Kung, Effect of Cu loading and addition of modifiers on the stability of Cu/ZSM-5 in lean NOx reduction catalysis, Catalysis Today, 33 (1997) 279-290.

[95] R.A. Grinsted, H.W. Jen, C.N. Montreuil, M.J. Rokosz, M. Shelef, THE RELATION BETWEEN DEACTIVATION OF CUZSM-5 IN THE SELECTIVE REDUCTION OF NO AND DEALUMINATION OF THE ZEOLITE, Zeolites, 13 (1993) 602-606.

[96] J.H. Park, H.J. Park, J.H. Baik, I.S. Nam, C.H. Shin, J.H. Lee, B.K. Cho, S.H. Oh, Hydrothermal stability of CuZSM5 catalyst in reducing NO by NH3 for the urea selective catalytic reduction process, Journal of Catalysis, 240 (2006) 47-57.

[97] G. Centi, S. Perathoner, NATURE OF ACTIVE SPECIES IN COPPER-BASED CATALYSTS AND THEIR CHEMISTRY OF TRANSFORMATION OF NITROGEN-OXIDES, Applied Catalysis a-General, 132 (1995) 179-259.

[98] M.H. Groothaert, J.A. van Bokhoven, A.A. Battiston, B.M. Weckhuysen, R.A. Schoonheydt, Bis(mu-oxo)dicopper in Cu-ZSM-5 and its role in the decomposition of NO: A combined in situ XAFS, UV-Vis-Near-IR, and kinetic study, Journal of the American Chemical Society, 125 (2003) 7629-7640.

[99] J.-S. McEwen, T. Anggara, W.F. Schneider, V.F. Kispersky, J.T. Miller, W.N. Delgass, F.H. Ribeiro, Integrated operando X-ray absorption and DFT characterization of Cu–SSZ-13exchange sites during the selective catalytic reduction of NOx with NH3, Catalysis Today, 184 (2012) 129-144.

[100] I.J. Drake, Y.H. Zhang, D. Briggs, B. Lim, T. Chau, A.T. Bell, The local environment of Cu+ in Cu-Y zeolite and its relationship to the synthesis of dimethyl carbonate, Journal of Physical Chemistry B, 110 (2006) 11654-11664.

[101] D.E. Mears, DIAGNOSTIC CRITERIA FOR HEAT TRANSPORT LIMITATIONS IN FIXED BED REACTORS, Journal of Catalysis, 20 (1971) 127.

[102] S. Yagi, D. Kunii, STUDIES ON HEAT TRANSFER NEAR WALL SURFACE IN PACKED BEDS, Aiche Journal, 6 (1960) 97-104.

[103] J.-S. McEwen, T. Anggara, W.F. Schneider, V.F. Kispersky, J.T. Miller, W.N. Delgass, F.H. Ribeiro, Integrated operando X-ray absorption and DFT characterization of Cu–SSZ-13exchange sites during the selective catalytic reduction of NOx with NH3, Catalysis Today, (2012) 10.1016/j.cattod.2011.1011.1037.

[104] S.L. Shannon, J.G. Goodwin, CHARACTERIZATION OF CATALYTIC SURFACES BY ISOTOPIC-TRANSIENT KINETICS DURING STEADY-STATE REACTION, Chemical Reviews, 95 (1995) 677-695.

[105] S. Pansare, A. Sirijaruphan, J.G. Goodwin, Investigation of Reaction at the Site Level Using SSITKA, in: J.S.J. Hargreaves, S.D. Jackson, G. Webb (Eds.) Isotopes in Heterogenous Catalysis, Imperial College Press, London, UK, 2006.

[106] V.G. Komvokis, E.F. Iliopoulou, I.A. Vasalos, K.S. Triantafyllidis, C.L. Marshall, Development of optimized Cu-ZSM-5 deNOx catalytic materials both for HC-SCR applications and as FCC catalytic additives, Applied Catalysis a-General, 325 (2007) 345-352.

[107] M.K. Neylon, C.L. Marshall, A.J. Kropf, In situ EXAFS analysis of the temperature-programmed reduction of Cu-ZSM-5, Journal of the American Chemical Society, 124 (2002) 5457-5465.

[108] J. Despres, M. Koebel, O. Krocher, M. Elsener, A. Wokaun, Adsorption and desorption of NO and NO2 on Cu-ZSM-5, Microporous and Mesoporous Materials, 58 (2003) 175-183.

[109] P.S. Metkar, V. Balakotaiah, M.P. Harold, Experimental and Kinetic Modeling Study of NO Oxidation: Comparison of Fe and Cu-Zeolite Catalysts, Catalysis Today, http://dx.doi.org/10.1016/j.cattod.2011.11.032 (2012).

[110] K. Otto, M. Shelef, J.T. Kummer, STUDIES OF SURFACE REACTIONS OF NITRIC OXIDE BY N-15 ISOTOPE LABELING .1. REACTION BETWEEN NITRIC OXIDE AND AMMONIA OVER SUPPORTED PLATINUM AT 200-250 DEGREES, Journal of Physical Chemistry, 74 (1970) 2690.

[111] S.A. Bates, A. Verma, C. Paolucci, A. Parekh, T. Anggara, W.F. Schneider, J.T. Miller, W.N. Delgass, F.H. Ribeiro, Identification of the Active Cu Site in Standard Selective Catalytic Reduction with Ammonia on Cu-SSZ-13, in preparation.

[112] M. Schwidder, M. Santhosh Kumar, U. Bentrup, J. Pérez-Ramírez, A. Brückner, W. Grünert, The role of Brønsted acidity in the SCR of NO over Fe-MFI catalysts, Microporous and Mesoporous Materials, 111 (2008) 124-133.

[113] E.-Y. Choi, I.-S. Nam, Y.G. Kim, TPD Study of Mordenite-Type Zeolites for Selective Catalytic Reduction of NO by NH3, Journal of Catalysis, 161 (1996) 597-604.
[114] P.A. Jacobs, R. Von Ballmoos, Framework hydroxyl groups of H-ZSM-5 zeolites, The Journal of Physical Chemistry, 86 (1982) 3050-3052.

[115] R. Gounder, A.J. Jones, R.T. Carr, E. Iglesia, Solvation and acid strength effects on catalysis by faujasite zeolites, Journal of Catalysis, 286 (2012) 214-223.

[116] A.I. Biaglow, D.J. Parrillo, G.T. Kokotailo, R.J. Gorte, A Study of Dealuminated Faujasites, Journal of Catalysis, 148 (1994) 213-223.

[117] E.P. Parry, An infrared study of pyridine adsorbed on acidic solids. Characterization of surface acidity, Journal of Catalysis, 2 (1963) 371-379.

[118] W.E. Farneth, R.J. Gorte, Methods for Characterizing Zeolite Acidity, Chemical Reviews, 95 (1995) 615-635.

[119] R.J. Gorte, What do we know about the acidity of solid acids?, Catalysis Letters, 62 (1999) 1-13.

[120] D.J. Parrillo, D. Dolenec, R.J. Gorte, R.W. McCabe, Adsorption Studies on Cu-ZSM-5: Characterization of the Unique Properties of Ion-Exchanged Cu, Journal of Catalysis, 142 (1993) 708-718.

[121] D.J. Parrillo, J.P. Fortney, R.J. Gorte, A Comparison of Adsorption and Reaction Properties in Cu-ZSM-5 and Cu-Y, Journal of Catalysis, 153 (1995) 190-193.

[122] H. Kraus, M. Müller, R. Prins, A.P.M. Kentgens, Comments on the 27Al NMR Visibility of Aluminas, The Journal of Physical Chemistry B, 102 (1998) 3862-3865.

[123] Z. Luz, A.J. Vega, Interaction of H-rho zeolite with water and methanol studied by multinuclear NMR spectroscopy, The Journal of Physical Chemistry, 91 (1987) 374-382.

[124] A. Omegna, J.A. van Bokhoven, R. Prins, Flexible Aluminum Coordination in Alumino−Silicates. Structure of Zeolite H−USY and Amorphous Silica−Alumina, The Journal of Physical Chemistry B, 107 (2003) 8854-8860.

[125] A. Omegna, R. Prins, J.A. van Bokhoven, Effect of Temperature on Aluminum Coordination in Zeolites H−Y and H−USY and Amorphous Silica−Alumina: An in Situ Al K Edge XANES Study, The Journal of Physical Chemistry B, 109 (2005) 9280-9283.

[126] Handbook of Chemistry and Physics, in.

# APPENDICES

Appendix A Supplementary Material from Chapter 2

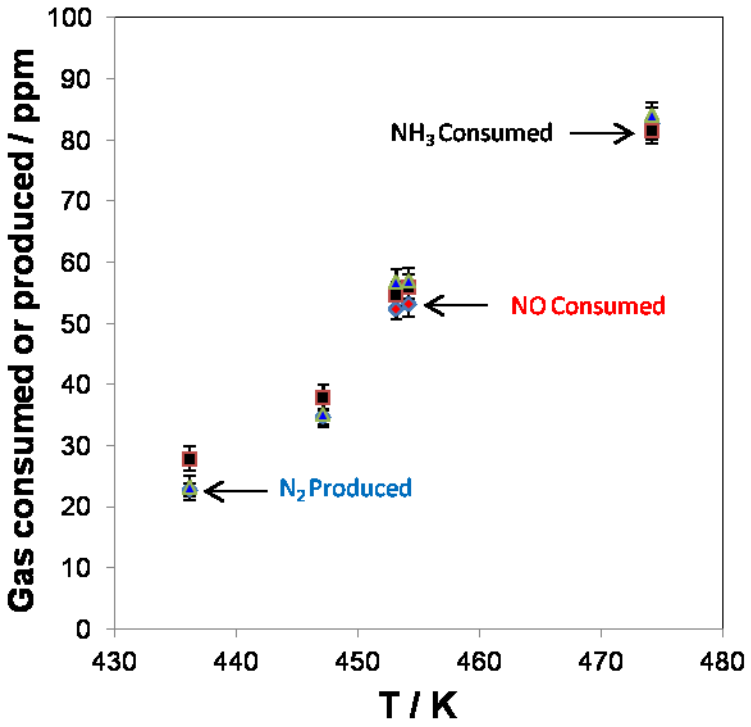


Figure A.1 Mass balance data collected for the Cu-SSZ-13 sample with Cu:Al=0.09 using gas chromatography to quantify N2 produced and gas phase FTIR to determine NO and $NH_3$ consumed in the standard SCR reaction. ±2 ppm reported for noise in FTIR signals for NO and $NH_3$, Standard deviation reported for $N_2$ produced.

Table A.1 Summary of kinetic data collected on each Cu-SSZ-13 sample.

| Cu Wt% | Si:Al Ratio* | Cu:Al Ratio* | $E_{a,app}$ / kJ $mol^{-1}$ | $A_o$ / $s^{-1}$ | Rate / $10^{-4}$ mol NO mol $Cu^{-1}$ $s^{-1}$ | Rate / $10^{-6}$ mol NO g $cat^{-1}$ $s^{-1}$ | NO Order | $NH_3$ Order | $O_2$ Order | Brønsted Acid Sites / $H^+$ $Al^{-1}$ |
|---|---|---|---|---|---|---|---|---|---|---|
| 0 | 4.5 | 0 | - | - | - | 0 | - | - | - | 0.65 |
| 0.31 | 4.3 | 0.02 | 42 | 1.35E2 | 32.4 | 0.2 | 0.7 | -0.2 | 0.5 | 0.45 |
| 0.82 | 4.3 | 0.04 | 68 | 4.29E5 | 132 | 1.7 | 0.7 | 0 | 0.5 | 0.60 |
| 1.74 | 4.5 | 0.09 | 64 | 9.74E4 | 74.3 | 2.0 | 0.8 | 0 | 0.3 | 0.42 |
| 3.04 | 4.5 | 0.16 | 70 | 8.5E5 | 61.9 | 3.0 | 0.8 | -0.1 | 0.3 | 0.32 |
| 3.75 | 4.5 | 0.2 | 71 | 4.24E5 | 66.0 | 3.8 | 0.9 | 0 | 0.3 | 0.30 |
| 6.39 | 4.5 | 0.35 | 71 | 2.16E5 | 29.4 | 3.0 | 0.7 | 0.1 | 0.2 | 0.24 |

*Atomic compositions and ratio determined by Atomic Absorption Spectroscopy.
Rated measured at 473 K. Associated Errors in measurements with 90% confidence interval: Ea,app = ±5 kJ $mol^{-1}$, Rate per gram catalysts = ± 0.2 x $10^{-6}$ mol NO $g^{-1}$ $s^{-1,}$ Rate per mole Cu = ± 0.2 x $10^{-4}$ mol NO mol $Cu^{-1}$ $s^{-1}$, Reaction orders = ±0.1, Brønsted Acid Sites = ±0.08 $H^+$:Al.

Additional Information on Brønsted Acid Site Count Quantification

For a complete summary of the Brønsted acid site count determinations on H-and Cu-SSZ-13, please refer to our previous study [41] (Chapter 4). Three $NH_3$ titration procedures and an n-propylamine decomposition [84-86] were compared for Brønsted acid site counts in H- and Cu-ZSM-5. The results showed that the $NH_3$ titrations were able to selectively titrate Brønsted acid sites as they gave equivalent results to the n-propylamine decomposition. Ammonia was determined to be a better titrant of Brønsted acid sites in H- and Cu-SSZ-13 than n-propylamine as it gave consistent total Brønsted acid site counts, while n-propylamine Brønsted acid site counts nearly four times lower because of mass transport limitations and spatial constraints of close proximity of acid sites. Figure A.2 below shows the result of the third $NH_3$ titration procedure on H- and Cu-SSZ-13 samples in this study. The samples were treated with ~500 ppm $NH_3$ in UHP-He at 433 K with a total flowrate of 350 ml $min^{-1}$ for two hours. At the end of the

saturation, the $NH_3$ signal was constant in the FTIR (MKS Multi-gas 2030 Gas Analyzer). Following this, the sample was flushed in UHP-He for eight hours at 433 K with a total flowrate of 350 ml $min^{-1}$. A TPD was performed on ~30 mg of sample in an Micrimeritics Autochem II unit with 50 sccm UHP-He flowing and 10 K $min^{-1}$ temperature ramp up to 873 K. One feature resulted in all the experiments corresponding to the Brønsted acid sites.

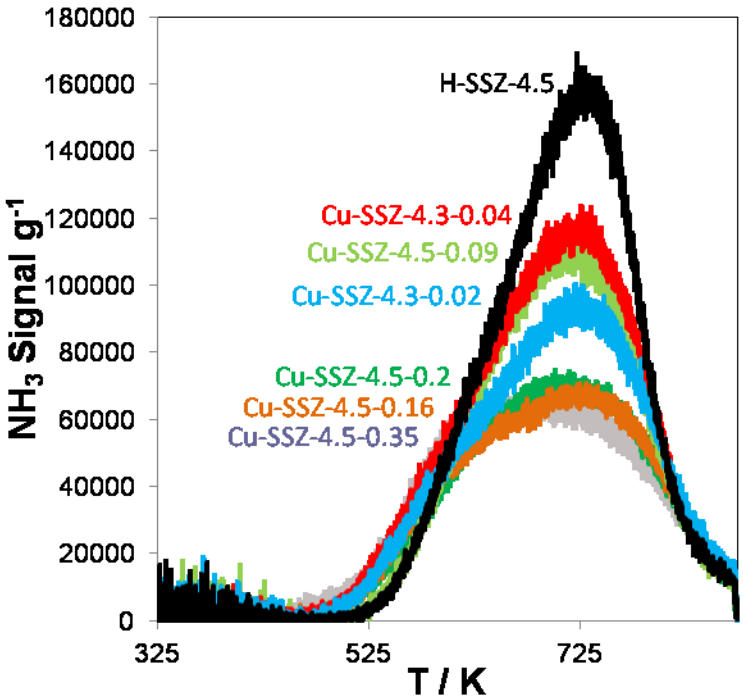


Figure A.2 $NH_3$ TPD experiments over Cu-SSZ-13 samples ranging from Cu:Al = 0 to 0.35 using $NH_3$ titration procedure #3 from our previous work [41].

Effect of $CO_2$ on kinetics for Cu-SSZ-13

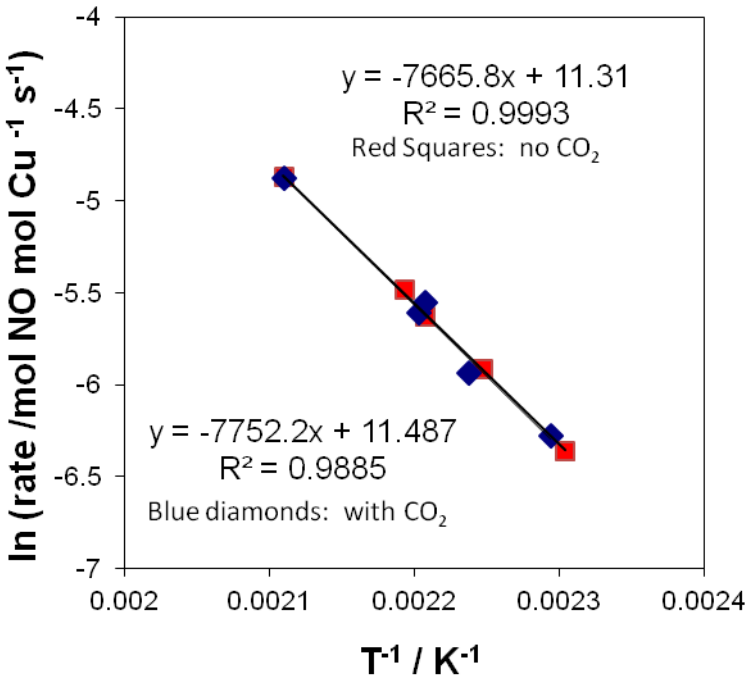


Figure A.3 Activation energy plot for a Cu-SSZ-13 (Cu:Al = 0.09) under standard SCR 320 ppm NO, 320ppm $NH_3$, 7% $H_2O$, 10% $O_2$, balance He with (blue diamonds) and without (red squares) 8% CO2 in the feed. Data were collected over 433-473 K at a total flow of ~1.5L min.-

Table A 2 Measured activation energy, pre-factor and rate for a Cu-SSZ-13 sample (Cu:Al = 0.09) under standard SCR gas conditions with and without $CO_2$ in the feed.

| Sample | Ea / kJ $mol^{-1}$ | $A_o$ / $10^4$ $s^{-1}$ | Rate (473 K) / $10^{-3}$ mol NO mol $Cu^{-1}$ $s^{-1}$ |
|---|---|---|---|
| Standard SCR with $CO_2$ | 64 | 9.74 | 7.43 |
| Standard SCR without $CO_2$ | 64 | 8.16 | 7.47 |

90% confidence interval for Ea and rate per mole Cu are ±5 kJ $mol^{-1}$ and ±0.2 x $10^{-4}$ mol NO mol $Cu^{-1}s^{-1}$.

Additional information on the $NH_3$ Quantification Experiments

Scheme A.1 shows the three individual $NH_3$ species quantified. The first is a weakly bound $NH_3$ species which is found during the same $NH_3$ cutoff experiment in which the reactive $NH_3$ is quantified. The $NH_3$ concentration was monitored in the FTIR during the $NH_3$ cutoff.

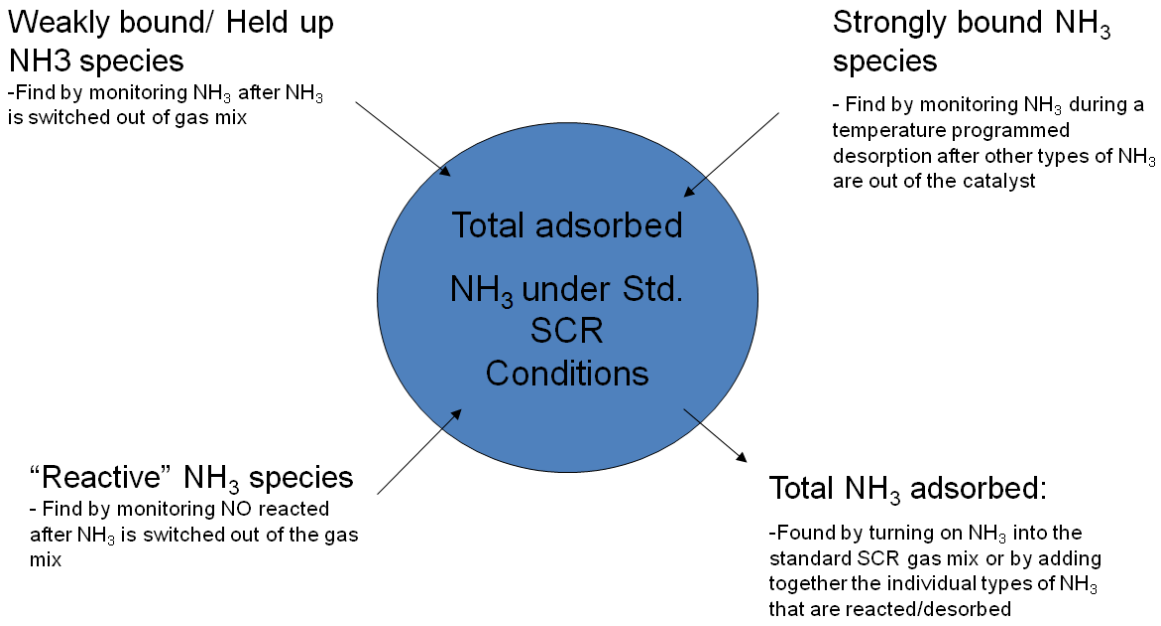


Scheme A.1 The overall $NH_3$ quantification flow diagram. The sum of weakly bound $NH_3$, reactive $NH_3$, and strongly bound $NH_3$ corresponded to the total adsorbed $NH_3$ present under standard SCR reaction conditions at 433 K. The total adsorbed $NH_3$ could also be determined separately as described in the scheme.

Figure A.4 shows an example for the Cu:Al = 0.09 sample. In the experiment shown, the $NH_3$ is removed from the gas phase within 5 – 7 minutes. Compared to the $CO_2$ tracer, there is a quantity of $NH_3$ that leaves when the $NH_3$ is removed from the gas phase. This may be a physisorbed species or $NH_3$ sticking in the lines of the system. At time zero,

Figure A.4 shows the $NH_3$ starting at a lower concentration. At this point in time, the valve had already been switched which caused a pressure spike in the IR; therefore, the real initial concentration was close to 300 ppm where the $CO_2$ was scaled.

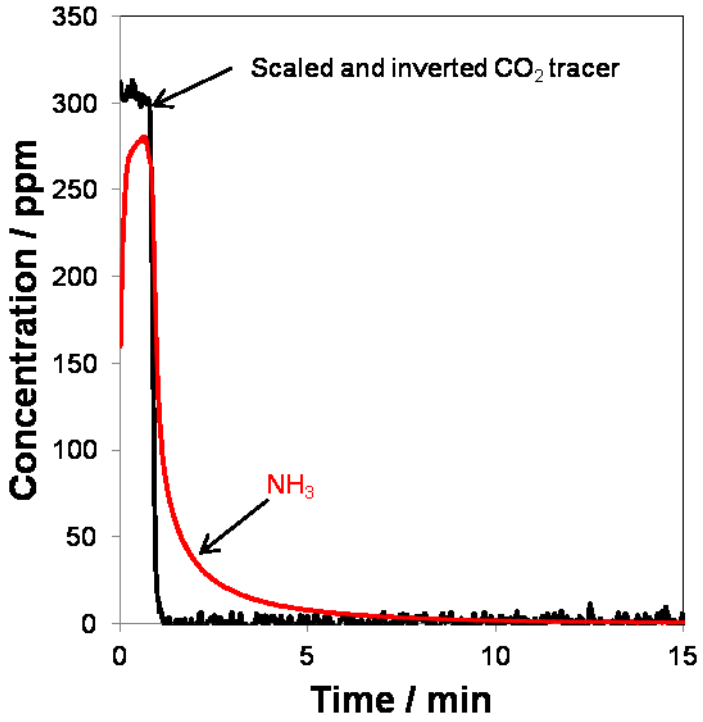


Figure A.4 $NH_3$ concentration over time as $NH_3$ was removed from the gas mixture and replaced with an equal flowrate of $CO_2$ for the Cu:Al = 0.09 Cu-SSZ-13 sample. The CO2 has been scaled and inverted to show the initial NH3 concentration as a comparison to see the lag in $NH_3$. Before $NH_3$ was removed, standard SCR conditions were present with 320 ppm NO, 320 ppm $NH_3$, 10% $O_2$, 6% $H_2O$, 8% $CO_2$, and balance Helium at 433 K. Total flowrate is 1.5 L $min^{-1}$.

Figure A.5 shows the weakly bound $NH_3$ determined over several Cu-SSZ-13 samples in this study. In general, a positive trend was observed as the Cu loading increased, indicating this weakly bound species may be related to an $NH_3$ associated with Cu; however, $NH_3$ from elsewhere cannot be ruled out.

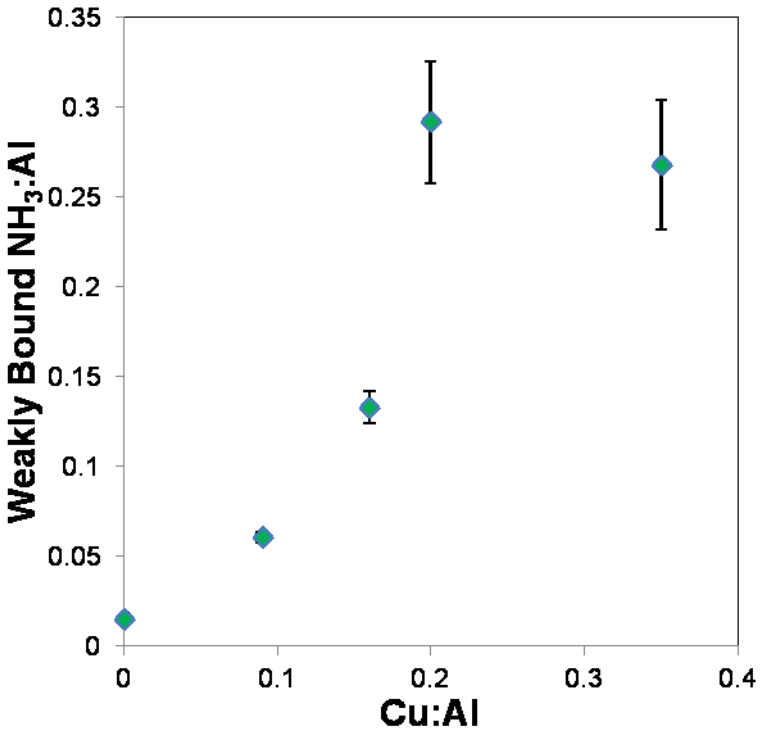


Figure A.5 The amount of weakly bound $NH_3$ determined in $NH_3$ cutoff experiments from standard SCR over different Cu:Al samples. Before $NH_3$ was removed, standard SCR conditions were present with 320 ppm NO, 320 ppm $NH_3$, 10% $O_2$, 6% $H_2O$, 8% $CO_2$, and balance Helium at 433 K. 90% confidence interval reported.

Figures 2.3 and A.6 show the data collected for the reactive $NH_3$ species, which was discussed in the main text of the study. Following that, Figures 2.3 and A.7-A.8 go through the TPD performed after the $NH_3$ cutoff experiment and flushing of the system.

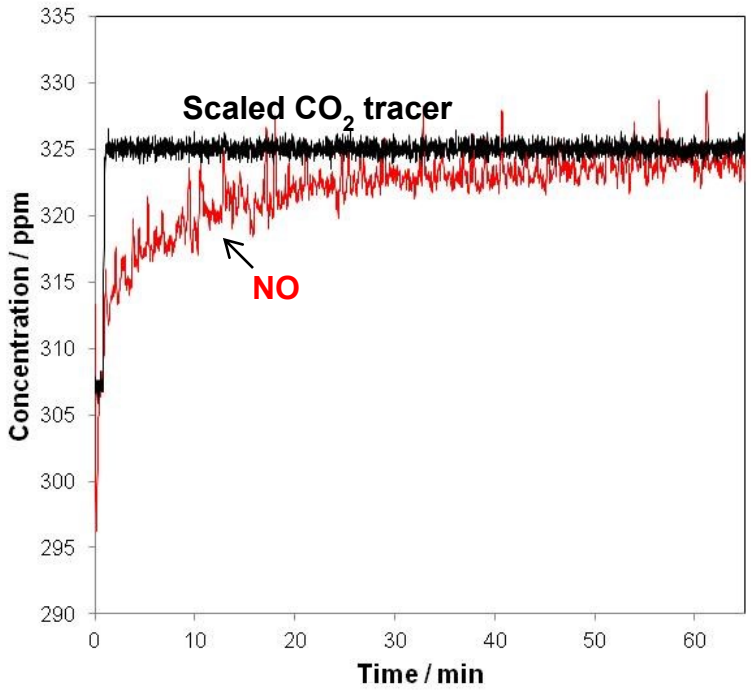


Figure A.6 Display of NO concentration over time as $NH_3$ was removed from the gas mixture and replaced with an equal flowrate of $CO_2$ for the Cu:Al = 0.09 Cu-SSZ-13 sample. The $CO_2$ is used as a tracer. Before $NH_3$ was removed, standard SCR conditions were present with 320 ppm NO, 320 ppm $NH_3$, 10% $O_2$, 6% $H_2O$, 8% $CO_2$, and balance Helium at 433 K. Total flowrate is 1.5 L $min^{-1}$.

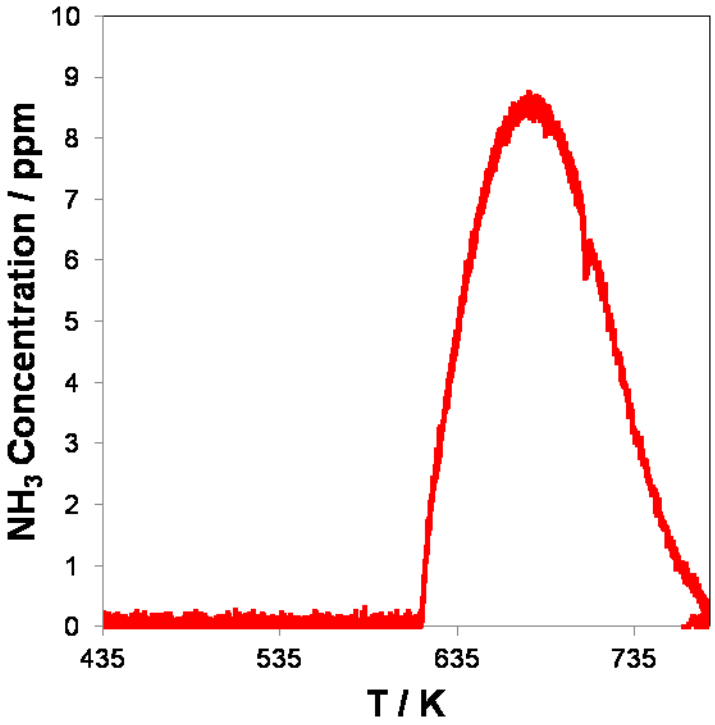


Figure A.7 $NH_3$ TPD following the $NH_3$ cutoff experiment from steady state standard SCR and a system flush for ~ 1hr with UHP helium for the Cu-SSZ-13 sample with Cu:Al = 0.09. The $NH_3$ observed has been called "strongly bound." The temperature ramp was 5 K min-1 starting from 433 K.

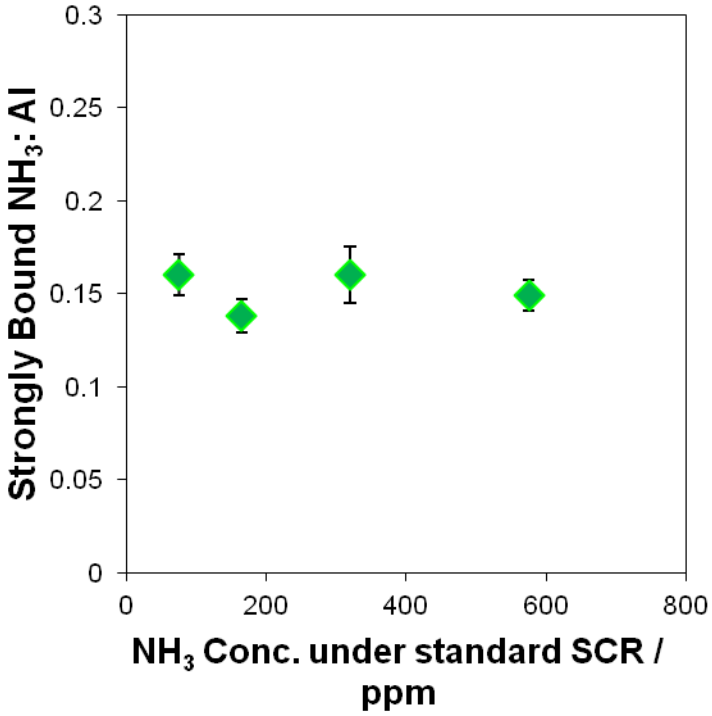


Figure A.8 The quantity of strongly bound $NH_3$ after different concentrations of $NH_3$ were used under steady state standard SCR conditions at 433 K for the Cu:Al = 0.09 Cu-SSZ-13 sample. $NH_3$ was then removed in a cutoff experiment and flushed for ~ 1hr in UHP He before the TPD was performed. 90% confidence interval reported.

The final step in the process was to quantify the total amount of $NH_3$ present under steady state standard SCR conditions, which can be used to compare to the sum of the three individual $NH_3$ species. This was performed starting with an $NH_3$-free catalyst surface with 320 ppm NO, 10% $O_2$, 6% $H_2O$, and an equal flow of $CO_2$ corresponding to the same flow of $NH_3$ which was removed in the earlier $NH_3$ cutoff experiment at 433 K. Ammonia was switched into the gas mixture and $CO_2$ removed. The result was an $NH_3$ adsorption curve shown in Figure A.9 which approached steady state standard SCR after ~ 30 minutes. The resulting area between the $NH_3$ and the scaled and inverted $CO_2$ tracer was integrated for the total $NH_3$ under standard SCR at 433 K. The sum of the individual

$NH_3$ species was then compared to the total $NH_3$ adsorbed under standard SCR conditions at 433 K. The results can be seen in Figure A.10, where a good agreement between all samples was observed except for the Cu:Al = 0.2 sample, which had significantly more $NH_3$ in the $NH_3$ adsorption experiment and was not characteristic of any of the other samples tested. One explanation of this was that in this particular set of adsorption experiments, some water had accumulated somewhere in the lines which was capturing some extra $NH_3$ and artificially inflating the value. Every time a new sample was loaded a significant amount of heating tape was used in the inlet and outlet of the reactor. If a cool spot was present, this was a plausible explanation.

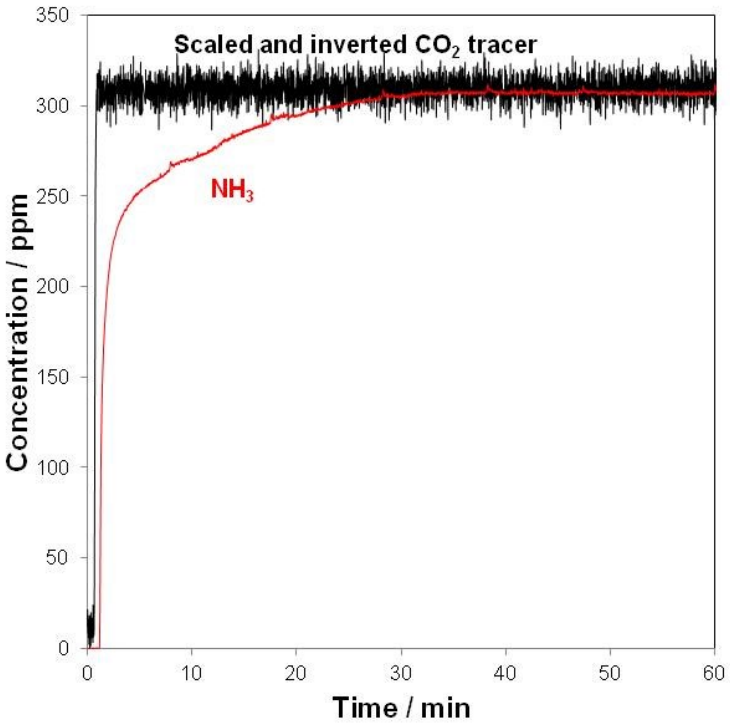


Figure A.9 Display of $NH_3$ concentration over time as $NH_3$ was added to the gas mixture and $CO_2$ removed for the Cu:Al = 0.09 Cu-SSZ-13 sample. The $CO_2$ has been scaled and inverted to show the initial $NH_3$ concentration as a comparison to see the lag in $NH_3$. Before $NH_3$ was added, an $NH_3$ free surface was obtained via TPD and standard SCR conditions minus $NH_3$ were present with 320 ppm NO, 10% $O_2$, 6% $H_2O$, 8% $CO_2$, and balance Helium at 433 K.

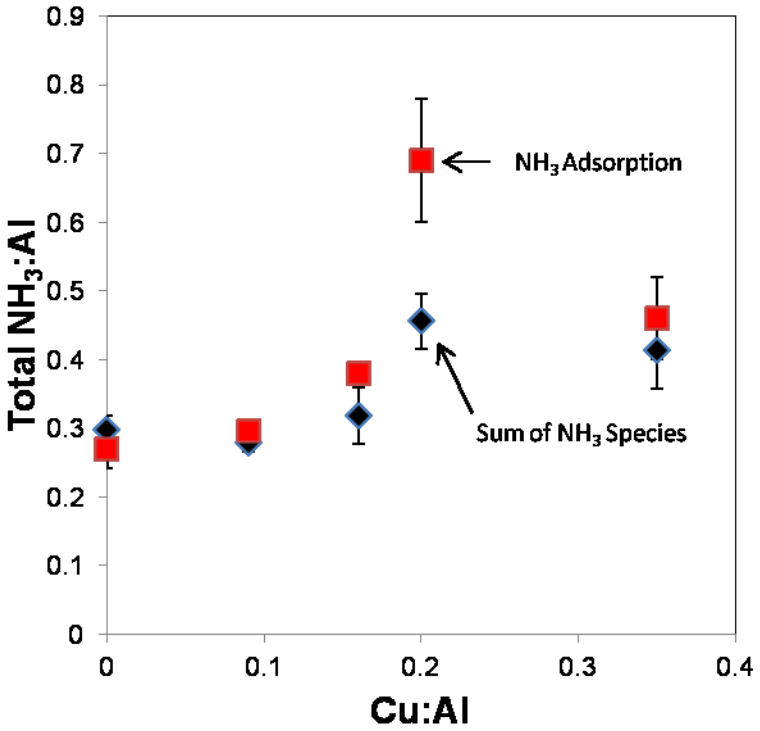


Figure A.10 Comparison of the total $NH_3$ present under standard SCR conditions at 433 K using two different methods. The sum of the individual $NH_3$ species is shown in black while the $NH_3$ from an adsorption experiment is shown in red. 90% confidence intervals are included.

UV-Vis-NIR Quantification of d-d transition for hydrated Cu(II)

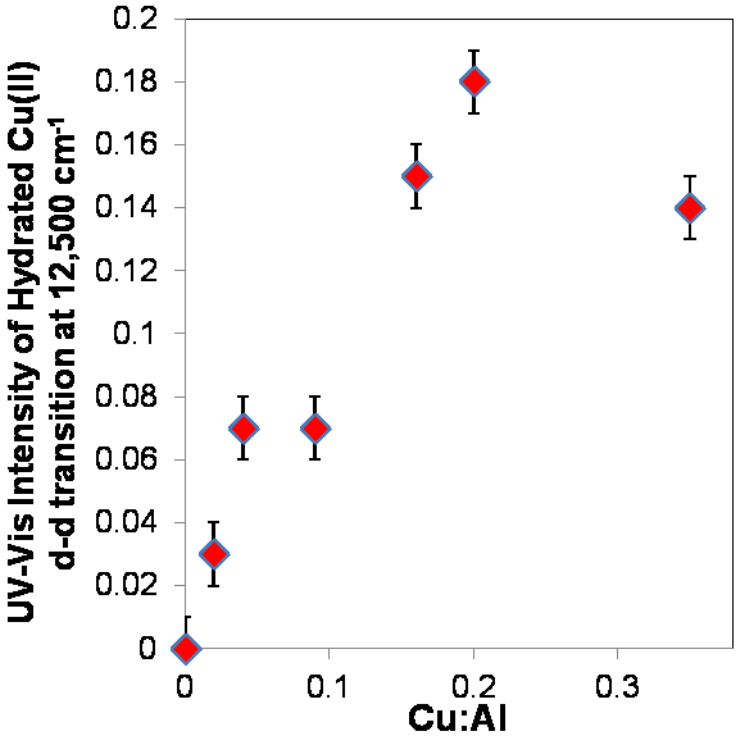


Figure A.11 UV-Vis-NIR intensity of the d-d transition for hydrated Cu(II) at 12,500 cm-1 in Kubelka-Munk units under ambient conditions. Cu:Al ranges from 0 to 0.35. 90% confidence intervals are included.

Additional XANES and EXAFS Spectra and analysis.

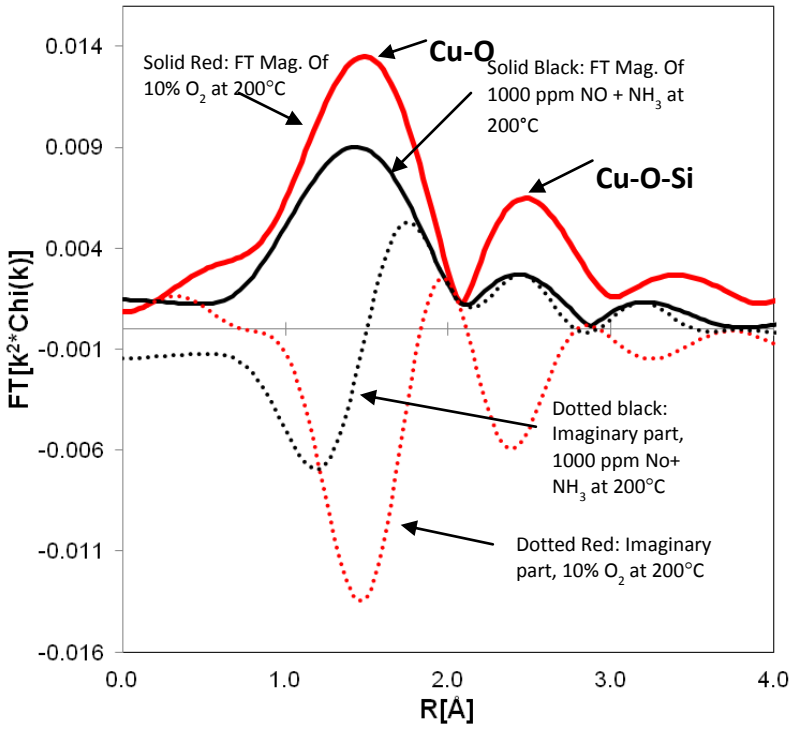


Figure A.12 EXAFS spectra for the isolated Cu(II) (red) and isolated Cu(I) (black) references. Solid lines indicate the Fourier transform magnitude. Dotted lines indicate the imaginary contribution.

Table A.3 EXAFS fit paremeters for isolated Cu(I) and isolated Cu(II).

| 0.31% Cu EXAFS of Cu-SSZ-13 | | | | | | | | |
|---|---|---|---|---|---|---|---|---|
| Sample | Treatment | XANES | | Absorber -Scatter | N | R / Å | $\Delta\sigma^2$ (x $10^3$) | $E_o$ / eV |
| | | Fraction Cu(II) | Fraction Cu(I) | | | | | |
| Cu(II) | RT, ambient | 1.0 | - | Cu-O | 3.9 | 1.96 | 2.0 | -8.5 |
| Cu(II) | 10% $O_2$, 473 K | 1.0 | - | Cu-O | 4.0 | 1.96 | 4.0 | -7.5 |
| Cu(I) | 1000 ppm $NH_3$ + 1000 ppm NO, 473 K | - | 1.0 | Cu-O | 2.2 | 1.85 | 4.0 | -5.1 |

Table A.4 Linear combination XANES fits for all Cu-SSZ-13 samples in air at room temperature included in this study.

| Sample | Cu:Al | Treatment | Cu(II)O | Isolated Cu (I) | Isolated Cu(II) | Hydrated Cu(II) |
|---|---|---|---|---|---|---|
| Cu-SSZ-13 | 0.02 | in air, room temperature | 4 | 0 | 0 | 96 |
| Cu-SSZ-13 | 0.04 | in air, room temperature | 0 | 0 | 0 | 100 |
| Cu-SSZ-13 | 0.08 | in air, room temperature | 0 | 0 | 0 | 100 |
| Cu-SSZ-13 | 0.16 | in air, room temperature | 0 | 0 | 0 | 100 |
| Cu-SSZ-13 | 0.2 | in air, room temperature | 0 | 0 | 0 | 100 |
| Cu-SSZ-13 | 0.35 | in air, room temperature | 25 | 0 | 0 | 75 |

±5% error associated with linear combination XANES fits

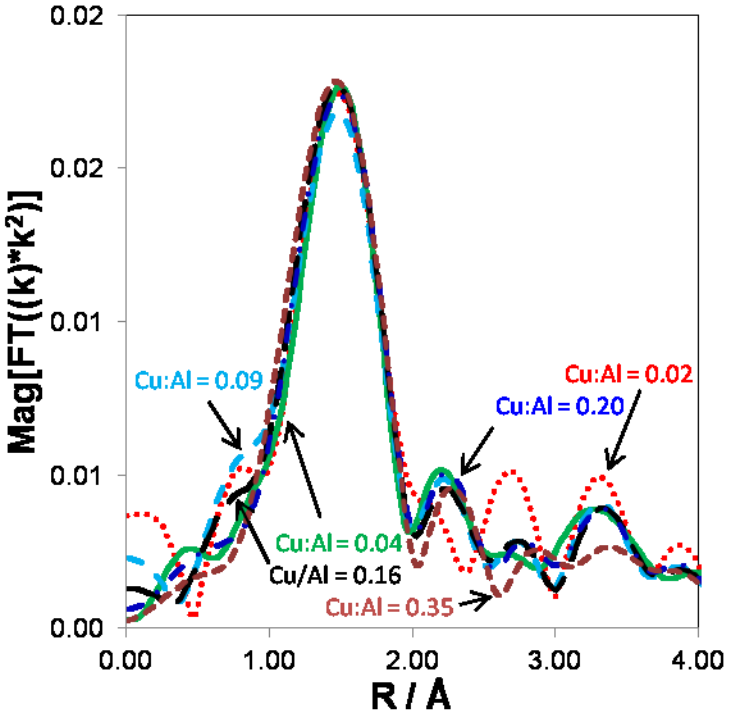


Figure A.13 EXAFS spectra all Cu-SSZ-13 samples in this study under ambient conditions (in air at room temperature).

Table A 5 EXAFS fit paremeters for all Cu-SSZ-13 samples in this study in air at room temperature.

| Sample | Cu:Al | Treatment | Absorber - Scatter | CN | R / Å | $\Delta\sigma^2$ / $10^{-3}$ Å | $E_o$ / eV |
|---|---|---|---|---|---|---|---|
| Cu-SSZ-13 | 0.02 | in air, room temperature | Cu-O | 4.0 | 1.94 | 2 | -9.5 |
| Cu-SSZ-13 | 0.04 | in air, room temperature | Cu-O | 3.9 | 1.94 | 2 | -10.3 |
| Cu-SSZ-13 | 0.08 | in air, room temperature | Cu-O | 3.9 | 1.94 | 2 | -10.4 |
| Cu-SSZ-13 | 0.16 | in air, room temperature | Cu-O | 4.1 | 1.94 | 2 | -10.2 |
| Cu-SSZ-13 | 0.2 | in air, room temperature | Cu-O | 4.1 | 1.94 | 2 | -10.6 |
| Cu-SSZ-13 | 0.35 | in air, room temperature | Cu-O | 4.3 | 1.94 | 2 | -11.2 |

Table A.6 Linear combination XANES fits for Cu-SSZ-13 samples under standard SCR reaction conditions. Standard SCR conditions used were 320 ppm NO, 320 ppm $NH_3$, 10% $O_2$, 8% $CO_2$, 6% $H_2O$, and balance Helium at 453 K.

| Cu:Al | Treatment | %Cu(II)O | % Isolated Cu(I) | % Isolated Cu(II) | % Hydrated Cu(II) | SCR Rate / $10^{-4}$ mol NO mol $Cu^{-1}$ $s^{-1}$ at 453 K |
|---|---|---|---|---|---|---|
| 0.09 | standard SCR, 453 K, operando XAS | 0 | 37 | 57 | 5 | 43.0 |
| 0.09 | standard SCR, 453 K, lab scale PFR | - | - | - | - | 43.2 |
| 0.16 | standard SCR, 453 K, operando XAS | 0 | 26 | 71 | 3 | 46.6 |
| 0.16 | standard SCR, 453 K, lab scale PFR | - | - | - | - | 37.4 |

±5% error associated with linear combination XANES fits.

The pre-edge feature we have identified as isolated Cu(I) at 8983 eV in *operando* XAS has also been attributed to $NH_3$ adsorbed on Cu(II) at low temperature by Deka et al [6]. The Cu-tetraamine XANES spectrum (Figure A14) contains a dip in white line intensity with two features appearing at 8994 eV and 8998 eV, which when compared to the isolated Cu(I) reference and samples under standard SCR conditions in Figure 3.6 cannot be ruled out as a possible contributor to the shape of the XANES spectra. It would not be able to give an intense pre-edge feature at 8983 eV, which was observed in this study for the isolated Cu(I) reference. On this basis and because the linear combination XANES did not give any reasonable fits, it was not included as a reference.

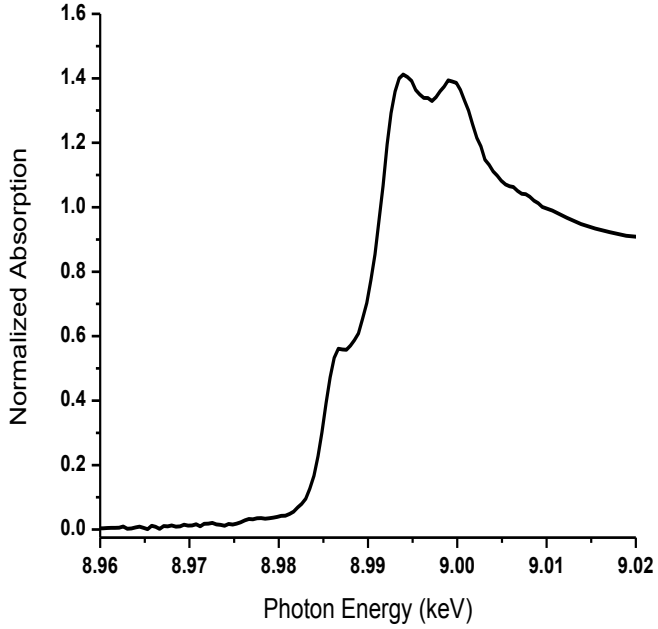


Figure A.14 XANES spectrum of the Cu(II)-tetraamine reference compound .

Details of stability of isolated Cu(II) cation

The optimized structure for relative stability of isolated Cu(II) in the SSZ-13 zeolite structure is shown in Figure below.

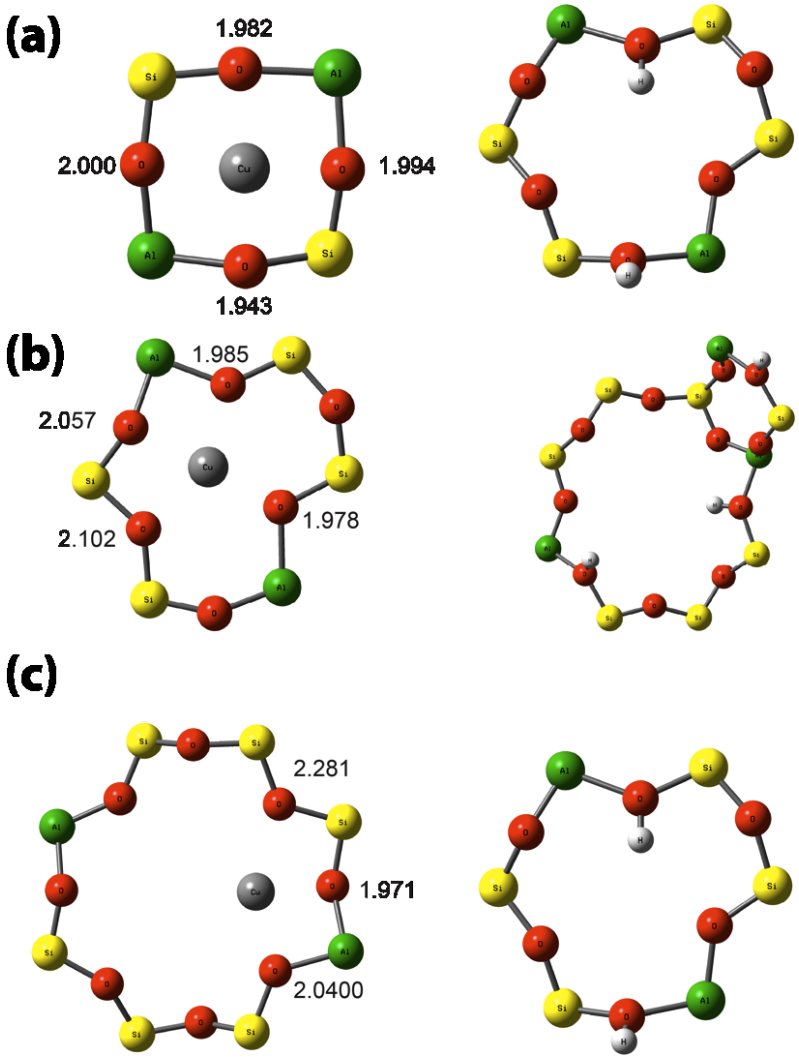


Figure A.15 Optimized structure of isolated Cu(II). (a) Isolated Cu(II) located in the 4-membered ring of SSZ-13 and two hydrogen attached to the oxygen in the 6-membered ring structure of the zeolite. (b) Isolated Cu(II) located in the 6-membered ring of SSZ-13 and two hydrogen attached to the oxygen in the 8-membered ring structure of the zeolite. (c) Isolated Cu(II) located in the 8-membered ring of SSZ-13 and two hydrogen attached to the oxygen in the 6-membered ring structure of the zeolite.

Exchange energy calculation for isolated Cu(II) in the 4-membered ring:

| | | | |
|---|---|---|---|
| $Z_4H_4 + Cu(s)$ | $\rightarrow Z_4H_2Cu + H_2$ (g) | $\Delta E$= 3.31 eV | (DFT) |
| $Cu(II) + 2e^-$ | $\rightarrow Cu(s)$ | $\Delta G$= -nFE = -2*1*0.34 eV | [126] |
| $H_2$ (g) | $\rightarrow 2H^+ + 2e^-$ | $\Delta G$= 0 eV | [126] |
| **$Z_4H_4 + Cu^{2+}$** | **$\rightarrow Z_4H_2Cu + 2\ H^+$** | **$\Delta E$= 2.63 eV** | |

Exchange energy calculation for isolated Cu(II) in the 6-membered ring:

| | | | |
|---|---|---|---|
| $Z_4H_4 + Cu(s)$ | $\rightarrow Z_4H_2Cu + H_2$ (g) | $\Delta E$= 2.18 eV | (DFT) |
| $Cu(II) + 2e^-$ | $\rightarrow Cu(s)$ | $\Delta G$= -0.68 eV | [126] |
| $H_2$ (g) | $\rightarrow 2H^+ + 2e^-$ | $\Delta G$= 0 eV | [126] |
| **$Z_4H_4 + Cu^{2+}$** | **$\rightarrow Z_4H_2Cu + 2\ H^+$** | **$\Delta E$= 1.50 eV** | |

Exchange energy calculation for isolated Cu(II) in the 8-membered ring:

| | | | |
|---|---|---|---|
| $Z_4H_4 + Cu(s)$ | $\rightarrow Z_4H_2Cu + H_2$ (g) | $\Delta E$= 3.68 eV | (DFT) |
| $Cu(II) + 2e^-$ | $\rightarrow Cu(s)$ | $\Delta E$= -0.68 eV | [126] |
| $H_2$ (g) | $\rightarrow 2H^+ + 2e^-$ | $\Delta E$= 0 eV | [126] |
| **$Z_4H_4 + Cu^{2+}$** | **$\rightarrow Z_4H_2Cu + 2\ H^+$** | **$\Delta E$= 3.00 eV** | |

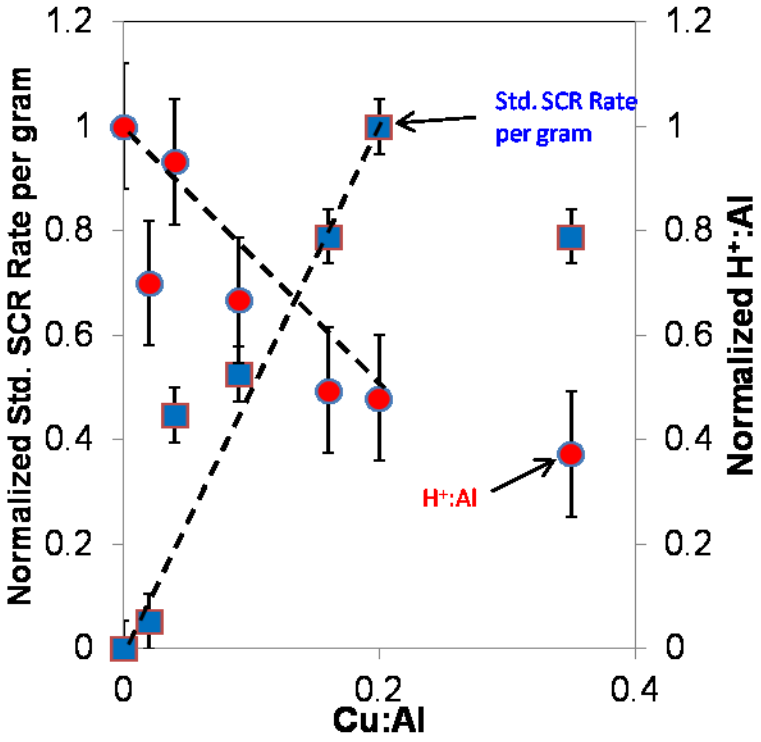


Figure A.16 Normalized Brønsted acid site count and normalized standard SCR rate per gram shown with respect to the Cu:Al in several Cu-SSZ-13 samples. 90% confidence intervals reported.

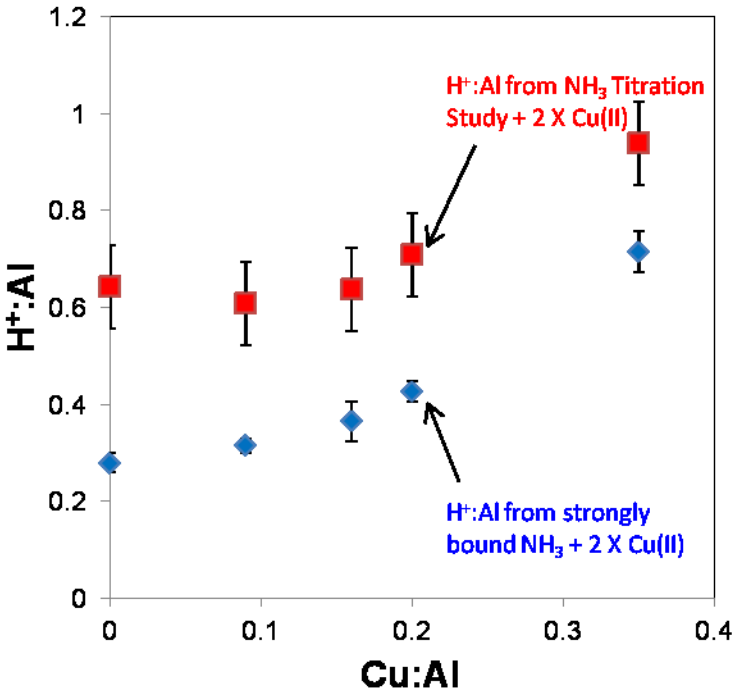


Figure A.17 The total number of Brønsted acid sites counted in a previous study using numbers from the $NH_3$ titration [41] and the strongly bound $NH_3$ in this study. Two Brønsted acid sites are added for each Cu(II) exchanged in the sample. 90% confidence intervals are reported.

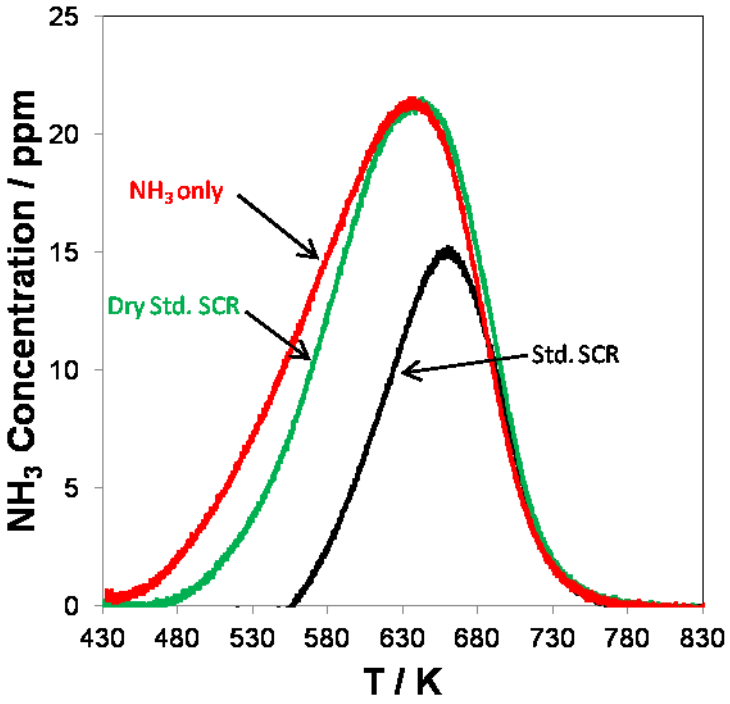


Figure A.18 TPDs following an $NH_3$ cutoff experiments at 433 K and system flush at 433 K. Conditions before the $NH_3$ cutoff are given in the labels.

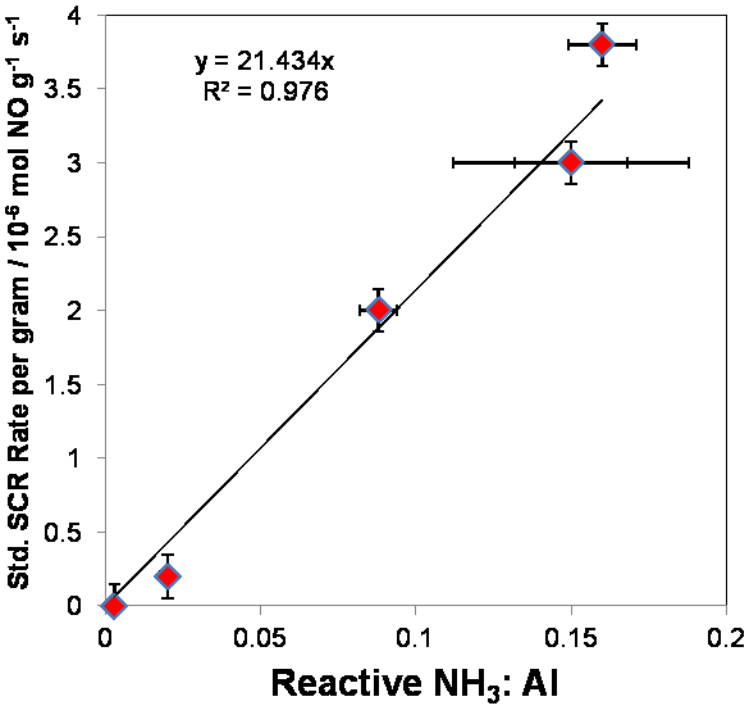


Figure A.19 Standard SCR rate per gram shown against the amount of reactive $NH_3$ per total Al in several Cu-SSZ-13 samples. 90% confidence intervals are reported.

# Appendix B Supplementary Material from Chapter 3

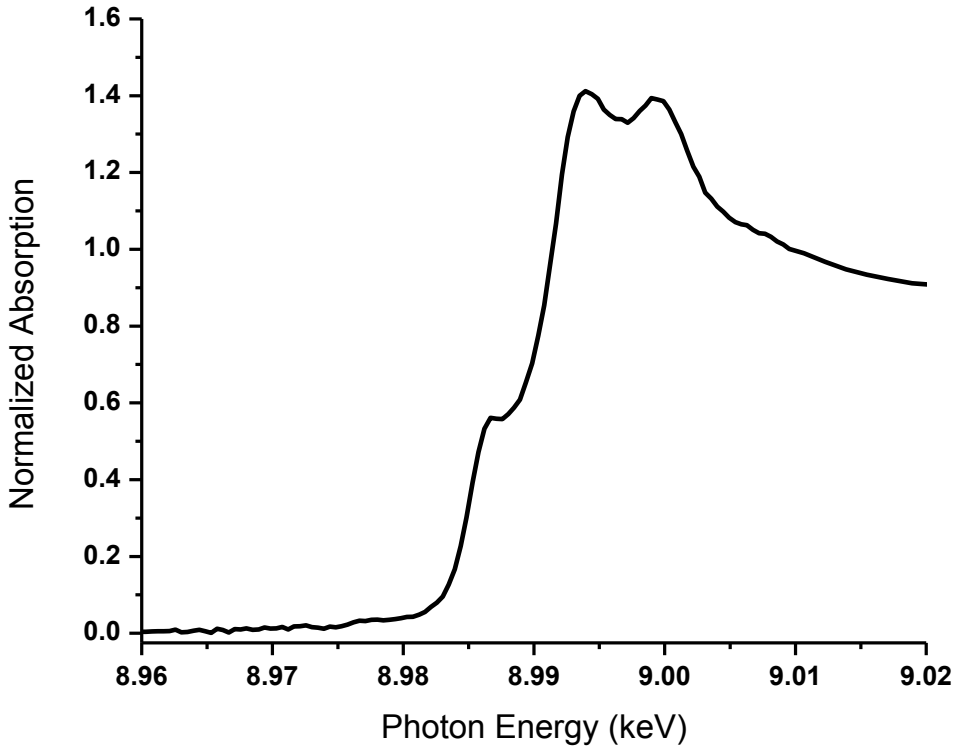


Figure B.1 XANES spectrum of the Cu(II)-tetraamine reference compound.

Effect of $CO_2$ on kinetics for Cu-SSZ-13

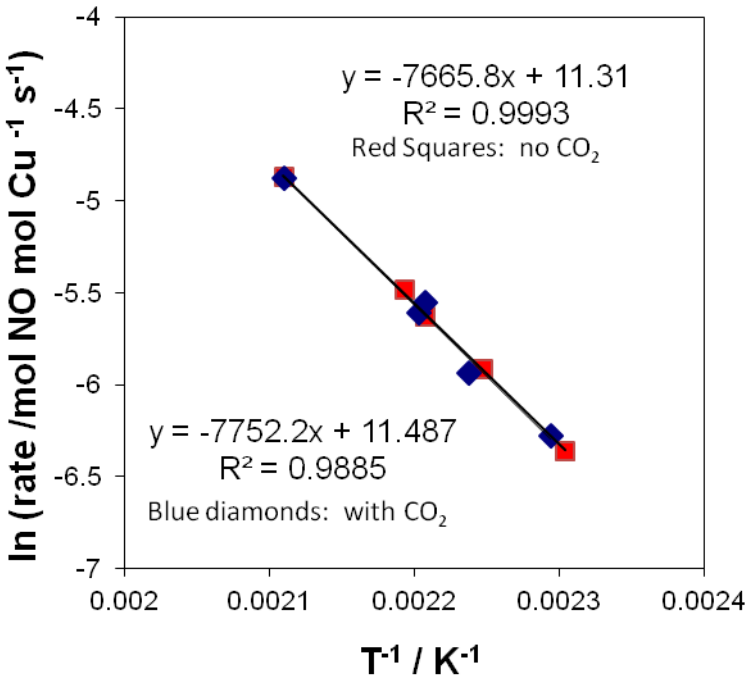


Figure B.2 Activation energy plot for a 1.7 wt% Cu-SSZ-13 (Cu:Al = 0.09) under standard SCR 320 ppm NO, 320ppm $NH_3$, 7% $H_2O$, 10% $O_2$, balance He with (blue diamonds) and without (red squares) 8% $CO_2$ in the feed. Data were collected over 433-473 K at a total flow of ~1.5L min.

Table B.1 Measured activation energy, pre-factor and rate for a 1.7 wt% Cu-SSZ-13 sample (Cu:Al = 0.09) under standard SCR gas conditions with and without $CO_2$ in the feed.

| Sample | Ea / kJ $mol^{-1}$ | $A_o$ / $10^4$ $s^{-1}$ | Rate (473 K) / $10^{-3}$ mol NO mol $Cu^{-1}$ $s^{-1}$ |
|---|---|---|---|
| Standard SCR with $CO_2$ | 64 | 9.74 | 7.43 |
| Standard SCR without $CO_2$ | 64 | 8.16 | 7.47 |

$NH_3$ Only Experiment

To investigate the effect of $NH_3$ alone on the Cu oxidation state, we flowed 300 ppm $NH_3$ over a fully oxidized catalyst. There was some small growth of the ~8983 eV edge feature but after 14 minutes the growth ceased. The size of the edge feature indicated reduction of about 5% of the total Cu to Cu(I). Nevertheless, the $NH_3$ was incapable of generating the 29% contribution from Cu(I) seen under steady state standard SCR. As the most reducing component in the reaction mixture, if $NH_3$ is incapable of generating the same amount of Cu(I) as the standard SCR reaction, then the Cu(I) must have appeared due to some other mechanism.

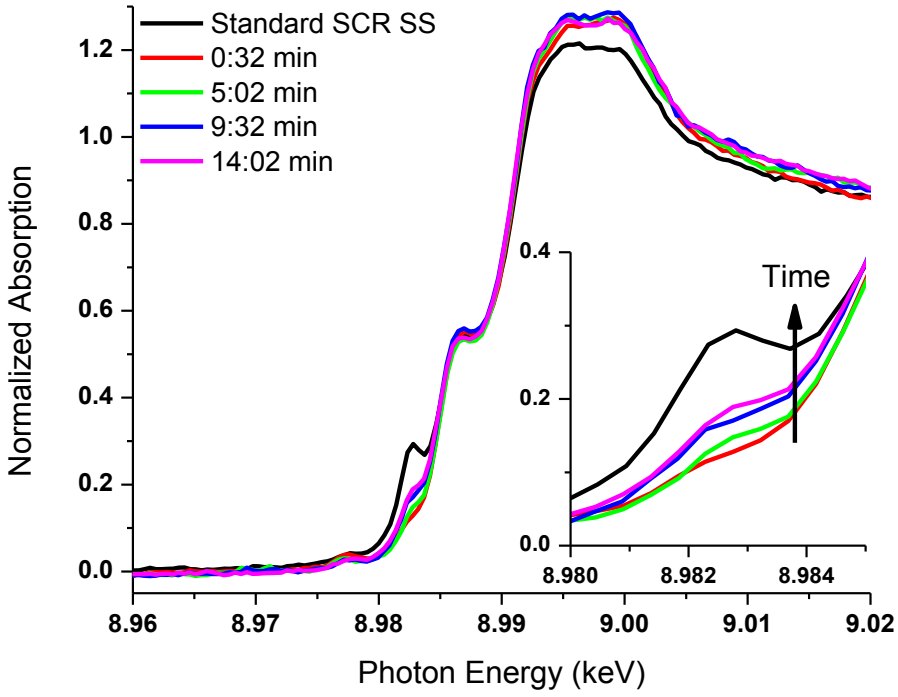


Figure B.3 Time resolved XAS of the 2.1 wt.% Cu-SSZ-13 catalyst flowing only 300 ppm $NH_3$ and balance He at 300 sccm. The catalyst was first pretreated in oxygen at 194 ˚C. Inset zooms in on the edge feature at ~9.9828 keV, the identifying feature of Cu(I) species. To clearly present the data, spectra are not linear in time resolution.

$NH_3$ Growth Curve in the NO Addition Experiment

The $NH_3$ concentration curve for this experiment could not be measured because the $NH_3$ concentration did not reach a steady state. It is unclear whether this was due to drift by the $NH_3$ MFC or some other phenomenon. As discussed in the text, the change in the concentration of $NH_3$ does not have an effect on the overall conclusions or result of the experiment.

Calculating the fraction of Cu species from Coordination Numbers in EXAFS

EXAFS fitting of this highly reduced sample determined the Cu to have a coordination number (CN) of 2.5 and Cu-O interatomic distance of 1.88 Å with a Debye-Waller Factor (DWF) of 0.005. Cu(II) and Cu(I) are well known to prefer 4-fold and 2-fold coordination, respectively. The bulk sampling performed by XAS allows us to extract the individual Cu fractions by linear combination of the coordination numbers. Thus we can calculate that the fraction of Cu(I) $x$ is given by:

$$2.5 = 2x + 4(1 - x)$$

Where 2.5 is the CN measured by EXAFS and the factors 2 and 4 represent the CN of each fraction of Cu(I) and Cu(II) respectively. The solution to the equation is $x = 0.75$ or that 75% of Cu was composed of Cu(I).

References used for Linear Combination XANES Fits within this study

Three references were utilized. The first was a hydrated Cu(II) species, $[Cu(H_2O)_6]^{2+}$, which we have observed to be the primary state of Cu in low loadings at room temperature in air, thus it was reasonable to include it in the references. The isolated Cu(II) and isolated Cu(I) were obtained with a 0.31 wt% Cu-SSZ-13 sample, which was the lowest we were able to achieve in the lab. The assumption for this sample was that it contained only the isolated Cu species at the very lowest loadings. The isolated Cu(II) reference was obtained *in situ* with 10% $O_2$/UHP He at 200°C. The isolated Cu(I) reference was obtained *in situ* with 1000 ppm NO and 1000 ppm $NH_3$ at 200°C. Figure B.4 shows the resulting XANES region used for linear combination fits. The EXAFS were observed to behave as expected in Figure B.5 and Table S2. Under the reducing conditions of NO and $NH_3$, the Cu-O coordination was 2.2 (or 2, with error), which was what we expected for an isolated Cu(I). Additionally, the oxidizing environment of $O_2$ gave a coordination of 4, which was as expected as well.

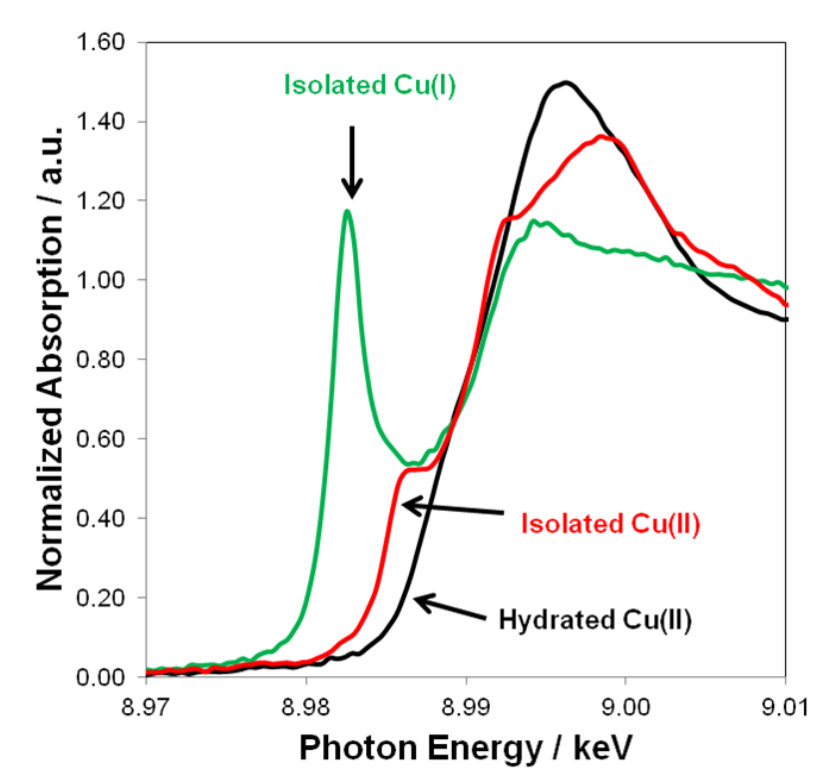


Figure B.4 Reference spectra used for linear combination XANES fits. Hydrated Cu(II) corresponds to a solution of $[Cu(H_2O)_6]^{2+}$ under ambient conditions. A 0.31 wt% Cu-SSZ-13 sample was used for isolated Cu(II) with 10% $O_2$ at 200°C and for the isolated Cu(I) with 1000 ppm NO + 1000 ppm $NH_3$ at 200°C.

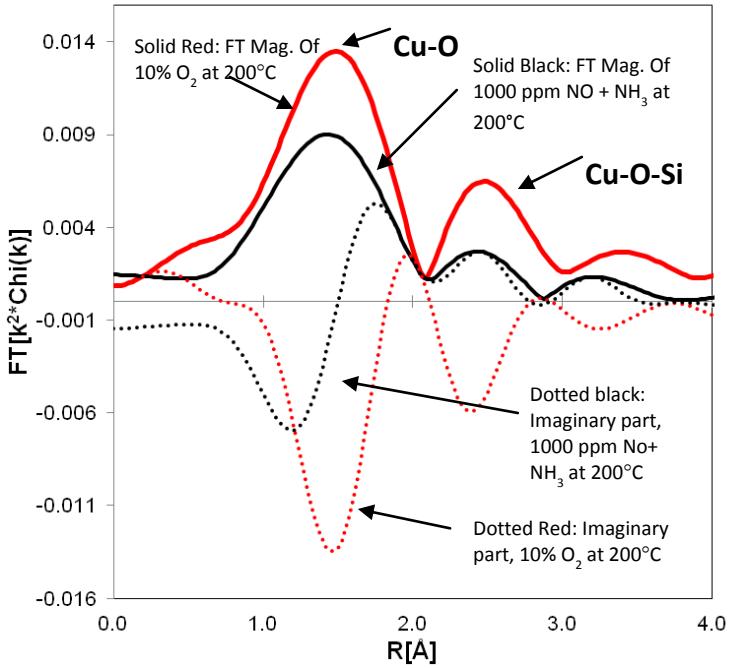


Figure B.5 EXAFS spectra for the isolated Cu(II) (red) and isolated Cu(I) (black) references. Solid lines indicate the Fourier transform magnitude. Dotted lines indicate the imaginary contribution.

Table B.2 EXAFS fit paremeters for isolated Cu(I) and isolated Cu(II).

| 0.31% Cu EXAFS of Cu-SSZ-13 | | | | | | | | |
|---|---|---|---|---|---|---|---|---|
| Sample | Treatment | XANES | | Absorber -Scatter | N | R / Å | $\Delta\sigma^2$ (x $10^3$) | $E_o$ / eV |
| | | Fraction Cu(II) | Fraction Cu(I) | | | | | |
| Cu(II) | RT, ambient | 1.0 | - | Cu-O | 3.9 | 1.96 | 2.0 | -8.5 |
| Cu(II) | 10% $O_2$, 473 K | 1.0 | - | Cu-O | 4.0 | 1.96 | 4.0 | -7.5 |
| Cu(I) | 1000 ppm $NH_3$ + 1000 ppm NO, 473 K | - | 1.0 | Cu-O | 2.2 | 1.85 | 4.0 | -5.1 |

Supplementary Data for the 2.1 wt% Cu-SSZ-13 sample discussed in this study

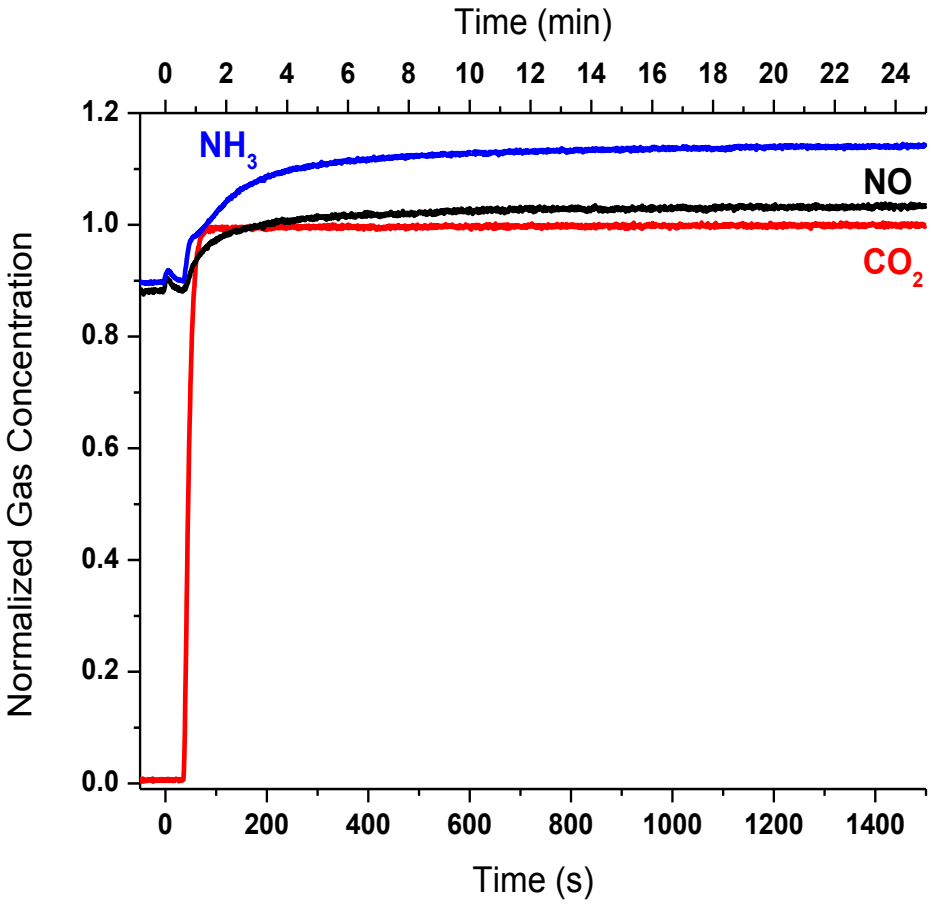


Figure B.6 Normalized gas concentration curves of $CO_2$ (red), NO (black) and $NH_3$ (blue) are shown as a function of time after $O_2$ cutoff from standard SCR gas conditions for the 2.1 wt% Cu-SSZ-13 sample. $O_2$ was cutoff and replaced by $CO_2$ at t = 0 s.

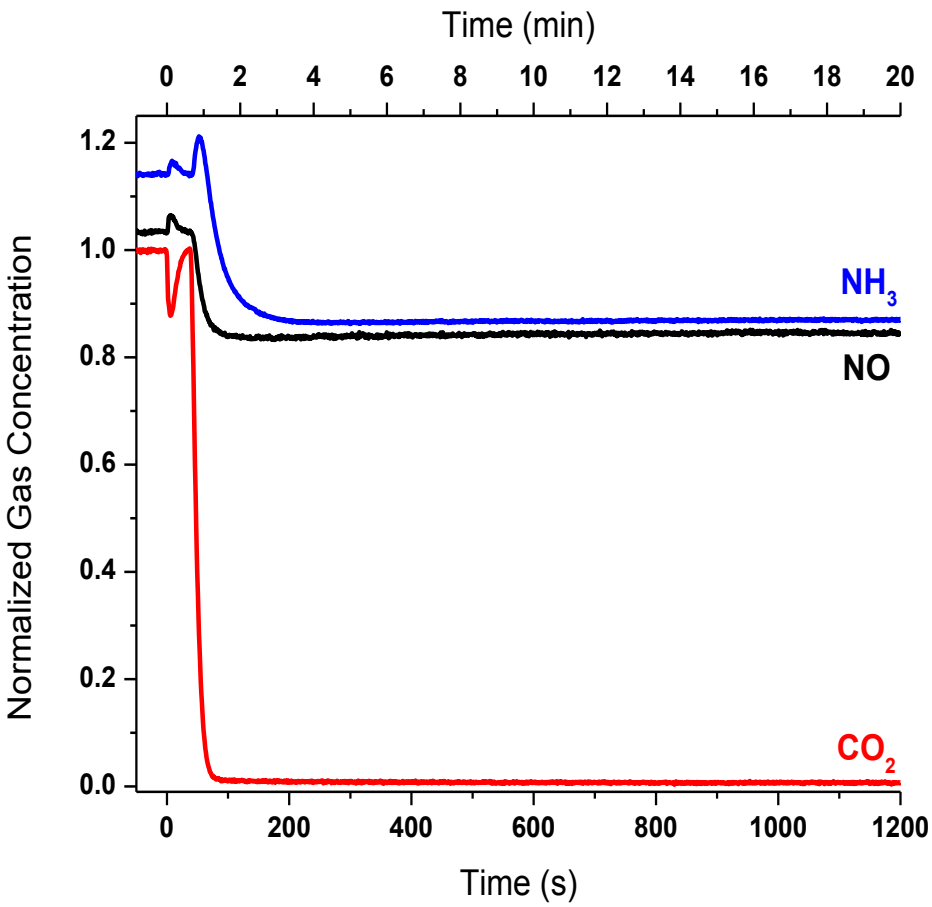


Figure B.7 Normalized gas concentration curves of $CO_2$ (red), NO (black) and $NH_3$ (blue) are shown as a function of time after $O_2$ addition to return to standard SCR gas conditions for the 2.1 wt% Cu-SSZ-13 sample. $CO_2$ was cutoff and replaced by $O_2$ at t = 0 s.

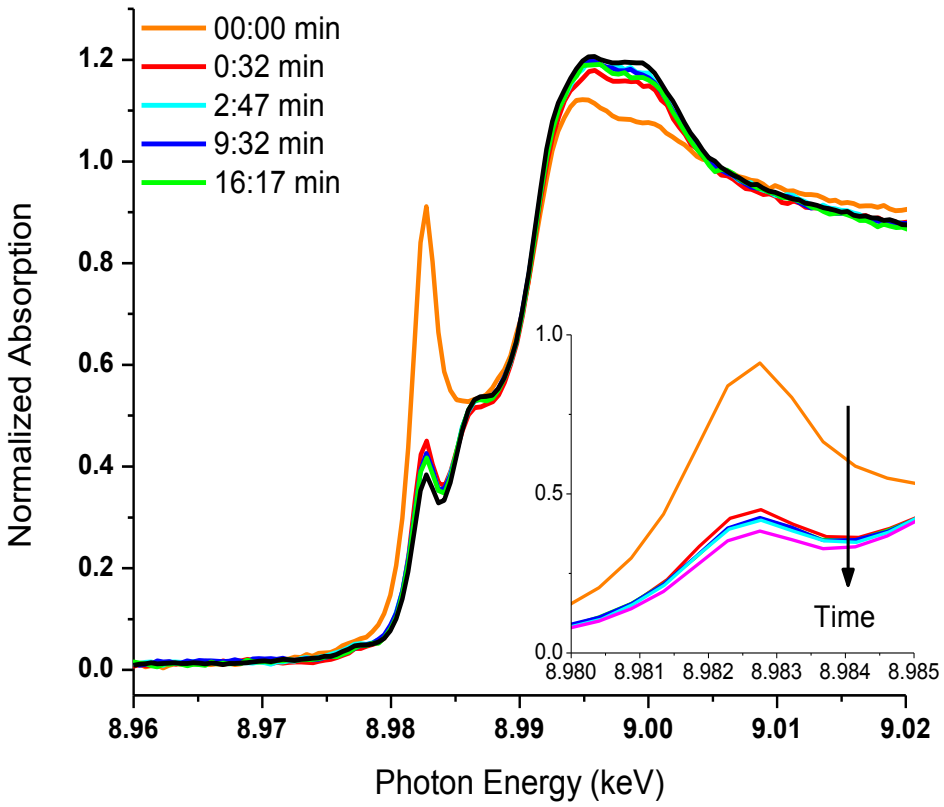


Figure B.8 Time resolved XAS of the 2.1 wt.% Cu-SSZ-13 catalyst after $O_2$ addition to the reaction mixture to return to standard SCR for the 2.1 wt% Cu-SSZ-13 sample. Inset zooms in on the edge feature at ~9.9828 keV, the identifying feature of Cu(I) species. To clearly present the data, spectra are not linear in time resolution.

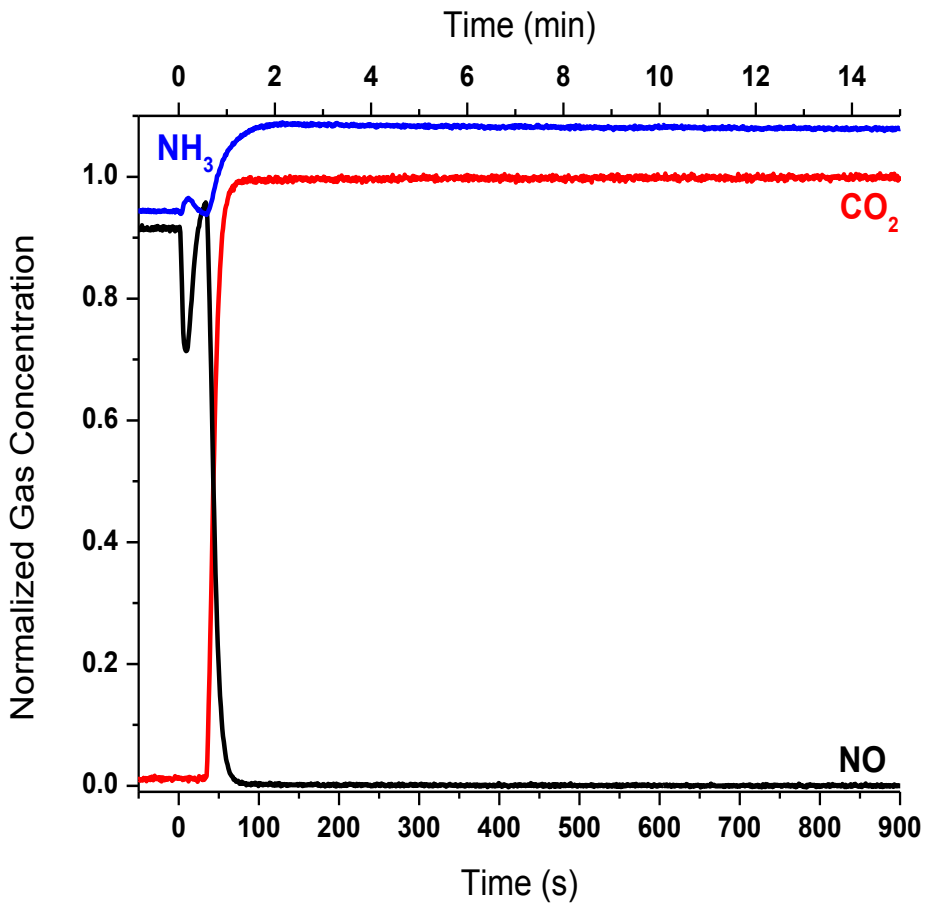


Figure B.9 Normalized gas concentration curves of $CO_2$ (red), NO (black) and $NH_3$ (blue) are shown as a function of time after NO cutoff from standard SCR gas conditions for the 2.1 wt% Cu-SSZ-13 sample. NO was cutoff and replaced by $CO_2$ at t = 0 s.

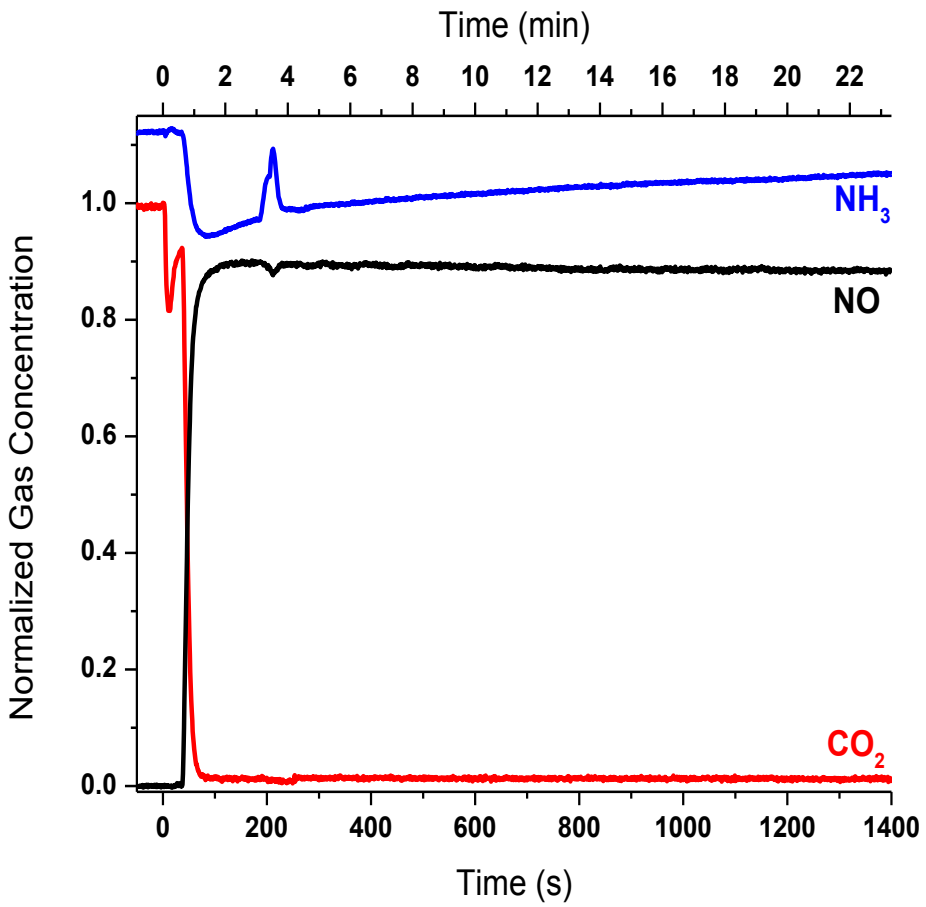


Figure B.10 Normalized gas concentration curves of $CO_2$ (red), NO (black) and $NH_3$ (blue) are shown as a function of time after NO addition to return to standard SCR gas conditions for the 2.1 wt% Cu-SSZ-13 sample. $CO_2$ was cutoff and replaced by NO at t = 0 s.

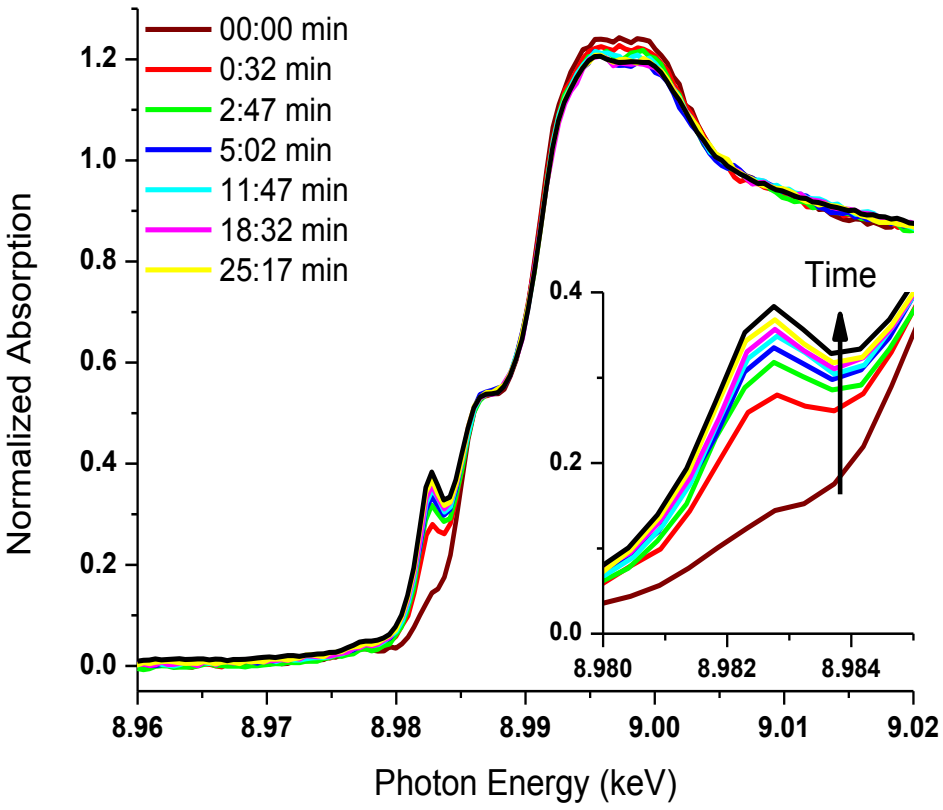


Figure B.11 Time resolved XAS of the 2.1 wt.% Cu-SSZ-13 catalyst after NO addition to the reaction mixture to return to standard SCR. Inset zooms in on the edge feature at ~9.9828 keV, the identifying feature of Cu(I) species. To clearly present the data, spectra are not linear in time resolution.

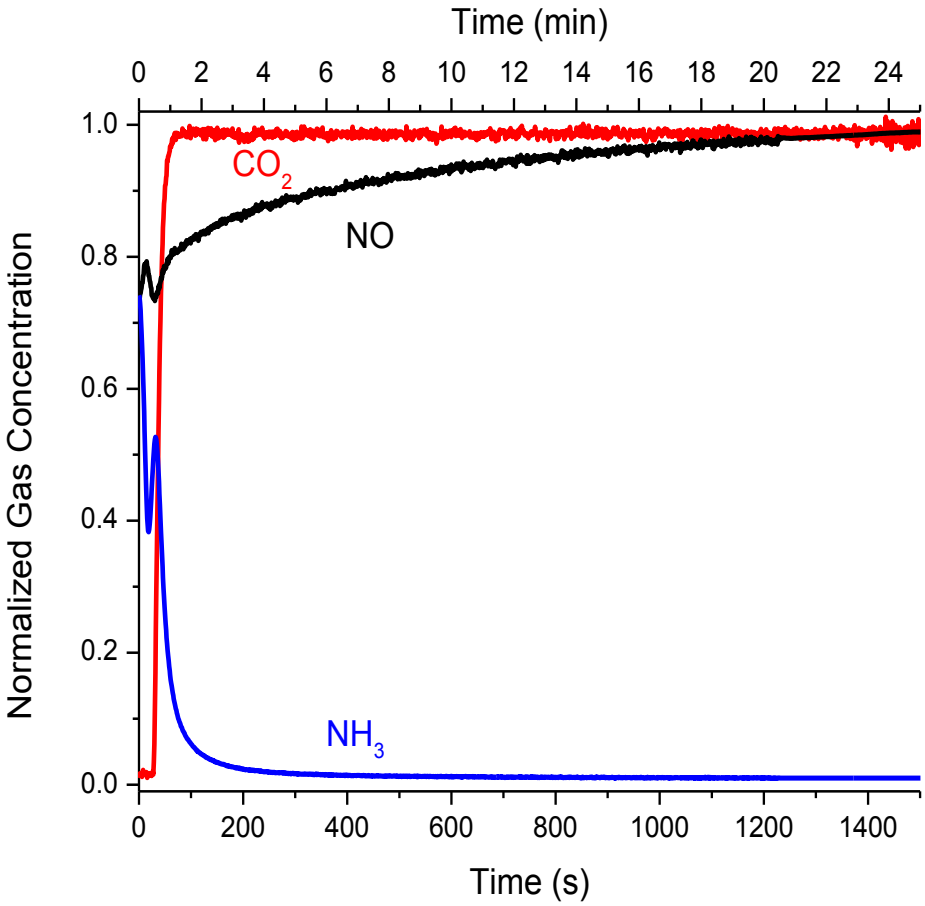


Figure B.12 Normalized gas concentration curves of $CO_2$ (red), NO (black) and $NH_3$ (blue) are shown as a function of time after $NH_3$ cutoff from standard SCR gas conditions for the 2.1 wt% Cu-SSZ-13 sample. $NH_3$ was cutoff and replaced by CO2 at t = 0 s.

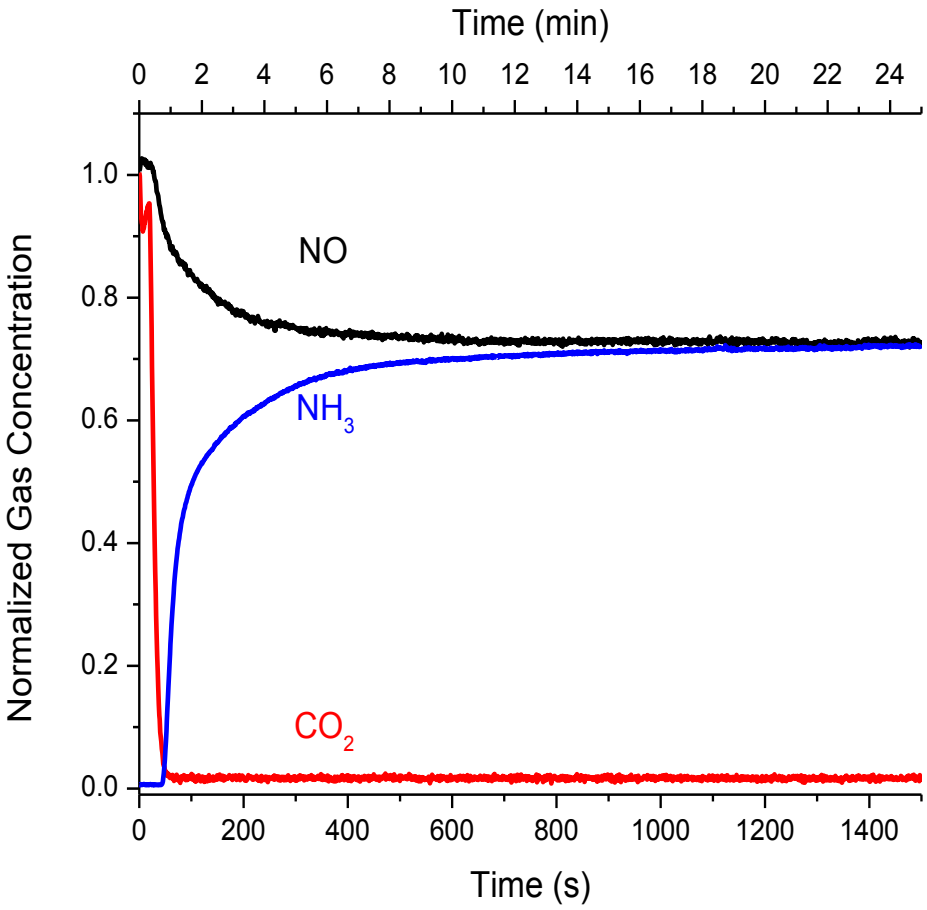


Figure B.13 Normalized gas concentration curves of $CO_2$ (red), NO (black) and $NH_3$ (blue) are shown as a function of time after $NH_3$ addition to return to standard SCR gas conditions for the 2.1 wt% Cu-SSZ-13 sample. $CO_2$ was cutoff and replaced by $NH_3$ at t = 0 s.

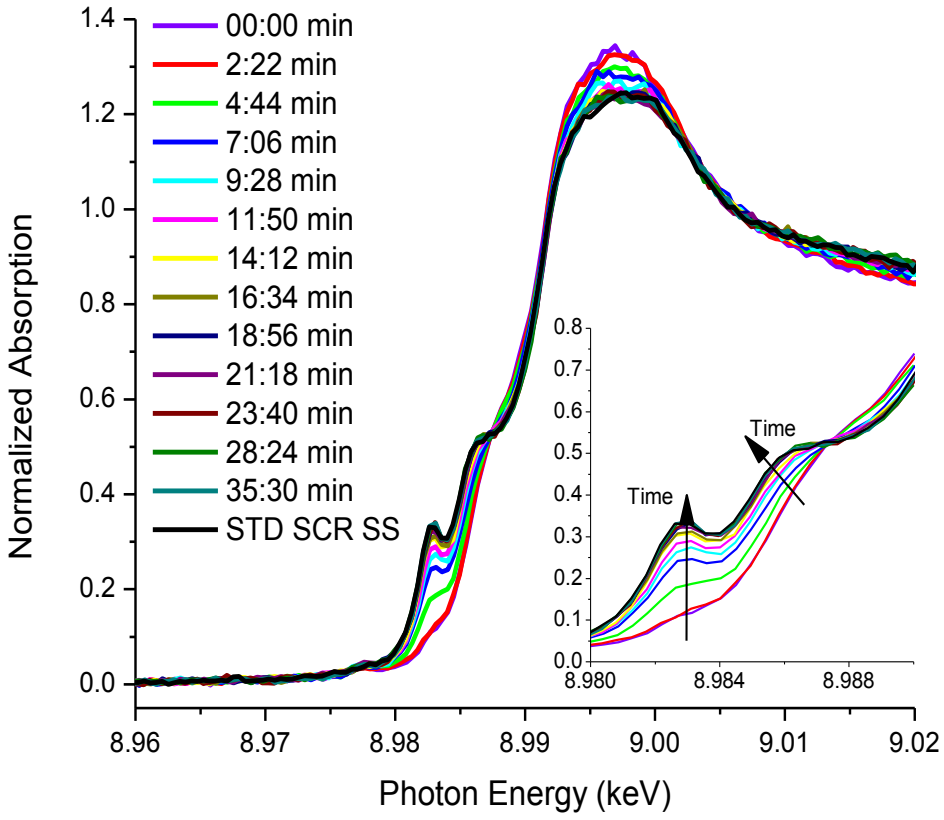


Figure B.14 Time resolved XAS of the 2.1 wt% Cu-SSZ-13 catalyst after $NH_3$ addition to the reaction mixture to return to standard SCR. Inset zooms in on the edge feature at ~9.9828 keV, the identifying feature of Cu(I) species. To clearly present the data, spectra are not linear in time resolution.

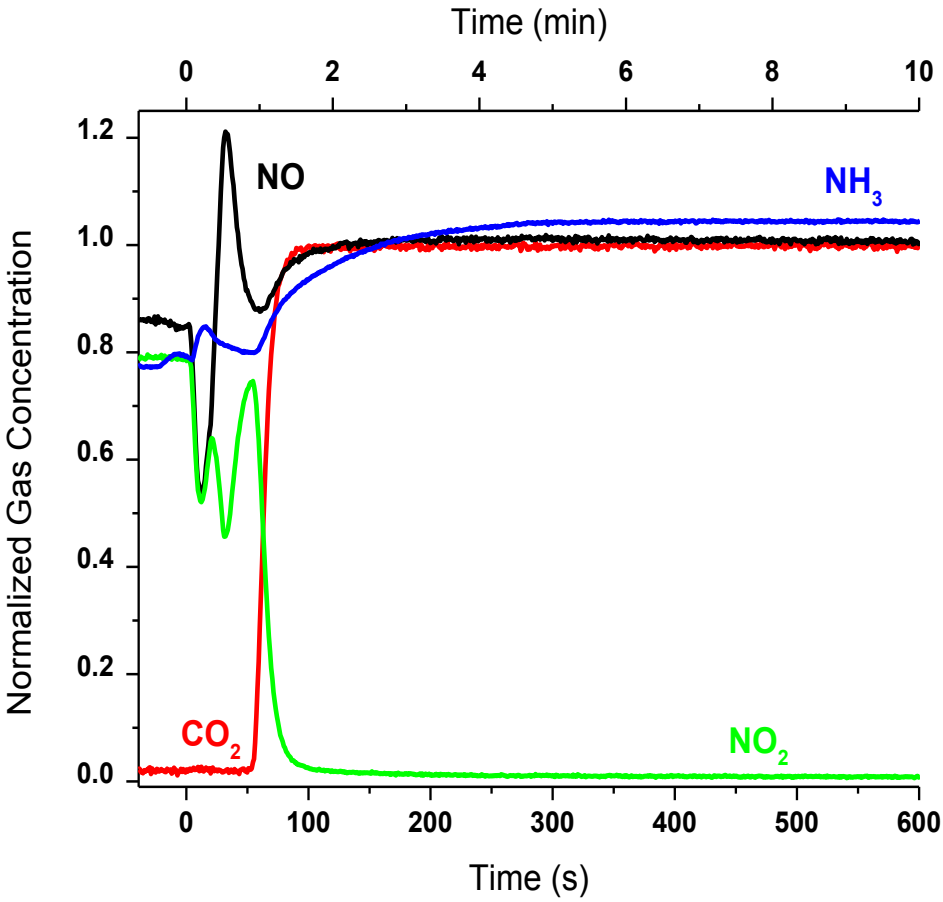


Figure B.15 Normalized gas concentration curves of $CO_2$ (red), NO (black), $NH_3$ (blue) and $NO_2$ (green) are shown as a function of time after $NO_2$ cutoff from fast SCR gas conditions to generate standard SCR conditions for the 2.1 wt% Cu-SSZ-13 sample. $NO_2$ was cutoff and replaced by $CO_2$ at t = 0 s.

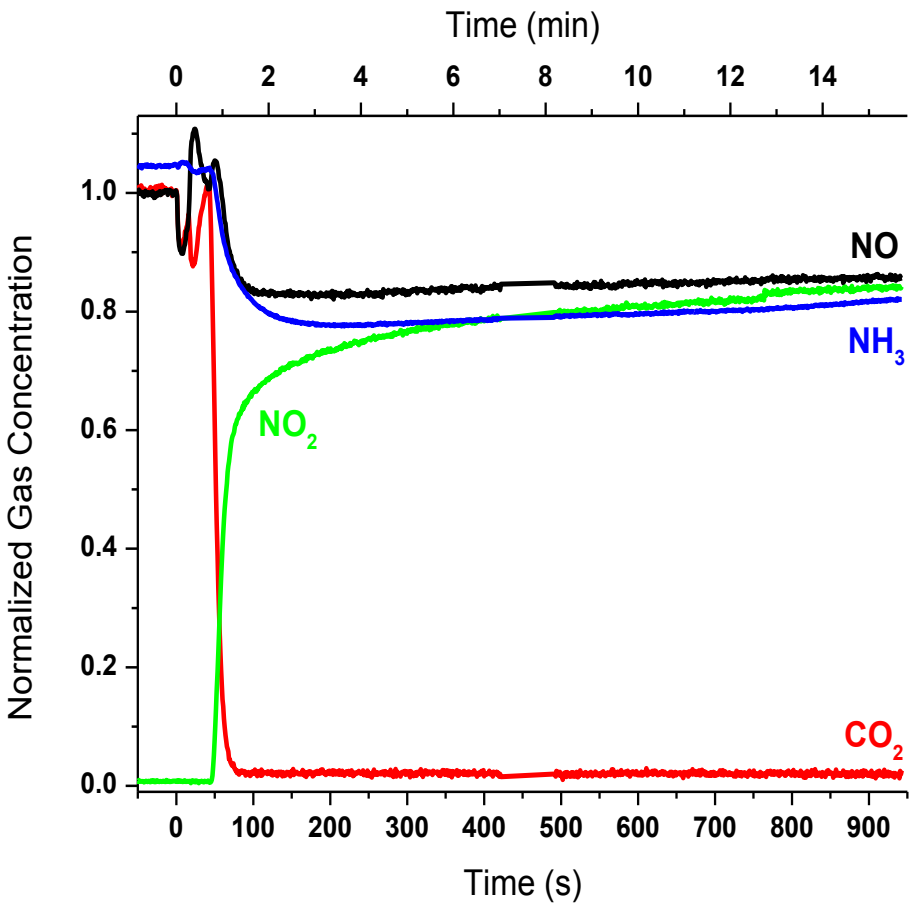


Figure B.16 Normalized gas concentration curves of $CO_2$ (red), NO (black), $NH_3$ (blue) and $NO_2$ (green) are shown as a function of time after $NO_2$ addition to standard SCR conditions to generate fast SCR gas conditions for the 2.1 wt% Cu-SSZ-13 sample. $CO_2$ was cutoff and replaced by $NO_2$ at t = 0 s.

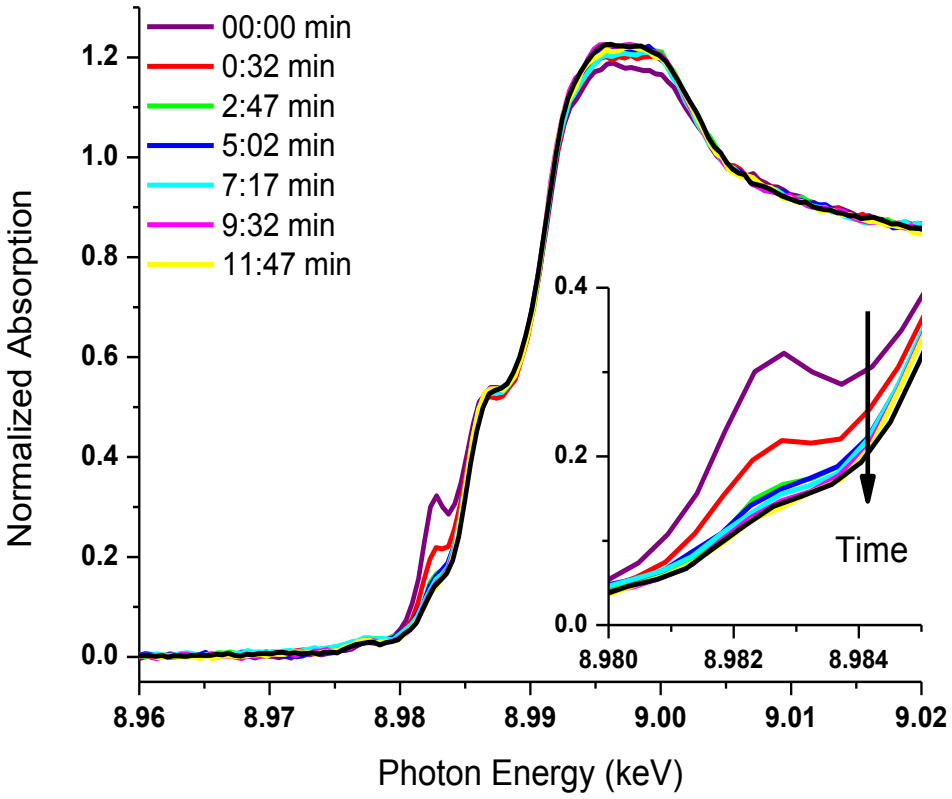


Figure B.17 Time resolved XAS of the 2.1 wt.% Cu-SSZ-13 catalyst after $NO_2$ addition to the reaction mixture to return to fast SCR. Inset zooms in on the edge feature at ~9.9828 keV, the identifying feature of Cu(I) species. To clearly present the data, spectra are not linear in time resolution.

The Full Set of Data for a secondary sample, a 3.04 wt% Cu-SSZ-13

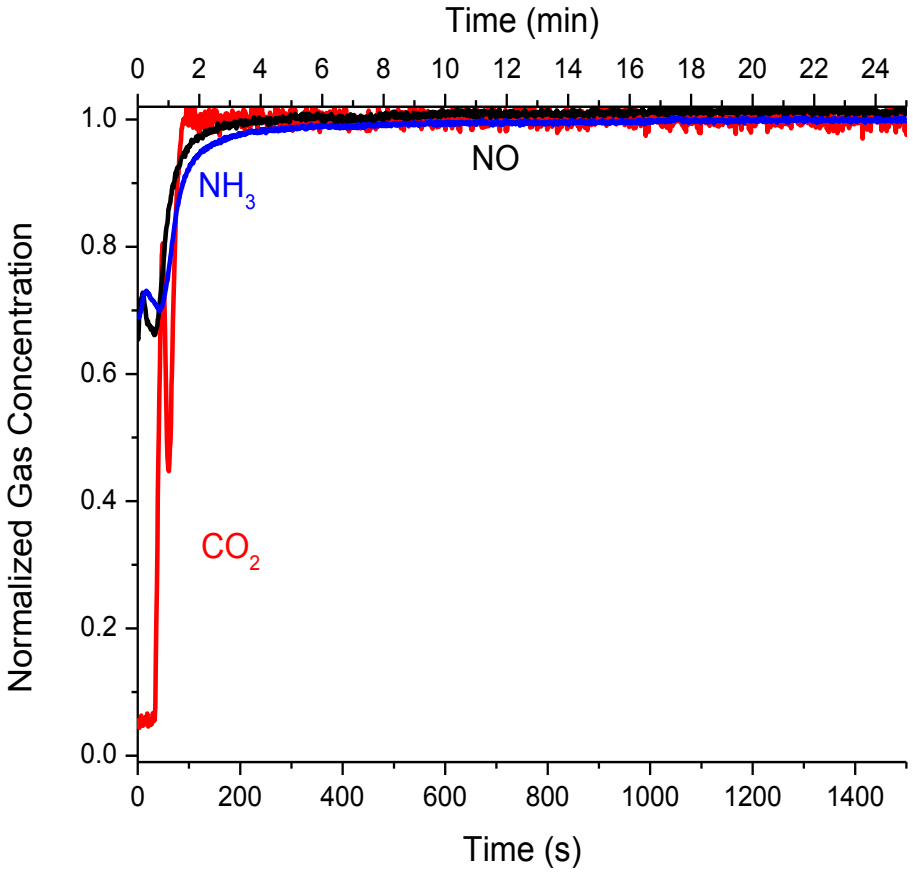


Figure B.18 Normalized gas concentration curves of $CO_2$ (red), NO (black) and $NH_3$ (blue) are shown as a function of time after $O_2$ cutoff from standard SCR gas conditions for the 3.04 wt% Cu-SSZ-13 sample. $O_2$ was cutoff and replaced by $CO_2$ at t = 0 s.

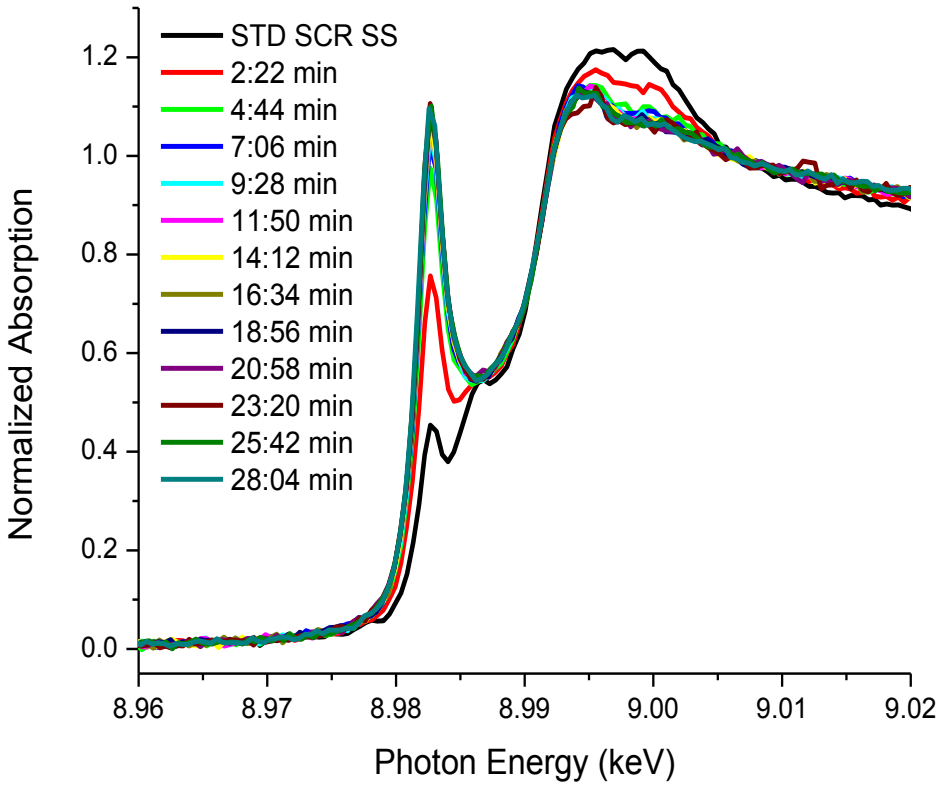


Figure B.19 Time resolved XAS of the 3.04 wt.% Cu-SSZ-13 catalyst after $O_2$ was cut off from the standard SCR reactant stream. To clearly present the data, spectra are not linear in time scale.

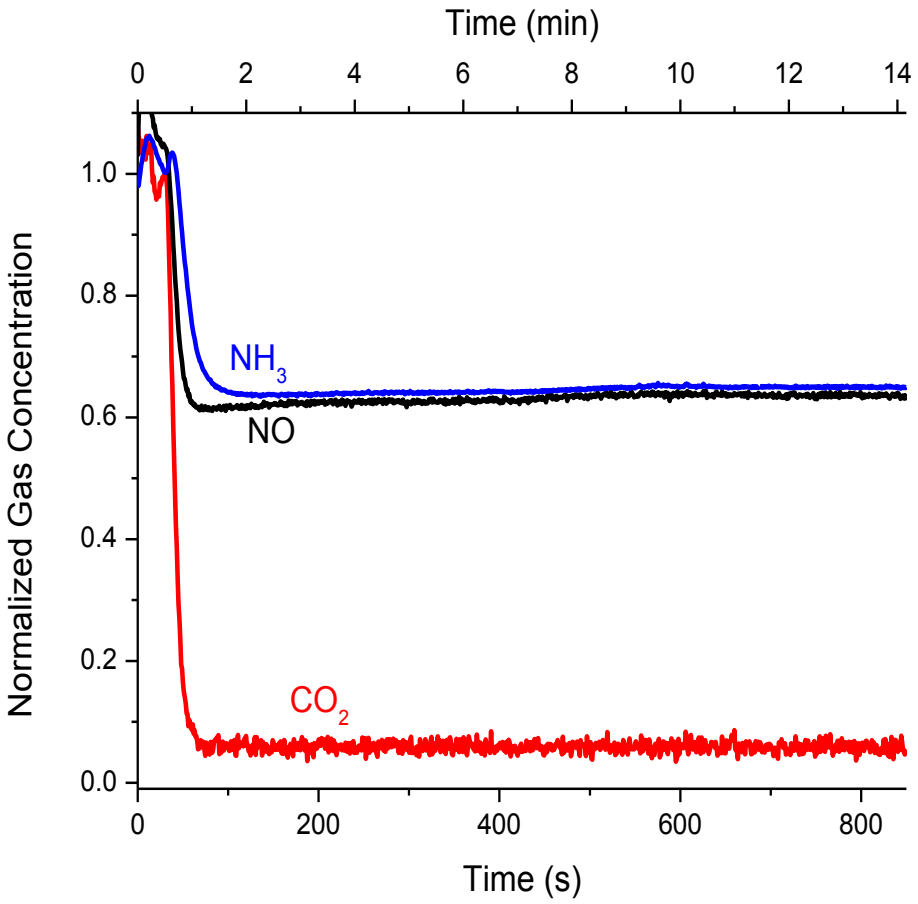


Figure B.20 Normalized gas concentration curves of $CO_2$ (red), NO (black) and $NH_3$ (blue) are shown as a function of time after $O_2$ addition to return to standard SCR gas conditions for the 3.04 wt% Cu-SSZ-13 sample. $CO_2$ was cutoff and replaced by $O_2$ at t = 0 s.

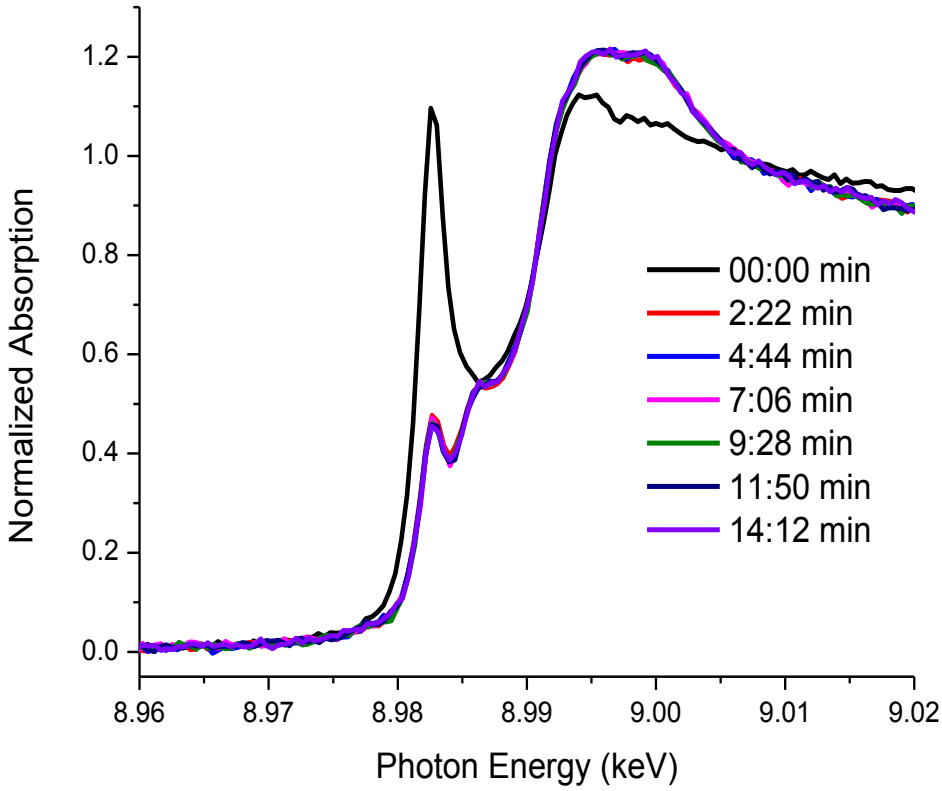


Figure B.21 Time resolved XAS of the 3.04 wt.% Cu-SSZ-13 catalyst after $O_2$ addition to the reaction mixture to return to standard SCR. To clearly present the data, spectra are not linear in time resolution.

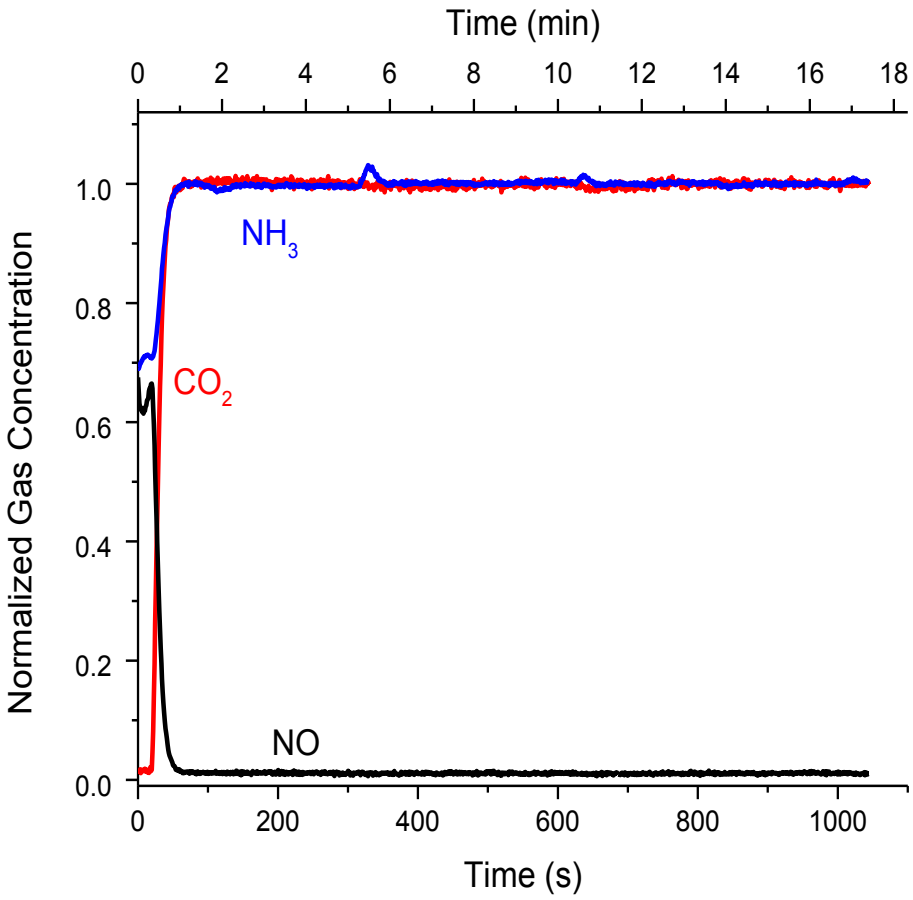


Figure B.22 Normalized gas concentration curves of $CO_2$ (red), NO (black) and $NH_3$ (blue) are shown as a function of time after NO cutoff from standard SCR gas conditions for the 3.04 wt% Cu-SSZ-13 sample. NO was cutoff and replaced by $CO_2$ at t = 0 s.

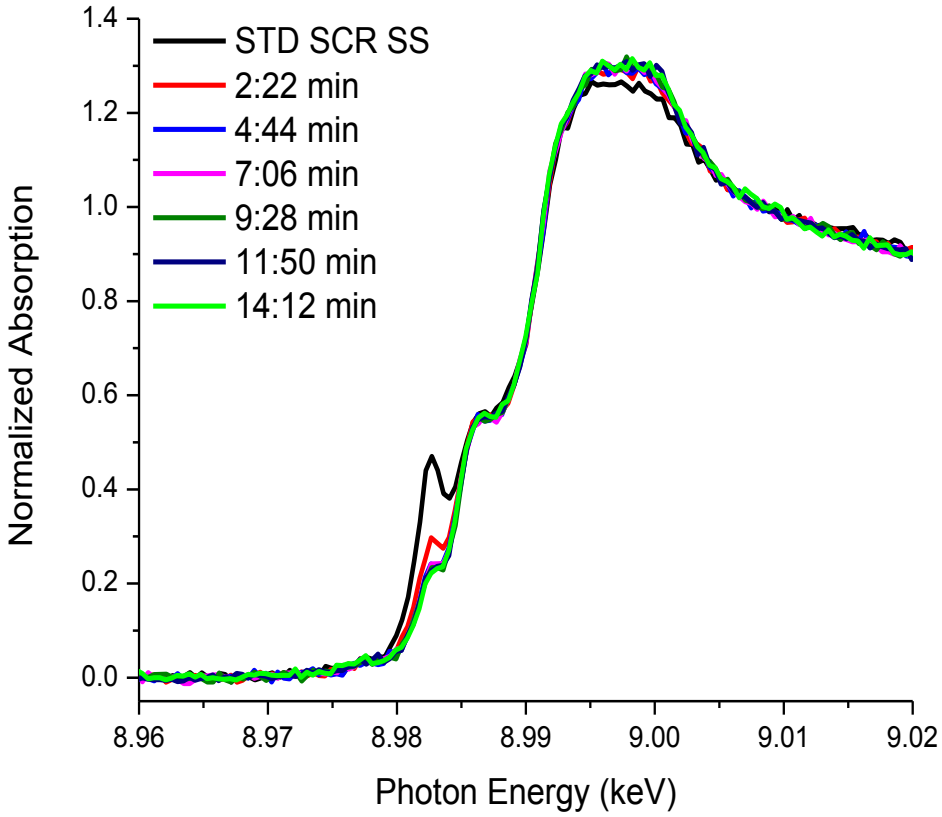


Figure B.23 Time resolved XAS of the 3.04 wt.% Cu-SSZ-13 catalyst after NO was cut off from the standard SCR reactant stream. To clearly present the data, spectra are not linear in time resolution.

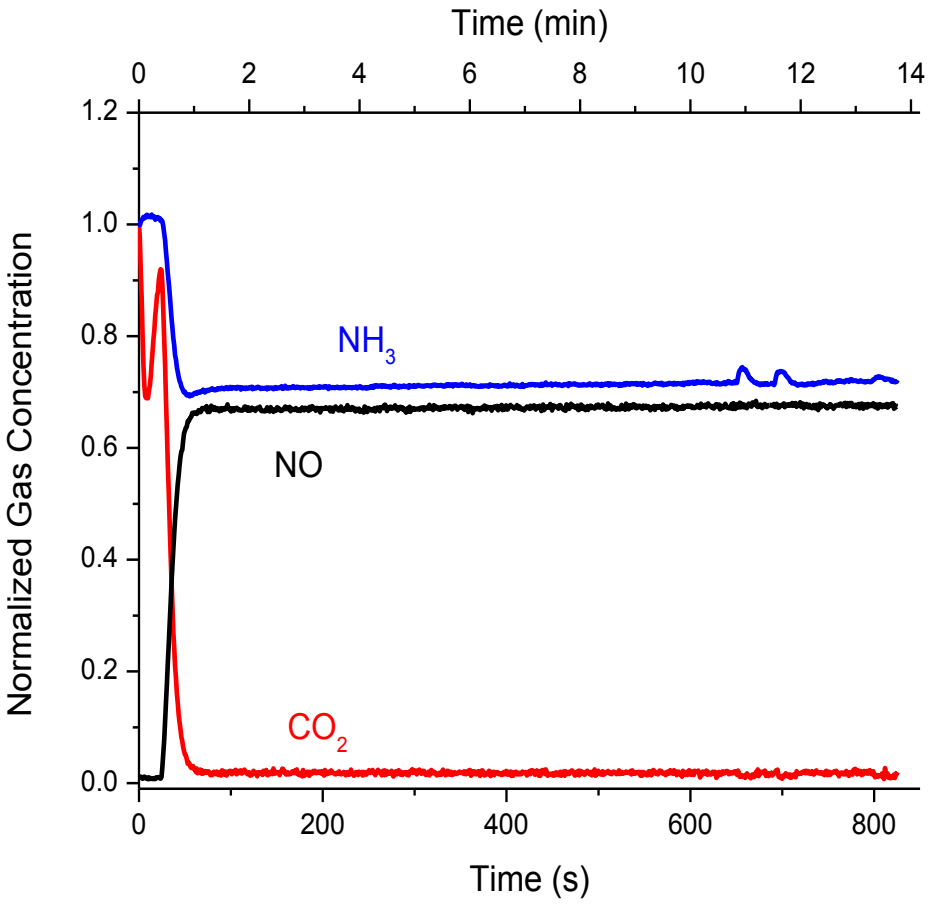


Figure B.24 Normalized gas concentration curves of $CO_2$ (red), NO (black) and $NH_3$ (blue) are shown as a function of time after NO addition to return to standard SCR gas conditions for the 3.04 wt% Cu-SSZ-13 sample. $CO_2$ was cutoff and replaced by NO at t = 0 s.

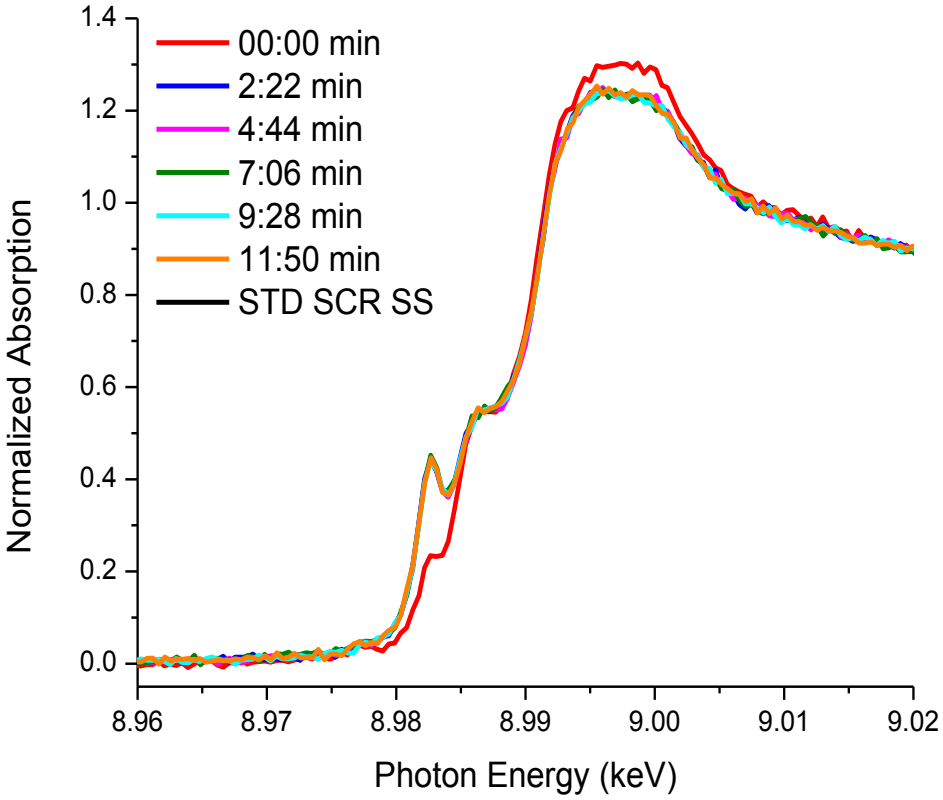


Figure B.25 Time resolved XAS of the 3.04 wt% Cu-SSZ-13 catalyst after NO addition to the reaction mixture to return to standard SCR. To clearly present the data, spectra are not linear in time resolution.

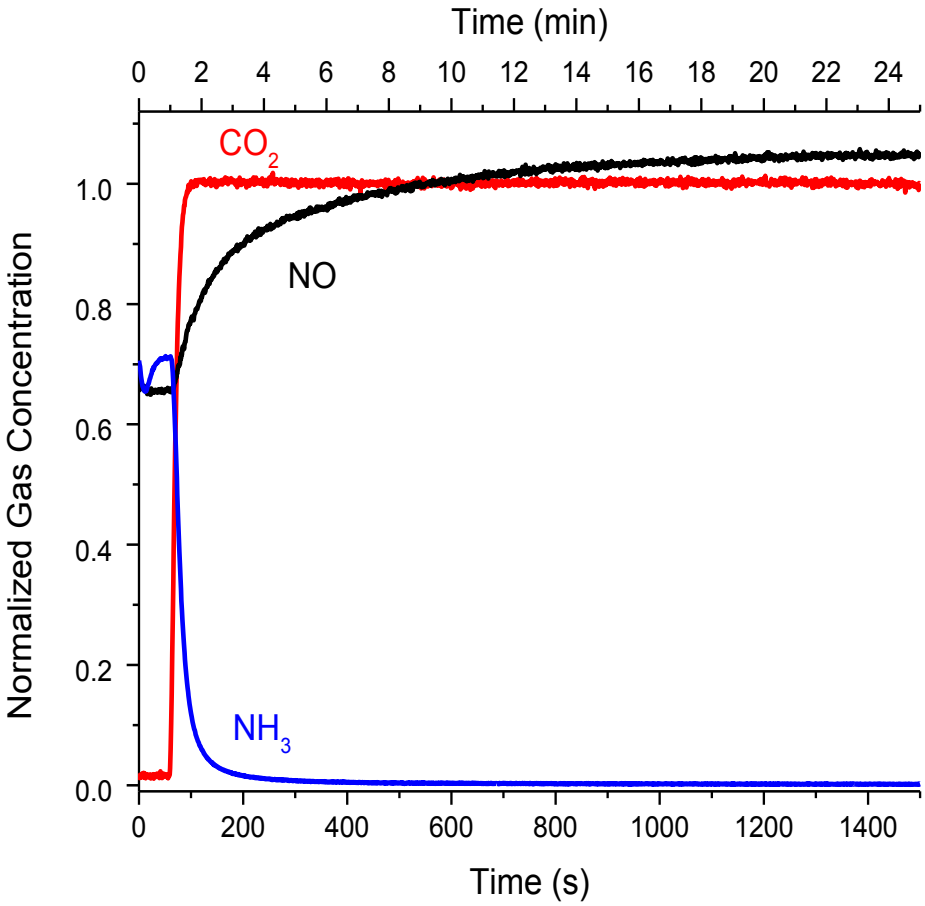


Figure B.26 Normalized gas concentration curves of $CO_2$ (red), NO (black) and $NH_3$ (blue) are shown as a function of time after $NH_3$ cutoff from standard SCR gas conditions for the 3.04 wt% Cu-SSZ-13 sample. $NH_3$ was cutoff and replaced by $CO_2$ at t = 0 s.

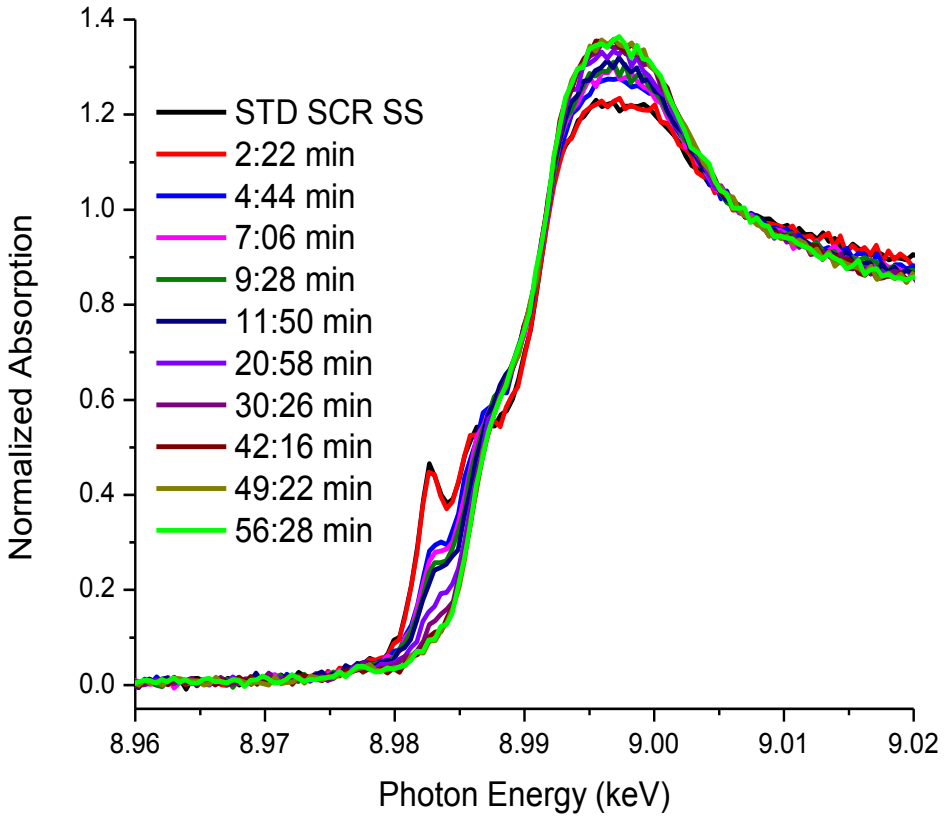


Figure B.27 Time resolved XAS of the 3.04 wt.% Cu-SSZ-13 catalyst after $NH_3$ was cut off from the standard SCR reactant stream. To clearly present the data, spectra are not linear in time resolution.

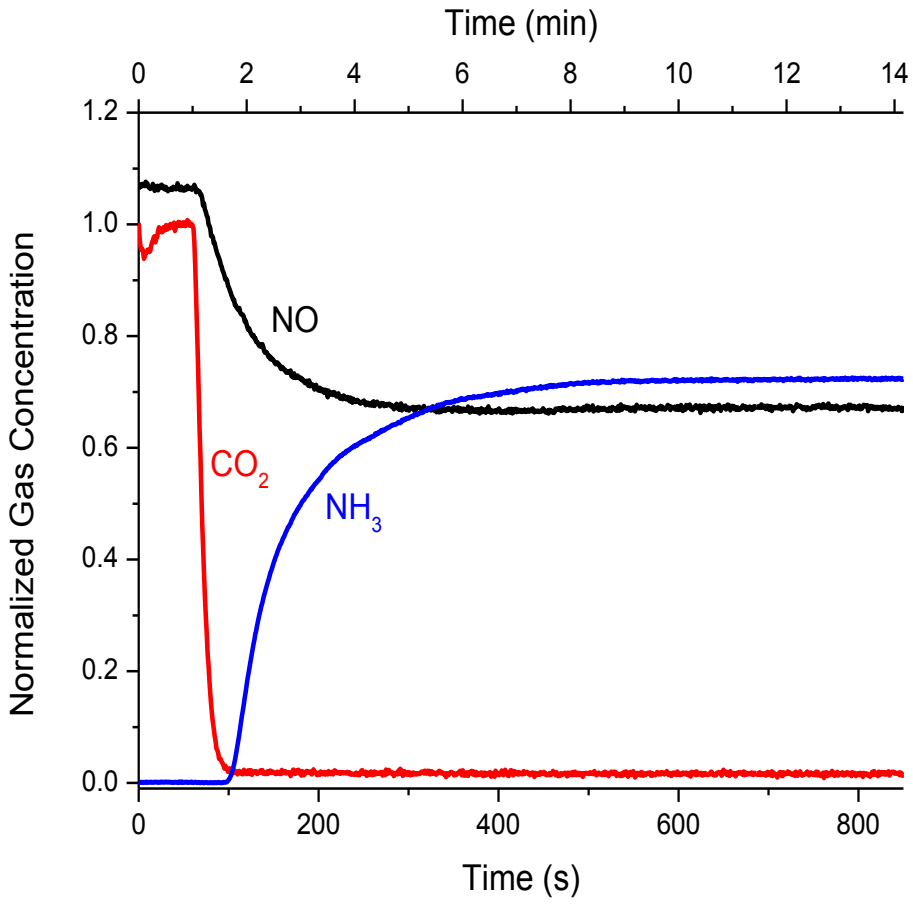


Figure B.28 Normalized gas concentration curves of $CO_2$ (red), NO (black) and $NH_3$ (blue) are shown as a function of time after $NH_3$ addition to return to standard SCR gas conditions for the 3.04 wt% Cu-SSZ-13 sample. $CO_2$ was cutoff and replaced by $NH_3$ at t = 0 s.

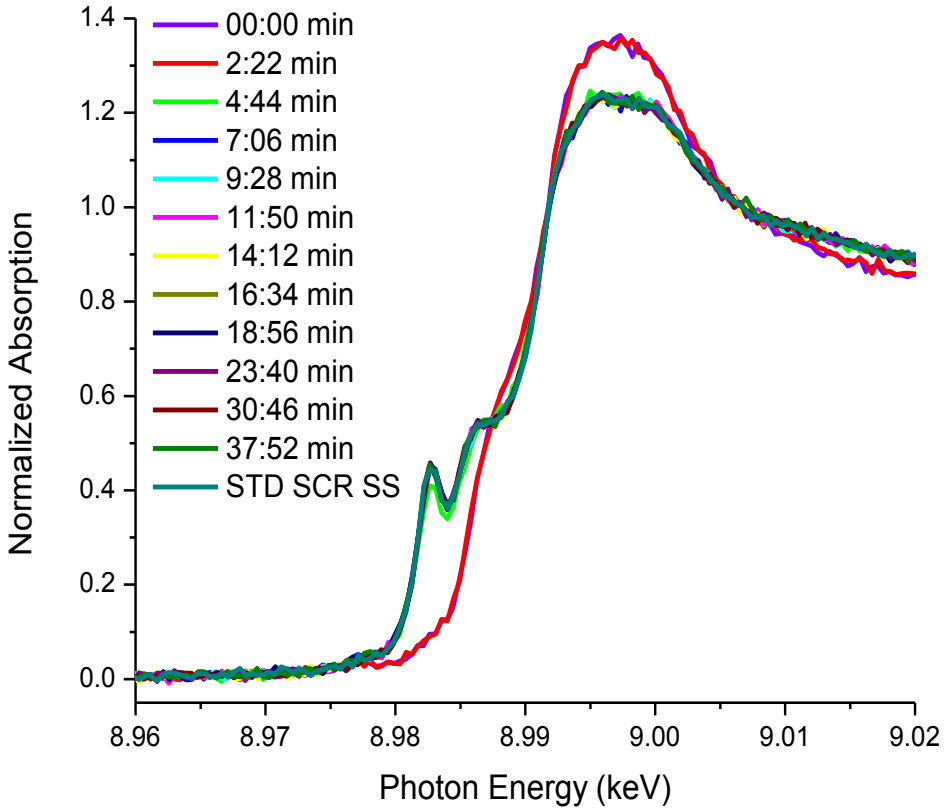


Figure B.29 Time resolved XAS of the 3.04 wt% Cu-SSZ-13 catalyst after $NH_3$ addition to the reaction mixture to return to standard SCR. To clearly present the data, spectra are not linear in time resolution.

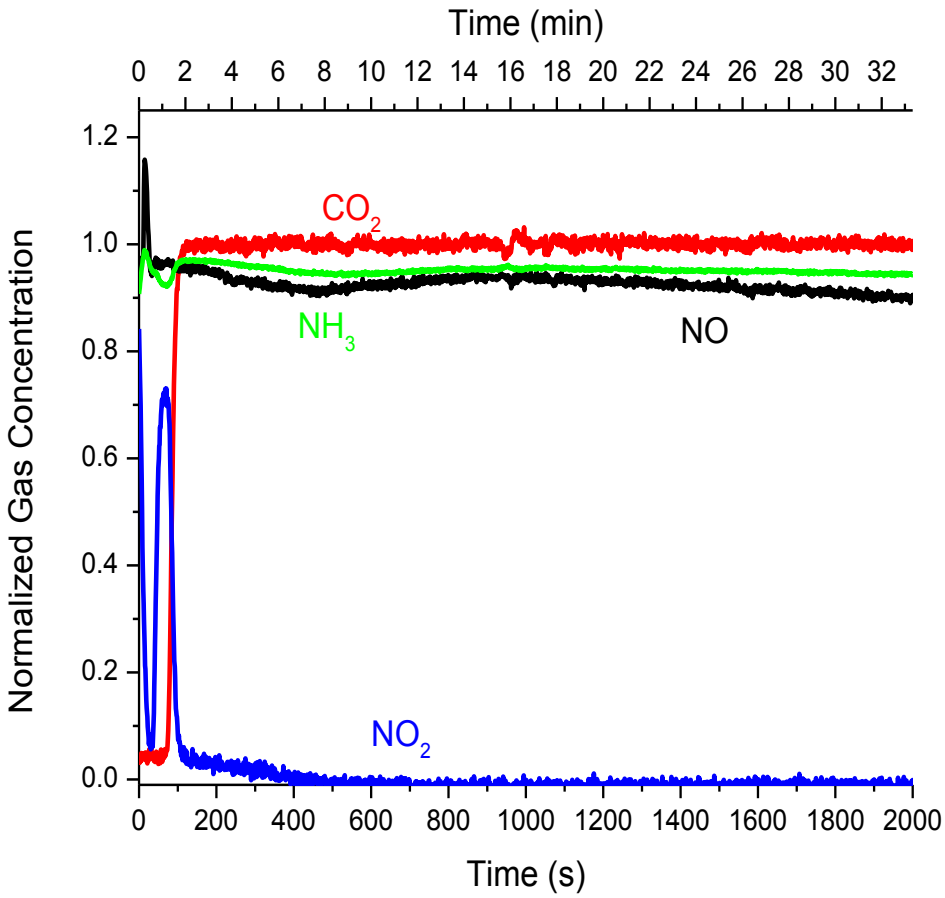


Figure B.30 Normalized gas concentration curves of $CO_2$ (red), NO (black), $NH_3$ (green) and $NO_2$ (blue) are shown as a function of time after $NO_2$ cutoff from fast SCR gas conditions to generate standard SCR conditions for the 3.04 wt% Cu-SSZ-13 sample. $NO_2$ was cutoff and replaced by $CO_2$ at t = 0 s.

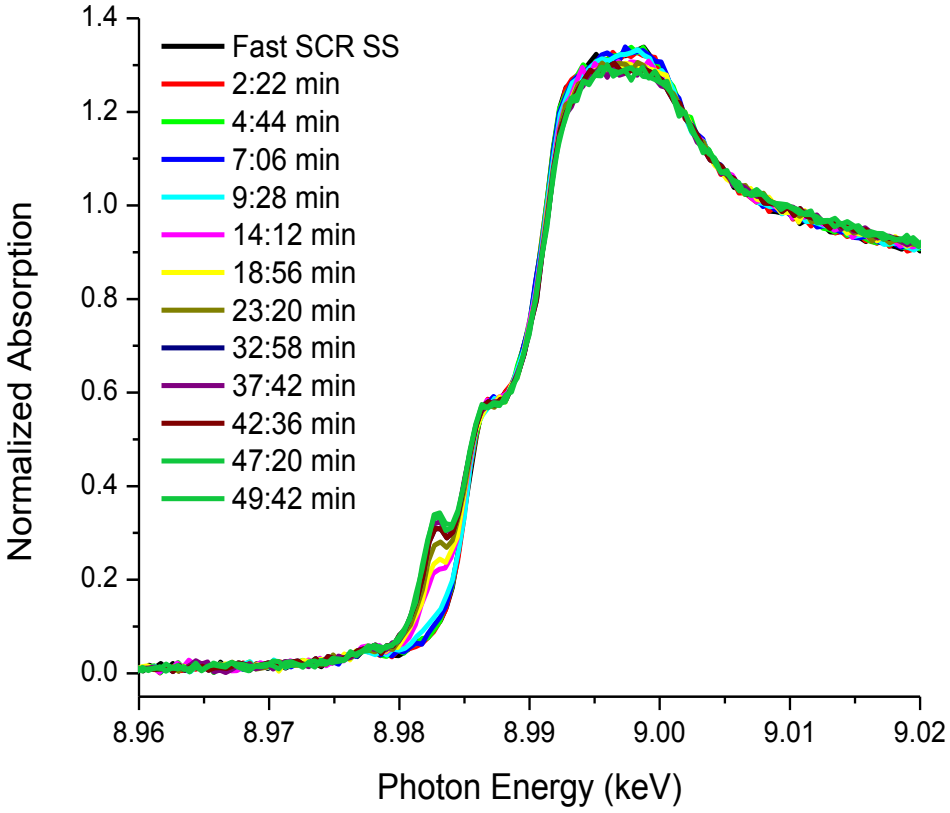


Figure B.31 Time resolved XAS of the 3.04 wt.% Cu-SSZ-13 catalyst after $NO_2$ was cut off from the fast SCR reactant stream. To clearly present the data, spectra are not linear in time resolution.

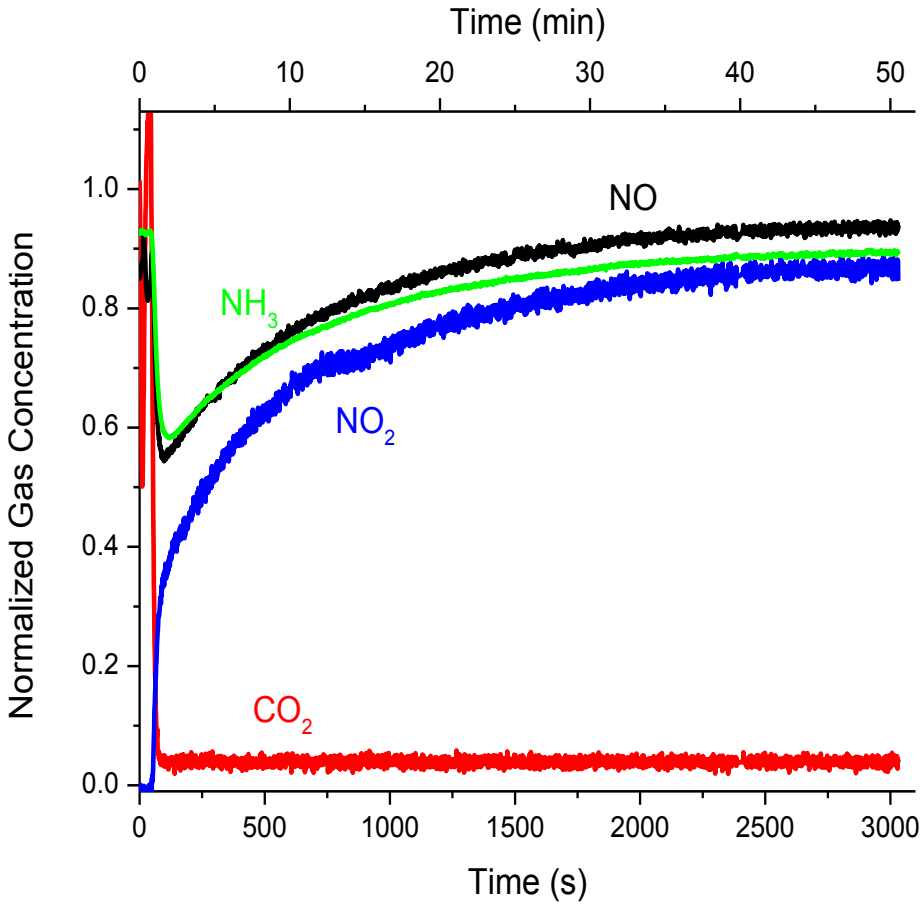


Figure B.32 Normalized gas concentration curves of $CO_2$ (red), NO (black), $NH_3$ (green) and $NO_2$ (blue) are shown as a function of time after $NO_2$ addition to standard SCR conditions to generate fast SCR gas conditions for the 3.04 wt% Cu-SSZ-13 sample. $CO_2$ was cutoff and replaced by $NO_2$ at t = 0 s.

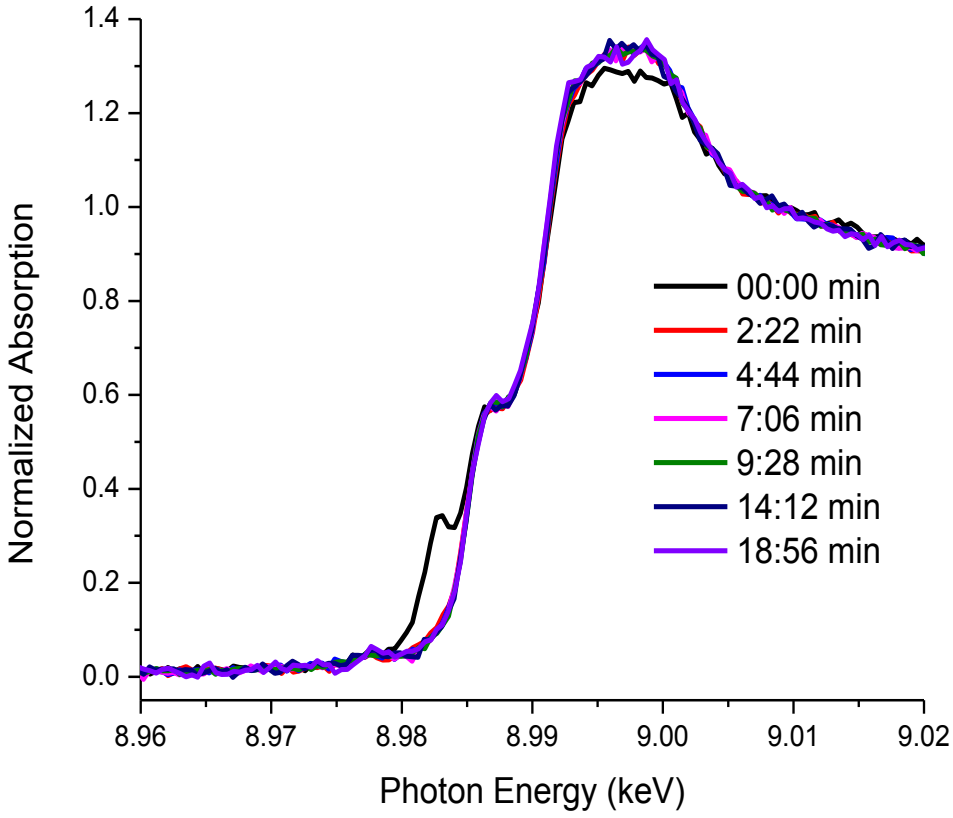


Figure B.33 Time resolved XAS of the 3.04 wt.% Cu-SSZ-13 catalyst after $NO_2$ addition to the reaction mixture to return to fast SCR. Inset zooms in on the edge feature at ~9.9828 keV, the identifying feature of Cu(I) species. To clearly present the data, spectra are not linear in time resolution.

# Appendix C Supplementary Material from Chapter 4

## Further Information on Catalyst Characterization

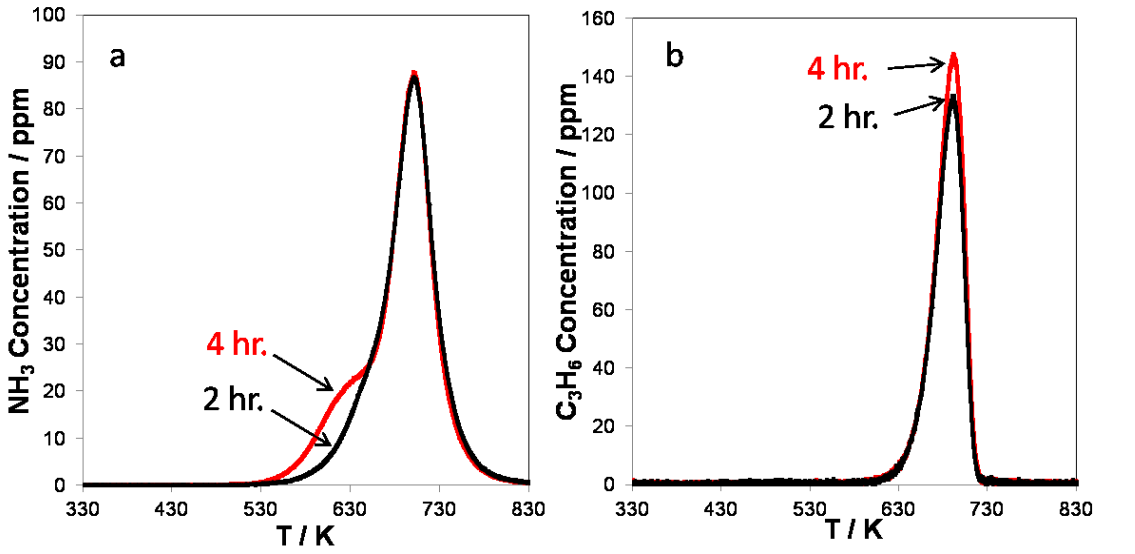


Figure C.1 N-propylamine saturation test on 25 mg of H-SSZ-4.5 with different times of saturation at 323 K. TPD spectra are shown to determine the effect.

Table C. 1 Quantification of n-propylamine decomposition over H-SSZ-4.5 in bench top reactor unit with different saturation times of n-propylamine at 323 K

| Time of treatment with NPA / hr | Calculated $H^+$:Al from $NH_3$ signal | Calculated $H^+$:Al from $C_3H_6$ signal |
|---|---|---|
| 2 | 0.26 | 0.25 |
| 4 | 0.28 | 0.27 |

*90% confidence interval for $H^+$:Al from $NH_3$ and $C_3H_6$ signal in NPA-TPD in bench-top unit is ±0.07 $H^+$:Al.

Table C.2 Summary of elemental analysis by atomic absorption and $N_2$ isotherms for all samples in this study.

| Sample Name | Zeolyst Call Number | Measured Si:Al* | Measured Cu:Al* | Measured BET Surface Area for / $m^2$ $g^{-1}$ | T-plot micropore volume / $cm^3$ $g^{-1}$ |
|---|---|---|---|---|---|
| H-ZSM-17 | CBV 3024E | 17 | - | 498 | 0.15 |
| H-ZSM-30 | CBV 5524G | 30 | - | 519 | 0.17 |
| H-ZSM-43 | CBV 8014 | 43 | - | 425 | 0.13 |
| H-ZSM-89 | CBV 1502 | 89 | - | 400 | 0.06 |
| H-SSZ-4.5 | - | 4.5 | - | 597 | 0.26 |
| Cu-ZSM-17-0.15 | - | 17 | 0.15 | 441 | 0.14 |
| Cu-ZSM-17-0.20 | - | 17 | 0.20 | 467 | 0.15 |
| Cu-ZSM-17-0.27 | - | 17 | 0.27 | 453 | 0.14 |
| Cu-SSZ-4.3-0.02 | - | 4.3 | 0.02 | 508 | 0.22 |
| Cu-SSZ-4.3-0.04 | - | 4.3 | 0.04 | 568 | 0.24 |
| Cu-SSZ-4.5-0.09 | - | 4.5 | 0.09 | 544 | 0.23 |
| Cu-SSZ-4.5-0.16 | - | 4.5 | 0.16 | 464 | 0.2 |
| Cu-SSZ-4.5-0.20 | - | 4.5 | 0.20 | 525 | 0.23 |
| Cu-SSZ-4.5-0.35 | - | 4.5 | 0.35 | 496 | 0.24 |

* Measured Si:Al and Cu:Al ratios were determined from atomic absorption spectroscopy. 90% confidence intervals for Surface area and micropore volume are ±51 $m^2g^{-1}$ and ±0.01 $cm^3g^{-1}$, respectively.

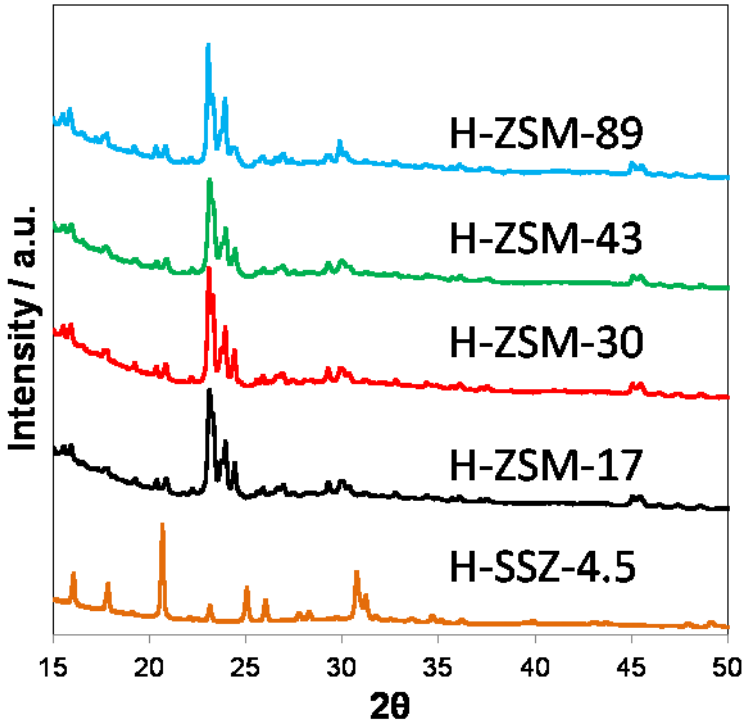


Figure C.2 X-ray diffraction patterns for the H-form of each ZSM-5 and SSZ-13 sample in this study.

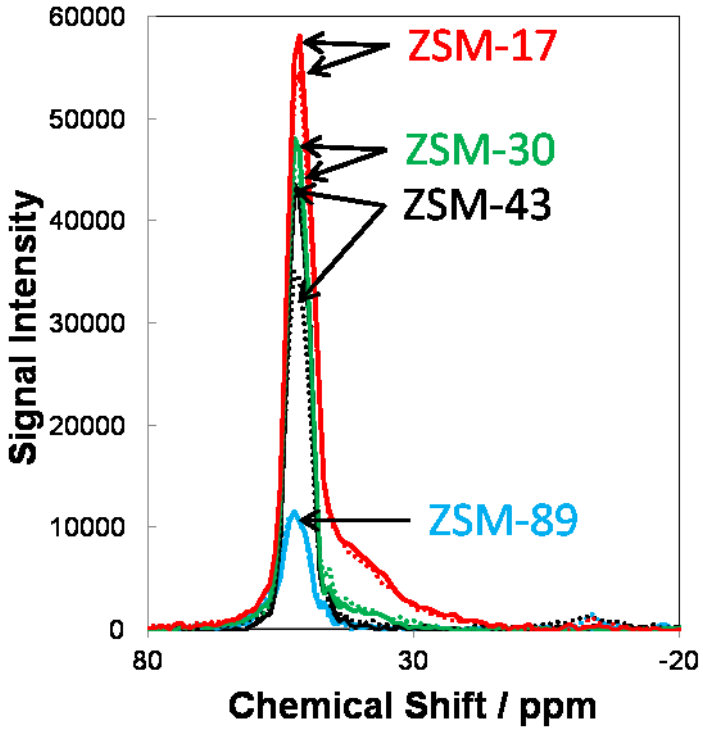


Figure C.3 $^{27}$Al NMR spectra for all four ZSM-5 samples. Solid lines (—) indicate $NH_4$-form of the zeolite. Dotted lines (•••) indicate the H-form of the zeolite.

Table C.3 $^{27}$Al NMR quantification results for H and $NH_4$ – ZSM-5 samples obtained from Zeolyst.

| Sample Name | Zeolyst Call Number | Measured Si:Al (by AA)* | % Al_fr for $NH_4$-form** | % Al_ex for $NH_4$-form | % Al_fr for H-form** | % Al_ex for H-form |
|---|---|---|---|---|---|---|
| H-ZSM-17 | CBV 3024E | 17 | 100 | 0 | 99 | 1 |
| H-ZSM-30 | CBV 5524G | 30 | 100 | 0 | 100 | 0 |
| H-ZSM-43 | CBV 8014 | 43 | 100 | 0 | 94 | 6 |
| H-ZSM-89 | CBV 1502 | 89 | 98 | 2 | 93 | 7 |

* Measured Si:Al ratios were determined from atomic absorption spectroscopy
**Al_fr contains the sum of areas for the tetrahedral and penta-coordinated Al species.

Table C.4 Summary of areas for the de-convolution of the Al_fr feature from 27Al NMR on the H and $NH_4$-ZSM-5 samples obtained from Zeolyst.

| Sample Name | Zeolyst Call Number | Measured Si:Al | % Tetra-hedral Al for $NH_4$ form | % Penta-coodinated Al for $NH_4$-form | % Octa-hedral Al for $NH_4$-form | % Tetra-hedral Al for H-form | % Penta-coodinated Al for H-form | % Octa-hedral Al for H form |
|---|---|---|---|---|---|---|---|---|
| H-ZSM-17 | CBV 3024E | 17 | 61 | 39 | 0 | 60 | 39 | 1 |
| H-ZSM-30 | CBV 5524G | 30 | 83 | 17 | 0 | 78 | 22 | 0 |
| H-ZSM-43 | CBV 8014 | 43 | 95 | 5 | 0 | 85 | 9 | 6 |
| H-ZSM-89 | CBV 1502 | 89 | 86 | 12 | 2 | 83 | 10 | 7 |

Additional TPD Spectra of H-ZSM-5 samples

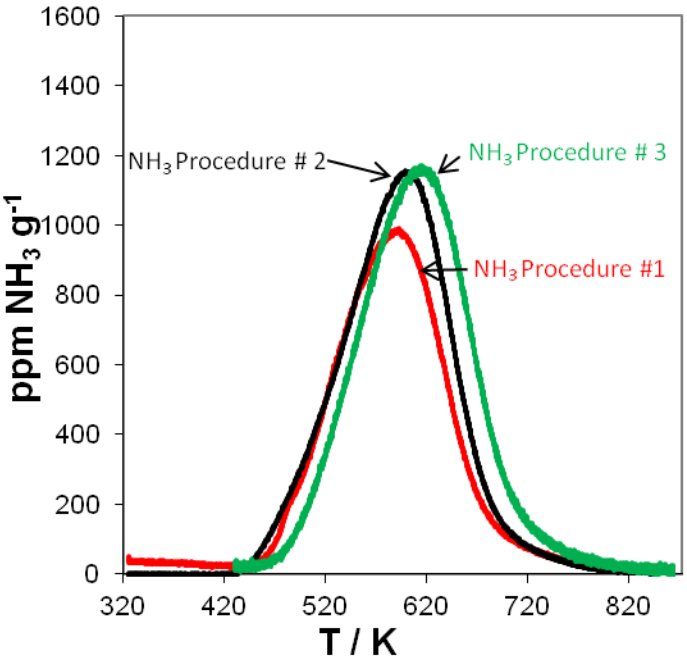


Figure C.4 $NH_3$ –TPDs performed on $NH_4$ –ZSM-5 with Si:Al = 30. This figure includes results from Procedures #1-3 where $NH_3$ was used to saturate the samples and different methods were used to drive off weakly bound $NH_3$ species. Note that the temperature ramp for each experiment was non-linear, therefore the features observed may not reflect the real shapes.

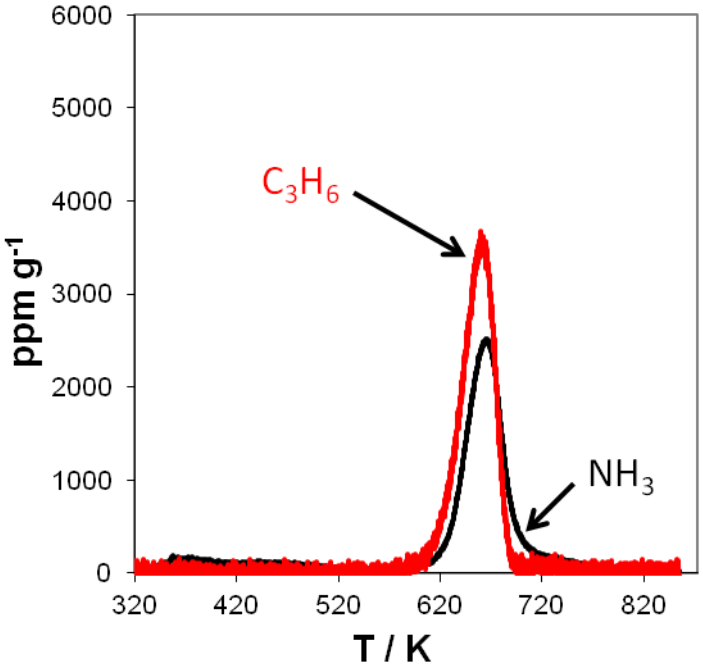


Figure C.5 N-propylamine decomposition over an H-ZSM-5 with Si:Al = 30. The products of the decomposition are $NH_3$ and $C_3H_6$. The temperature was ramped to 823 K at 5 K $min^{-1}$ from 323 K in 350 ml $min^{-1}$. Note that the ramp was non-linear due to constraints of the system.

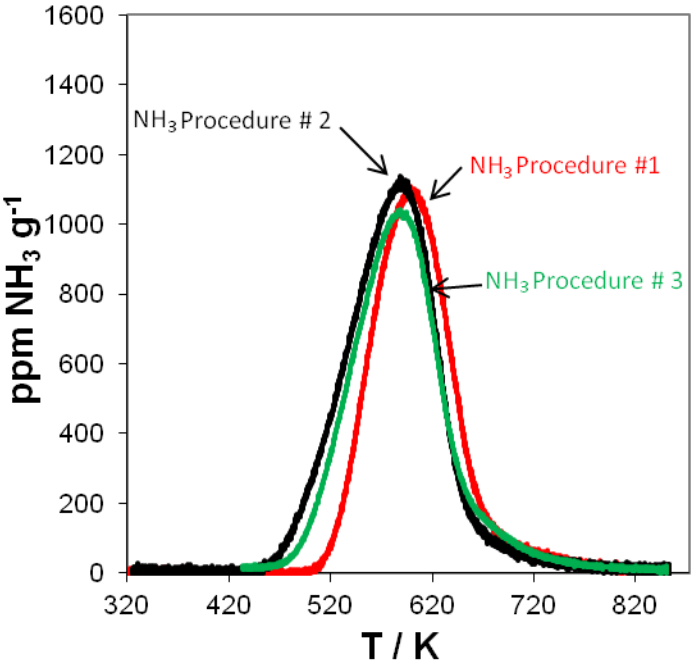


Figure C.6 $NH_3$ –TPDs performed on $NH_4$ –ZSM-5 with Si:Al = 43. This figure includes results from Procedures #1-3 where $NH_3$ was used to saturate the samples and different methods were used to drive off weakly bound $NH_3$ species. Note that the temperature ramp for each experiment was non-linear; therefore the features observed may not reflect the real shapes.

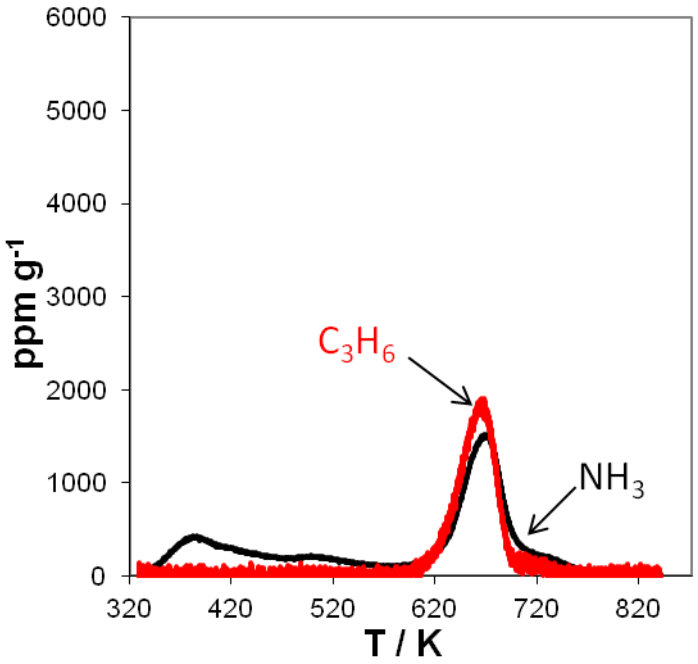


Figure C.7 N-propylamine decomposition over an H-ZSM-5 with Si:Al = 43. The products of the decomposition are $NH_3$ and $C_3H_6$. The temperature was ramped to 823 K at 5 K $min^{-1}$ from 323 K in 350 ml $min^{-1}$. Note that the ramp was non-linear due to constraints of the system.

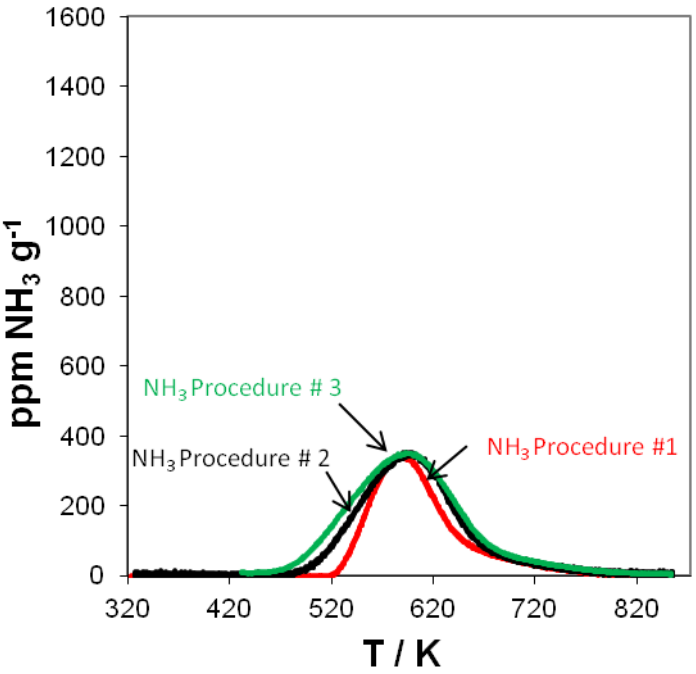


Figure C.8 $NH_3$ –TPDs performed on $NH_4$ –ZSM-5 with Si:Al = 89. This figure includes results from Procedures #1-3 where $NH_3$ was used to saturate the samples and different methods were used to drive off weakly bound $NH_3$ species. Note that the temperature ramp for each experiment was non-linear, therefore the features observed may not reflect the real shapes.

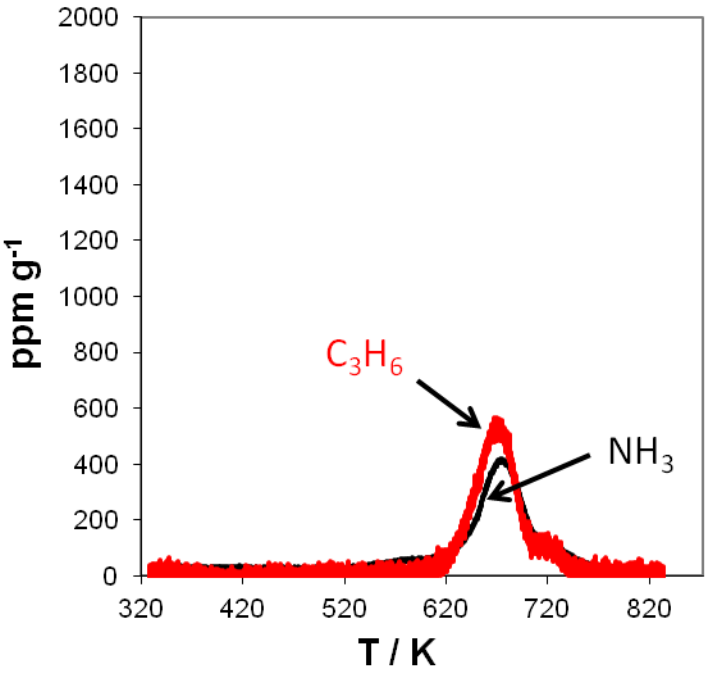


Figure C.9 N-propylamine decomposition over an H-ZSM-5 with Si:Al = 89. The products of the decomposition are $NH_3$ and $C_3H_6$. The temperature was ramped to 823 K at 5 K $min^{-1}$ from 323 K in 350 ml $min^{-1}$. Note that the ramp was non-linear due to constraints of the system.

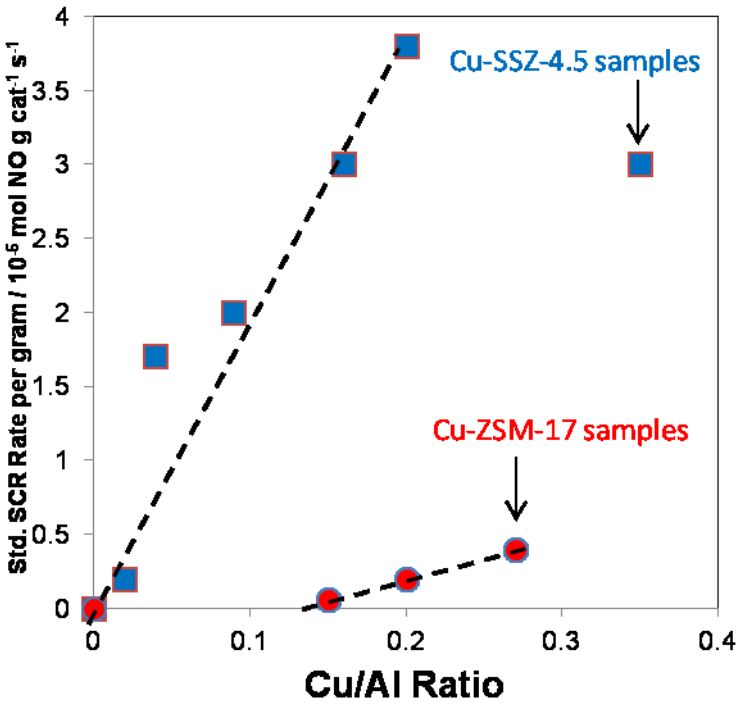


Figure C.10 Standard SCR Rates per gram catalyst for all samples in this study including H- and Cu- forms of ZSM-5 and SSZ-13. Rates are reported at 473 K. Gas conditions used were 320 ppm NO, 320 ppm $NH_3$, 10% $O_2$, 8% $CO_2$, and 7% $H_2O$ in balance UHP He with a total flowrate of 1.5 L $min^{-1}$. 90% confidence interval for rate per gram was ±0.2 mol NO $g^{-1}$ $s^{-1}$.

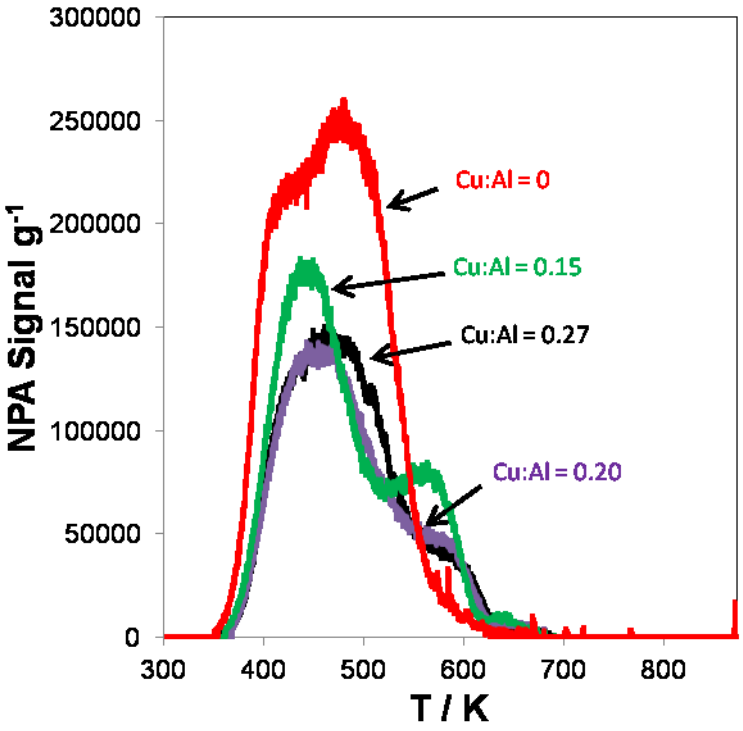


Figure C.11 N-propylamine – TPDs performed on Cu –ZSM-5 samples with Si:Al = 17. This figure includes n-propylamine signal from Procedure #4 where n-propylamine was used to saturate the samples in the gas phase at 323 K and flushed following the adsorption.

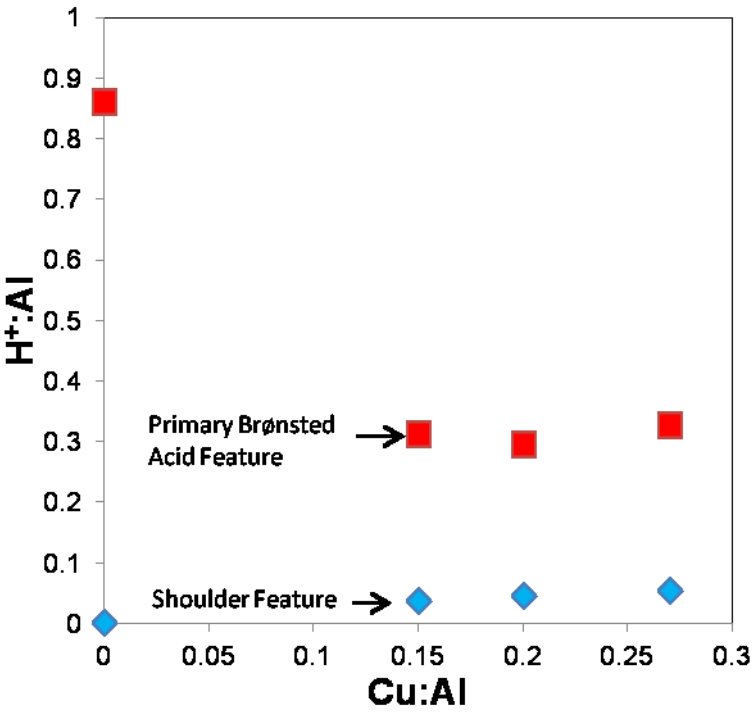


Figure C.12 Summary of de-convoluted features in $C_3H_6$ signal for the n-propylamine decomposition over H- and Cu-ZSM-17 samples.

Determination of the Intermediate Saturation Temperatures used in $NH_3$ Titration Procedure #3

The intermediate temperature chosen in $NH_3$ titration procedure #3 is most easily explained by first examining TPDs in which the samples were saturated with $NH_3$ at a lower temperature. Figure S14-S15 show full TPDs with saturation of H-ZSM-43 and H-SSZ-4.5 with 500 ppm $NH_3$ at 323 K with a total flowrate of 350 ml $min^{-1}$. Both TPDs show a low temperature feature with a peak max at ~ 430 K, which is the basis for the intermediate temperature used in $NH_3$ titration procedure #3. The result of using an intermediate temperature of 433 K on H-ZSM-17 in Figure 4 was one feature centered at ~675 K. This was assigned to Brønsted acid sites based on a study by Woolery et al. [63], which used intermediate temperatures followed by a steaming ($H_2O$) step to remove weakly bound or Lewis-type $NH_3$ species in H-ZSM-5. A similar conclusion was drawn with the H-SSZ-4.5 samples which showed one feature after the $NH_3$ titration (procedure #3) centered at ~725 K in Figure 2, which we assigned to Brønsted acid sites just as in H-ZSM-17.

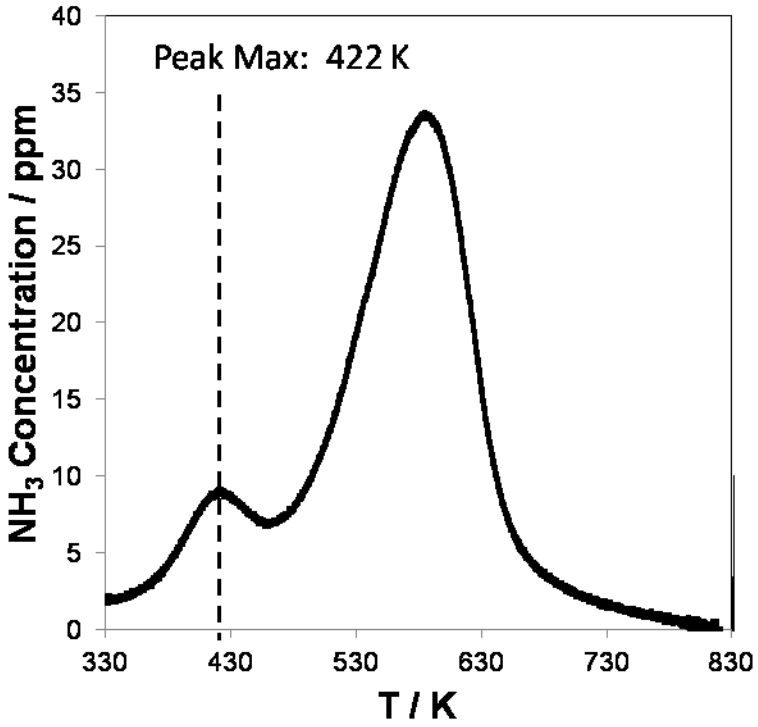


Figure C.13 Full $NH_3$ TPD on H-ZSM-43 sample starting from 323 K and ramped 5 K min-1 to 823 K in UHP He with a total flowrate of 350 ml $min^{-1}$.

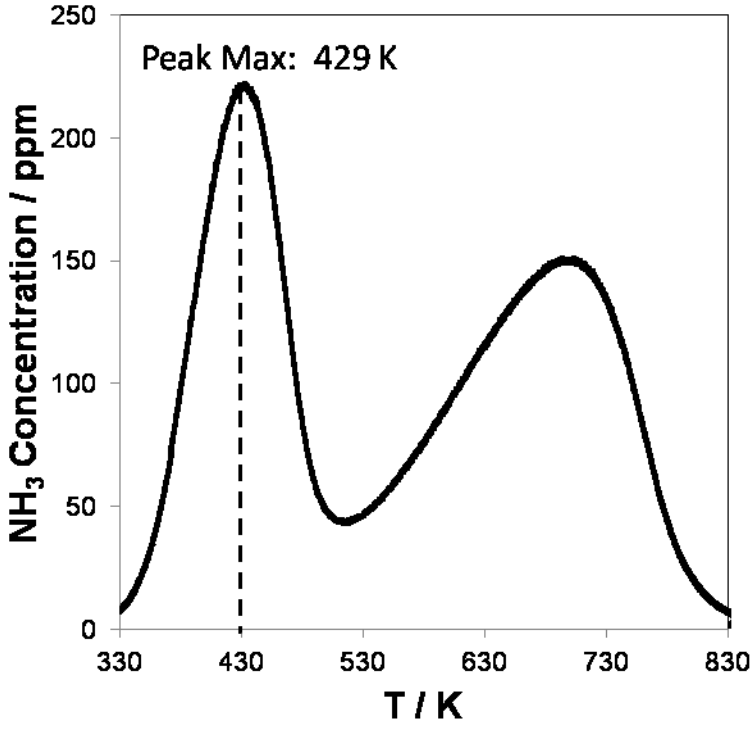


Figure C.14 Full $NH_3$ TPD on H-SSZ-4.5 sample starting from 323 K and ramped 5 K min-1 to 823 K in UHP He with a total flowrate of 350 ml $min^{-1}$.

VITA

# VITA

Shane Adam Bates received his B.S. in chemical engineering at Penn State University, State College, PA in 2008. While at Penn State, Shane had an internship at Lord Corporation. This is where he had his first industrial experience working in a chemical plant. Shane also worked for Professor Ali Borhan during his senior year where he performed work on transport of Newtonian and visco-elastic fluids. In 2010, he received an M.S. in chemical engineering under Professor Chelsey Baertsch. His research topic was to determine the active site in iron molybdate catalysts for the oxidative dehydrogenation of ethanol to acetaldehyde. Upon finishing the M.S. degree, Shane joined the research group of Professor Fabio H. Ribeiro and Professor W. Nicholas Delgass, where he began to work with SCR catalysts and understanding how they work. During this time, Shane learned about many techniques to characterize catalysts, with the primary one being *operando* x-ray absorption spectroscopy. While at Purdue, Shane received some awards. In 2011, Shane received second place for Outstanding Poster at the Annual GSO Symposium. In 2012, Shane received for prize for Outstanding Student poster at the 33$^{rd}$ annual Michigan Catalysis Society Spring Symposium. Shane also received the Andrews Environmental Travel Grant for 2012. After completing his PhD, Shane is going to work for Albemarle Corporation in Baton Rouge, LA for their Fine Chemicals division.